Design of plasmonic nanoparticles and their use for biotoxin immunosensing

Lu Zhang

Sorbonne Université

Nanyang Technological University

Physique et Chimie des Matériaux

School of Materials Science and Engineering

Design of plasmonic nanoparticles and their use for biotoxin immunosensing

Submitted by Lu ZHANG

For the dual degree of Doctor of Philosophy (Ph.D.) of

Sorbonne Université and Nanyang Technological University

Defense scheduled for the 16 November 2018

In front of a jury composed of:

Mrs.	Sabine SZUNERITS	Professor	Reviewer
Mr.	Borja SEPULVEDA	Researcher	Reviewer
Mr.	Shuzhou LI	Associate Professor	Examiner
Mrs.	Sierin LIM	Associate Professor	Examiner
Mrs.	Michèle SALMAIN	Research Director	Examiner
Mr.	Ali ABOU-HASSAN	Associate Professor	Examiner
Mrs.	Souhir BOUJDAY	Professor	Supervisor
Mr.	Bo LIEDBERG	Professor	Co-supervisor

Acknowledgments

The work presented in this thesis has been carried out from October 2015 to September 2018 enrolled under the dual degree PhD programme between Sorbonne Université in France and Nanyang Technological University in Singapore.

This work would not have been possible without numerous support. I thus acknowledge a great number of people.

Foremost, I would like to acknowledge and extend my heartfelt gratitude to my supervisors Pr. Souhir Boujday and Pr. Bo Liedberg who have accepted me as their student in this exciting and challenging project and kept me on track throughout the whole of this journey. Although they have given me the freedom to find my own way sometimes, they have always been around for guidance and for sharing their great knowledge and brilliant ideas. And my sincere thanks undoubtedly go to Dr. Michèle Salmain. I appreciate a lot that she is always there for discussions concerning scientific matters and everything else. Her encouragement for me along all these three years has lighted my journey of research and made me more confident achieving the goals.

I sincerely thank Pr. Sabine Szunerits and Dr. Borja Sepulveda for being reviewers of my thesis, as well as Assoc. Pr. Shuzhou Li, Assoc. Pr. Sierin Lim, and Assoc. Pr. Ali Abou-Hassan for agreeing to be members of the jury of my thesis.

I am very grateful to all the people that have come and gone throughout these three years in the three labs, Laboratoire de Réactisvité de Surface (LRS) and Institut Parisien de Chimie Moléculare (IPCM) in Sorbonne Université and Centre for Biomimetic Sensor Science (CBSS) in Nanyang Technological University. All of you have made my time inside as well as outside the labs very pleasurable and instructive.

I want to thank Pr. Hélène Pernot, director of LRS, that has received me in this lab. I would also thank Dr. Juliette Blanchard that recommended me to this project and also for her support through these years. Thanks also go to Dalil Brouri and Sandra Casale for helping me with the electron microscopy, Clément Guibert for sharing the knowledge of colloidal nanoparticles, Sonia M'Barek, Annie Mettendorff, Sabine Même and Isabelle Vuillaume for administrative support. I'm also very grateful to my colleagues Maroua Ben Haddada, David Hu, Alexis

Loiseau, Médéric Lequeux, Yacine Mazouzi, Vincent Pellas and Somia Tomane for their help, support, and sharing the pleasurable time in lab. Thanks also Elisa Silva-Gomes and Ricardo Garcia de Castro for their understanding and support especially during the period of redaction of my thesis.

I would also thank Anne Vessieres, Nathalie Duran, Yong Wang, Liang Chang from IPCM for sharing the experience of research and life.

I also acknowledge my colleagues from CBSS, Xueling Feng, Peng Chen, James Ho, Gaurav Sinsinbar, Garima Goyal, Gopal Ammanath, Nevena Klisara, and Amit Kumar. With their help and support, I could have had a good time in Singapore. Special thanks to Meixia Tay for her help with administrative activities.

Finally, I would like to thank my parents, my brother, my sister-in-law, my super lovely niece and nephew for supporting, encouraging and believing in me. And Christoph Steininger for all patience and love.

Thanks to all again. Without the invaluable help and support from all of you, none of this work would have been possible.

Paris, October 2018.

Lu Zhang

Contents

General Introduction

Biotoxins are toxic substances produced by microorganisms (bacteria, fungi, microalgae *etc.*) for predation or defense of predation from other species. Food contaminated by these microorganisms and/or biotoxins at some stages of the food production chain and subsequently ingested by human is a threat to the human health. For instance, staphylococcal enterotoxins (SEs) produced by some *Staphylococcus aureus* strains are a major cause of food poising and especially represent the second cause of foodborne diseases in France.[1] It is generally admitted that ingestion of as low as 100 ng is sufficient to cause intoxication symptoms in the form of severe gastroenteritis. Until now, at least 21 different serotypes have been identified with serotype A (SEA) being the most frequently encountered biotoxin in food poisoning outbreaks by *S. aureus*.[2] SEA is a small monomeric protein (28 kDa) with high thermal and proteolytic stability[3], so that even consumption of cooked food can be deleterious to health if contaminated. For example, in year 2000, SEA caused the poisoning of more than 14 000 Japanese who consumed contaminated milk from Japan's biggest dairy factory.[4] Thus, control of food safety all along the production chain and early detection of biotoxin are required to prevent food poisoning outbreaks.

Detection of SEA in food matrices is rather difficult since it is usually present at very low concentrations and the matrix (milk, cheese *etc.*) contains many other potentially interfering proteins that may lead to false results. Enzyme immunoassay techniques for SEA detection [5-6] provide good sensitivity. However, the multi-step procedure is generally time-consuming. Radioimmunoassay of SEA[7] also provides good sensitivity, but the handling of the radioactive waste remains problematic. As an alternative, biosensors operating with optical[8-10], acoustic[11-14] or electrical[15] transduction modes for the detection of SEA were also developed with variable working range and sensitivity. These analytical methods provided results in a much shorter time than ELISA-type assays. However, these tests requiring expensive instruments and well-trained technicians are therefore needed to be carried out in dedicated laboratories.

Nanomaterials have drawn a lot of interest in the development of toxin biosensing.[16] The high surface area-to-volume ratio of nanomaterials provides more active surface regions and thus potentially improves the biosensing performances. Among the nanomaterials, gold nanoparticles (AuNPs) are especially attractive[17] because of their ease of synthesis and functionalization, biocompatibility, and inertness and, more importantly, their unique optical

properties owing to the Localized Surface Plasmon Resonance (LSPR) phenomenon[18-19]. The so-called LSPR phenomenon is generated by an incident light wave trapped within conductive nanoparticles smaller than the wavelength of incident light. The conduction electrons in nanoparticles oscillate collectively at a resonance frequency induced by the incident light. As a result, AuNPs absorb or scatter the light very intensely at a certain wavelength.

The extremely high extinction coefficient of AuNPs in the visible spectral range promoted the development of lateral flow immunoassays to visually detect SEA[20]. However, they do not usually provide quantitative information and display limited sensitivity. Another family of AuNP-based biosensing assays relies on the sensitivity of the LSPR band to local refractive index change on AuNP upon binding SEA.[16] Although this biosensing assay was fast and provided high sensitivity, the detection required a spectrometer with high spectral resolution. Clearly, there is an urgent need of specific, sensitive, as well as rapid, easy-to-use and cost-effective analytical methods to detect and quantify SEA in food matrices.

My work, presented in this thesis, has been focused on the design of plasmonic nanoparticles and their applications for SEA immunosensing in milk, especially aiming at the development of biosensing devices from which SEA detection could be achieved by naked-eye readout.

This thesis is comprised of the following chapters written as scientific publications.

I. Antibody-Gold Nanoparticle Bioconjugates - Applications in Optical Biosensing (Literature Review).
II. Direct Quantification of Surface Coverage of Antibody in IgG-Gold Nanoparticles Conjugates.
III. Naked-Eye Immunosensing of a Food Biotoxin using Gold Nanoparticles-Antibody Bioconjugate.
IV. Spatially Controlled Reduction and Growth of Silver in Hollow Gold Nanoshell Particles.
V. Core-Shell Gold Silver Nanoparticles for Plasmonic Biosensing of Toxins: Towards Naked-Eye Detection.

Globally, these papers are divided into two closely linked parts, where the first part is based on pure spherical gold nanoparticles (AuNPs) (papers I to III) and the second part is focused on gold-silver nanoparticles (papers IV-V). The work contained in each paper is briefly summarized before each paper.

REFERENCES

1. Kérouanton, A.; Hennekinne, J. A.; Letertre, C.; Petit, L.; Chesneau, O.; Brisabois, A.; De Buyser, M. L., Characterization of Staphylococcus aureus strains associated with food poisoning outbreaks in France. *Int. J. Food Microbiol.* **2007,** *115* (3), 369-375.

2. Balaban, N.; Rasooly, A., Staphylococcal enterotoxins. *Int. J. Food Microbiol.* **2000,** *61* (1), 1-10.

3. Schantz, E. J.; Roessler, W. G.; Woodburn, M. J.; Lynch, J. M.; Jacoby, H. M.; Silverman, S. J.; Gorman, J. C.; Spero, L., Purification and some chemical and physical properties of staphylococcal enterotoxin A. *Biochemistry* **1972,** *11* (3), 360-366.

4. Asao, T.; Kumeda, Y.; Kawai, T.; Shibata, T.; Oda, H.; Haruki, K.; Nakazawa, H.; Kozaki, S., An extensive outbreak of staphylococcal food poisoning due to low-fat milk in Japan: estimation of enterotoxin A in the incriminated milk and powdered skim milk. *Epidemiol. Infect.* **2003,** *130* (1), 33-40.

5. Freed, R. C.; Evenson, M. L.; Reiser, R. F.; Bergdoll, M. S., Enzyme-linked immunosorbent assay for detection of staphylococcal enterotoxins in foods. *Appl. Environ. Microbiol* **1982,** *44* (6), 1349-1355.

6. Park, C. E.; Akhtar, M.; Rayman, M. K., Simple solutions to false-positive staphylococcal enterotoxin assays with seafood tested with an enzyme-linked immunosorbent assay kit (TECRA). *Appl. Environ. Microbiol* **1993,** *59* (7), 2210-2213.

7. Miller, B. A.; Reiser, R. F.; Bergdoll, M. S., Detection of staphylococcal enterotoxins A, B, C, D, and E in foods by radioimnunoassay, using staphyloccal cells containing protein A as immunoadsorbent. *Appl. Environ. Microbiol* **1978,** *36* (3), 421-426.

8. Medina, M. B., A biosensor method for detection of Staphylococcal enterotoxin A in raw whole egg. *J. Rapid Methods Autom. Microbiol.* **2006,** *14* (2), 119-132.

9. Rasooly, L.; Rasooly, A., Real time biosensor analysis of staphylococcal enterotoxin A in food. *Int. J. Food Microbiol.* **1999,** *49* (3), 119-127.

10. Tsai, W.-C.; Li, I.-C., SPR-based immunosensor for determining staphylococcal enterotoxin A. *Sens. Actuators B* **2009,** *136* (1), 8-12.

11. Salmain, M.; Ghasemi, M.; Boujday, S.; Spadavecchia, J.; Técher, C.; Val, F.; Le Moigne, V.; Gautier, M.; Briandet, R.; Pradier, C.-M., Piezoelectric immunosensor for direct and rapid detection of staphylococcal enterotoxin A (SEA) at the ng level. *Biosens. Bioelectron.* **2011,** *29* (1), 140-144.

12. Salmain, M.; Ghasemi, M.; Boujday, S.; Pradier, C.-M., Elaboration of a reusable immunosensor for the detection of staphylococcal enterotoxin A (SEA) in milk with a quartz crystal microbalance. *Sens. Actuators B* **2012,** *173*, 148-156.

13. Karaseva, N.; Ermolaeva, T., A regenerable piezoelectric immunosensor on the basis of electropolymerized polypyrrole for highly selective detection of Staphylococcal Enterotoxin A in foodstuffs. *Microchim. Acta* **2015,** *182* (7-8), 1329-1335.

14. Ben Haddada, M.; Salmain, M.; Boujday, S., Gold colloid-nanostructured surfaces for enhanced piezoelectric immunosensing of staphylococcal enterotoxin A. *Sens. Actuators B* **2018,** *255*, 1604-1613.

15. Pimenta-Martins, M. G. R.; Furtado, R. F.; Heneine, L. G. D.; Dias, R. S.; de Fátima Borges, M.; Alves, C. R., Development of an amperometric immunosensor for detection of staphylococcal enterotoxin type A in cheese. *J. Microbiol. Methods* **2012,** *91* (1), 138-143.

16. Ben Haddada, M.; Hu, D.; Salmain, M.; Zhang, L.; Peng, C.; Wang, Y.; Liedberg, B.; Boujday, S., Gold nanoparticle-based localized surface plasmon immunosensor for staphylococcal enterotoxin A (SEA) detection. *Anal. Bioanal. Chem.* **2017,** *409* (26), 6227-6234.

17. Li, Y.; Schluesener, H. J.; Xu, S., Gold nanoparticle-based biosensors. *Gold Bulletin* **2010,** *43* (1), 29-41.

18. Faraday, M., X. The Bakerian Lecture.—Experimental relations of gold (and other metals) to light. *Philos. Trans. R. Soc. London* **1857,** *147* (159), 145-181.

19. Mie, G., Beiträge zur Optik trüber Medien, speziell kolloidaler Metallösungen. *Ann. Phys.* **1908,** *330* (3), 377-445.

20. Wang, W.; Liu, L.; Xu, L.; Kuang, H.; Zhu, J.; Xu, C., Gold-Nanoparticle-Based Multiplexed Immunochromatographic Strip for Simultaneous Detection of Staphylococcal Enterotoxin A, B, C, D, and E. *Part. Part. Syst. Charact.* **2016,** *33* (7), 388-395.

Paper I

Antibody-Gold Nanoparticle Bioconjugates - Applications in Optical Biosensing (Literature Review)

Preface

Taking advantage of the striking optical properties of gold nanoparticles (AuNPs) owing to the Localized Surface Plasmon Resonance (LSPR) phenomenon and the incomparable affinity and specificity of antibody (Ab) for its antigen, we were interested in applying AuNPs as transducer and Ab as bioreceptor to design biosensing platforms. In the first stage, a survey of the recent literature was carried out which highlighted the different strategies employed for conjugation of the Ab on AuNPs. The conjugation approaches include physisorption of Ab on AuNPs which is straightforward and chemisorption of Ab on AuNPs where chemical modifications of Ab or AuNPs are required. The chemical modifications of functional groups or sites in Ab and the modifications of AuNP surface have been presented in detail. Besides, the quantification methods of Ab surface coverage in AuNP-Ab conjugates were also summarized, including both direct and indirect approaches. We noticed that although the quantification of Ab surface coverage is important to assess the bioconjugation, it still remains challenging. In addition, selected applications of AuNP-Ab bioconjugates in optical biosensing were presented, which covered the LSPR, surface enhanced Raman scattering (SERS), fluorescence-enhancement or quenching/dequenching(recovery) biosensing platforms.

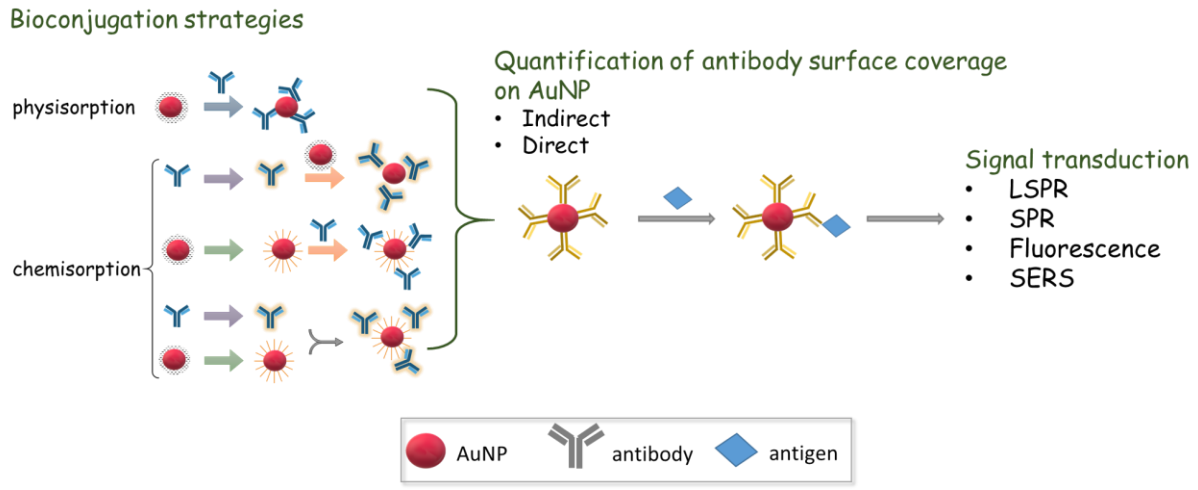

Figure I: Literature review contents: bioconjugation strategies, quantification of antibody surface coverage on gold nanoparticles and signal transduction in biosensing.

Antibody-Gold Nanoparticle Bioconjugates - Applications in Optical Biosensing (Literature Review)

Lu Zhang[1,2,3,4], Michèle Salmain[2], Bo Liedberg[3], and Souhir Boujday[1]*

[1] Sorbonne Université, CNRS, Laboratoire de Réactivité de Surface (LRS), 4 place Jussieu, F-75005 Paris, France.

[2] Sorbonne Université, CNRS, Institut Parisien de Chimie Moléculaire (IPCM), 4 place Jussieu F-75005 Paris, France.

[3] Centre for Biomimetic Sensor Science, School of Material Science and Engineering, Nanyang Technological University, 637553 Singapore.

[4] Sorbonne University and Nanyang Technological University Dual Degree PhD Programme.

Laboratoire de Réactivité de Surface, UMR CNRS 7197, *Sorbonne Université,* case 178, 4 Place Jussieu, 75252 Paris cedex 05, France.

Tel: +33144276001, Fax: +33144276033, souhir.boujday@sorbonne-universite.fr

Contents

INTRODUCTION

Gold nanoparticles (AuNPs) are widely used in the fields of biosensing, diagnostics, nanomedicine *etc*.[1-5] Because of the incomparable affinity and specificity to target, antibody (Ab) as bioreceptor long has been used in conjunction with AuNPs. A good conjugation method should produce stable AuNP-Ab conjugates while maintaining the ability of the Ab to recognize and bind to its corresponding antigen. Thus, a robust conjugation method is of critical importance for improving the sensitivity of biosensors. To evaluate the coupling chemistry between Ab and AuNPs and quantify the Ab surface coverage on AuNPs, various quantification methods have been applied via direct or indirect approaches. In this review, we will focus on IgG-type antibodies conjugated to spherical AuNPs and present the strategies of conjugation, followed by quantification methods of Ab surface coverage, and finally selected applications in optical biosensing.

BIOCONJUGATION METHODS

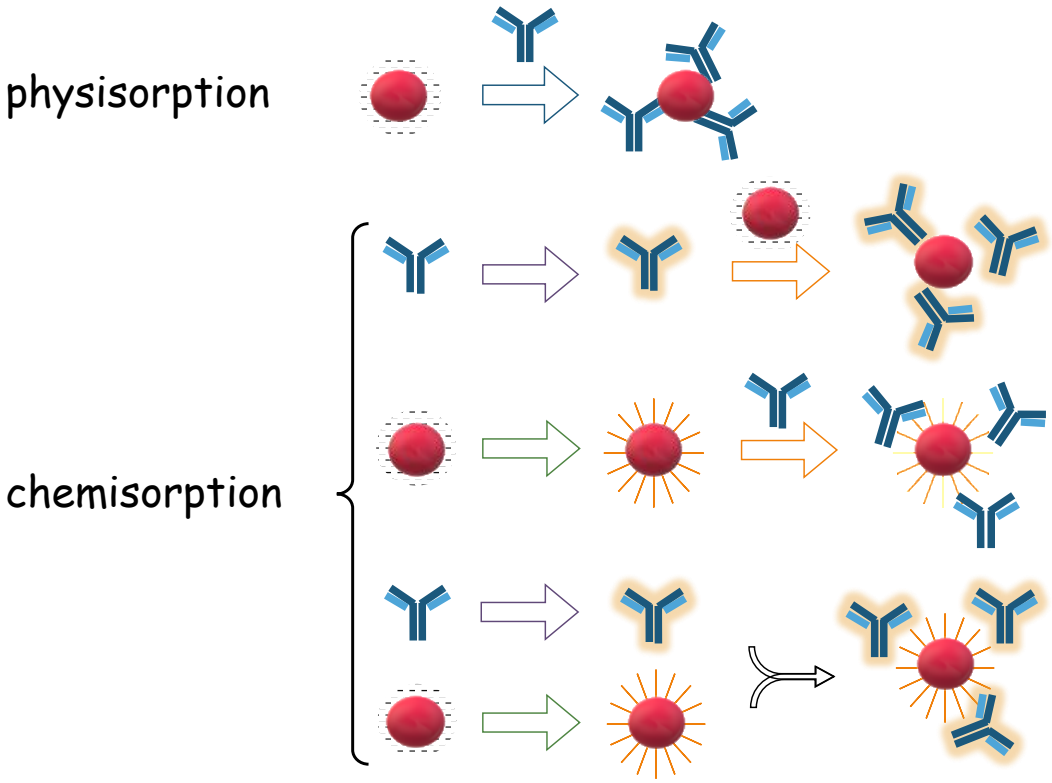

Figure 1 : Conjugation of antibody on gold nanoparticles via physisorption and chemisorption via (i). modification of antibody, (ii). modification of gold nanoparticle and (iii). modification of antibody and gold nanoparticle at same time.

In this section, we will describe different strategies that have been applied to AuNP-Ab conjugation. These strategies are based on physisorption or chemisorption via modification of Ab and/or of AuNPs. (Figure 1)

Physisorption

Physisorption is generally established through electrostatic, hydrogen bonding, hydrophobic, and Van der Waals attractive forces between AuNPs and Ab. It is the simplest and most straightforward conjugation method. It requires minimal expertise in synthesis. Its easiness is based on the fact that it is not necessary to chemically modify the Ab nor the AuNPs.

During the preparation of AuNP-Ab conjugates by physisorption, several parameters should be considered: (a) the isoelectric point (pI) of the Ab, (b) the pH of adsorption solution, and (c) the added quantity of Ab.[6] It is generally agreed that maximal adsorption of proteins occurs when the pH is close to or slightly above their pI.[7-11] For many proteins, especially antiserum-derived immunoglobulins, the average pI spans over a broad range of pH values. The optimal coupling pH for a given Ab should be determined through measurement of the relative pI range of Ab. In practice, conjugation is tested at different pH to find the optimal value. However, many antibodies are best adsorbed at a pH 8-9. Next, the added quantity of Ab for adsorption is determined through the flocculation test. This test allows to determine the minimum amount of Ab to maintain AuNPs stability against salt-induced aggregation, *e.g.* 10% NaCl. Aggregation may be monitored by the color change of the colloidal solution or by measuring the absorbance of the solution at its λ_{max}.[12] In practice, the final added amount of Ab is the minimum amount plus 10% - 20%[13-14] to produce the AuNP-Ab conjugates. Finally, many protocols include a subsequent step to stabilize the conjugate suspension by addition of polyethylene glycol (PEG, 1%)[12-13, 15] or BSA (0.25%)[14, 16]. These blocking agents also mask any remaining free sites on AuNPs, thus preventing nonspecific binding during assaying.[17] Most protocols of Ab physisorption to AuNPs were established as mentioned above.[18-20]

Tokuyasu reported that addition of large excess of protein to AuNPs yields conjugates with high specific activity.[21] Nevertheless, there was evidence that overloading may cause progressive loss of loosely bound protein.[22] Byzova *et al.* found that Ab concentration used for conjugation can be reduced below the stabilizing concentration without losing antigen-capturing activity of the conjugates.[23] Hence, the optimal Ab concentration should be chosen for each individual case considering the colloidal stability and retention of Ab activity. Besides

the factor of Ab concentration, Geng *et al.* showed that additional purification of synthesized AuNPs prior to conjugation to polyclonal Ab at acidic pH improved the reproducibility of conjugate preparation and this conjugate displayed excellent analytical performances.[24]

Physisorption of Ab to AuNPs displays two main drawbacks: (1) the Ab is randomly immobilized on AuNPs; (2) the attachment is weak. Under binding equilibrium, AuNP-bound and free Ab co-exist in the conjugate sample. And multilayer adsorption of polyclonal antibodies may occur. The loosely bound layers except first and second layers may desorb, thus making the conjugates less stable over time.

Chemisorption

Chemisorption of Ab is not as straightforward as physisorption, but the former provides higher stability and better reproducibility. It requires several steps, for instance, chemical modification of Ab or/and AuNPs prior to conjugation depending on the coupling chemistry selected.

Chemical modification of antibody

The sulfhydryl group is very attractive for conjugation of Ab to AuNPs since it forms a strong Au-S bond. However, there are no free sulfhydryl groups in antibodies. Thus, the sulfhydryl groups need to be created (by reaction of appropriate thiolation reagent systems) or generated (by reduction of endogenous disulfides). This section will discuss modification of the functional groups on antibodies used for covalent binding, including common groups such as amine, carboxylate, carbohydrate moieties, disulfides, and also special sites like the nucleotide binding site (NBS). (Figure 2)

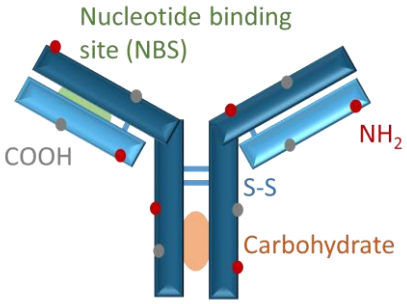

Figure 2 : Important functional groups on immunoglobulin G (IgG).

Binding through amino groups

Amino groups are abundant in antibodies and are mostly located at the surface owing to their polarity and charge (positive at physiological pH). They are found on the side chain of lysines and at the N-terminal position of the light and heavy chains of IgG. What is more, amines are very reactive towards many reagents without any previous activation owing to their nucleophilicity.

For example, Traut's reagent (2-iminothiolane, Figure 3) undergoes ring-opening reaction with a primary amine to generate a sulfhydryl group (Figure 4). This process is very efficient and proceeds rapidly at slightly basic pH.[25-27] Another similar reagent, N-acetyl homocysteine thiolactone (also called citiolone or 2-acetamido-4-mercaptobutyric acid, Figure 3) can be used alternatively. The corresponding thiolation reaction is much like the reaction of Traut's reagent. But Ab modification often results in much lower yields unless the reaction is done for extended period of time and at very basic pH (10-11).[25]

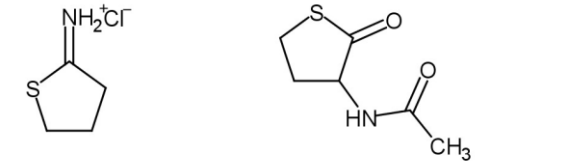

Traut's Reagent; 2-Iminothiolane Mw 137.6

N-Acetyl Homocysteine Thiolactone Mw 159

Figure 3 : Thiolation reagents: Traut's reagent (2-iminothiolane) and N-acetyl homocysteine thiolactone (citiolone or 2-acetamido-4-mercaptobutyric acid).

Amine Containing Antibody Traut's Reagent Thiolated Antibody

Figure 4 : Traut's reagent reacts with amino group of antibody.

Since Bragg and Hou introduced N-hydroxysuccinimide (NHS) esters as activated carboxylic acids in 1980,[28] they became the major amine-coupling reagents in bioconjugation chemistry as a result of their excellent reactivity toward primary amines at physiological pH. For instance,

N-succinimidyl S-acetylthioacetate (SATA, Figure 5) and N-succinimidyl S-acetylthiopropionate (SATP, Figure 5) react with proteins amino groups forming stable amide linkages and protected sulfhydryl groups in the form of thioesters (Figure 6). This protecting group can be released with hydroxylamine to form free –SH just before conjugation to AuNPs.[25]

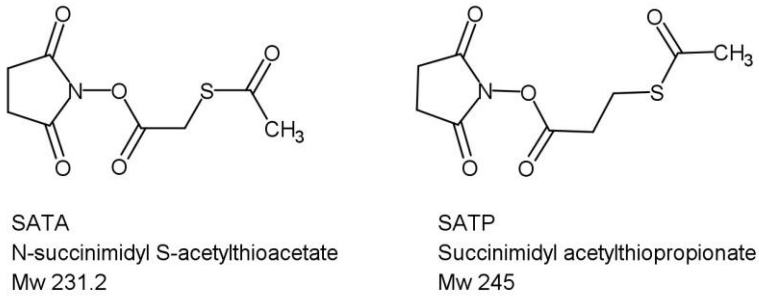

Figure 5 : Reagents: N-succinimidyl S-acetylthioacetate (SATA) and N-succinimidyl S-acetylthiopropionate (SATP).

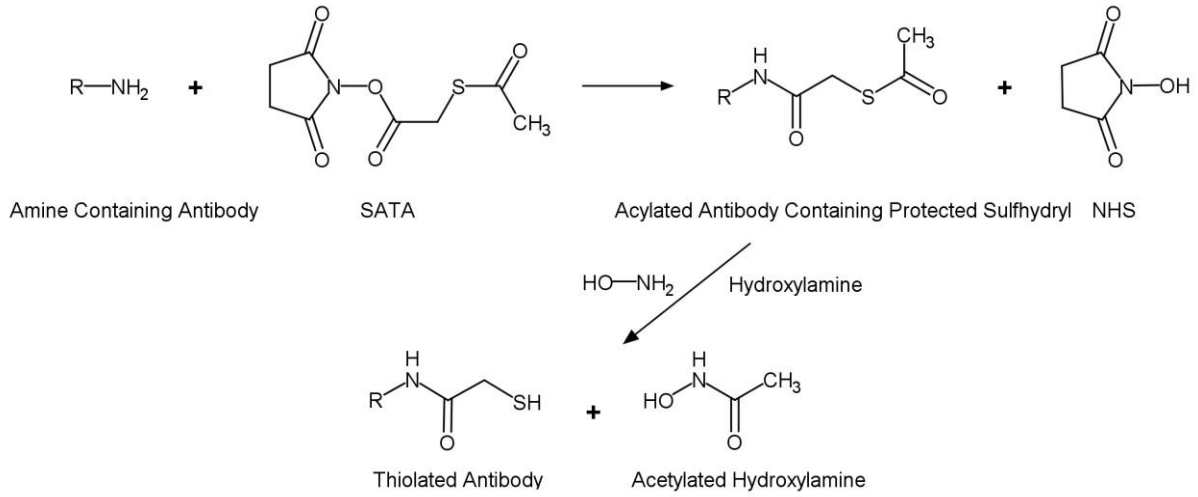

Figure 6 : SATA reacts with available amino groups of antibody.

In addition, disulfide bond-containing NHS esters are very attractive as the disulfide self-assembles on AuNPs by formation of Au-S bonds. For example, sulfoNHS-activated modifier 3,3'-dithiobis(sulfosuccinimidylpropionate) (DSPPT),[29] N-succinimidyl 3-(2-pyridyldithio)propionate (SPDP)[30] and N-succinimidyl 6-(3(2-pyridyldithio)propionamido)hexanoate) (LC-SPDP)[31] (Figure 7) were used to modify amino groups of Ab prior to AuNPs chemisorption. Reagent including poly(ethylene glycol) (PEG) linker, like OPSS-PEG-NHS (Figure 7) was also applied.[32] The length of the PEG linker could

be controlled, thus the Ab could be a bit far away from AuNP, having less risk of steric hindrance. At the same time, PEG also helps to prevent nonspecific protein binding on AuNPs.

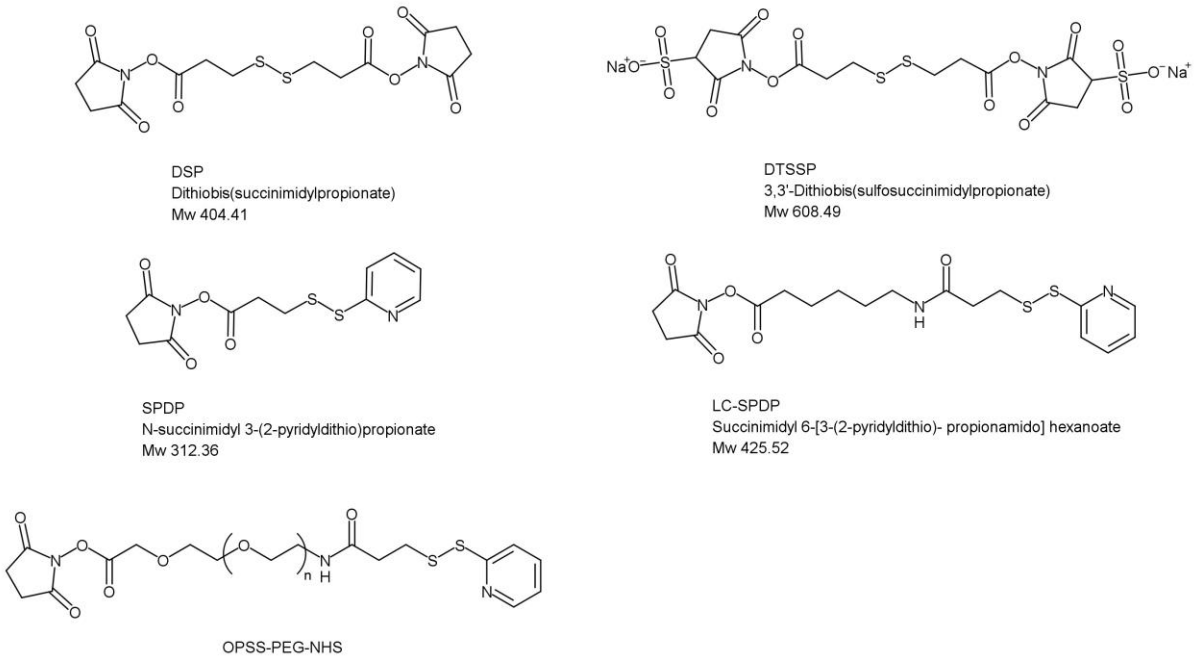

Figure 7 : Reagents: disulfide bond containing NHS esters.

However, amine reactive coupling chemistry via NHS esters presents a major drawback owing to the rapid degradation of NHS esters by hydrolysis whose rate is comparable to the acylation rate.[33] Thus, large excess of Ab is required to favor the acylation reaction. This strategy, binding via amino groups, results in randomly oriented Ab molecules on AuNPs. (Figure 8) This may cause partial loss of antigen binding capacity due to direct binding of the antigen binding site on AuNPs or steric hindrance with 'head-on' and 'side-on' spatial orientations.

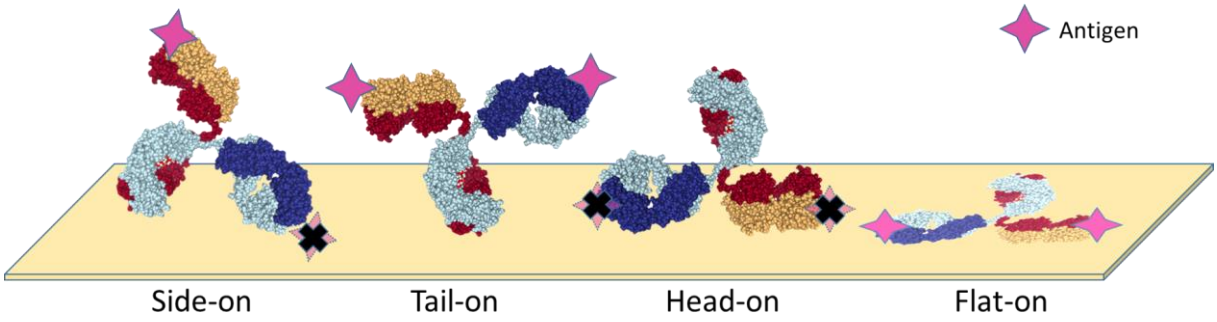

Figure 8 : Possible spatial orientations of antibody on surface.

Binding via carboxylate groups

Carboxylate groups (present on the side chain of glutamic acid and aspartic acid and at the C-terminal position of the light and heavy chains of IgG) are not as reactive as amino groups, so they need to be previously activated for example by NHS/EDC. However, after the carboxylate group is activated, it may react with the amino groups of another Ab molecule resulting in antibody crosslinking. Thus, it is not suitable for the following conjugation to AuNPs.

Binding via carbohydrate groups

The Fc region of polyclonal IgG produced by the major species (rabbit, goat and so on) contains carbohydrate chains. (Figure 2) Binding through these sugar moieties, the antibody will be immobilized on AuNPs in oriented fashion. This strategy requires a first step in which the carbohydrates are mildly oxidized by sodium periodate ($NaIO_4$) to create reactive aldehydes. Then aldehyde-activated sugars can react with hydrazide, for example 2-acetamido-4-mercaptobutyric acid hydrazide (AMBH), forming hydrazone linkage (also called Schiff base) and leaving a free terminal sulfhydryl group. The Schiff base is further stabilized by reduction with sodium cyanoborohydride (Figure 9).[25] Other heterobifunctional PEG linkers, like monothiol-PEG-hydrazide or dithiol-PEG- hydrazide (Figure 10) have been widely used by different research groups.[34-38]

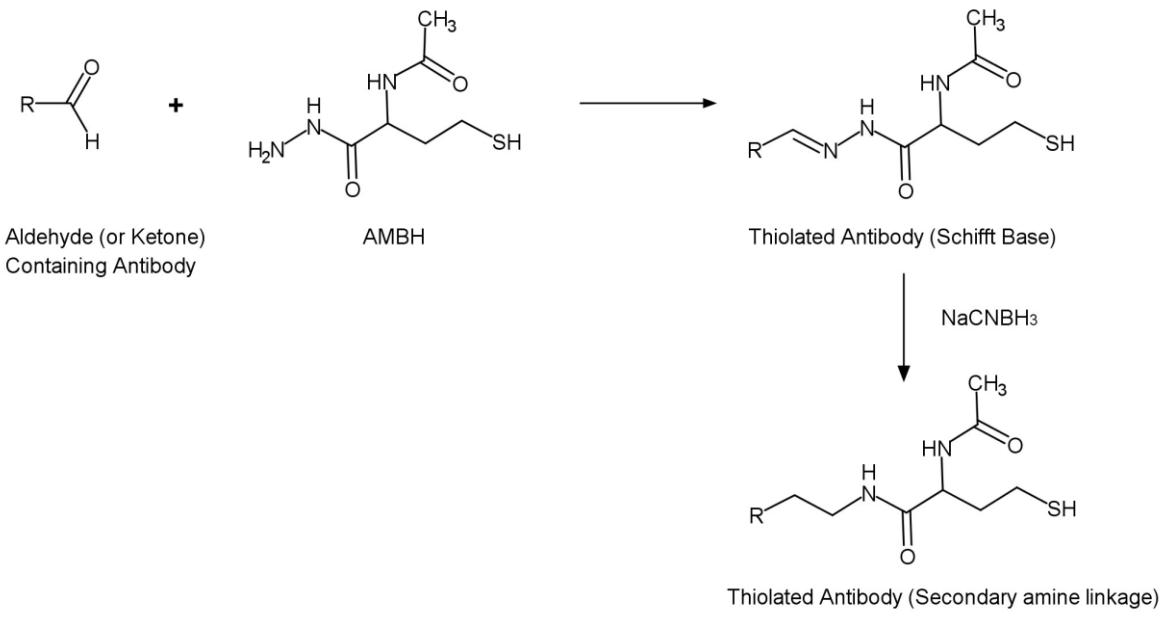

Figure 9 : Hydrazide reacts with aldehyde on antibody.

A major limitation of this strategy is that Ab should be glycosylated. Polyclonal antibodies (from antisera) are usually glycosylated, but some other Ab preparations may not have carbohydrates such as recombinant antibodies fermented in bacteria, or some monoclonal antibodies that did not undergo post-translational glycosylation.

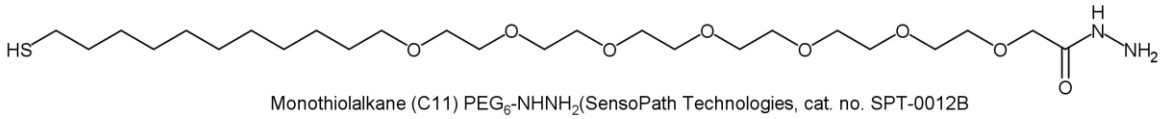

Monothiolalkane (C11) PEG_6-$NHNH_2$(SensoPath Technologies, cat. no. SPT-0012B
Mw 540.76

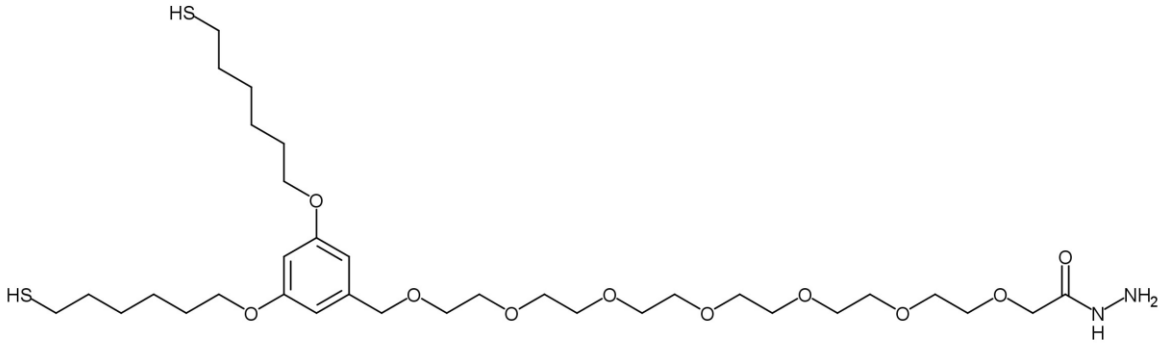

Dithiolalkanearomatic PEG_6-$NHNH_2$ (SensoPath Technologies, cat. no. SPT-0014B
Mw 708.97

Figure 10 : Commercial thiol-PEG- hydrazide linkers.

Binding via sulfhydryl groups

UV-PIT. Ab can be directly immobilized on gold surfaces by using a UV light-induced approach, known as photochemical immobilization technique (PIT).[39] (Figure 11) Briefly, tryptophan residues absorb UV light and relax by transferring the absorbed energy to their neighbors. If a cystine (formed by 2 cysteines bound together by a disulfide bridge) is close enough to the tryptophan, the photon energy is virtually absorbed by cystine, leading to cleavage of disulfide bridge. The resulting free thiol groups can anchor efficiently to gold substrates. The native structural and functional properties of Ab are preserved. An increase of sensor sensitivity and of linear range has been shown using PIT method.[40] This method was shown effective also for the conjugation of Ab to AuNPs.[41]

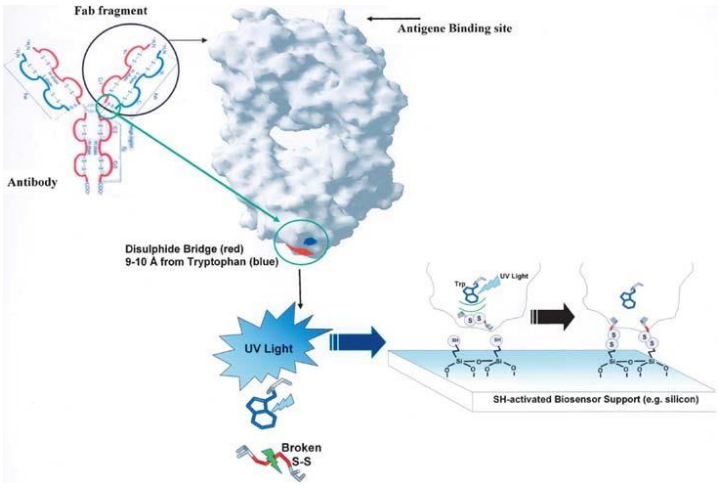

Figure 11 : Location of tryptophan residues on antibody and photochemical immobilization technique (PIT). Picture is adapted from ref.[39].

Fragmentation. In antibodies, the sulfhydryl groups borne by the cysteine residues are all engaged in disulfide bridges, and they are important to the Ab function as they: i) contribute to the tertiary structure of each Ab subunit (intrachain S-S bridges), and covalently connect ii) the heavy to the light chains and iii) the two heavy chains at the hinge region (interchain S-S bridges). (Figure 12) As only free sulfhydryl groups of Ab can be conjugated directly to AuNPs, the native disulfide bonds must be selectively cleaved by reducing agents while preserving the antigen-binding capacity. The reduction of Ab is affected by several factors, for example, Ab host, pH, reductant and reductant concentration. By careful manipulation of these factors, high yield of half-Ab fragments can be obtained.[42]

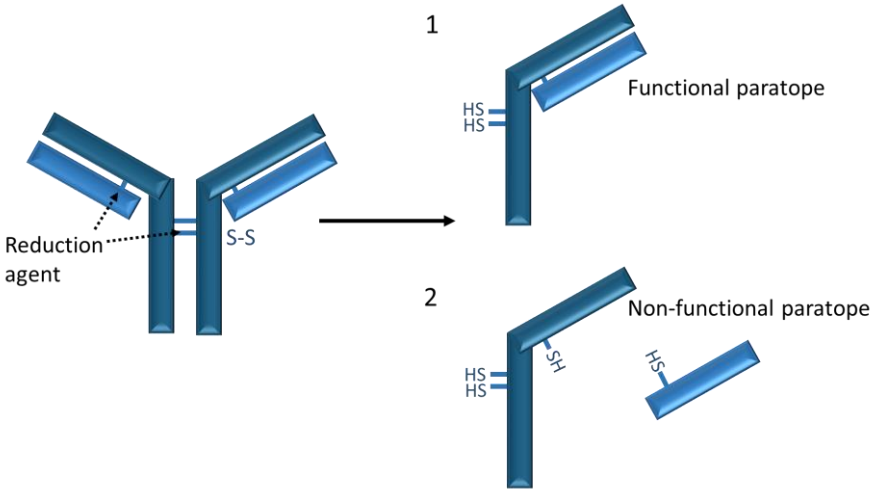

Figure 12 : Reduction of antibody: (1) antibody fragments with functional paratope; (2) antibody fragments with non-functional paratope.

For instance, at moderate concentration of dithiothreitol (DTT, Figure 13 and Figure 14-A) and absence of denaturant (such as urea, guanidine or SDS), limited cleavage of disulfide bridges of antibodies can result in reducing mainly the ones between the two heavy chains in the hinge region (rabbit and goat IgGs have two disulfide bridges in this region). This produces two half-antibodies, each containing one antigen binding site and free sulfhydryls at the hinge region (Figure 12-1).[26, 43-44] Other reducing reagents, such as 2-mercaptoethanolamine (2-MEA, Figure 13 and Figure 14-B)[45-47] and tris(2-carboxyethyl)phosphine (TCEP, Figure 13 and Figure 14-C)[48-50], are widely used for Ab reduction. Both 2-MEA and DTT contain thiol groups that may compete with the reduced antibodies in the adsorption step to AuNPs. Therefore, the reducing agents 2-MEA and DTT need to be removed from the reduced Ab solution prior to conjugation to AuNPs. Such a separation adds one more step to the protocol that may lead to loss of the reduced Ab and trace of reducing agent may still remain. TCEP is a more stable and stronger reducing agent than 2-MEA and DTT. Since TCEP is sulphur-free reagent, it does not compete with the reduced Ab during adsorption to AuNPs, and therefore a separation step is not essential. This makes it a more convenient reducing reagent of Ab for chemisorption to AuNPs.

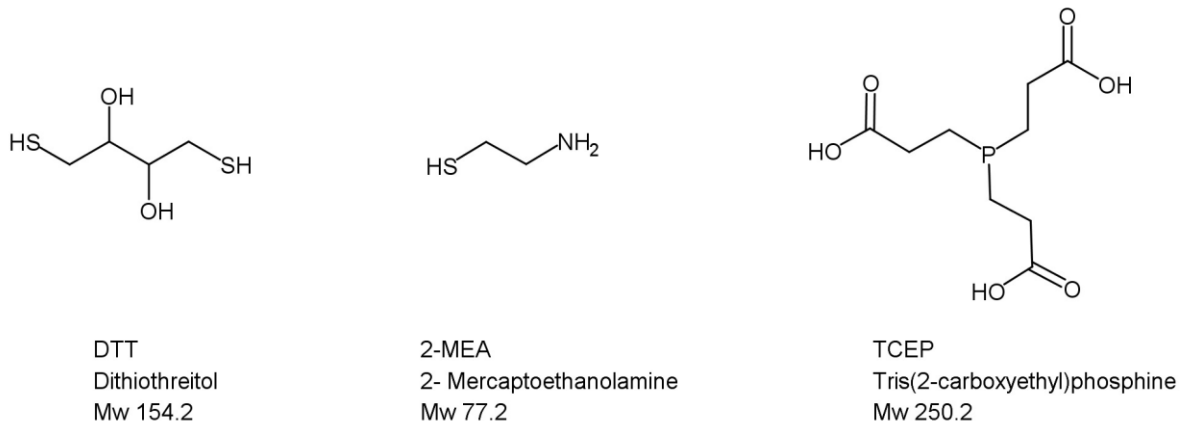

Figure 13 : Commonly used reductants for antibody fragmentation: dithiothreitol (DTT), 2-mercaptoethanolamine (2-MEA) and tris(2-carboxyethyl)phosphine (TCEP).

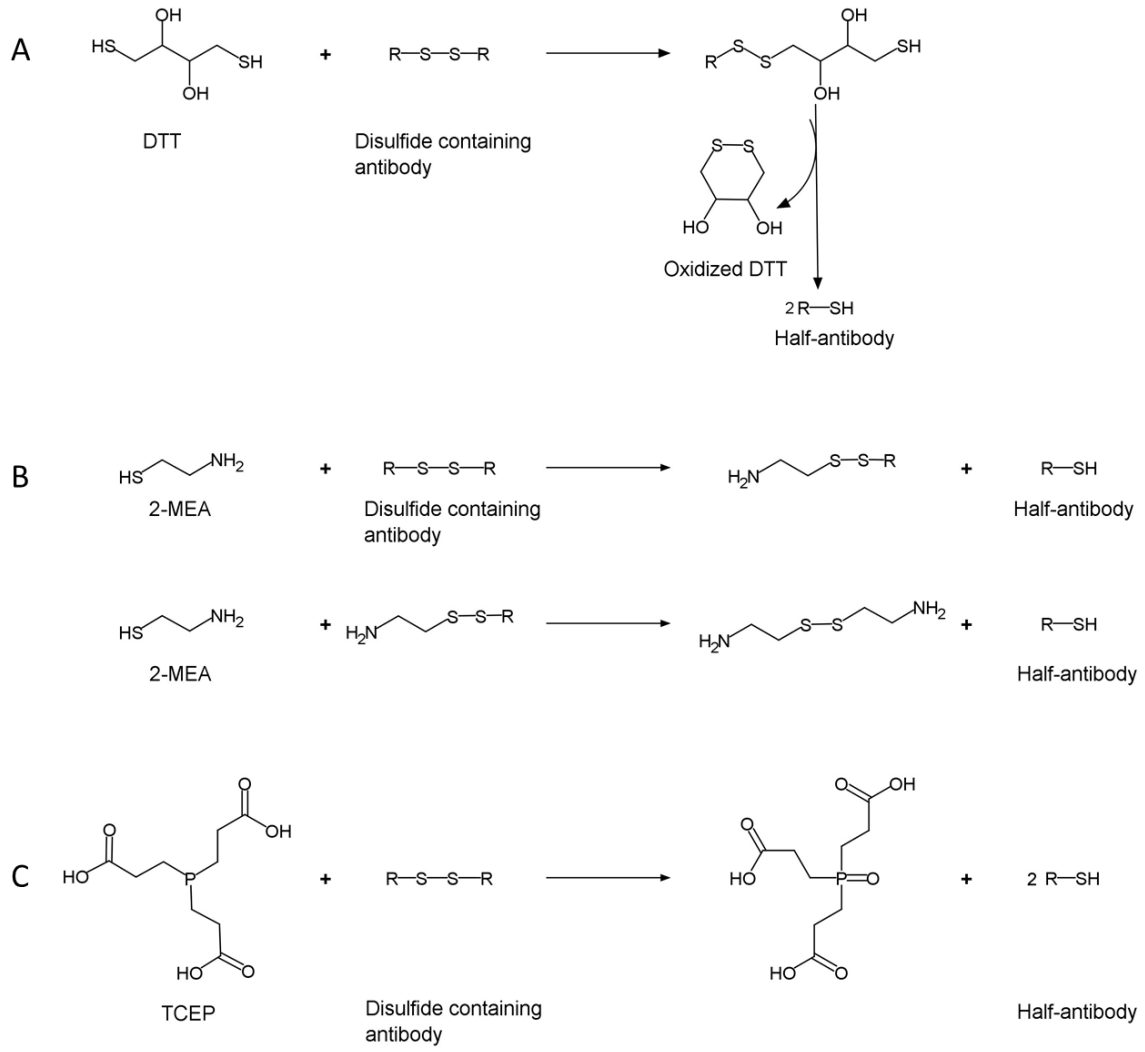

Figure 14 : Reduction of antibody to half-antibody fragments using dithiothreitol (DTT) (A), 2-mercaptoethanolamine (2-MEA) (B) and tris(2-carboxyethyl)phosphine (C).

Through this strategy, the antigen binding site is directed away from AuNPs, and because of the reduced size, a higher number of antigen binding sites per nm^2 on the AuNP surface can be achieved, thus giving a better antigen binding capacity. Balevicius *et al.* demonstrated that Ab fragment modified surface interacted with antigens more efficiently in comparison with that modified by whole Ab.[51] However recent studies showed that this strategy induced inactivation of the antigen binding capacity of the Ab fragments due to conformational and/or orientation change of fragments on the gold surface with time. The activity disappeared almost completely 60 min after immobilization. This inactivation can be slowed down if the Ab fragments are co-adsorbed with polyethylene glycol (PEG).[52] (Figure 15)

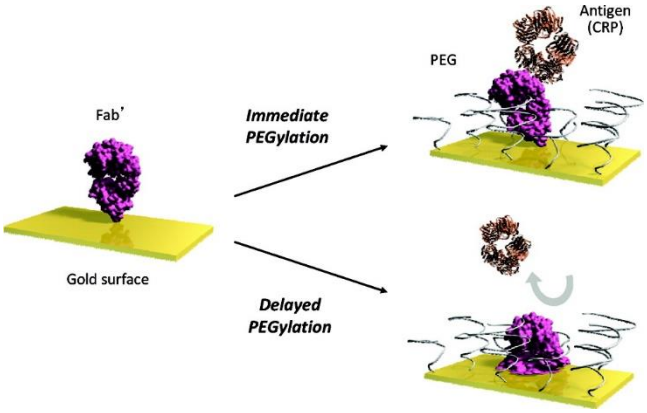

Figure 15 : Illustration of time-dependent inactivation of antibody fragments. Picture is adapted from ref.[52].

Binding through nucleotide-binding site (NBS)

Even across different isotypes, antibodies contain a largely conserved sequence between the heavy and light chains of the Fab region known as nucleotide binding site (NBS, location shown in Figure 16). Targeting the NBS using a small indole molecule and UV irradiation, oriented immobilization of Ab on surface could be achieved. Alves *et al.* found that this method provided 8-fold better antigen sensitivity compared to physical adsorption.[53] Mustafaoglu *et al.* applied this method to conjugation of Ab to AuNPs.[49] (Figure 17) In practice, the indole-containing molecule, tryptamine-PEG_8-lipoamide, was photo-cross-linked to the NBS of Ab upon exposure to UV light. Then functionalized antibodies were immobilized on AuNPs in an oriented manner via S–Au bonds. They also compared the antigen recognition sensitivity of this system to other conjugation methods, *e.g.* physisorption, EDC-NHS method, thiol reduction (Ab fragmentation), and concluded this UV-NBS method gave enhanced antigen detection capability and sensitivity with a high level of selectivity.

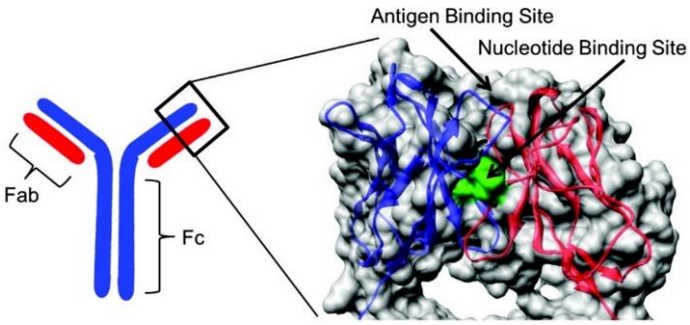

Figure 16 : Location of the nucleotide binding site (NBS) in antibody is shown in a cartoon representation and on the crystal structure of the antibody Fv region. Picture is adapted from ref.[53].

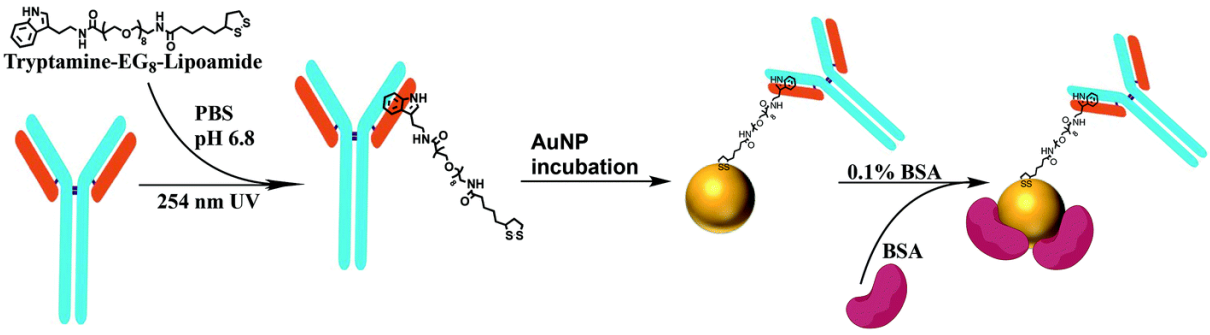

Figure 17 : Indole derivative used for UV-NBS method and conjugation scheme adapted from ref.[49].

Modification of AuNP

AuNPs are readily modified by low molecular weight thiols or disulfides. Various heterobifunctional ligands containing thiols or disulfides were used for stable anchoring onto AuNPs with another functional terminal group, *e.g.* carboxylate group, for binding antibodies.

Carboxyl or NHS ester groups

AuNPs have been decorated with carboxyl functions by binding a COOH-terminated crosslinker though Au-S bond. In some crosslinkers, carboxyl groups are already activated in the form of NHS/sulfo-NHS esters, whereby direct chemisorption of Ab could be realized through formation of amide bonds; while some are native carboxylates, in this case, NHS (or sulfo-NHS)/EDC chemistry should be applied to activate the carboxylate group prior to Ab adsorption.

NHS (or sulfo-NHS) heterobifunctional crosslinker, such as 3,3'-dithiobis(sulfosuccinimidyl propionate) (DTSSP) (Figure 7) was chemisorbed on AuNPs followed by direct immobilization of Ab.[29, 54] Special chemical groups could be implanted in the crosslinker for appropriate application. For example, Grubisha *et al.* synthesized 5,5'-dithiobis(succinimidyl-2-nitrobenzoate) (DSNB, Figure 18) containing NO_2 group which gives a strong Raman signal.[55] Meanwhile, heterobifunctional PEG linkers, HS-PEG-COOH, were also used, for instance, monothiol-PEG-COOH[30, 37, 56-59] and dithiol-PEG-COOH linker[57, 60]. After self-assembling on AuNPs though Au-S bond, NHS (or sulfoNHS)/EDC chemistry was used to activate the carboxyl group to N-succinimidyl ester, which then reacted with amine group on the Ab forming stable amide bond between PEG and Ab.

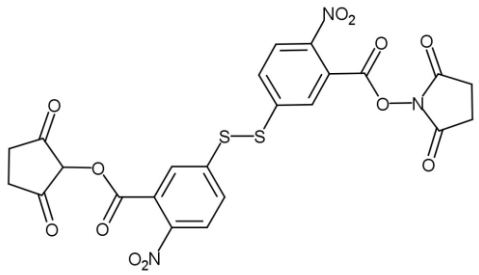

DSNB
5,5'-Dithiobis(succinimidyl-2-nitrobenzoate)
Mw 589.5

Figure 18 : Reagent : 5,5'-dithiobis(succinimidyl-2-nitrobenzoate) (DSNB).

Coupling of Ab to the NHS-activated AuNPs proceeds in a random orientation via any free amino groups present on Ab. In this way an Ab can react with more than one AuNP and thus induce AuNPs cross-linking.

AuNP-Fc binding protein

Ab-binding proteins such as protein G/A specifically bind to the Fc region of Ab. Ab immobilized on Fc-binding protein-coated surfaces is therefore properly oriented for optimal antigen binding. What is more, protein G/A could bind various IgG subclasses like from rabbit, mouse, human and other mammalian species. As Ab modification is not required for immobilization, bound Ab fully retains its binding ability. In practice, protein A was first reacted with N-succinimidyl 3-(2-pyridyldithio)-propionate (SPDP).[30, 61] Upon addition of the SPDP-modified protein A to AuNPs, the thiolated ligand displaced the citrate layer on AuNPs. Ab was subsequently immobilized on protein A via Fc region in an oriented configuration on AuNPs. Alternatively, protein G was physically adsorbed on AuNPs prior to Ab immobilization.[58] Another Fc specific polyclonal Ab, for instance, rabbit anti-mouse IgG (RAM) was widely used in SPR sensor for oriented immobilization of Ab.[62]

One of the major concerns associated with this method is the additional immobilization process of Fc-binding protein coating on AuNP surface prior to Ab immobilization. Protein G/A-Ab binding is also less stable than the other covalent immobilization methods.

Modification of AuNP and antibody

In some strategies, modifications of both AuNPs and Ab are performed at the same time.

Reductive amination

The sugar moieties of Ab are oxidized with $NaIO_4$ creating aldehyde groups. On the other hand, AuNPs were decorated with primary amino groups using for instance NH_2-PEG-SH. The stable attachment of Ab on AuNPs was realized in presence of $NaCNBH_3$ (reaction mechanism shown in Figure 9).[30]

Biotin-Streptavidin (STV) association

Biotinylated Ab is commercially available. It can interact with streptavidin that has been attached to AuNPs.[63-64]

Hybridization

Ab conjugation to AuNPs can be also achieved via DNA hybridization using specific Watson-Crick base pairing of two complementary nucleic acids. This strategy basically requires a two-step process: conjugation between Ab and DNA single strand sequence, and conjugation between AuNPs and complementary DNA sequence. Combined with biotin-streptavidin association (STV),[65-66] directional attachment of Ab on AuNPs was achieved. (Figure 19-A) Experimentally, DNA-STV was prepared from thiolated oligonucleotides and recombinant streptavidin using heterobifunctional cross-linker sulfosuccinimidyl 4-(N-maleimidomethyl) cyclohexane-1-carboxylate (sulfoSMCC). Then DNA-STV was conjugated to biotinylated Ab through high affinity between biotin and STV. On the other hand, complementary capture oligonucleotides were chemisorbed to AuNPs through Au-S bond. In the end, the DNA-STV Ab bound to DNA-AuNPs via Watson-Crick base pairing. Similarly, instead of biotin-STV, protein G was also combined to DNA base pairing for oriented attachment of Ab.[67] (Figure 19-B)

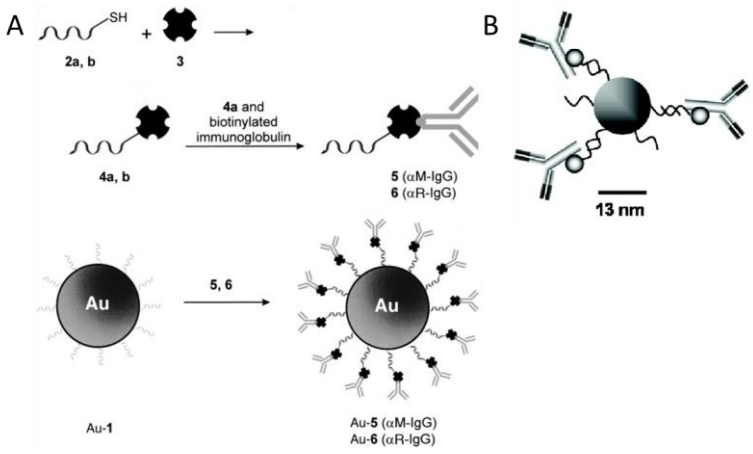

Figure 19 : DNA sequence combined with biotin-streptavidin (A)[65] or protein G (B) [67].

Click chemistry

Ab was reacted with azido-PEG_8-NHS ester to introduce azido groups on the Ab in a random fashion. On the other hand, a synthetic copolymer coating was grown on AuNP surface, one of the monomers bearing an alkyne functionality. This thin polymer layer on the surface stabilized the colloidal suspension.[68] Azido-containing Ab was then conjugated to alkyne-carrying AuNPs by copper-catalyzed azide-alkyne cycloaddition. (Figure 20)

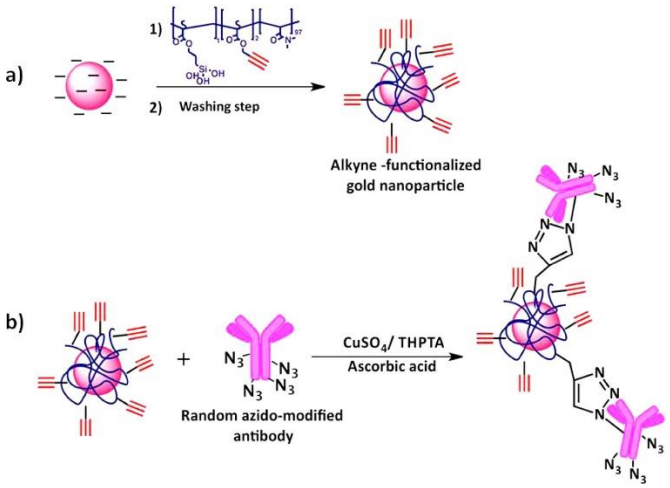

Figure 20 : Schematic representation of surface modification of AuNPs with a synthetic copolymer and subsequent conjugation with azido-modified antibody. Picture is adapted from ref.[68].

Current methods concerning the conjugation of Ab to AuNPs, via strategies of physisorption and chemisorption, have been presented. The particular characteristics of antibodies, including their shape, function and chemical stability, make their attachment to AuNPs a challenging task.

The orientation of Ab molecules and how they are linked are important to keep the Ab activity intact for the desired application of the conjugates.

QUANTIFICATION OF ANTIBODY IN AUNP-AB CONJUGATES

The performance of AuNP-based biosensors is markedly affected by the applied conjugation strategy between Ab and AuNPs that in turn controls surface coverage and Ab orientation.[38, 69-71] In the previous section, we have presented various conjugation strategies. To assess these strategies, information about orientation and surface coverage of Ab on AuNPs is highly desirable. Characterization techniques of Ab orientation on planar sensor surface have been reported in refs.[71-72]. In addition, several quantitative methods to measure surface coverage of Ab on AuNPs have been reported to date. We will present the different methods in this section.

Indirect quantification

Most quantification methods rely on the indirect analysis of Ab surface coverage via the quantitation of unbound Ab remaining in the supernatant after adsorption to AuNPs. In practice, excess unbound Ab in supernatant can be quantified with bicinchoninic acid (BCA)[24] or Bradford total protein assays.[34, 54, 70] Then the total number of Ab adsorbed on AuNPs is calculated as the difference between the initial amount of Ab added to the AuNP suspension and the amount of unbound Ab that remained in the supernatant. However, Ab conjugation to AuNPs is generally followed by a blocking step with another protein, typically BSA[14, 73], to prevent aggregation of the nanoparticles in saline environment and increase the long-term stability of the colloidal solution. This additional step, leading to the presence of another protein, makes the previous classical protein assays inapplicable. In this case, Ab assay in the supernatant can be achieved by enzyme-linked immunosorbent assay (ELISA) using a microtiter plate coated with the corresponding antigen.[27] Alternatively, prior to conjugation, Ab can be labeled with a fluorescent dye to achieve sufficient sensitivity of detection and non-bound Ab in supernatant is measured by spectrofluorimetry at the excitation/emission wavelengths of the fluorescent dye.[35, 38] It should be noted that Ab quantification by these indirect methods implies no loss of Ab during the purification process, *e.g.* during transfer of the solution from one container to another, or Ab adsorption to the container walls. This is why indirect methods often lead to an overestimation of Ab surface coverage on AuNP.[54]

Direct quantification

Ab adsorption on AuNPs has been quantified from the LSPR peak shift due to the local refractive index (RI) change caused by Ab adsorption.[41, 74] Although this approach provides a direct quantification of the adsorbed Ab, it requires accurate knowledge of RI of proteins at the nanoparticles surface. This is quite challenging because the RI depends on the surface coverage, protein orientation, and water content, none of which are constant.[75-77] Other methods, like dynamic light scattering (DLS) and nanoparticle tracking analysis (NTA) measure the increase in hydrodynamic diameter after adsorption of protein on AuNPs to derive information on surface coverages.[32, 77-78] The thickness of the bound protein layer does not directly provide accurate information on bound proteins per nanoparticles. Some models were derived allowing to correlate the average number of bound protein to the hydrodynamic diameter increment, for instance, Taylor dispersion analysis (TDA).[79]

BCA protein assay[31] and ELISA[26, 30, 32, 58, 70] were also used to directly quantify the adsorbed Ab. Even with some careful calibration treatment, *i.e.* removal of the nanoparticle contribution by subtracting a spectrum of pure nanoparticle solution, overestimation of the Ab on nanoparticle was obtained, demonstrating that nanoparticles interfere chemically and/or electromagnetically with the BCA assay.[31] Similar problems may happen for fluorescence[36]-based direct quantification Ab in conjugates.

To avoid interference from the matrix, dissolution of nanoparticles or digestion of Ab strategy has been reported. The former method relies on the dissolution of the AuNPs in AuNP-Ab conjugates by KI/I_2 mixture, followed by labeling of recovered Ab by the fluorescent dye NanoOrange and spectrofluorimetric measurement.[54] Though this method gives more reliable results than the indirect protein assay methods, it is not applicable to BSA-blocked AuNP-Ab conjugates. The latter method is based on the complete digestion of the protein in AuNP-protein conjugates in 6 N HCl followed by fluorescent labeling of the generated aminoacids and assay of glycine derivative by HPLC-fluorescence detection.[80] To note, this method is not applicable to BSA-blocked AuNP-Ab conjugates either.

On the other hand, radioactive labeling of Ab in quantification is a robust method[52], however, the handling of the radioactive waste remains challenging.

By comparing different quantification methods, we see well that accurate quantification of surface coverage of Ab still remains challenging.

APPLICATIONS OF AUNP-ANTIBODY CONJUGATES IN OPTICAL BIOSENSING

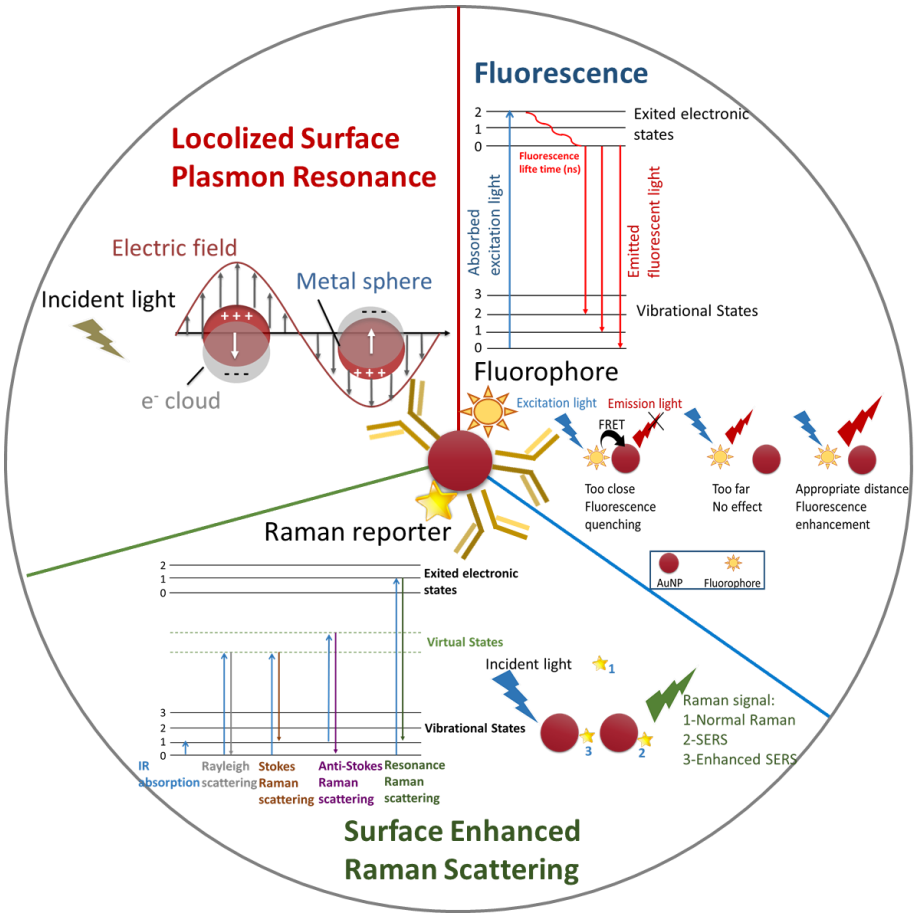

Figure 21 : Optical properties of AuNPs: Localized Surface Plasmon Resonance (LSPR), Surface Enhanced Raman Scattering (SERS) and fluorescence enhancement and quenching.

Historically, highly light absorbing and color dense Ab-conjugated AuNPs were shown to provide high capability for sensitive staining techniques. For instance, AuNP-Ab conjugates have long been used as indicators in lateral flow assays (LFA) using immunochromatographic test strips,[81-82] that provide simple, rapid, low cost, and user-friendly detection of various analytes. In addition, these conjugates are widely used in immunohistochemical (IHC) staining combined with electron microscopy.[12-14, 21, 83] Here we will present recent applications of AuNP-Ab conjugates based on the optical properties of AuNPs, *i.e.* Localized Surface Plasmon Resonance (LSPR), surface enhanced Raman scattering (SERS) and fluorescence enhancement

or quenching/dequenching. (Figure 21) According to the signal transduction type, the current well-developed immunoassays based on AuNP-Ab conjugates can be divided into four broad categories: LSPR, SPR, fluorescence, and SERS immunoassay. (Figure 22)

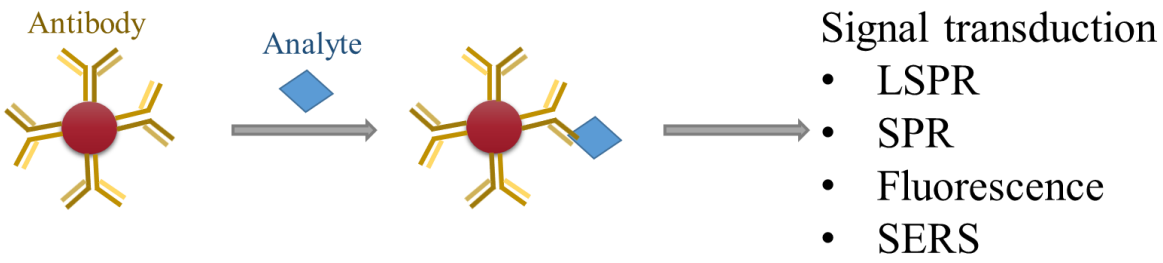

Figure 22 : AuNP-antibody bioconjugates in optical biosensing.

AuNP-antibody bioconjugates in LSPR sensors

The general principle behind LSPR-based sensors is the LSPR peak shift arising from local refractive index (RI) change caused by binding event between AuNP-Ab and antigen or from antigen-induced crosslinking aggregation. (Figure 23) LSPR-based assays have been conducted both in homogeneous solution and on planar surfaces coated with AuNP monolayer.

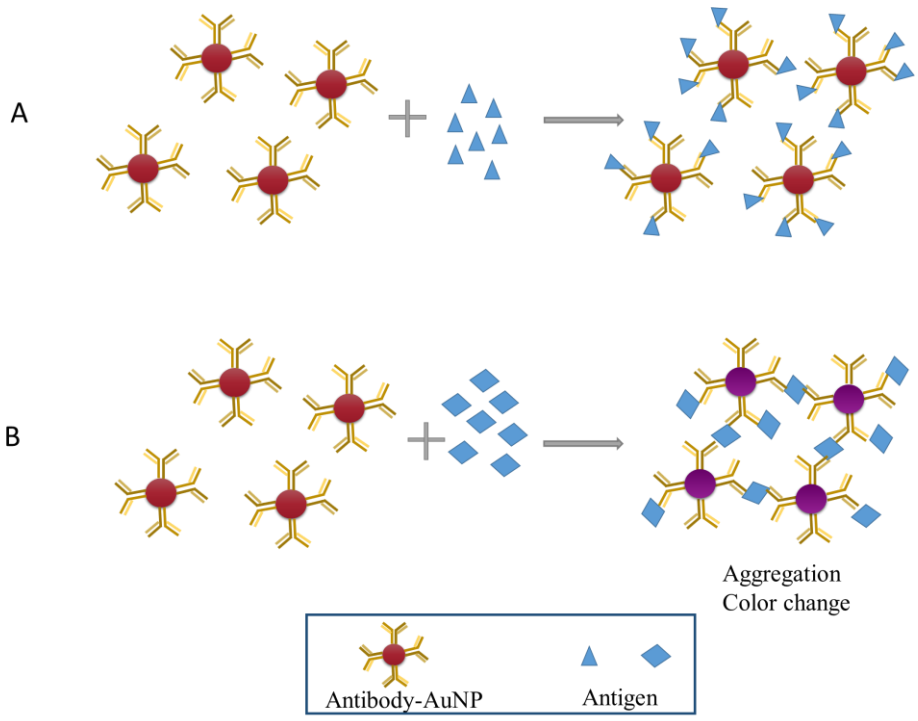

Figure 23 : Schematic illustration of analyte-induced LSPR absorption change. (A) Local refractive index change; (B) analyte-induced crosslinking aggregation.

For example, when AuNP-Ab binds to the target with only one epitope (Figure 23A), the LSPR peak of AuNP red-shifts because of an increase in the RI close to AuNPs. What is more, the peak shift is proportional to the target concentration. Thus, this assay is useful for quantitative detection.[84-85] In case there are multiple binding sites on the target (epitopes), the target acts as a linker and interparticle crosslinking-induced aggregation of AuNPs occurs (Figure 23B).[27, 41, 86-87] Moreover, the aggregation induces interparticle surface plasmon coupling of AuNPs, leading to the change of the absorbance spectrum and even to a color change of the colloidal solution. The degree of AuNPs aggregation (or redispersion of aggregates) is proportional to the target concentration, thus allowing this assay to be useful in quantitative detection. Alternatively, a non-crosslinking aggregation of AuNP-Ab induced by an increasing salt concentration can be used as in ref.[88].

Other sensors based on LSPR band shift have been fabricated by coating AuNPs onto substrate surface. (Figure 24) For example, AuNPs were attached to quartz,[89] ITO-glass,[90] polystyrene[64], *etc*. Ab was then immobilized on AuNPs, consequently, the sensing platform was employed to quantitatively detect antigens based on the LSPR peak shift which resulted from local RI change of binding target. These fabricated LSPR immunosensors showed high sensitivity and selectivity. For instance, the limit of detection (LOD) of HIV-1 was estimated at 200 fg/mL,[90] which is 70 fold better than that of previously reported detection method[91]. Inci *et al.* applied this technology for quantitative detection of intact virus in whole blood sample at clinically relevant concentrations.[64]

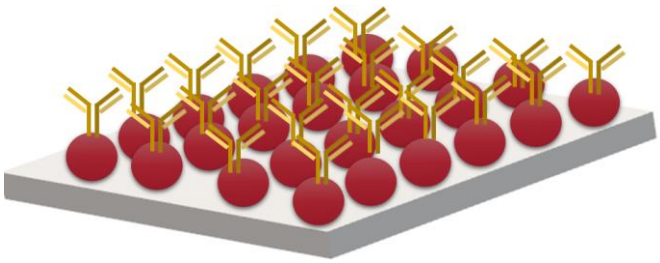

Figure 24 : LSPR sensor on planar surface: AuNPs are coated on substrates, followed by antibody immobilization.

AuNP-antibody conjugates for enhanced SPR biosensors

AuNPs have been incorporated in SPR biosensors, providing an effective way to increase sensor response, which results from the electronic coupling interaction of the propagating surface plasmons with localized surface plasmons of AuNPs. There are two different types, (i) AuNPs

are immobilized on SPR sensor surface directly, and (ii) AuNPs are immobilized on top of the sensing layer. (Figure 25)

For example, a layer of AuNPs was first coated on SPR sensor surface, followed by coating another layer of AuNP-Ab. The two layers of AuNPs enhanced the sensitivity of the following detection of target.[92] Alternatively, AuNP-Ab conjugates were bound at the last step forming a sandwich format. (Figure 25-B) Briefly, a layer of capture Ab was immobilized on SPR sensor surface. After sample injection, AuNP-Ab finally bound to sensor surface. Signal amplification and lower limit of detection were evidenced. This strategy was applied for detection of human IgG[93], prostate-specific antigen[94-96] and carcinoembryonic antigen (CEA).[57]

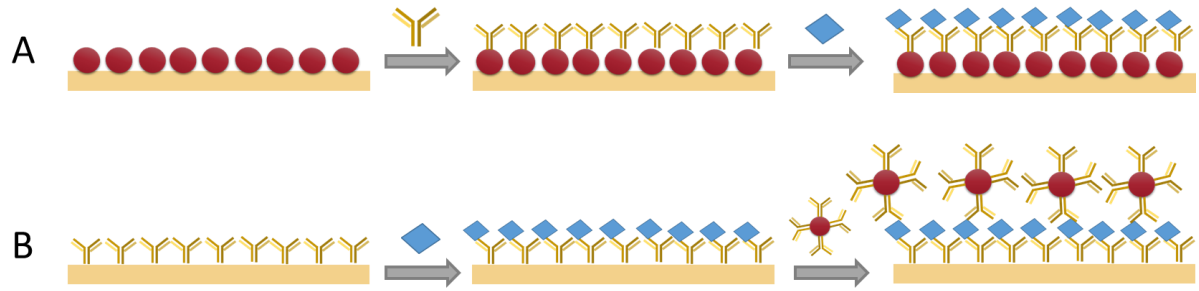

Figure 25 : AuNP-based enhanced SPR sensors: (A) AuNPs are immobilized on SPR sensor surface directly; (B) AuNPs are immobilized on top of sensing layer.

AuNP-based plasmon resonance scattering sensing

The light-scattering cross-section of a AuNP with a diameter of 60 nm is 200-300 times stronger than that of a polystyrene bead of same size, and 4-5 orders of magnitude stronger than that of a fluorescent dye, *e.g.*, fluorescein.[97-98] Dynamic light scattering (DLS) is a technique routinely used to analyze the size and size distribution of nanoparticles. Combining the use of AuNPs as light scattering enhancer and DLS as readout provides a useful sensor design.

In practice, when AuNP-Ab is mixed with a sample containing the target, depending on its concentration, the target binding will cause AuNPs to form dimers, oligomers, or aggregates. The relative ratio of different forms can be measured quantitatively through DLS analysis. This ratio increases accordingly with increased amount of antigen in sample solution, and such a correlation forms the analytical basis of a homogeneous immunoassay. By exploiting this sensing platform, human IgG[99], prostate-specific antigen[49, 100] and virus[17] have been detected.

The one-step assay does not involve any washing step and yields highly sensitive, specific and rapid results. Moreover, extremely small amounts of samples are needed for the assay.

AuNP-based fluorescence sensing

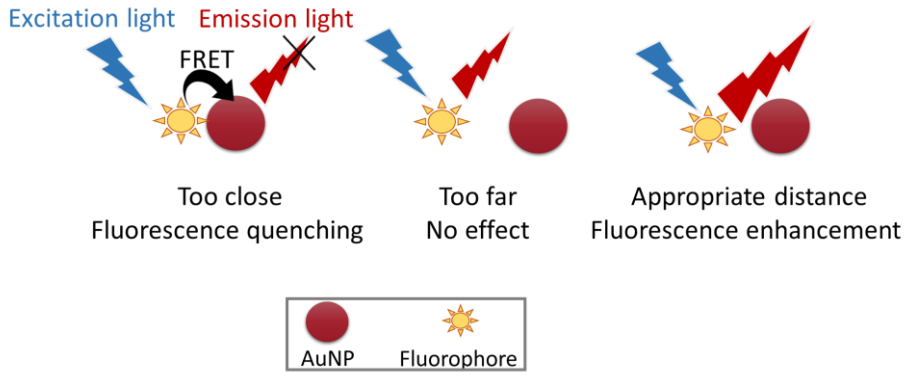

Figure 26 : Schematic illustration of the effect of distance between AuNP and fluorophore on fluorescence emission.

AuNP can lead to both fluorophore quenching and enhancement which can be explained by a well-established Förster resonance energy transfer (FRET) mechanism.[101] (Figure 26) When AuNP and fluorophore are close to each other, FRET occurs from the fluorophore to AuNP and thus quenching happens.[102] In contrast, at an appropriate distance to AuNP, fluorescence enhancement can happen, which is typically referred to as plasmon-enhanced fluorescence (PEF).[103] Especially, Anger *et al.*[104] experimentally and theoretically investigated the relationship between the fluorescence rate and the distance between AuNP and fluorophore and demonstrated a continuous transition from fluorescence enhancement to fluorescence quenching of a single molecule on AuNP.

Generally, an AuNP-based fluorescence probe system consists of two functional components: the recognition element, here Ab, which provides specific binding of target, and the fluorescent dye, which is used for analyzing the binding event. The high loading efficiency of the fluorescent dye on AuNP surface with high area-to-volume ratio and high fluorescence enhancement or quenching/unquenching abilities of the fluorescent dye-AuNP pairs make this probe ultrasensitive. Assays are typically designed via fluorescence-nanoprobe labeling and analyte-induced fluorescence quenching/dequenching (recovery).

Alternative assay platforms, for instance, fiber-optic biosensors based on AuNP-fluorescent dye enhancement, have been applied by different research groups.[91, 105-106] Briefly, a capture Ab was immobilized on the surface of an optical fiber. After sample injection, fluorescence probe consisting of fluorophore-labeled Ab-conjugated AuNPs was added. Subsequently, the fluorescence signal was then excited and measured by the photomultiplier tube. (Figure 27) In this assay, two factors were considered to enhance the assay sensitivity. First, electromagnetic field around the AuNP surface efficiently enhanced the fluorescence signal. Second, there were multiple fluorophores labeled on each AuNP allowing several fluorophores to be simultaneously excited during measurement. These two effects combine, producing a significant improvement in the sensitivity of the system compared to a conventional fluorescence probe or ELISA.

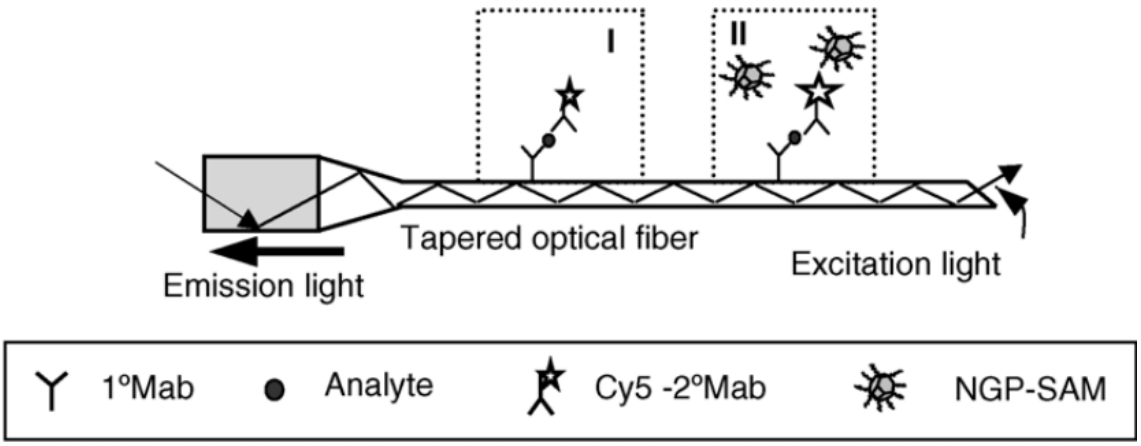

Figure 27 : Schematic diagram of fluorescence measurement in biosensor: (I) regular immunosensing with fluorophore-labeled antibody; (II) immunosensing using AuNPs as fluorescence enhancer. Picture is adapted from ref.[105].

Based on the latter format, the dequenching format, porcine reproductive and respiratory syndrome virus was detected.[107] A fluorophore-labeled Ab was immobilized on protein A-AuNPs. In such case was the fluorescence quenched by AuNPs. Upon binding of antigen, conformational change within the biosensor complex increased the distance between the fluorescent dye and AuNP, leading to a dequenching (recovery) effect by the AuNP.

Liu *et al.* also explored an AuNP-based fluorescence-activatable immunoassay for detecting ultralow levels of cancer biomarker (PSA) in patient serum samples (Figure 28).[108] Each AuNP was labeled with thousands of fluorescent dyes (rhodamine B isothiocyanate) and the dye layer on AuNPs was covered with Ab that was bound through electrostatic interactions. Consequently, in the presence of target PSA, the Ab-dye-AuNP conjugates were captured onto

the substrate and the fluorescence of dye on AuNP surface was highly quenched via the nanoparticle surface energy transfer effect. After addition of cysteamine into this detection system, the fluorescent dyes were competitively displaced from the AuNP surface, leading to significant restoration of dye fluorescence. Thus, the concentration of PSA in serum samples was quantified according to the intensity of the recovered fluorescence. The LOD of the developed probe for PSA was more than 2 orders of magnitude lower than that of the conventional fluorescence probe.

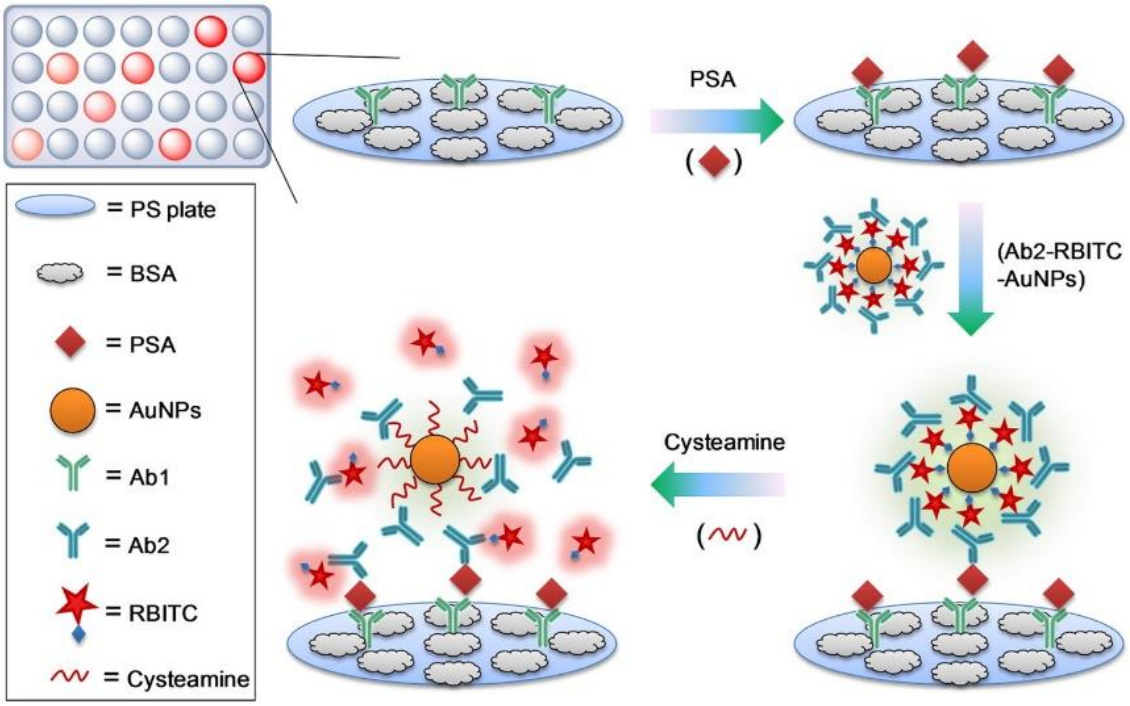

Figure 28 : Schematic illustration of dequenching (recovery) of fluorescent dyes. Picture is adapted from ref.[108].

AuNP-based SERS sensing

SERS is a powerful spectroscopic technique that provides in situ nondestructive fingerprint information. More importantly, its ultrahigh signal enhancement is up to 10^{14} that is capable for single-molecule detection. In the AuNP-based SERS sensing, upon exciting the LSPR of AuNPs, the large electromagnetic field that localized at AuNP surface is exploited to measure enhanced vibrational molecular signatures. SERS nanoprobes have been widely applied in immunoassays. As the probe, the essential design is the use of AuNPs with Ab and Raman reporter molecules. The total enhancement factor results from (i) LSPR-enhanced Raman scattering and (ii) chemical enhancement. The assays are typically designed as SERS-

nanoprobe based optical labeling and analyte-induced SERS nanoprobe aggregation/antiaggregation assays.

SERS nanoprobe-based optical labeling

The SERS substrate, here AuNPs offer a stronger Raman enhancement than individual nanostructures due to the formation of hotspots at AuNPs junctions. The SERS nanoprobe could be used in direct optical labeling.

For example, Grubisha *et al.* reported a sandwich format immunoassay using SERS nanoprobes as optical labels. As the probe, AuNPs were functionalized with a monolayer of intrinsically strong Raman reporter (DSNB, Figure 18) followed by coating Ab layer.[55] In this case, the distance between the Raman reporter and the AuNP surface was minimal and the number of the Raman-reporters on each AuNP was maximized. These two factors led to an enhanced sensitivity of this assay.

Li *et al.* presented a SERS-based immunochromatographic assay (ICA) for ultrasensitive and quantitative detection of phenylethanolamine A (PA) (Figure 29).[109] The principle of this new sandwich assay is similar to conventional ICA based on AuNPs but using a SERS probe which consisted of Au-Ag core-shell nanoparticles labeled with Ab and 4-mercaptobenzoic acid (MBA, Raman reporter) (Au^{MBA}@Ag-Ab). After the ICA procedure, the specific Raman scattering intensity of MBA on the test line was measured for quantitative detection of PA. The LOD of this assay was improved by 1−3 orders of magnitude compared with other immunoassays.

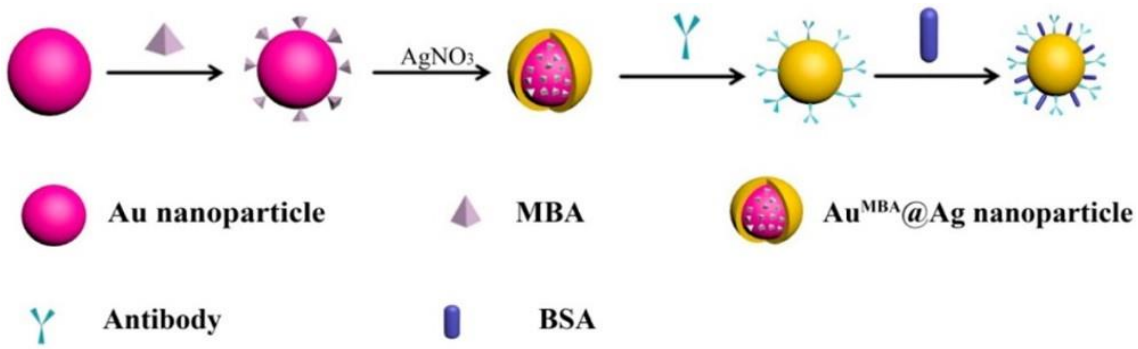

Figure 29 : Preparation of SERS nanoprobe: Au^{MBA}@Ag-Ab. Picture is adapted from ref.[109].

Qian *et al*. successfully applied pegylated SERS nanoprobe for tumor targeting and detection.[110] Large optical enhancement was achieved under in vivo conditions for tumor detection in live animal. Similarly, Cho *et al.* applied it in isolation and analysis of circulating cancer stem cells through Raman imaging based on SERS nanoprobe.[111]

Analyte-induced SERS nanoprobe aggregation/anti-aggregation

Another assay format is based on antigen-induced aggregation/anti-aggregation of SERS nanoprobes.

Wang *et al.* reported the application of SERS nanoprobes in target-induced aggregation assay.[50] In the system, there were two SERS nanoprobes, spherical AuNPs and gold nanorod (AuNR). Both were decorated with Raman reporter and half-fragment Ab (as shown in Figure 30). In the presence of target, the SERS nanoprobes aggregated leading to strong SERS enhancement arising from plasmonic coupling, and SERS spectra were acquired directly on the sample solution. Instead, after the SERS nanoprobes reacted with target, the aggregated nanoparticles were captured and concentrated through a membrane filter. SERS analysis was acquired from membrane surface.[29, 112]

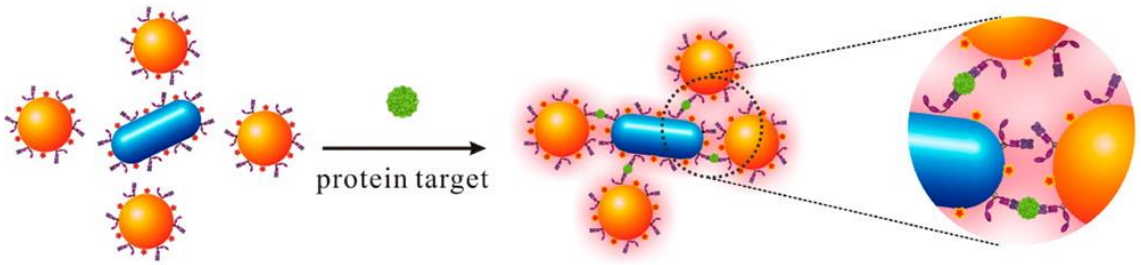

Figure 30 : Schematic illustration of single-step SERS immunoassay via target-controlled assembly of SERS nanoprobes. Picture is adapted from ref.[50].

Wu *et al.* presented a SERS immunoassay in anti-aggregation format for ultrasensitive detection of folic acid (FA) by controlling the assembly of AuNPs and silver nanoparticles (AgNPs) heterodimers through antigen-Ab binding (Figure 31).[113] In practice, the AuNPs were coated with Ab (against FA) and Raman reporter (4-aminothiophenol (4-ATP)); the AgNPs were coated with antigen (FA-BSA conjugates) and Raman reporter (4-ATP). Without target in sample, the Ab/Raman reporter-labeled AuNPs and the antigen/Raman reporter-labeled AgNPs assembled completely, forming heterodimers and showing strong SERS intensity. However, in the presence of FA, free FA competed with the AgNP-labeled antigen for binding to AuNP-

labeled Ab, thus reducing the assembly of heterodimers. Consequently, the concentration of target FA was revealed by the significantly reduced Raman intensity of the Raman reporter.

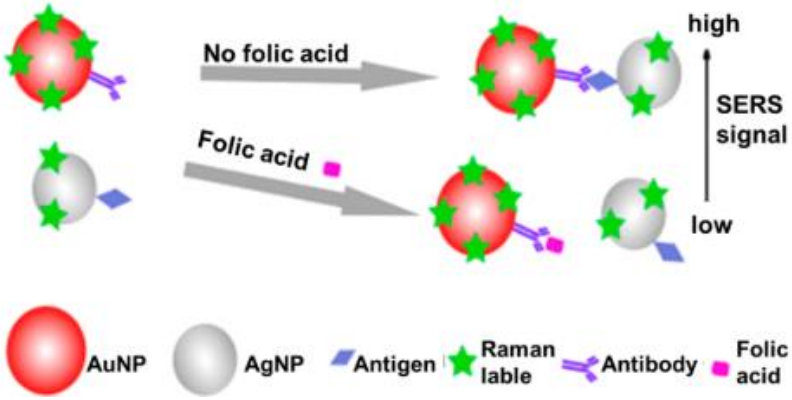

Figure 31 : Schematic illustration of the SERS immunoassay for detection of folic acid (FA) based on AuNP−AgNP heterodimers formation. Picture is adapted from ref.[113].

Besides the applications of AuNP-Ab in optical biosensing mentioned above, AuNP-Ab conjugates have also been used in other transduction techniques, for example, piezoelectric transduction using quartz crystal microbalance (QCM). The sensing design is the same as for AuNP-enhanced SPR sensor and the incorporation of AuNPs into QCM-based sensing systems enhanced detection sensitivity by their high surface area[47, 114] and by serving as a "mass enhancer.[115-116]

CONCLUSIONS AND PERSPECTIVES

Here, we have summarized and discussed various conjugation strategies, quantification methods of surface coverage and applications of AuNP-Ab conjugates that have been designed and successfully applied in optical biosensing. With the excellent properties of AuNPs, as well as various signal transduction approaches, nanomaterials have paved the way for the development of easy, rapid, low-cost immunoassays. The optimization of conjugation for the sensing systems is still required to meet the demands of clinical diagnostics in complex biological fluids such as urine, serum, and blood. For example, further miniaturization of Ab allows increment of binding sites on AuNP surface. Assays can be further integrated into mobile phones or computers for real-time monitoring. The fundamental advantages of AuNPs will continue to contribute to the development of biosensors in the following years.

REFERENCES

1. Saha, K.; Agasti, S. S.; Kim, C.; Li, X.; Rotello, V. M., Gold Nanoparticles in Chemical and Biological Sensing. *Chem. Rev.* **2012,** *112* (5), 2739-2779.

2. Wilson, R., The use of gold nanoparticles in diagnostics and detection. *Chem. Soc. Rev.* **2008,** *37* (9), 2028-2028.

3. Chen, P. C.; Mwakwari, S. C.; Oyelere, A., Gold nanoparticles: From nanomedicine to nanosensing. *Nanotechnol. Sci. Appl.* **2008,** *1,* 45-66.

4. Tang, L.; Li, J., Plasmon-Based Colorimetric Nanosensors for Ultrasensitive Molecular Diagnostics. *ACS Sensors* **2017,** *2* (7), 857-875.

5. Sepulveda, B.; Angelome, P. C.; Lechuga, L. M.; Liz-Marzan, L. M., LSPR-based nanobiosensors. *Nano Today* **2009,** *4* (3), 244-251.

6. Geoghegan, W. D., The effect of three variables on adsorption of rabbit IgG to colloidal gold. *J. Histochem. Cytochem.* **1988,** *36* (4), 401-407.

7. Bagchi, P.; Birnbaum, S. M., Effect of pH on the adsorption of immunoglobulin G on anionic poly(vinyltoluene) model latex particles. *J. Colloid Interface Sci.* **1981,** *83* (2), 460-478.

8. Demanèche, S.; Chapel, J.-P.; Monrozier, L. J.; Quiquampoix, H., Dissimilar pH-dependent adsorption features of bovine serum albumin and α-chymotrypsin on mica probed by AFM. *Colloids Surf. B* **2009,** *70* (2), 226-231.

9. Geoghegan, W. D.; Ackerman, G. A., Adsorption of horseradish peroxidase, ovomucoid and anti-immunoglobulin to colloidal gold for the indirect detection of concanavalin A, wheat germ agglutinin and goat anti-human immunoglobulin G on cell surfaces at the electron microscopic level: a new me. *J. Histochem. Cytochem.* **1977,** *25* (11), 1187-1200.

10. Hook, F.; Rodahl, M.; Kasemo, B.; Brzezinski, P., Structural changes in hemoglobin during adsorption to solid surfaces: Effects of pH, ionic strength, and ligand binding. *Proc. Natl Acad. Sci.* **1998,** *95* (21), 12271-12276.

11. Peng, Z. G.; Hidajat, K.; Uddin, M. S., Adsorption of bovine serum albumin on nanosized magnetic particles. *J. Colloid Interface Sci.* **2004,** *271* (2), 277-283.

12. Horisberger, M.; Rosset, J.; Bauer, H., Colloidal gold granules as markers for cell surface receptors in the scanning electron microscope. *Experientia* **1975,** *31* (10), 1147-1149.

13. Horisberger, M.; Rosset, J., Colloidal gold, a useful marker for transmission and scanning electron microscopy. *J. Histochem. Cytochem.* **1977,** *25* (4), 295-305.

14. De Mey, J.; Moeremans, M.; Geuens, G.; Nuydens, R.; De Brabander, M., High resolution light and electron microscopic localization of tubulin with the IGS (immuno gold staining) method. *Cell Biol. Int. Rep.* **1981,** *5* (9), 889-899.

15. El-Sayed, I. H.; Huang, X.; El-Sayed, M. A., Surface Plasmon Resonance Scattering and Absorption of anti-EGFR Antibody Conjugated Gold Nanoparticles in Cancer Diagnostics: Applications in Oral Cancer. *Nano Lett.* **2005,** *5* (5), 829-834.

16. Hermanson, G. T., Preparation of Liposome Conjugates and Derivatives. In *Bioconjugate techniques*, Elsevier: 2008; pp 858-899.

17. Lai, Y. H.; Koo, S.; Oh, S. H.; Driskell, E. A.; Driskell, J. D., Rapid screening of antibody–antigen binding using dynamic light scattering (DLS) and gold nanoparticles. *Anal. Methods.* **2015,** *7* (17), 7249-7255.

18. Rayavarapu, R. G.; Petersen, W.; Ungureanu, C.; Post, J. N.; van Leeuwen, T. G.; Manohar, S., Synthesis and Bioconjugation of Gold Nanoparticles as Potential Molecular Probes for Light-Based Imaging Techniques. *Int. J. Biomed. Imaging* **2007,** *2007*, 1-10.

19. Safenkova, I. V.; Zherdev, A. V.; Dzantiev, B. B., Correlation between the composition of multivalent antibody conjugates with colloidal gold nanoparticles and their affinity. *J. Immunol. Methods* **2010,** *357* (1-2), 17-25.

20. Lou, S.; Ye, J.-y.; Li, K.-q.; Wu, A., A gold nanoparticle-based immunochromatographic assay: The influence of nanoparticulate size. *Analyst* **2012,** *137* (5), 1174-1181.

21. Tokuyasu, K. T., Present state of immunocryoultramicrotomy. *J. Histochem. Cytochem.* **1983,** *31* (1A), 164-167.

22. Horisberger, M.; Clerc, M. F., Labelling of colloidal gold with protein A. *Histochem.* **1985,** *82* (3), 219-223.

23. Byzova, N. A.; Safenkova, I. V.; Slutskaya, E. S.; Zherdev, A. V.; Dzantiev, B. B., Less is More: A Comparison of Antibody–Gold Nanoparticle Conjugates of Different Ratios. *Bioconjugate Chem.* **2017,** *28* (11), 2737-2746.

24. Geng, S. B.; Wu, J.; Alam, M. E.; Schultz, J. S.; Dickinson, C. D.; Seminer, C. R.; Tessier, P. M., Facile Preparation of Stable Antibody–Gold Conjugates and Application to Affinity-Capture Self-Interaction Nanoparticle Spectroscopy. *Bioconjugate Chem.* **2016,** *27* (10), 2287-2300.

25. Hermanson, G. T., Fluorescent Probes. In *Bioconjugate techniques*, Elsevier: 2008; pp 396-497.

26. Wang, X.; Mei, Z.; Wang, Y.; Tang, L., Comparison of four methods for the biofunctionalization of gold nanorods by the introduction of sulfhydryl groups to antibodies. *Beilstein J. Nanotechnol.* **2017,** *8* (1), 372-380.

27. Ben Haddada, M.; Hu, D.; Salmain, M.; Zhang, L.; Peng, C.; Wang, Y.; Liedberg, B.; Boujday, S., Gold nanoparticle-based localized surface plasmon immunosensor for staphylococcal enterotoxin A (SEA) detection. *Anal. Bioanal. Chem.* **2017,** *409* (26), 6227-6234.

28. Bragg, P. D.; Hou, C., A Cross-Linking Study of the Ca2+, Mg2+-Activated Adenosine Triphosphatase of Escherichia coli. *Eur. J. Biochem.* **1980,** *106* (2), 495-503.

29. Filbrun, S. L.; Filbrun, A. B.; Lovato, F. L.; Oh, S. H.; Driskell, E. A.; Driskell, J. D., Chemical modification of antibodies enables the formation of stable antibody–gold nanoparticle conjugates for biosensing. *Analyst* **2017,** *142* (23), 4456-4467.

30. Van Der Heide, S.; Russell, D. A., Optimisation of immuno-gold nanoparticle complexes for antigen detection. *J. Colloid Interface Sci.* **2016,** *471*, 127-135.

31. Liao, H.; Hafner, J. H., Gold Nanorod Bioconjugates. *Chem. Mat.* **2005,** *17* (18), 4636-4641.

32. Day, E. S.; Bickford, L. R.; Slater, J. H.; Riggall, N. S.; Drezek, R. A.; West, J. L., Antibody-conjugated gold-gold sulfide nanoparticles as multifunctional agents for imaging and therapy of breast cancer. *International Journal of Nanomedicine* **2010,** *5* (1), 445-454.

33. Lim, C. Y.; Owens, N. A.; Wampler, R. D.; Ying, Y.; Granger, J. H.; Porter, M. D.; Takahashi, M.; Shimazu, K., Succinimidyl Ester Surface Chemistry: Implications of the Competition between Aminolysis and Hydrolysis on Covalent Protein Immobilization. *Langmuir* **2014,** *30* (43), 12868-12878.

34. Raoof, M.; Corr, S. J.; Kaluarachchi, W. D.; Massey, K. L.; Briggs, K.; Zhu, C.; Cheney, M. A.; Wilson, L. J.; Curley, S. A., Stability of antibody-conjugated gold nanoparticles in the endolysosomal nanoenvironment: implications for noninvasive radiofrequency-based cancer therapy. *Nanomedicine: Nanotechnology, Biology and Medicine* **2012,** *8* (7), 1096-1105.

35. Kumar, S.; Aaron, J.; Sokolov, K., Directional conjugation of antibodies to nanoparticles for synthesis of multiplexed optical contrast agents with both delivery and targeting moieties. *Nature Prot.* **2008,** *3* (2), 314-320.

36. Joshi, P. P.; Yoon, S. J.; Hardin, W. G.; Emelianov, S.; Sokolov, K. V., Conjugation of Antibodies to Gold Nanorods through Fc Portion: Synthesis and Molecular Specific Imaging. *Bioconjugate Chem.* **2013,** *24* (6), 878-888.

37. Ciaurriz, P.; Fernández, F.; Tellechea, E.; Moran, J. F.; Asensio, A. C., Comparison of four functionalization methods of gold nanoparticles for enhancing the enzyme-linked immunosorbent assay (ELISA). *Beilstein J. Nanotechnol.* **2017,** *8* (1), 244-253.

38. García-Fernández, L.; Garcia-Pardo, J.; Tort, O.; Prior, I.; Brust, M.; Casals, E.; Lorenzo, J.; Puntes, V. F., Conserved effects and altered trafficking of Cetuximab antibodies conjugated to gold nanoparticles with precise control of their number and orientation. *Nanoscale* **2017,** *9* (18), 6111-6121.

39. Neves-Petersen, M. T., Photonic activation of disulfide bridges achieves oriented protein immobilization on biosensor surfaces. *Protein Sci.* **2006,** *15* (2), 343-351.

40. Della Ventura, B.; Schiavo, L.; Altucci, C.; Esposito, R.; Velotta, R., Light assisted antibody immobilization for bio-sensing. *Biomed. Opt. Express* **2011,** *2* (11), 3223-3231.

41. Iarossi, M.; Schiattarella, C.; Rea, I.; De Stefano, L.; Fittipaldi, R.; Vecchione, A.; Velotta, R.; Ventura, B. D., Colorimetric Immunosensor by Aggregation of Photochemically Functionalized Gold Nanoparticles. *ACS Omega* **2018,** *3* (4), 3805-3812.

42. Makaraviciute, A.; Jackson, C. D.; Millner, P. A.; Ramanaviciene, A., Considerations in producing preferentially reduced half-antibody fragments. *J. Immunol. Methods* **2016,** *429*, 50-56.

43. Bewley, T. A.; Li, C. H., The reduction of protein disulfide bonds in the absence of denaturants. *Int. J. Prot. Res.* **1969,** *1* (1-4), 117-124.

44. Vikholm-Lundin, I.; Albers, W. M., Site-directed immobilisation of antibody fragments for detection of C-reactive protein. *Biosens. Bioelectron.* **2006,** *21* (7), 1141-1148.

45. Wang, H.; Wu, J.; Li, J.; Ding, Y.; Shen, G.; Yu, R., Nanogold particle-enhanced oriented adsorption of antibody fragments for immunosensing platforms. *Biosens. Bioelectron.* **2005,** *20* (11), 2210-2217.

46. Karyakin, A. A.; Presnova, G. V.; Rubtsova, M. Y.; Egorov, A. M., Oriented immobilization of antibodies onto the gold surfaces via their native thiol groups. *Anal. Chem.* **2000,** *72* (16), 3805-3811.

47. Makaraviciute, A.; Ruzgas, T.; Ramanavicius, A.; Ramanaviciene, A., Antibody fragment immobilization on planar gold and gold nanoparticle modified quartz crystal microbalance with dissipation sensor surfaces for immunosensor applications. *Anal. Methods* **2014,** *6* (7), 2134-2140.

48. Sharma, H.; Mutharasan, R., Half Antibody Fragments Improve Biosensor Sensitivity without Loss of Selectivity. *Anal. Chem.* **2013,** *85* (4), 2472-2477.

49. Mustafaoglu, N.; Kiziltepe, T.; Bilgicer, B., Site-specific conjugation of an antibody on a gold nanoparticle surface for one-step diagnosis of prostate specific antigen with dynamic light scattering. *Nanoscale* **2017,** *9* (25), 8684-8694.

50. Wang, Y.; Tang, L. J.; Jiang, J. H., Surface-enhanced raman spectroscopy-based, homogeneous, multiplexed immunoassay with antibody-fragments-decorated gold nanoparticles. *Anal. Chem.* **2013,** *85* (19), 9213-9220.

51. Balevicius, Z.; Ramanaviciene, A.; Baleviciute, I.; Makaraviciute, A.; Mikoliunaite, L.; Ramanavicius, A., Evaluation of intact- and fragmented-antibody based immunosensors by total internal reflection ellipsometry. *Sens. Actuators B* **2011,** *160* (1), 555-562.

52. Yoshimoto, K.; Nishio, M.; Sugasawa, H.; Nagasaki, Y., Direct Observation of Adsorption-Induced Inactivation of Antibody Fragments Surrounded by Mixed-PEG Layer on a Gold Surface. *J. Am. Chem. Soc.* **2010,** *132* (23), 7982-7989.

53. Alves, N. J.; Kiziltepe, T.; Bilgicer, B., Oriented Surface Immobilization of Antibodies at the Conserved Nucleotide Binding Site for Enhanced Antigen Detection. *Langmuir* **2012,** *28* (25), 9640-9648.

54. Filbrun, S. L.; Driskell, J. D., A fluorescence-based method to directly quantify antibodies immobilized on gold nanoparticles. *Analyst* **2016,** *141* (12), 3851-3857.

55. Grubisha, D. S.; Lipert, R. J.; Park, H.-Y.; Driskell, J.; Porter, M. D., Femtomolar Detection of Prostate-Specific Antigen: An Immunoassay Based on Surface-Enhanced Raman Scattering and Immunogold Labels. *Anal. Chem.* **2003,** *75* (21), 5936-5943.

56. Stuchinskaya, T.; Moreno, M.; Cook, M. J.; Edwards, D. R.; Russell, D. A., Targeted photodynamic therapy of breast cancer cells using antibody–phthalocyanine–gold nanoparticle conjugates. *Photochem. Photobiol. Sci.* **2011,** *10* (5), 822-831.

57. Špringer, T.; Chadtová Song, X.; Ermini, M. L.; Lamačová, J.; Homola, J., Functional gold nanoparticles for optical affinity biosensing. *Anal. Bioanal. Chem.* **2017,** *409* (16), 4087-4097.

58. Hinterwirth, H.; Stübiger, G.; Lindner, W.; Lämmerhofer, M., Gold Nanoparticle-Conjugated Anti-Oxidized Low-Density Lipoprotein Antibodies for Targeted Lipidomics of Oxidative Stress Biomarkers. *Anal. Chem.* **2013,** *85* (17), 8376-8384.

59. Haller, E.; Lindner, W.; Lämmerhofer, M., Gold nanoparticle–antibody conjugates for specific extraction and subsequent analysis by liquid chromatography–tandem mass spectrometry of malondialdehyde-modified low density lipoprotein as biomarker for cardiovascular risk. *Anal. Chim. Acta* **2015,** *857,* 53-63.

60. Eck, W.; Craig, G.; Sigdel, A.; Ritter, G.; Old, L. J.; Tang, L.; Brennan, M. F.; Allen, P. J.; Mason, M. D., PEGylated Gold Nanoparticles Conjugated to Monoclonal F19 Antibodies as Targeted Labeling Agents for Human Pancreatic Carcinoma Tissue. *ACS Nano* **2008,** *2* (11), 2263-2272.

61. Leggett, R.; Lee-Smith, E. E.; Jickells, S. M.; Russell, D. A., "Intelligent" Fingerprinting: Simultaneous Identification of Drug Metabolites and Individuals by Using Antibody-Functionalized Nanoparticles. *Angew. Chem. Int. Ed.* **2007,** *46* (22), 4100-4103.

62. Cummins, M.; Dogovski, C.; Robert, R.; Alderton, M.; Chong, D.; Proll, D.; Pontes-Braz, L.; Raicevic, A.; Hattarki, M.; Nuttall, S., Kinetic characterization of a panel of high-affinity monoclonal antibodies targeting ricin and recombinant re-formatting for biosensor applications. *Antibodies* **2014,** *3* (2), 215-231.

63. Malaspina, D. C.; Longo, G.; Szleifer, I., Behavior of ligand binding assays with crowded surfaces: Molecular model of antigen capture by antibody-conjugated nanoparticles. *PLOS ONE* **2017,** *12* (9), e0185518-e0185518.

64. Inci, F.; Tokel, O.; Wang, S.; Gurkan, U. A.; Tasoglu, S.; Kuritzkes, D. R.; Demirci, U., Nanoplasmonic quantitative detection of intact viruses from unprocessed whole blood. *ACS Nano* **2013,** *7* (6), 4733-4745.

65. Niemeyer, C. M.; Ceyhan, B., DNA-Directed Functionalization of Colloidal Gold with Proteins *Angew. Chem. Int. Ed.* **2001,** *40* (19), 3685-3688.

66. Hazarika, P.; Ceyhan, B.; Niemeyer, C. M., Sensitive Detection of Proteins Using Difunctional DNA-Gold Nanoparticles. *Small* **2005,** *1* (8-9), 844-848.

67. Jung, Y.; Lee, J. M.; Jung, H.; Chung, B. H., Self-Directed and Self-Oriented Immobilization of Antibody by Protein G−DNA Conjugate. *Anal. Chem.* **2007,** *79* (17), 6534-6541.

68. Finetti, C.; Sola, L.; Pezzullo, M.; Prosperi, D.; Colombo, M.; Riva, B.; Avvakumova, S.; Morasso, C.; Picciolini, S.; Chiari, M., Click Chemistry Immobilization of Antibodies on Polymer Coated Gold Nanoparticles. *Langmuir* **2016,** *32* (29), 7435-7441.

69. Saha, B.; Evers, T. H.; Prins, M. W. J., How Antibody Surface Coverage on Nanoparticles Determines the Activity and Kinetics of Antigen Capturing for Biosensing. *Anal. Chem.* **2014,** *86* (16), 8158-8166.

70. Tripathi, K.; Driskell, J. D., Quantifying Bound and Active Antibodies Conjugated to Gold Nanoparticles: A Comprehensive and Robust Approach To Evaluate Immobilization Chemistry. *ACS Omega* **2018,** *3* (7), 8253-8259.

71. Welch, N. G.; Scoble, J. A.; Muir, B. W.; Pigram, P. J., Orientation and characterization of immobilized antibodies for improved immunoassays (Review). *Biointerphases* **2017,** *12* (2), 02D301-02D301.

72. Trilling, A. K.; Beekwilder, J.; Zuilhof, H., Antibody orientation on biosensor surfaces: A minireview. *Analyst* **2013,** *138* (6), 1619-1627.

73. Hermanson, G. T., Mass Tags and Isotope Tags. In *Bioconjugate techniques*, Elsevier: 2008; pp 649-665.

74. Pollitt, M. J.; Buckton, G.; Piper, R.; Brocchini, S., Measuring antibody coatings on gold nanoparticles by optical spectroscopy. *RSC Adv.* **2015,** *5* (31), 24521-24527.

75. Vörös, J., The Density and Refractive Index of Adsorbing Protein Layers. *Biophys. J.* **2004,** *87* (1), 553-561.

76. Zhao, H.; Brown, P. H.; Schuck, P., On the distribution of protein refractive index increments. *Biophys. J.* **2011,** *100* (9), 2309-2317.

77. Bell, N. C.; Minelli, C.; Shard, A. G., Quantitation of IgG protein adsorption to gold nanoparticles using particle size measurement. *Anal. Methods.* **2013,** *5* (18), 4591-4601.

78. James, A. E.; Driskell, J. D., Monitoring gold nanoparticle conjugation and analysis of biomolecular binding with nanoparticle tracking analysis (NTA) and dynamic light scattering (DLS). *Analyst* **2013,** *138* (4), 1212-1218.

79. Höldrich, M.; Liu, S.; Epe, M.; Lämmerhofer, M., Taylor dispersion analysis, resonant mass measurement and bioactivity of pepsin-coated gold nanoparticles. *Talanta* **2017,** *167*, 67-74.

80. Fountoulakis, M.; Lahm, H.-w., Hydrolysis and amino acid composition analysis of proteins. *J. Chromatog. A* **1998,** *826* (2), 109-134.

81. Hsu, Y.-H., Immunogold for detection of antigen on nitrocellulose paper. *Anal. Biochem.* **1984,** *142* (1), 221-225.

82. Moeremans, M.; Daneels, G.; Van Dijck, A.; Langanger, G.; De Mey, J., Sensitive visualization of antigen-antibody reactions in dot and blot immune overlay assays with immunogold and immunogold/silver staining. *J. Immunol. Methods* **1984,** *74* (2), 353-360.

83. Ghosh, B. K.; Ghosh, A., Subcellular localization of alkaline phosphatase in Bacillus licheniformis 749/C by immunoelectron microscopy with colloidal gold. *J. Bacteriol.* **1984,** *159* (2), 668-677.

84. Englebienne, P., Use of colloidal gold surface plasmon resonance peak shift to infer affinity constants from the interactions between protein antigens and antibodies specific for single or multiple epitopes. *Analyst* **1998,** *123* (7), 1599-1603.

85. Englebienne, P.; Van Hoonacker, A.; Verhas, M., High-throughput screening using the surface plasmon resonance effect of colloidal gold nanoparticles. *Analyst* **2001,** *126* (10), 1645-1651.

86. Dykman, L. A.; Bogatyrev, V. A.; Khlebtsov, B. N.; Khlebtsov, N. G., A protein assay based on colloidal gold conjugates with trypsin. *Anal. Biochem.* **2005,** *341* (1), 16-21.

87. Liu, Y.; Liu, Y.; Mernaugh, R. L.; Zeng, X., Single chain fragment variable recombinant antibody functionalized gold nanoparticles for a highly sensitive colorimetric immunoassay. *Biosens. Bioelectron.* **2009,** *24* (9), 2853-2857.

88. Sharma, P.; Kumar, B.; Suri, C. R., Antibody Functionalised Gold Nanoprobes Based Colorimetric Assay for the Direct Detection of Phenylurea Herbicide. *Environ. Pollut.* **2012,** *1* (1), 12-19.

89. Frederix, F.; Friedt, J.-M.; Choi, K.-H.; Laureyn, W.; Campitelli, A.; Mondelaers, D.; Maes, G.; Borghs, G., Biosensing Based on Light Absorption of Nanoscaled Gold and Silver Particles. *Anal. Chem.* **2003,** *75* (24), 6894-6900.

90. Lee, J. H.; Kim, B. C.; Oh, B. K.; Choi, J. W., Highly sensitive localized surface plasmon resonance immunosensor for label-free detection of HIV-1. *Nanomedicine* **2013,** *9* (7), 1018-1026.

91. Chang, Y. F.; Wang, S. F.; Huang, J. C.; Su, L. C.; Yao, L.; Li, Y. C.; Wu, S. C.; Chen, Y. M. A.; Hsieh, J. P.; Chou, C., Detection of swine-origin influenza A (H1N1) viruses using a localized surface plasmon coupled fluorescence fiber-optic biosensor. *Biosens. Bioelectron.* **2010,** *26* (3), 1068-1073.

92. Wang, J.; Wang, L.; Sun, Y.; Zhu, X.; Cao, Y.; Wang, X.; Zhang, H.; Song, D., Surface plasmon resonance biosensor based on Au nanoparticle in titania sol-gel membrane. *Colloids Surf. B* **2010,** *75* (2), 520-525.

93. Andrew Lyon, L.; Musick, M. D.; Natan, M. J., Colloidal Au-enhanced surface plasmon resonance immunosensing. *Anal. Chem.* **1998,** *70* (24), 5177-5183.

94. Besselink, G. A. J.; Kooyman, R. P. H.; van Os, P. J. H. J.; Engbers, G. H. M.; Schasfoort, R. B. M., Signal amplification on planar and gel-type sensor surfaces in surface plasmon resonance-based detection of prostate-specific antigen. *Anal. Biochem.* **2004,** *333* (1), 165-173.

95. Choi, J. W.; Kang, D. Y.; Jang, Y. H.; Kim, H. H.; Min, J.; Oh, B. K., Ultra-sensitive surface plasmon resonance based immunosensor for prostate-specific antigen using gold nanoparticle-antibody complex. *Colloids Surf. A* **2008,** *313-314*, 655-659.

96. Uludag, Y.; Tothill, I. E., Cancer biomarker detection in serum samples using surface plasmon resonance and quartz crystal microbalance sensors with nanoparticle signal amplification. *Anal. Chem.* **2012,** *84* (14), 5898-5904.

97. Lee, K. S.; El-Sayed, M. A., Gold and silver nanoparticles in sensing and imaging: Sensitivity of plasmon response to size, shape, and metal composition. *J. Phys. Chem. B* **2006,** *110* (39), 19220-19225.

98. Yguerabide, J.; Yguerabide, E. E., Light-scattering submicroscopic particles as highly fluorescent analogs and their use as tracer labels in clinical and biological applications II. Experimental characterization. *Anal. Biochem.* **1998,** *262* (2), 157-176.

99. Jans, H.; Liu, X.; Austin, L.; Maes, G.; Huo, Q., Dynamic Light Scattering as a Powerful Tool for Gold Nanoparticle Bioconjugation and Biomolecular Binding Studies. *Anal. Chem.* **2009,** *81* (22), 9425-9432.

100. Liu, X.; Dai, Q.; Austin, L.; Coutts, J.; Knowles, G.; Zou, J.; Chen, H.; Huo, Q., A One-Step Homogeneous Immunoassay for Cancer Biomarker Detection Using Gold Nanoparticle Probes Coupled with Dynamic Light Scattering. *J. Am. Chem. Soc.* **2008,** *130* (9), 2780-2782.

101. Clegg, R. M., Fluorescence resonance energy transfer. *Cur. Opin. Biotechnol.* **1995,** *6* (1), 103-110.

102. Schneider, G.; Decher, G.; Nerambourg, N.; Praho, R.; Werts, M. H. V.; Blanchard-Desce, M., Distance-dependent fluorescence quenching on gold nanoparticles ensheathed with layer-by-layer assembled polyelectrolytes. *Nano Lett.* **2006,** *6* (3), 530-536.

103. Kühn, S.; Håkanson, U.; Rogobete, L.; Sandoghdar, V., Enhancement of single-molecule fluorescence using a gold nanoparticle as an optical nanoantenna. *Phys. Rev. Lett.* **2006,** *97* (1), 1-4.

104. Anger, P.; Bharadwaj, P.; Novotny, L., Enhancement and quenching of single-molecule fluorescence. *Phys. Rev. Lett.* **2006,** *96* (11), 3-6.

105. Hong, B.; Kang, K. A., Biocompatible, nanogold-particle fluorescence enhancer for fluorophore mediated, optical immunosensor. *Biosens. Bioelectron.* **2006,** *21* (7), 1333-1338.

106. Hsieh, B.-Y.; Chang, Y.-F.; Ng, M.-Y.; Liu, W.-C.; Lin, C.-H.; Wu, H.-T.; Chou, C., Localized Surface Plasmon Coupled Fluorescence Fiber-Optic Biosensor with Gold Nanoparticles. *Anal. Chem.* **2007,** *79* (9), 3487-3493.

107. Stringer, R. C.; Schommer, S.; Hoehn, D.; Grant, S. A., Development of an optical biosensor using gold nanoparticles and quantum dots for the detection of Porcine Reproductive and Respiratory Syndrome Virus. *Sens. Actuators B* **2008,** *134* (2), 427-431.

108. Liu, D.; Huang, X.; Wang, Z.; Jin, A.; Sun, X.; Zhu, L.; Wang, F.; Ma, Y.; Niu, G.; Hight Walker, A. R.; Chen, X., Gold Nanoparticle-Based Activatable Probe for Sensing Ultralow Levels of Prostate-Specific Antigen. *ACS Nano* **2013,** *7* (6), 5568-5576.

109. Li, M.; Yang, H.; Li, S.; Zhao, K.; Li, J.; Jiang, D.; Sun, L.; Deng, A., Ultrasensitive and quantitative detection of a new β-agonist phenylethanolamine a by a novel immunochromatographic assay based on surface-enhanced Raman scattering (SERS). *J. Agr. Food Chem.* **2014,** *62* (45), 10896-10902.

110. Qian, X.; Peng, X. H.; Ansari, D. O.; Yin-Goen, Q.; Chen, G. Z.; Shin, D. M.; Yang, L.; Young, A. N.; Wang, M. D.; Nie, S., In vivo tumor targeting and spectroscopic detection with surface-enhanced Raman nanoparticle tags. *Nature Biotechnol.* **2008,** *26* (1), 83-90.

111. Cho, H.-Y.; Hossain, M. K.; Lee, J.-H.; Han, J.; Lee, H. J.; Kim, K.-J.; Kim, J.-H.; Lee, K.-B.; Choi, J.-W., Selective isolation and noninvasive analysis of circulating cancer stem cells through Raman imaging. *Biosens. Bioelectron.* **2018,** *102*, 372-382.

112. Lopez, A.; Lovato, F.; Hwan Oh, S.; Lai, Y. H.; Filbrun, S.; Driskell, E. A.; Driskell, J. D., SERS immunoassay based on the capture and concentration of antigen-assembled gold nanoparticles. *Talanta* **2016,** *146*, 388-393.

113. Wu, X.; Chen, X.; Gao, F.; Ma, W.; Xu, L.; Kuang, H.; Li, A.; Xu, C., SERS encoded nanoparticle heterodimers for the ultrasensitive detection of folic acid. *Biosens. Bioelectron.* **2016,** *75*, 55-58.

114. Ben Haddada, M.; Salmain, M.; Boujday, S., Gold colloid-nanostructured surfaces for enhanced piezoelectric immunosensing of staphylococcal enterotoxin A. *Sens. Actuators B* **2018,** *255*, 1604-1613.

115. Jin, X.; Jin, X.; Chen, L.; Jiang, J.; Shen, G.; Yu, R., Piezoelectric immunosensor with gold nanoparticles enhanced competitive immunoreaction technique for quantification of aflatoxin B1. *Biosens. Bioelectron.* **2009,** *24* (8), 2580-2585.

116. Chu, X.; Zhao, Z.-L.; Shen, G.-L.; Yu, R.-Q., Quartz crystal microbalance immunoassay with dendritic amplification using colloidal gold immunocomplex. *Sens. Actuators B* **2006,** *114* (2), 696-704.

Paper II

Direct Quantification of Surface Coverage of Antibody in IgG-Gold Nanoparticles Conjugates

Preface

As mentioned in Paper I, accurate and direct determination of antibody (Ab) surface coverage in gold nanoparticle-Ab (AuNP-Ab) bioconjugates still remains challenging. In this paper, we aimed at developing a fluorescence-based method for direct quantification of Ab surface coverage.

Rabbit immunoglobulin G (IgG), as Ab model, was first labeled by a fluorescent dye, fluorescein isothiocyanate (FITC), prior to conjugation to AuNPs. The prepared conjugates AuNP-IgG(FITC) were dissolved in NaCN and subsequently assayed using spectrofluorometry. For comparison, the non-bound IgG(FITC) in the supernatant was also quantified using spectrofluorometry and ELISA. The direct quantification gave an IgG surface coverage in good agreement with that obtained from calculation according to LSPR band shift induced by refractive index change consecutive to IgGs conjugation to AuNPs. In contrast, the indirect quantification methods overestimated the IgG surface coverage. Furthermore, the direct fluorescence-based quantification method was successfully applied to bioconjugates prepared through both physisorption and chemisorption strategies.

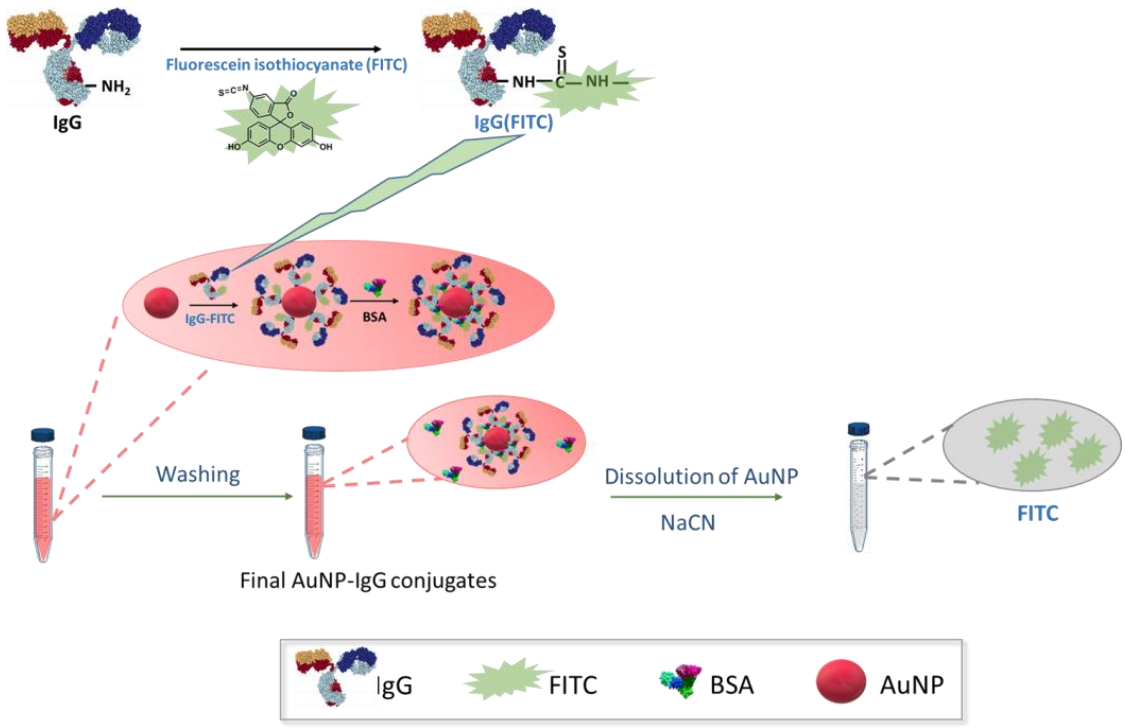

Figure II: Schematic illustration of the direct quantification of antibody surface coverage: labeling of IgG by FITC, bioconjugation of IgG to AuNP, dissolution of AuNP by NaCN and subsequent spectrofluorimetric assay of FITC.

Direct Quantification of Surface Coverage of Antibody in IgG-Gold Nanoparticles Conjugates

Lu Zhang[1,2,3,4], David Hu[1], Michèle Salmain[2], Bo Liedberg[3], and Souhir Boujday[1]*

[1] Sorbonne Université, CNRS, Laboratoire de Réactivité de Surface (LRS), 4 place Jussieu, F-75005 Paris, France.

[2] Sorbonne Université, CNRS, Institut Parisien de Chimie Moléculaire (IPCM), 4 place Jussieu F-75005 Paris, France.

[3] Centre for Biomimetic Sensor Science, School of Material Science and Engineering, Nanyang Technological University, 637553 Singapore.

[4] Sorbonne University and Nanyang Technological University Dual Degree PhD Programme.

Laboratoire de Réactivité de Surface, UMR CNRS 7197, *Sorbonne Université,* case 178, 4 Place Jussieu, 75252 Paris cedex 05, France.

Tel: +33144276001, Fax: +33144276033, souhir.boujday@sorbonne-universite.fr

ABSTRACT

It is of paramount importance to be able to accurately quantify surface coverage of antibodies on gold nanoparticles (AuNPs) so as to optimize the sensitivity of AuNP-based immunosensors. Herein, we developed a fluorescence-based method to directly quantify rabbit immunoglobulin G (IgG) used as antibody (Ab) model bound to AuNPs. Rabbit IgG was first labeled with fluorescein-5-isothiocyanate (FITC) prior to conjugation with AuNPs *via* either physisorption or chemisorption. IgG-conjugated AuNPs were treated with NaCN to dissolve the AuNPs and restore the fluorescence emission that was quenched in the presence of the metallic colloids, followed by quantification of fluorescein by spectrofluorimetry. For comparison, we also applied two indirect quantification methods based on the analysis of unbound IgGs remaining in the supernatant using fluorescence assay and enzyme-linked immunosorbent assay (ELISA). The direct assay indicated that about 4 IgGs were bound to every 15-nm diameter AuNP for both immobilization strategies. This surface coverage value is in good agreement with that obtained from the theoretical value deduced from the shift in the maximum of absorbance of the Localized Surface Plasmon Resonance band (LSPR). The indirect assays, either fluorescence or ELISA, commonly used to assess the Ab coverage on AuNPs, clearly overestimate the IgG surface coverage to a large extent, up to 3 to 4 times higher coverage was measured. Therefore, the direct fluorescence method designed and described in this paper is the most accurate method for quantification of surface coverage of Ab on AuNPs.

KEYWORDS. Gold nanoparticles, Immunoglobulin G (IgG), Quantification, Fluorescence, Adsorption.

INTRODUCTION

Antibody-modified gold nanoparticles (AuNP-Ab) are widely used in optical biosensing technologies.[1-10] The performance of AuNP-based biosensors is markedly dependent on the conjugation chemistry between antibodies and AuNPs that in turn controls surface coverage and Ab orientation.[11-15] In order to optimize the surface coupling chemistry and by thereby, the assay sensitivity, an accurate method for determination of Ab surface coverage is highly desirable. Quantification of Ab surface coverage is also needed to assess the reproducibility of AuNP-Ab bioconjugates preparations.

Several quantitative methods to measure surface coverage of antibodies conjugated to AuNPs have been reported to date. Generally, the quantity of adsorbed antibodies, and thus the surface coverage, is indirectly deduced from the amount of non-bound antibodies remaining in the supernatant after adsorption to AuNPs. Bicinchoninic acid (BCA) and Bradford total protein assays are typically capable of detecting low concentrations of proteins.[16-19] However, antibodies quantification by these indirect methods relies on the assumption that no Ab is lost during the purification process, *e.g.* during transfer of the solution from one container to another, or due to Ab adsorption to the container walls. This is why supernatant quantification often leads to an overestimation of Ab surface coverage on AuNP. Moreover, Ab conjugation to AuNPs is generally followed by a blocking step with another protein, typically BSA, to prevent aggregation of the nanoparticles in saline environment and, thereby, to increase the long-term stability of the colloidal solution.[20] This additional step, leading to the presence of another protein, makes the classical protein assays inapplicable. In this case, Ab assay in the supernatant can be achieved by ELISA using a microtiter plate coated with the corresponding antigen.[21]

BCA protein assay[22] and ELISA[23-24] have also been reported to directly quantify the antibodies in conjugates. While even with some careful calibration treatment, *i.e.* removal of nanoparticles contribution by subtracting a spectrum of pure nanoparticle solution, overestimation of Ab was still obtained. To eliminate the interference of nanoparticles, two methods consisting of proteins separation from nanoparticles prior to quantification have been recently reported. One of them relies on the dissolution of AuNPs in AuNP-Ab conjugates in a KI/I_2 mixture, followed by labeling of recovered Ab by the fluorescent dye NanoOrange and spectrofluorimetric measurement.[25] Although this method gives more reliable results than indirect protein assay

methods, it is still not applicable to Ab-conjugated AuNPs that are subsequently blocked by BSA. The second method is based on the complete digestion of protein in AuNP-protein conjugates in 6 N HCl followed by fluorescent labeling of the generated amino acids and assay of glycine derivative by HPLC-fluorescence detection.[26]

Alternatively, Ab attachment to AuNPs can be quantified from the LSPR peak shift caused by Ab-induced changes in the local refractive index (RI).[27-28] Though this approach provides a direct quantification of the adsorbed Ab, it requires accurate knowledge of proteins' RI at the nanoparticles surface. This is quite challenging because the RI depends on the surface coverage, protein orientation, and water content, none of which are known.[29-31]

Interestingly, surface coverage of DNA on AuNPs has been previously quantified by a fluorescence-based method involving fluorescently-labeled DNA strands. Its principle is based on the displacement of DNA strands chemisorbed on AuNPs by mercaptoethanol or by nanoparticle dissolution in KCN followed by spectrofluorimetric measurement.[32] Such a strategy could be translated to AuNP-Ab conjugates using fluorescently labeled Ab. Since the Ab is labeled by the fluorophore prior to AuNP adsorption, only the adsorbed Ab and not the other proteins will be eventually quantified.

In this paper, we wish to report the setup of a fluorescence-based method for the direct determination of surface coverage of a model Ab, namely rabbit immunoglobulin (IgG), on spherical AuNPs. FITC-labeled IgG (FITC = fluorescein-5-isothiocyanate) is first conjugated to AuNPs. Then the AuNP conjugates are dissolved by NaCN to release FITC-labelled IgG[33-34] which is subsequently assayed using spectrofluorimetry. This direct method is benchmarked against two indirect methods that rely on quantification of non-bound FITC-labelled IgG in the supernatant using spectrofluorimetry or ELISA. To further demonstrate the utility of the fluorescence-based method, two surface immobilization chemistries of IgGs on AuNPs are compared: non-covalent physisorption and covalent chemisorption through sulfur-gold bonds.

EXPERIMENTAL SECTION

Materials: Gold(III) chloride trihydrate (99.9%), sodium citrate dihydrate, tannic acid, 2-iminothiolane hydrochloride (Traut's reagent), bovine serum albumin (BSA), rabbit IgG (I-5006), goat anti-rabbit IgG (R-5001), fluorescein-5-isothiocyanate (FITC) were purchased from

Sigma-Aldrich. Phosphate-buffered saline (PBS) (pH = 7.4) was obtained from Fisher. Milli-Q water (18 MΩ·cm, Millipore) was used for the preparation of aqueous solutions.

Gold nanoparticle synthesis: Colloidal spherical AuNPs were prepared according to the Slot & Geuze method.[35] Two stock solutions were firstly prepared: solution A, 1 mL of 1% (w/v) $HAuCl_4$ and 79 mL of deionized water; solution B, 4 mL of 1% sodium citrate, 0.025 mL of 1% tannic acid, and 16 mL of deionized water. Solutions A and B were heated to 60 °C and mixed while stirring. Then the mixture was heated up to 90 °C, once the solution turned red. The temperature was increased until boiling and kept under reflux for 30 min. Finally, the solution was cooled on ice bath and stored in a light-proof container at 4 °C. The colloidal solution of AuNPs was characterized by UV-Vis spectroscopy, Dynamic Light Scattering (DLS), zeta potential and Transmission Electron Microscopy (TEM).

Chemical modification of IgG: ***FITC labeling of IgG.*** To a solution of rabbit IgG (2 mg/mL in 0.1 M sodium carbonate buffer, pH 9, 500 µL), was slowly added a solution of FITC (1 mg/mL in anhydrous DMSO, 25 µL) while gently and continuously stirring the protein solution. The reaction mixture was incubated overnight at 4°C in the dark. A solution of NH_4Cl (2 M, 12.5 µL) was added to a final concentration of 50 mM and incubated for 2 h at 4 °C, to quench the reaction. Then glycerol (25 µL) was added to a final concentration of 5%. Unbound FITC was separated from the IgG(FITC) conjugate by diafiltration in PBS using an Amicon Ultracentrifugal filter (30 kDa cutoff). The concentration of FITC in filtrates after each centrifugation was quantified by reading the absorbance at 495 nm. Cycles of concentration/dilution were repeated until the concentration of FITC in filtrates no longer decreased. The IgG(FITC) conjugate in PBS was recovered and stored in a light-proof container at -20°C. IgG concentration of IgG(FITC) sample was determined from the absorbance at 280 nm (A_{280}) and the absorbance at 495 nm (A_{495}) according to equation 1

$$IgG\left(\frac{mg}{ml}\right) = \frac{A_{280} - 0.35 * A_{495}}{1.4} \qquad \text{Equation 1}$$

Where 1.4 is the A_{280} of IgG from most species at a concentration of 1.0 mg/ml at pH 7.0, and ($0.35 \times A_{495}$) is the correction factor due to the absorbance of FITC at 280 nm. The F/P ratio is defined as the number of Fluorescein entities (F) per molecule of IgG (P stands for Protein) in the conjugate. It was calculated according to equation 2

$$\frac{F}{P} = \frac{2.77 * A_{495}}{A_{280} - 0.35 * A_{495}} \qquad \text{Equation 2}$$

Thiolation of IgG(FITC). Traut's reagent (1 mg/mL, 40 equiv.) was allowed to react with IgG(FITC) in 40 mM phosphate buffer, pH 8.0 for 1 h at room temperature to generate sulfhydryl groups.[36] The thiolated IgG(FITC)-SH was separated from excess Traut's reagent by gel filtration (Dextran desalt column, 10 mL, ThermoFisher) using 10 mM phosphate buffer, pH 7.4 (PB) as eluent. One-ml fractions were collected and analyzed at 280 nm. The fractions containing the protein were pooled and the resulting IgG(FITC)-SH solution was concentrated by ultrafiltration using a centrifugal filter (Amicon ultra-4, 50 kDa cutoff, Millipore).

Conjugation of IgG to gold nanoparticles: For chemisorption of IgGs to AuNPs, the colloidal AuNP solution (5 mL) was adjusted to pH 8-9 with K_2CO_3 solution (0.1 M), followed by addition of 55 µg of IgG(FITC)-SH (in 10 mM phosphate buffer, pH 7.4). The solution was incubated for 1 h at room temperature, then BSA was added to a final concentration of 0.5% (w/v) to block the free binding sites on the AuNPs. After another 1 h, the solution was centrifuged at 10,000g for 30 min at 4°C and the supernatant (S1 in Fig. S2) was retrieved and re-centrifuged to give S1a that was kept for analysis (Fig. S2). The first (P1) and second (P1a) pellets were pooled and redispersed in 10 mM PB, pH 7.4 with 0.25% BSA (5 mL). The solution was submitted to a second round of centrifugation and the resulting pellet was finally re-dispersed in storage buffer (10 mM PB, pH 7.4 with 0.25% BSA, 4 mL) while the supernatant (S2a, Fig. S2) was kept for analysis. The final conjugate is named AuNP-S-IgG(FITC). Physisorption of IgG(FITC) to AuNPs was carried out according to the same protocol using IgG(FITC) and the final conjugate is named AuNP-IgG(FITC).

Dissolution of IgG-conjugated AuNP: AuNPs or IgG(FITC)-conjugated AuNPs (500 µL) were mixed with NaCN (1 mg/mL adjusted to pH 12 with NaOH, 325 µL) and incubated overnight. Complete dissolution of the nanoparticles was evidenced by the disappearance of the LSPR peak of AuNPs (Fig. S5).

Quantification by spectrofluorimetry: Quantification of fluorescein in the supernatants (S1a and S2a) and in the bioconjugates after dissolution of nanoparticles according to the above procedure was done by spectrofluorimetry. Fluorescent signal is highly sensitive to medium change. In order to build up accurate calibration curves, standard solutions were prepared in the same matrix as the samples. The appropriate steps performed to match the matrix are given in

the supplementary part and illustrated in Fig. S6 and the calibration curves are shown in Fig. S7-9.

Quantification of IgG by ELISA: Goat anti-rabbit IgG (10 µg/mL in carbonate buffer, pH 9.5, 100 µL) was pipetted into each well of a flat-bottomed polystyrene 96-well plate (Greiner bio-one) and incubated overnight at 4°C. The content was discarded and non-specific sites were blocked by PBS-0.1% BSA (100 µL) for 1 h at room temperature. Wells were washed 3 times with PBS-0.05% Tween 20. Standard solutions of IgG(FITC) or samples (100 µL) to be quantified were dispensed into the wells. The plate was incubated 2 h at room temperature. After washing with PBS-0.05% Tween 20 (3x100 µL), HRP-labelled goat anti-rabbit IgG conjugate (1/4000, 100 µL) was added to each well and incubated 1 h at room temperature. After washing with PBS-0.05% Tween 20, a mixture of o-phenylenediamine dihydrochloride (OPD) and H_2O_2 (7 mg OPD + 4 µL H_2O_2 in 10 mL of citrate-phosphate buffer, pH 5, 100 µL) substrate solution was added to each well. After the color developed, H_2SO_4 (2.5 M, 50 µL) was added to each well to stop the enzymatic reaction. After 10 min in the dark, the absorbance of each well was read at 485 nm with a microplate reader (Fluostar Optima, BMG Labtech). The concentration of IgG(FITC) or IgG(FITC)-SH in the samples was deduced from the calibration curve established by plotting A_{485} vs. IgG(FITC) concentration (Fig. S11).

Characterization techniques: UV-Visible (***UV-Vis***) spectra were acquired on a Cary 50 spectrophotometer (Varian, Inc.). Analysis of colloidal solutions was performed in the range 300 - 800 nm. Protein solutions were analyzed at 280 nm and 495 nm (for FITC). Milli-Q H_2O was used as the blank. Dynamic Light Scattering (***DLS***), and zeta potential (***ELS***) measurements were performed using Litesizer™ 500 apparatus (Anton Paar) equipped with a 658 nm laser operating at 40 mW. The backscattered light collection angle was set to 90°. The zeta potential was measured in a Ω-shaped capillary tube cuvette with an applied potential of 150 V. AuNPs were visualized using a JEOL JEM 1011 Transmission Electron Microscope (***TEM***) operating at an accelerating voltage of 100 kV. A drop of AuNP colloidal solution was dispensed on a carbon-coated copper grid and dried at room temperature before imagining. The size distribution of AuNPs was determined using Image J. ***Fluorescence*** spectra were acquired with a FP-6200 spectrofluorimeter (Jasco) using a 1-cm pathlength quartz cuvette. The bandwidth of emission/excitation is 5 nm/5nm. Excitation was set at 485 nm and emission was measured in the range of 495 nm to 600 nm with a scanning speed of 250 nm/min. Temperature was controlled by a Peltier element and set at 20 ± 0.1 °C.

RESULTS AND DISCUSSIONS

Gold nanoparticle synthesis and characterization: As synthesized AuNPs were characterized by UV-visible spectroscopy, TEM, DLS and zeta potential measurements. The absorption spectrum exhibits a distinct plasmon peak at ~520 nm (Figure 1-A), corresponding to spherical AuNPs with a narrow distribution in size and shape. This observation is confirmed by TEM micrographs (Figure 1-C and D). The size distribution taken by analyzing ca. 1000 particles is narrow (Figure 1-B) and the average size of AuNPs is centered at 14.8 ± 1 nm obtained by Gaussian distribution. The concentration of AuNP solution was determined to equal to 2.8 nM using an extinction coefficient of 3.8 x 10^8 M^{-1} cm^{-1} taken from the literature.[37] The colloidal solution was further characterized using DLS and zeta potential measurements. Hydrodynamic diameter (intensity weighted peak) of AuNPs is 20.9 nm with polydispersity of 0.12, and the mean zeta potential is -55.75 ± 2.5 mV.

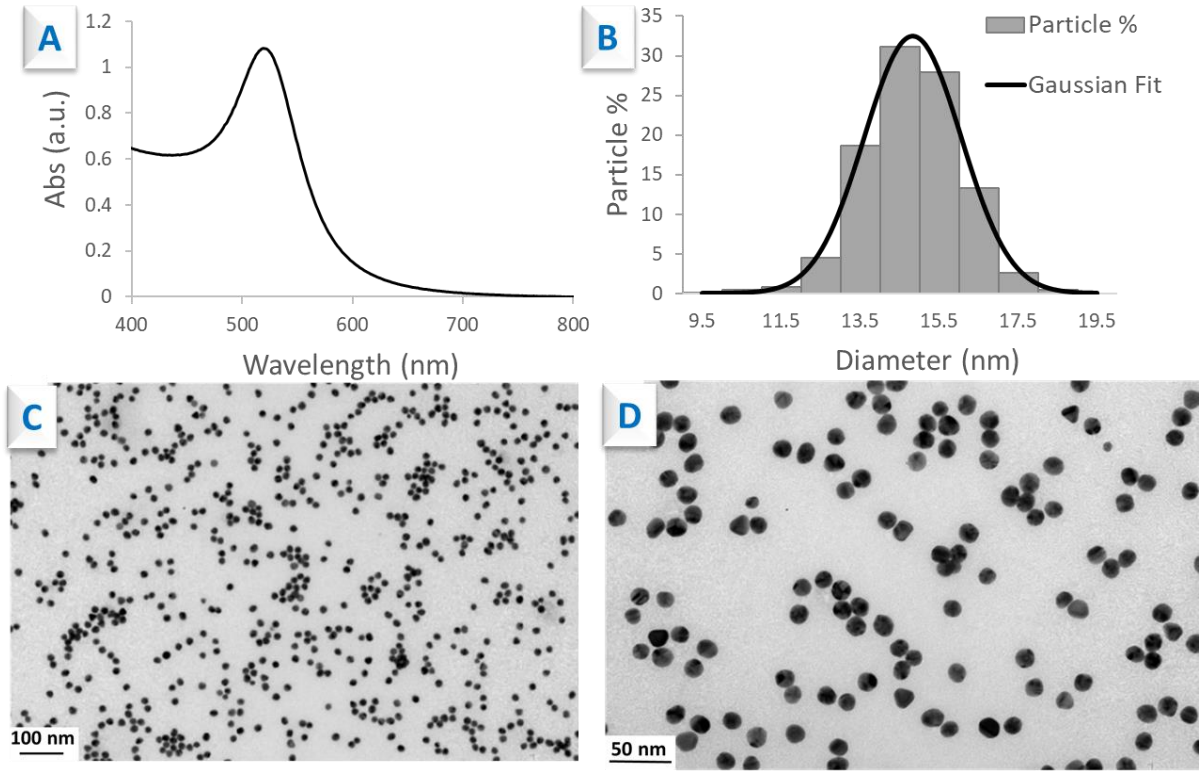

Figure 1 : Characterization of AuNP: A. UV-Vis absorption spectrum of colloidal AuNP solution, B. histogram of AuNP size distribution; C. and D. TEM micrographs of AuNPs.

Chemical modification of IgG: Labelling of rabbit IgG by FITC was done according to Figure 2-A to yied an IgG(FITC) conjugate with a F/P ratio of 1.9 (Fig. S1 and Table S1).

IgG(FITC) was used as such for physisorption to AuNPs. Alternatively, since rabbit IgG does not contain any free cysteines, thiol functions were chemically introduced on the lysines amino groups using Traut's reagent to produce IgG(FITC)-SH (Figure 2-B). This thiolated bioconjugate was then used for chemisorption to AuNPs by formation of S-Au bonds. Surprisingly, the calculated F/P ratio of IgG(FITC)-SH is 1.34. (Table S1) The decrease of F/P may be due to the additional diafiltration steps performed after thiolation that may have further removed weakly bound FITC.

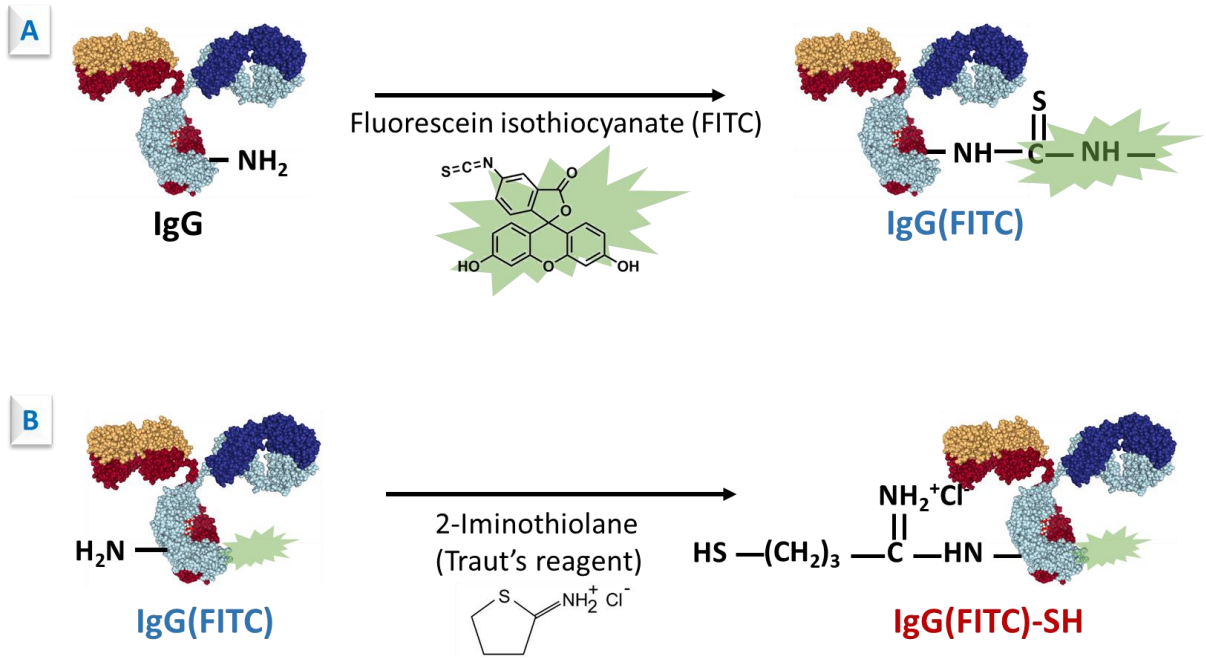

Figure 2 : Schematic illustration of chemical modification of IgG: A. FITC labeling of IgG; B. thiolation of IgG(FITC).

Engineering of IgG(FITC)-AuNP bioconjugates: Stepwise conjugation of IgG(FITC)-SH to AuNPs was characterized by absorption spectroscopy. Figure 3-A shows the absorption spectrum of the colloidal solution of AuNPs before and after chemisorption of IgG(FITC)-SH. The position of LSPR peak was determined following the zero value of the first derivative of spectrum shown in Figure 3-C as recommended in the literature.[38] The LSPR peak of AuNPs initially at 519 nm (black trace) shifted to 522 nm (red trace) after 1 h incubation, as a result of chemisorption of IgG(FITC)-SH on the AuNPs. Addition of BSA to block the free binding sites led to a further shift of the LSPR peak to 526 nm (not shown). The final AuNP-S-IgG conjugate was re-analyzed after centrifugation and re-suspension in storage buffer and its LSPR peak appeared at 527 nm (dark cyan trace). Physisorption of IgG(FITC) on AuNPs induced the same trend on the LSPR peak of AuNPs, as shown in Figure 3-B and D. We noticed that LSPR peak

shift for the IgG adsorption step (*i.e.* 3 nm, for both chemisorption and physisorption) was smaller than that of native IgGs on AuNPs (Fig. S3, 5 nm). The UV-Vis spectrum of IgG(FITC) (Fig. S1) displays a peak at 495 nm owing to the contribution of FITC that is quite close to that of AuNPs. Its presence interferes with the peak of AuNPs, by counterbalancing the red-shift due to Ab adsorption, thus leading to an overall smaller peak shift after adsorption of IgG(FITC).

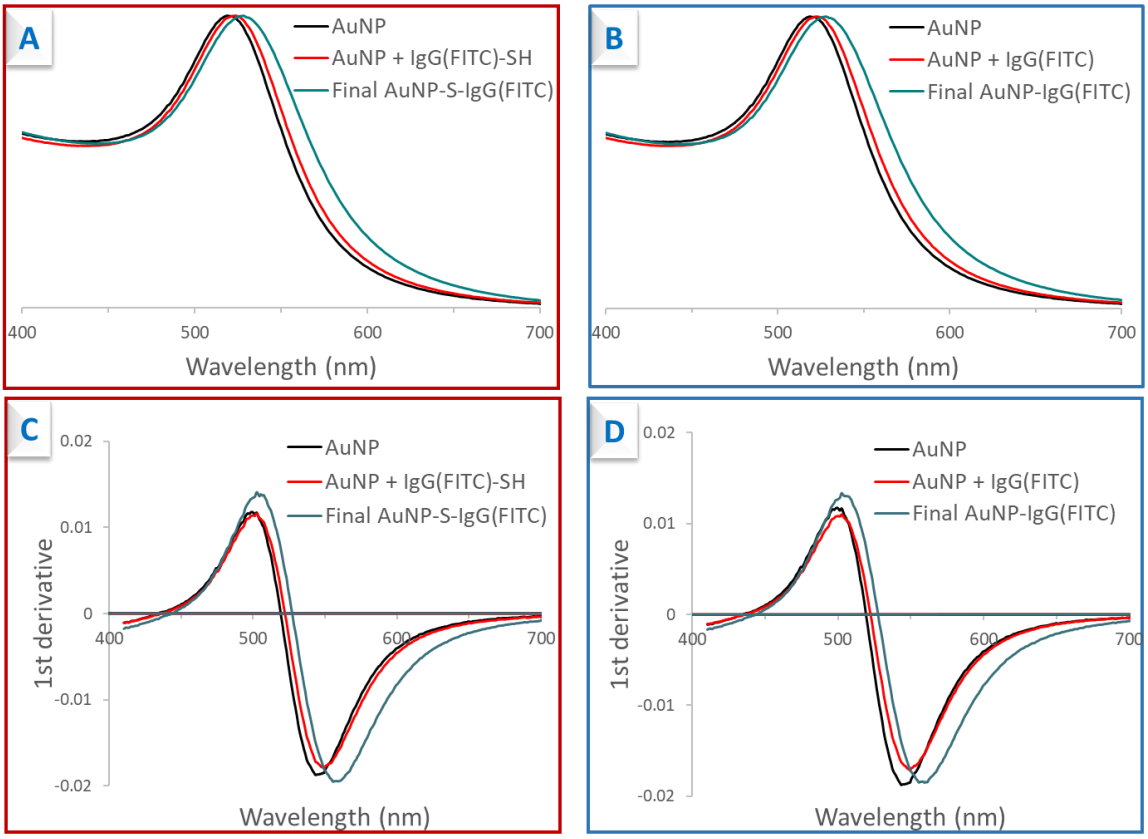

Figure 3 : Normalized UV-Vis absorption spectra of A. chemisorption and B. physisorption of IgG(FITC)-SH and IgG(FITC) on AuNPs. First order derivative of UV-Vis absorption spectra in A and B are shown in C. and D.

DLS and zeta potential measurements were performed on the colloidal solution before and after conjugation, in order to check the changes in the hydrodynamic diameter (D_H) and the zeta potential due to the adsorption of IgG(FITC) to AuNPs. The results are summarized in Table 1. Chemisorption of IgG(FITC)-SH followed by BSA blocking step induced a large increase of the D_H of nanoparticles from 20.9 nm to 101.9 nm while physisorption of IgG(FITC) resulted in an increase of D_H to 120.4 nm. Let us note that a large amount of BSA was used at the blocking step (0.5% w/v) and that the final storage buffer also contains a large amount of BSA

(0.25% w/v). We can reasonably suppose that a multilayer of BSA molecules formed on top of the layer of IgG molecules, resulting in the large increase of D_H.[19] On the other hand, the zeta potential increased from -55.8 mV to -15.7 mV for AuNP-S-IgG(FITC) and -18.3 mV for the AuNP-IgG(FITC) conjugates. The net charge of the bioconjugates is expected to be close to that of the protein itself at the working pH, if the protein fully covers the surface of AuNPs. Here AuNP surface is covered by a mixture of IgG and BSA. The zeta potential of rabbit IgG is -16.1 mV[21] and we measured the zeta potential of BSA which is -10.9 mV at pH 7.4. The zeta potential of the bioconjugates measured here is in agreement with the values for rabbit IgG and BSA.

Table 1 : Hydrodynamic diameter and zeta potential of AuNPs and IgG-conjugated AuNPs.

Nanoparticles	**D_H (nm)**	**Polydispersity**	**Mean zeta potential (mV)**
AuNP	20.9	0.12	-55.8 ± 2.6
AuNP-S-IgG	101.9	0.24	-15.7 ± 0.7
AuNP-IgG	120.4	0.28	-18.3 ± 0.6

Quantification of surface coverage by fluorescence spectrometry: FITC-based fluorescence assay was set up to quantify IgGs adsorbed on AuNPs. Not surprisingly, once adsorbed on AuNPs, the emission of fluorescein entities of Ig(FITC) was mostly quenched (Figure 4).[39-40] To recover the FITC fluorescence emission, the AuNPs had to be dissolved by NaCN. Complete dissolution of the IgG-conjugated nanoparticles was assessed by the disappearance of the LSPR peak of AuNPs (Fig. S5). Subsequent release of IgG(FITC) restored the fluorescence emission of fluorescein entities bound to IgG which was detected and quantified by spectrofluorimetry (Figure 4). The concentration of IgG(FITC) was calculated according to the related calibration equation (Table S3). The concentration of AuNPs in the biconjugate was calculated from the optical density of the colloidal solution at 527 nm (before cyanidation) assuming the same extinction coefficient as the citrate-coated AuNPs ($\varepsilon = 3.8 \times 10^8$ $M^{-1}.cm^{-1}$). An Ab surface coverage of 3.9 or 4.3 IgGs per AuNP was calculated for the AuNP-S-IgG and AuNP-IgG conjugates, respectively. The surface coverage of IgGs immobilized via chemisorption did not differ significantly from the surface coverage resulting from physisorption of IgGs to AuNPs.

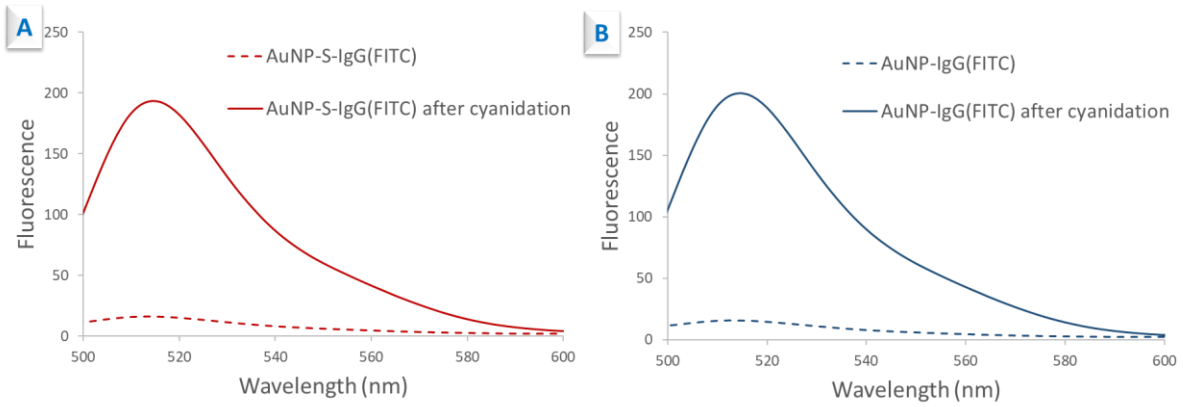

Figure 4 : Fluorescence emission spectra of conjugates before and after cyanidation. (A) AuNP-S-IgG(FITC) and (B) AuNP-IgG(FITC).

Indirect quantification of surface coverage by fluorimetry: The concentration of excess IgG(FITC) in the supernatants S1a and S2a collected after both washing steps was also measured using fluorescein emission and the related calibration equations listed in Table S3. The quantity of IgG(FITC) bound to the AuNPs was assumed to be the difference between added IgG(FITC) and the unbound IgG(FITC) present in both supernatants. As a result, the surface coverage of antibodies was found equal to 13.3 IgGs per AuNP for AuNP-S-IgG and 15 IgGs per AuNP for AuNP-IgG. These values are much higher than those measured by the direct fluorescence-based method.

Indirect quantification of surface coverage by ELISA: In the process of cyanidation at basic pH, both inter-chain and intra-chain disulfide bonds of IgG are cleaved by cyanide, followed by elimination of thiocyanate ions.[41] The alkali solution also leads to the degradation of IgG.[42] Both effects lead to the denaturation of IgG that prevente its quantification by ELISA. So ELISA was only used to quantify excess IgG in supernatants S1a and S2a. The calibration curve of IgG concentration is shown in Fig. S11. After subtracting the quantity of IgG in supernatants, surface coverages of 6.9 IgGs per AuNP for AuNP-S-IgG and 9.9 IgGs per AuNP for AuNP-IgG were calculated. Again the coverages are substantially higher than those observed with the direct method.

The bar chart in Figure 5 gathers the experimental surface coverages of IgG determined by the three methods. For comparison, the monolayer surface coverage of IgG on 14.8-nm diameter spherical gold nanoparticles theoretically estimated from the surface area of one nanoparticle and the average footprint of one Ab was calculated to be 9.8 IgGs per nanoparticle (see

Appendix). We also evaluated the surface coverage from the LSPR peak shift consecutive to adsorption of native IgGs to AuNPs (Fig. S3) that gave a value of 3.9 IgGs per AuNP (see detailed calculations in Appendix). This value is in very good agreement with the fluorescence-based direct method to quantify Ab coverage.

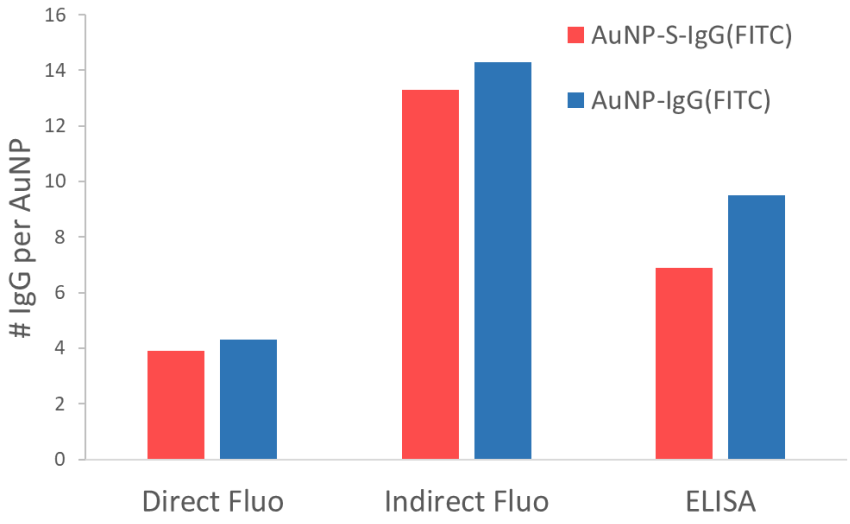

Figure 5 : Surface coverages of adsorbed IgGs on AuNPs measured by direct fluorescence-based assay of IgG(FITC) released from the AuNP conjugates (direct Fluo), indirect fluorescence assay (indirect Fluo) and ELISA by analysis of unbound IgG(FITC) in the supernatants.

Experimentally, the direct fluorescence assay gave around 4 IgGs per AuNP for both AuNP-S-IgG and AuNP-IgG, which is in agreement with the calculation according to LSPR shift, but lower than the theoretical value of 9.8 calculated from the IgG footprint assuming equal probability of IgG orientations on AuNPs. We then compared surface coverages of differently oriented IgG on AuNPs (Fig. S4 and Table S2) and we found the value obtained from 'flat-on' mode is very close to the direct fluorescence assay result. With this mode, the contact surface between IgG and AuNP is maximized, leading to stronger electrostatic interactions between IgG and AuNP, therefore, better stability of conjugates. For chemisorption, electrostatic interactions between IgG and AuNP may still predominant even in the presence of S-Au bonds. The indirect fluorescence assay gave 13.3 or 15 IgGs per AuNP, this overestimation may be partially due to the loss of IgG in the washing steps. Errors in the estimation of IgG(FITC) concentration may also arise from the fluorescence measurements themselves since, as mentioned above, emission of fluorescein is highly sensitive to the medium. Indeed, the two supernatants correspond to two different media, and even if great care was taken that the standard solutions of IgG(FITC) be prepared in the same media, there is still more chance of

calibration errors compared to the indirect ELISA method. On the whole, both adsorption methods gave similar surface coverages of IgGs on AuNP as measured by the fluorescence-based assays. In contrast, for a still unknown reason, the indirect ELISA method gave IgGs per AuNP of 9.9 for the physisorbed bioconjugate and 6.9 for the chemisorbed bioconjugate.

CONCLUSIONS

In this paper, we quantified the IgGs adsorbed on AuNP *via* two different coupling chemistries, *i.e.* physisorption and chemisorption of thiolated antibodies, by both direct and indirect fluorescence-based assays as well as by indirect ELISA. We found that the direct fluorescence assay of the bioconjugates after dissolution by NaCN gave an accurate quantification of IgG surface coverage compared to the other indirect methods based on the difference between added IgGs and excess IgGs in supernatants. The method of preparation of IgG-conjugated AuNPs, either by physisorption or by chemisorption, did not influence the final IgG-to-AuNP ratio, according to the direct fluorescence assay. Conversely, more IgGs were adsorbed on AuNPs *via* physisorption compared to chemisorption as calculated by indirect ELISA. We believe that the direct fluorescence-based method is reliable for quantification of Ab surface coverage on AuNP. It can be clearly seen that the method is applicable to both physisorption and chemisorption, thus it could be applied to evaluate novel coupling chemistries of Ab on AuNP and the reproducibility of the AuNP-Ab bioconjugation.

ACKNOWLEDGMENTS

This work was supported by the French-Singaporean PHC programme Merlion (grant 5.03.15). This work was also supported by ANR (Agence Nationale de la Recherche) and FWF (Deutsche Forschungsgemeinschaft), ANR-FWF programme, project NanoBioSensor (grant no: ANR-15-CE9-0026-02).

REFERENCES

1. Choi, D. H.; Lee, S. K.; Oh, Y. K.; Bae, B. W.; Lee, S. D.; Kim, S.; Shin, Y.-B.; Kim, M.-G., A dual gold nanoparticle conjugate-based lateral flow assay (LFA) method for the analysis of troponin I. *Biosens. Bioelectron.* **2010,** *25* (8), 1999-2002.

2. Ben Haddada, M.; Hu, D.; Salmain, M.; Zhang, L.; Peng, C.; Wang, Y.; Liedberg, B.; Boujday, S., Gold nanoparticle-based localized surface plasmon immunosensor for

staphylococcal enterotoxin A (SEA) detection. *Anal. Bioanal. Chem.* **2017,** *409* (26), 6227-6234.

3. Inci, F.; Tokel, O.; Wang, S.; Gurkan, U. A.; Tasoglu, S.; Kuritzkes, D. R.; Demirci, U., Nanoplasmonic quantitative detection of intact viruses from unprocessed whole blood. *ACS Nano* **2013,** *7* (6), 4733-4745.

4. Uludag, Y.; Tothill, I. E., Cancer biomarker detection in serum samples using surface plasmon resonance and quartz crystal microbalance sensors with nanoparticle signal amplification. *Anal. Chem.* **2012,** *84* (14), 5898-5904.

5. Liu, X.; Dai, Q.; Austin, L.; Coutts, J.; Knowles, G.; Zou, J.; Chen, H.; Huo, Q., A One-Step Homogeneous Immunoassay for Cancer Biomarker Detection Using Gold Nanoparticle Probes Coupled with Dynamic Light Scattering. *J. Am. Chem. Soc.* **2008,** *130* (9), 2780-2782.

6. Hsieh, B.-Y.; Chang, Y.-F.; Ng, M.-Y.; Liu, W.-C.; Lin, C.-H.; Wu, H.-T.; Chou, C., Localized Surface Plasmon Coupled Fluorescence Fiber-Optic Biosensor with Gold Nanoparticles. *Anal. Chem.* **2007,** *79* (9), 3487-3493.

7. Liu, D.; Huang, X.; Wang, Z.; Jin, A.; Sun, X.; Zhu, L.; Wang, F.; Ma, Y.; Niu, G.; Hight Walker, A. R.; Chen, X., Gold Nanoparticle-Based Activatable Probe for Sensing Ultralow Levels of Prostate-Specific Antigen. *ACS Nano* **2013,** *7* (6), 5568-5576.

8. Qian, X.; Peng, X. H.; Ansari, D. O.; Yin-Goen, Q.; Chen, G. Z.; Shin, D. M.; Yang, L.; Young, A. N.; Wang, M. D.; Nie, S., In vivo tumor targeting and spectroscopic detection with surface-enhanced Raman nanoparticle tags. *Nature Biotechnol.* **2008,** *26* (1), 83-90.

9. Wang, Y.; Tang, L. J.; Jiang, J. H., Surface-enhanced raman spectroscopy-based, homogeneous, multiplexed immunoassay with antibody-fragments-decorated gold nanoparticles. *Anal. Chem.* **2013,** *85* (19), 9213-9220.

10. Lopez, A.; Lovato, F.; Hwan Oh, S.; Lai, Y. H.; Filbrun, S.; Driskell, E. A.; Driskell, J. D., SERS immunoassay based on the capture and concentration of antigen-assembled gold nanoparticles. *Talanta* **2016,** *146*, 388-393.

11. Van Der Heide, S.; Russell, D. A., Optimisation of immuno-gold nanoparticle complexes for antigen detection. *J. Colloid Interface Sci.* **2016,** *471*, 127-135.

12. Byzova, N. A.; Safenkova, I. V.; Slutskaya, E. S.; Zherdev, A. V.; Dzantiev, B. B., Less is More: A Comparison of Antibody–Gold Nanoparticle Conjugates of Different Ratios. *Bioconjugate Chem.* **2017,** *28* (11), 2737-2746.

13. Welch, N. G.; Scoble, J. A.; Muir, B. W.; Pigram, P. J., Orientation and characterization of immobilized antibodies for improved immunoassays (Review). *Biointerphases* **2017,** *12* (2), 02D301-02D301.

14. Filbrun, S. L.; Filbrun, A. B.; Lovato, F. L.; Oh, S. H.; Driskell, E. A.; Driskell, J. D., Chemical modification of antibodies enables the formation of stable antibody–gold nanoparticle conjugates for biosensing. *Analyst* **2017,** *142* (23), 4456-4467.

15. Ciaurriz, P.; Fernández, F.; Tellechea, E.; Moran, J. F.; Asensio, A. C., Comparison of four functionalization methods of gold nanoparticles for enhancing the enzyme-linked immunosorbent assay (ELISA). *Beilstein J. Nanotechnol.* **2017,** *8* (1), 244-253.

16. Geng, S. B.; Wu, J.; Alam, M. E.; Schultz, J. S.; Dickinson, C. D.; Seminer, C. R.; Tessier, P. M., Facile Preparation of Stable Antibody–Gold Conjugates and Application to Affinity-Capture Self-Interaction Nanoparticle Spectroscopy. *Bioconjugate Chem.* **2016,** *27* (10), 2287-2300.

17. Raoof, M.; Corr, S. J.; Kaluarachchi, W. D.; Massey, K. L.; Briggs, K.; Zhu, C.; Cheney, M. A.; Wilson, L. J.; Curley, S. A., Stability of antibody-conjugated gold nanoparticles in the endolysosomal nanoenvironment: implications for noninvasive radiofrequency-based cancer therapy. *Nanomed. Nanotechnol.* **2012,** *8* (7), 1096-1105.

18. Tripathi, K.; Driskell, J. D., Quantifying Bound and Active Antibodies Conjugated to Gold Nanoparticles: A Comprehensive and Robust Approach To Evaluate Immobilization Chemistry. *ACS Omega* **2018,** *3* (7), 8253-8259.

19. Filbrun, S. L.; Driskell, J. D., A fluorescence-based method to directly quantify antibodies immobilized on gold nanoparticles. *Analyst* **2016,** *141* (12), 3851-3857.

20. Hermanson, G. T., Chapter 24 - Preparation of Colloidal Gold-Labeled Proteins. In *Bioconjugate Techniques (Second Edition)*, Hermanson, G. T., Ed. Academic Press: New York, 2008; pp 924-935.

21. Haddada, M. B.; Hu, D.; Salmain, M.; Zhang, L.; Peng, C.; Wang, Y.; Liedberg, B.; Boujday, S., Gold nanoparticle-based localized surface plasmon immunosensor for staphylococcal enterotoxin A (SEA) detection. *Anal. Bioanal. Chem.* **2017,** *409* (26), 6227-6234.

22. Liao, H.; Hafner, J. H., Gold Nanorod Bioconjugates. *Chem. Mat.* **2005,** *17* (18), 4636-4641.

23. Day, E. S.; Bickford, L. R.; Slater, J. H.; Riggall, N. S.; Drezek, R. A.; West, J. L., Antibody-conjugated gold-gold sulfide nanoparticles as multifunctional agents for imaging and therapy of breast cancer. *Int. J. Nanomed.* **2010,** *5* (1), 445-454.

24. Hinterwirth, H.; Stübiger, G.; Lindner, W.; Lämmerhofer, M., Gold Nanoparticle-Conjugated Anti-Oxidized Low-Density Lipoprotein Antibodies for Targeted Lipidomics of Oxidative Stress Biomarkers. *Anal. Chem.* **2013,** *85* (17), 8376-8384.

25. Filbrun, S. L.; Driskell, J. D., A fluorescence-based method to directly quantify antibodies immobilized on gold nanoparticles. *Analyst* **2016,** *141* (12), 3851-3857.

26. Liu, S. Y.; Horak, J.; Holdrich, M.; Lammerhofer, M., Accurate and reliable quantification of the protein surface coverage on protein-functionalized nanoparticles. *Anal. Chim. Acta* **2017,** *989*, 29-37.

27. Iarossi, M.; Schiattarella, C.; Rea, I.; De Stefano, L.; Fittipaldi, R.; Vecchione, A.; Velotta, R.; Ventura, B. D., Colorimetric Immunosensor by Aggregation of Photochemically Functionalized Gold Nanoparticles. *ACS Omega* **2018,** *3* (4), 3805-3812.

28. Pollitt, M. J.; Buckton, G.; Piper, R.; Brocchini, S., Measuring antibody coatings on gold nanoparticles by optical spectroscopy. *RSC Adv.* **2015,** *5* (31), 24521-24527.

29. Bell, N. C.; Minelli, C.; Shard, A. G., Quantitation of IgG protein adsorption to gold nanoparticles using particle size measurement. *Anal.l Methods.* **2013,** *5* (18), 4591-4601.

30. Zhao, H.; Brown, P. H.; Schuck, P., On the distribution of protein refractive index increments. *Biophys. J.* **2011,** *100* (9), 2309-2317.

31. Vörös, J., The Density and Refractive Index of Adsorbing Protein Layers. *Biophys. J.* **2004,** *87* (1), 553-561.

32. Demers, L. M.; Mirkin, C. A.; Mucic, R. C.; Reynolds, R. A.; Letsinger, R. L.; Elghanian, R.; Viswanadham, G., A Fluorescence-Based Method for Determining the Surface Coverage and Hybridization Efficiency of Thiol-Capped Oligonucleotides Bound to Gold Thin Films and Nanoparticles. *Anal. Chem.* **2000,** *72* (22), 5535-5541.

33. Baldock, B. L.; Hutchison, J. E., UV–Visible Spectroscopy-Based Quantification of Unlabeled DNA Bound to Gold Nanoparticles. *Anal. Chem.* **2016,** *88* (24), 12072-12080.

34. Liu, Y.; Shipton, M. K.; Ryan, J.; Kaufman, E. D.; Franzen, S.; Feldheim, D. L., Synthesis, stability, and cellular internalization of gold nanoparticles containing mixed peptide− poly (ethylene glycol) monolayers. *Anal. Chem.* **2007,** *79* (6), 2221-2229.

35. Slot, J.; Geuze, H., A method to prepare isodisperse colloidal gold sols in the size range 3–17 nm. *Ultramicroscopy* **1984,** *15* (4), 383.

36. Hermanson, G. T., Chapter 1 - Functional Targets. In *Bioconjugate Techniques (Second Edition)*, Hermanson, G. T., Ed. Academic Press: New York, 2008; pp 1-168.

37. Liu, X.; Atwater, M.; Wang, J.; Huo, Q., Extinction coefficient of gold nanoparticles with different sizes and different capping ligands. *Colloids Surf., B* **2007,** *58* (1), 3-7.

38. Chen, P.; Tran, N. T.; Wen, X.; Xiong, Q.; Liedberg, B., Inflection Point of the Localized Surface Plasmon Resonance Peak: A General Method to Improve the Sensitivity. *ACS Sens.* **2017,** *2* (2), 235-242.

39. Huang, T.; Murray, R. W., Quenching of [Ru(bpy)3]2+ fluorescence by binding to Au nanoparticles. *Langmuir* **2002,** *18* (18), 7077-7081.

40. Ghosh, S. K.; Pal, A.; Kundu, S.; Nath, S.; Pal, T., Fluorescence quenching of 1-methylaminopyrene near gold nanoparticles: Size regime dependence of the small metallic particles. *Chem. Phys. Lett.* **2004,** *395* (4-6), 366-372.

41. Catsimpoolas, N.; Wood, J. L., The reaction of cyanide with bovine serum albumin. *J. Biol. Chem.* **1964,** *239* (12), 4132-4137.

42. Florence, T. M., Degradation of protein disulphide bonds in dilute alkali. *Biochem. J.* **1980,** *189* (3), 507-520.

Supporting information for

Direct Quantification of Surface Coverage of Antibody in IgG-Gold Nanoparticles Conjugates

Lu Zhang[1,2,3,4], David Hu[1], Michèle Salmain[2], Bo Liedberg[3], and Souhir Boujday[1]*

[1] Sorbonne Université, CNRS, Laboratoire de Réactivité de Surface (LRS), 4 place Jussieu, F-75005 Paris, France.

[2] Sorbonne Université, CNRS, Institut Parisien de Chimie Moléculaire (IPCM), 4 place Jussieu F-75005 Paris, France.

[3] Centre for Biomimetic Sensor Science, School of Material Science and Engineering, Nanyang Technological University, 637553 Singapore.

[4] Sorbonne University and Nanyang Technological University Dual Degree PhD Programme.

Chemical modification of IgG

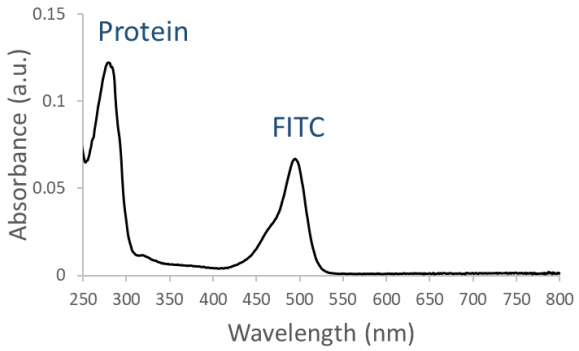

Fig. S1 : UV-Vis absorption spectrum of IgG(FITC).

Table S1 : Chemical modification of IgG: fluorescein/protein ratio and concentration of IgG(FITC) and IgG(FITC)-SH.

	Dilution factor	A_{280}	A_{495}	F/P	C(protein) in mg/mL
IgG(FITC)	10	0.594	0.330	1.9	3.4
IgG(FITC)-SH	1	0.520	0.216	1.34	0.32

Engineering of IgG-AuNP conjugates

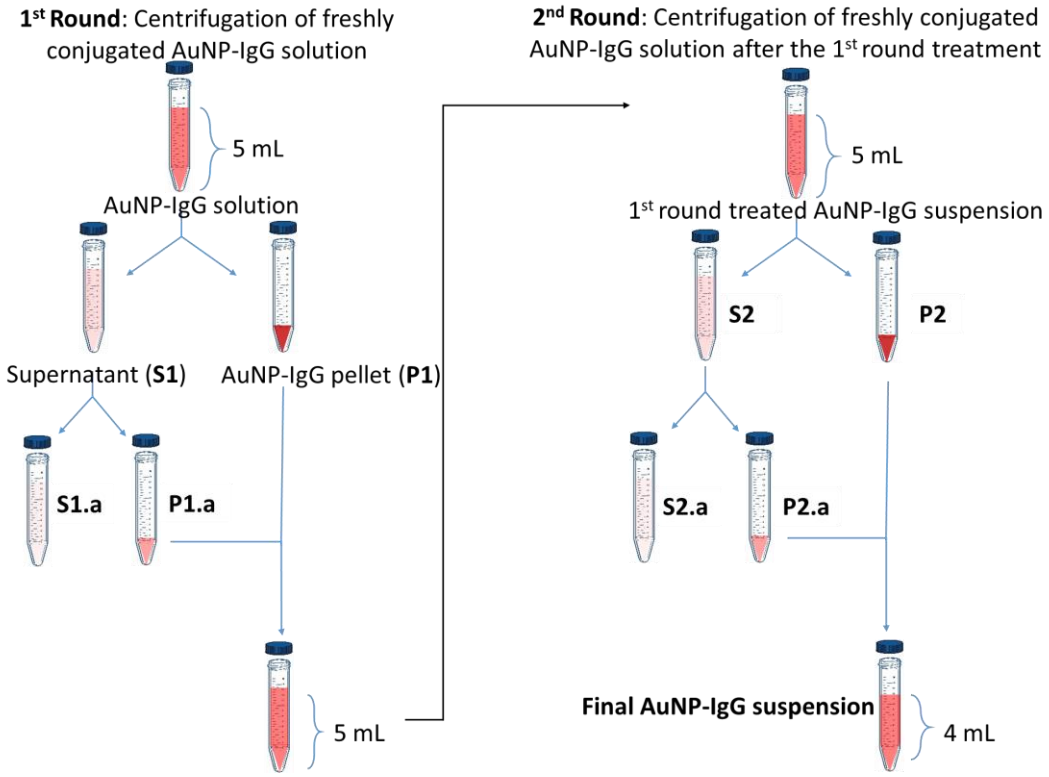

Fig. S2 : Schematic purification process employed in the conjugation of IgGs to AuNPs.

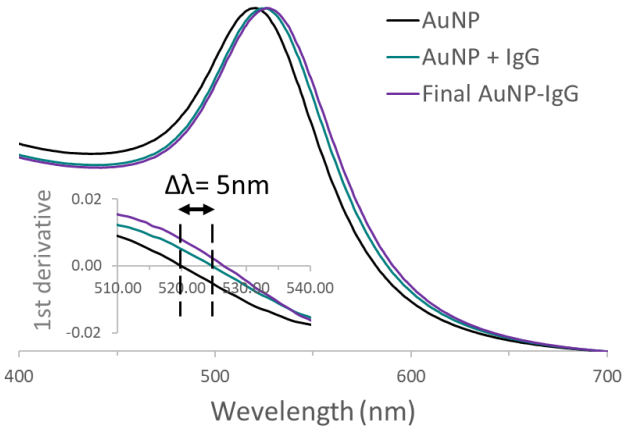

Fig. S3 : Native IgGs conjugated to AuNPs: UV-Vis absorption spectra and first derivative of absorption spectra (inset).

Theoretical estimation of IgG/AuNP ratio

Method 1: Theoretical estimation of monolayer surface coverage of IgG according to the footprint of IgG.

The number of IgGs molecules forming a monolayer on spherical AuNPs was estimated knowing the footprint of IgG and the surface area of AuNP.

AuNP surface area s(AuNP) = πD^2 with D = average diameter in nm = 15 nm;

IgG dimensions taken from reference[1] are a=14.5, b=8.5, c=4 nm (shown in Fig. S4-A); 3 possible footprints: S_1 = a * b, S_2 = a * c, S_3 = b * c (Fig. S4-B); Assuming equal probability for three footprints, average s(footprint) = (S_1 + S_2 + S_3)/3;

$$\text{IgG/AuNP} = \frac{s\,(AuNP\,)}{s\,(footprint\ of\ IgG)} = \frac{\pi D^2}{(S_1+S_2+S_3)/3} = \frac{3\pi D^2}{ab+ac+bc} = 9.8.$$

Number of IgGs on AuNP for each footprint is also calculated, and the surface coverage is summarized in Table S.2.

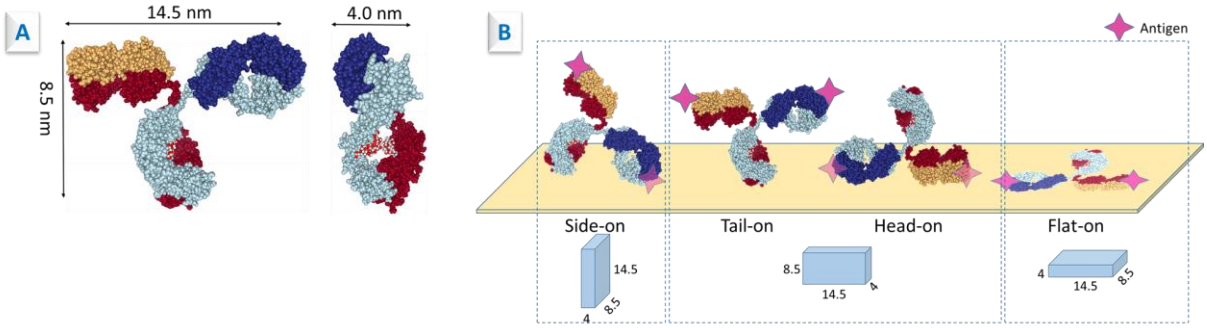

Fig. S4 : A. X-ray structure of mouse IgG (PDB code 1IGT); B. Possible orientations of IgG on surface.

Table S2 : Possible orientations of IgG on surface and approximative calculated surface coverages.

Orientation of IgG on surface	**# IgG/AuNP**
Side-on	20.8
Tail-on and/or Head-on	12.2
Flat-on	5.7

Method 2: Theoretical estimation of IgG per AuNP according to LSPR shift.

Adsorption of IgGs on AuNPs led to LSPR peak shift due to the change of local refractive index. Hence the adsorbed IgGs could be quantified through the magnitude of LSPR peak shift.[2-3]

Taking d as core diameter of AuNPs (= 14.8 nm in TEM micrographs, shown in Figure 1-C and D); s as thickness of coating IgG shell; g as fraction of coating shell in the AuNP-IgG assembly; then:

$$\frac{(\frac{d}{2})^3}{(\frac{d}{2}+s)^3} + g = 1 \qquad \text{Equation S1}$$

The LSPR peak shift Δλ (= 5 nm, shown in Fig. S3) is given by Equation S2.

$$\Delta\lambda = \frac{\lambda_p^2(\varepsilon_s - \varepsilon_m)g}{\lambda_{max,0}[1 + 2\alpha_s(1-g)]} \qquad \text{Equation S2}$$

With $\lambda_{max,0}$ is LSPR peak position of citrate-coated AuNPs (= 520 nm, shown in Fig. S3); λ_p is the free electron oscillation wavelength (131 nm for gold); ε is the dielectric constant (the subscripts s and m refer to the IgG coating shell and the surrounding medium, respectively. ε_s = 2.02 assuming that the refractive index n_s of IgG is 1.42[4-5] in a medium of dielectric constant ε_m = 1.77 assuming the refractive index n_m for water is 1.33); α_s is the polarizability of IgG shell in water ($=\frac{\varepsilon_s-\varepsilon_m}{\varepsilon_s+2\varepsilon_m}$).

The absolute amount of adsorbed IgG Γ is given by the De Feijlter formula, Equation S3

$$\Gamma = s\frac{n_s - n_m}{\frac{dn}{dC}} \qquad \text{Equation S3}$$

Where dn/dC is the refractive index increment due to the increase of concentration (= 0.19 mL/g for IgG[6]).

By inverting Equation S2, we get g = 0.63, which in turn provides s ~ 2.9 nm through Equation S1. Equation S3 provides Γ ~ 138 ng/cm^2, which corresponds approximately to 3.9 IgGs (M_w of IgG is approximately 150 kDa) on a spherical AuNP of d =15 nm.

Dissolution of IgG(FITC)-AuNP conjugates

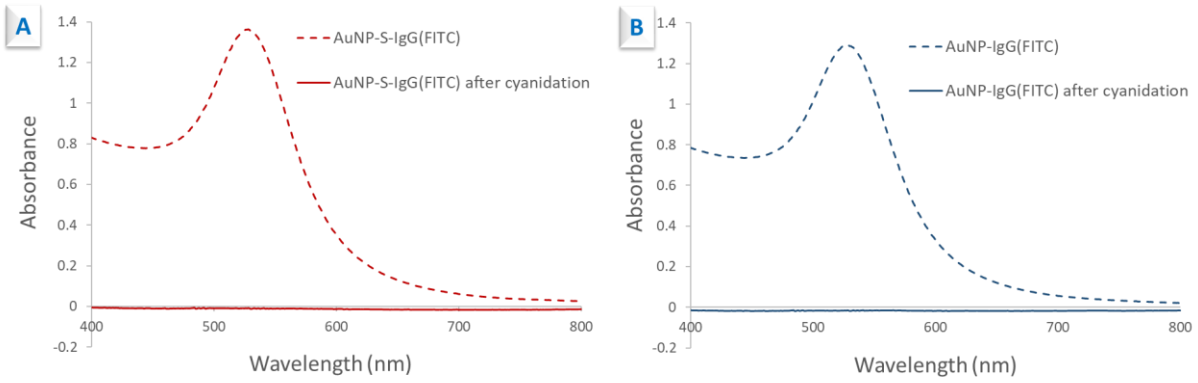

Fig. S5 : Absorption spectra of IgG(FITC)-AuNP conjugates before and after treatment with NaCN confirming the dissolution of AuNP-S-IgG (A) and AuNP-IgG (B).

Direct and indirect fluorescence-based assays

Calibration

In order to build up accurate calibration curves, standard solutions of IgG(FITC) were prepared in the same matrices as the samples to be assayed. On the whole, there are 3 different samples, *i.e.* IgG(FITC)-AuNPs after cyanidation (sample 1), supernatants S1a (sample 2) and S2a (sample 3). Fig. S6 illustrates the preparation of matrices of samples 1 and 2.

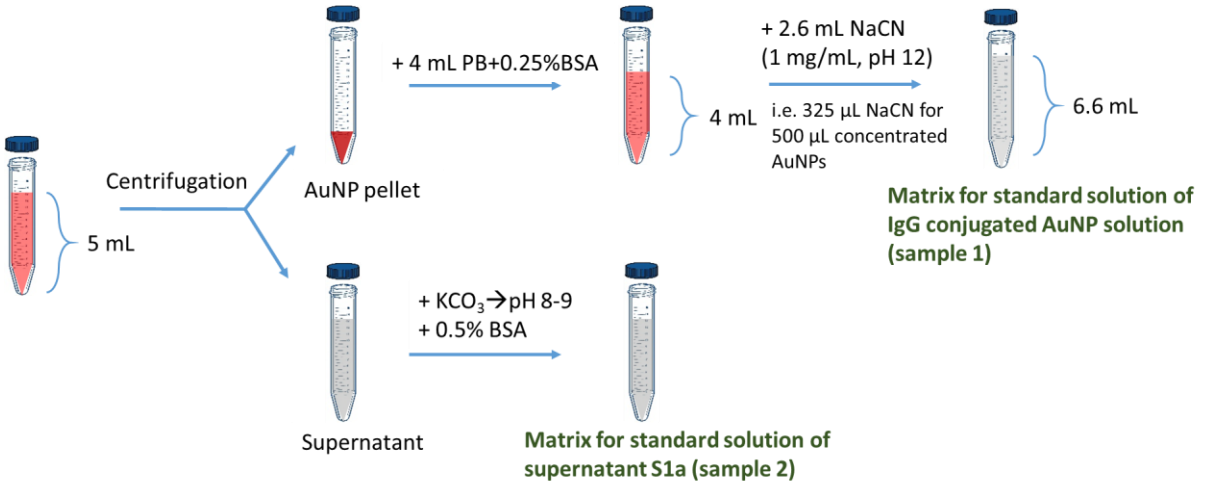

Fig. S6 : Schematic representation of the preparation of the different matrices of standard solutions.

Matrix for samples 1 was prepared as follows: AuNP colloidal solution (5 mL) was centrifuged at 10,000g for 30 min at 4°C, the supernatant was discarded and the pellet resuspended in 10 mM PB, pH 7.4 + 0.25% BSA (4 mL) to which was added NaCN (1 mg/mL adjusted to pH 12 with NaOH).

Matrix for samples 2 was prepared as follows: AuNP colloidal solution (5 mL) was centrifuged at 10,000g for 30 min at 4°C and the supernatant was adjusted to pH 8-9 with 0.1 M K_2CO_3 followed by addition of 0.5% BSA (w/v).

Matrix for samples 3: 10 mM PB pH 7.4 + 0.25% BSA (w/v).

Known amounts of IgG(FITC) were added to each matrix. The standard solutions were analyzed on a spectrofluorimeter and calibration curves were established by plotting the emission intensity at 515 nm as a function of IgG(FITC) concentration. Then the IgG(FITC) concentration in the samples was calculated according to the related calibration equations. The

average number of IgGs per particle was obtained by dividing the IgG(FITC) concentration by the AuNP concentration.

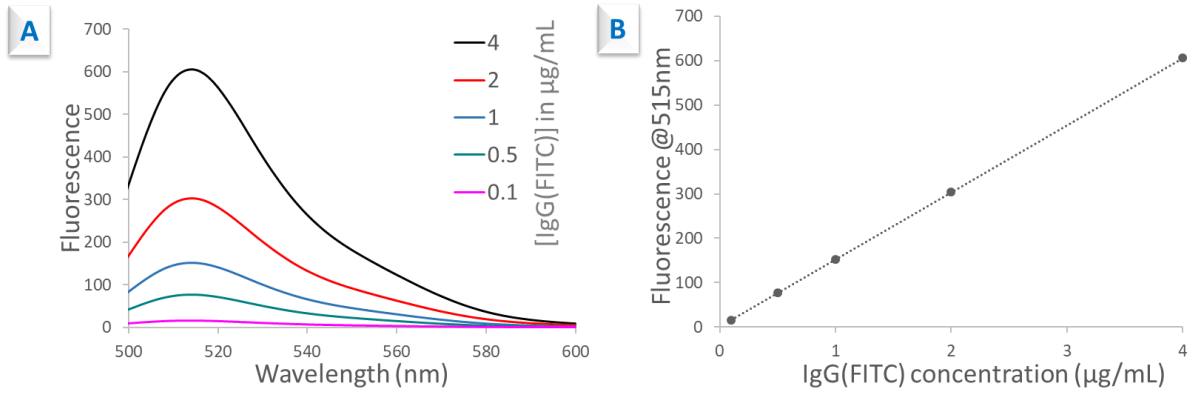

Fig. S7 : Fluorescence emission spectra of known amounts of IgG(FITC) in mimetic matrix of bioconjugates after cyanidation (A); Calibration curve (emission measured at 515 nm) (B).

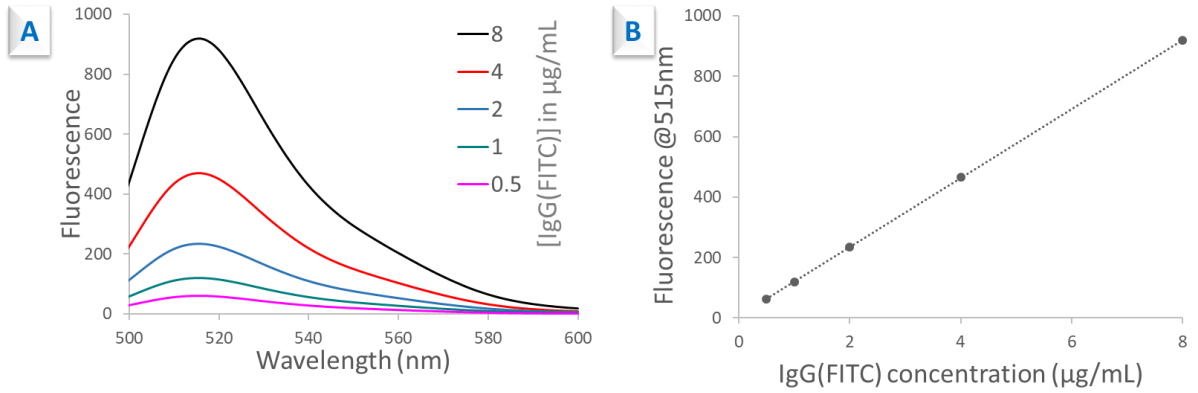

Fig. S8 : Fluorescence emission spectra of known amounts of IgG(FITC) in mimetic matrix of S1a (A); Calibration curve (emission measured at 515 nm) (B).

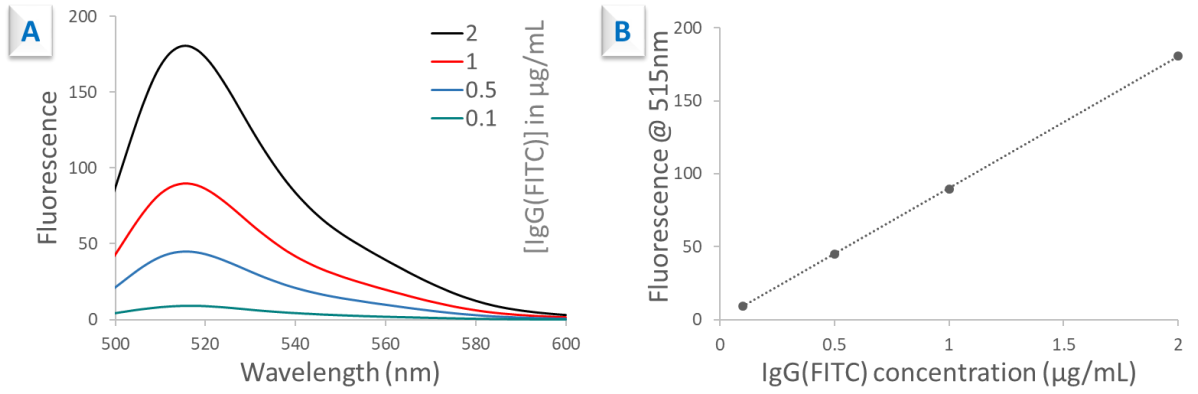

Fig. S9 : Fluorescence emission spectra of known amounts of IgG(FITC) in mimetic matrix of S2a (A); Calibration curve (emission measured at 515 nm) (B).

Table S3 : Calibration equations in different matrices.

Matrix	Calibration equation
Bioconjugate dissolved by NaCN	$y = 151.67x$; R^2=0.99998
Supernatant S1a	$y = 115.45x$; R^2=0.99991
Supernatant S2a	$y = 90.15x$; R^2=0.99998

Calculation of the IgG/AuNP ratios

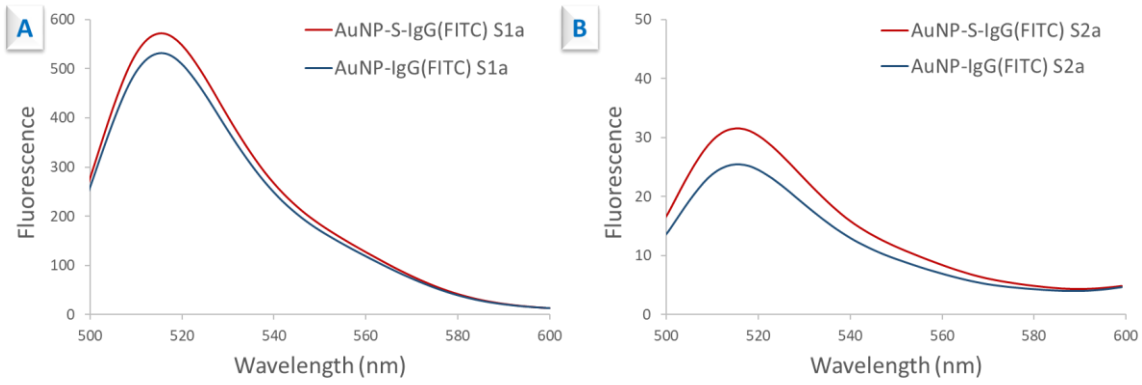

Fig. S10 : Fluorescence emission spectra of supernatants S1a (A) and supernatants S2a (B).

Table S4 : Direct and indirect fluorescence quantification.

Before conjugation	V = 5 mL [AuNP]=2.85 nM [IgG]=11 µg/mL= 73.3 nM	
After conjugation	V = 4 mL; [AuNP]= A/(εl)	
	[AuNP]=3.58 nM	[AuNP]=3.4 nM
	Chemisorption AuNP-S-IgG	**Physisorption AuNP-IgG**
Direct assay		
In IgG-AuNP conjugate after cyanidation V=V(bioconjugate) + V(NaCN) = 500+325 = 825 µL		
Calibration equation	$y = 151.67x$	
x	y= 193.65 $\rightarrow x = \frac{193.65}{151.67} = 1.28$	y= 200.65 $\rightarrow x = \frac{200.65}{151.67} = 1.32$
In 500 µL conjugate		
[IgG]	$1.28 * \frac{825}{500}$ =2.11 µg/mL = 14.04 nM	$1.32 * \frac{825}{500}$ = 2.18 µg/mL = 14.55 nM
IgG/AuNP	$\mathbf{\frac{14.04}{3.58} = 3.9}$	$\mathbf{\frac{14.55}{3.4} = 4.3}$
Indirect assay		
In 5 mL of S1a		
Calibration equation	$y = 115.45x$	
[IgG]	y = 572.36 $\rightarrow x = \frac{572.36}{115.45}$ = 4.96 µg/mL = 33.0 nM	y= 531.7 $\rightarrow x = \frac{531.7}{115.45}$ = 4.61 µg/mL = 30.7 nM
In 5 mL of S2a		
Calibration equation	$y = 90.15x$	
[IgG]	y = 31.56 $\rightarrow$x=$\frac{31.56}{90.15}$ = 0.35µg/mL = 2.33 nM	y = 25.42 $\rightarrow$x=$\frac{25.42}{90.15}$ = 0.28 µg/mL = 1.88 nM
[IgG] bound to AuNP (subtraction)	$(73.3 - 33.0 - 2.33) * \frac{5}{4}$ = 47.5 nM	$(73.3 - 30.7 - 1.88) * \frac{5}{4}$ = 50.9 nM
IgG/AuNP	$\mathbf{\frac{47.5}{3.58} = 13.3}$	$\mathbf{\frac{50.9}{3.4} = 15}$

Indirect IgG assay by ELISA

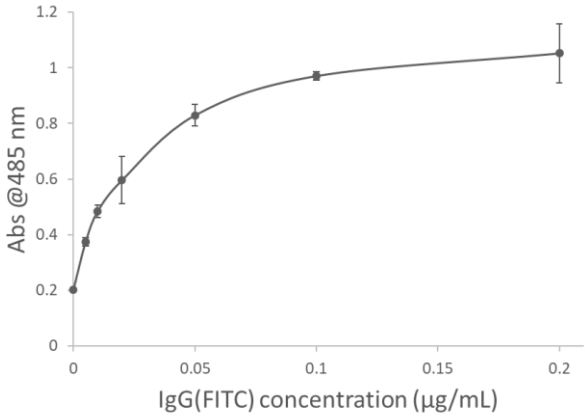

Fig. S11 : Calibration curve for the assay of IgG by ELISA. Each concentration was analyzed in duplicate and the error bars represent the standard deviation.

Table S5 : ELISA of the supernatants (A_{485nm})

	Dilution factor	**Chemisorption AuNP-S-IgG**	**Physisorption AuNP-IgG**
Supernatant S1a	200	0.773 ± 0.027	0.742 ± 0.064
	400	0.567 ± 0.016	0.534 ± 0.026
Supernatant S2a	20	0.550 ± 0.036	0.479 ± 0.048
	40	0.407 ± 0.030	--

The IgG concentrations were calculated using Optima Mars data analysis software and point-to-point fitting.

Table S6 : ELISA quantification of surface coverage.

	Chemisorption AuNP-S-IgG	**Physisorption AuNP-IgG**
Before conjugation	V = 5 mL [AuNP]=2.85 nM [IgG]=11 µg/mL= 73.3 nM	
After conjugation	V = 4 mL; [AuNP]= A/(εl)	
	[AuNP]= 3.58 nM	[AuNP]= 3.4 nM
S1a	7.76 ± 1.15 µg/mL	6.75 ± 1.39 µg/mL
S2a	0.29 ± 0.04 µg/mL	0.2 µg/mL
m (IgG) in supernatant (µg)	$(7.76 + 0.29) * 5 = 40.25$	$(6.75 + 0.2) * 5$=34.74
m(IgG) in conjugate (µg)	$55 - 40.25 = 14.75$	$55 - 34.74 = 20.26$
[IgG] bound to AuNP	$\frac{14.75}{4} = 3.69$ µg/mL = 24.63 nM	$\frac{20.26}{4} = 5.07$ µg/mL =33.77 nM
IgG/AuNP	**6.9 ± 2.8**	**9.9 ± 3.4**

REFERENCES

1. Tan, Y. H.; Liu, M.; Nolting, B.; Go, J. G.; Gervay-Hague, J.; Liu, G.-y., A nanoengineering approach for investigation and regulation of protein immobilization. *ACS nano* **2008,** *2* (11), 2374-2384.

2. Iarossi, M.; Schiattarella, C.; Rea, I.; De Stefano, L.; Fittipaldi, R.; Vecchione, A.; Velotta, R.; Ventura, B. D., Colorimetric Immunosensor by Aggregation of Photochemically Functionalized Gold Nanoparticles. *ACS Omega* **2018,** *3* (4), 3805-3812.

3. Pollitt, M. J.; Buckton, G.; Piper, R.; Brocchini, S., Measuring antibody coatings on gold nanoparticles by optical spectroscopy. *Rsc Advances* **2015,** *5* (31), 24521-24527.

4. Bell, N. C.; Minelli, C.; Shard, A. G., Quantitation of IgG protein adsorption to gold nanoparticles using particle size measurement. *Analytical Methods* **2013,** *5* (18), 4591-4601.

5. Vörös, J., The Density and Refractive Index of Adsorbing Protein Layers. *Biophysical Journal* **2004,** *87* (1), 553-561.

6. Zhao, H.; Brown, P. H.; Schuck, P., On the distribution of protein refractive index increments. *Biophysical journal* **2011,** *100* (9), 2309-2317.

Paper III

Naked Eye Immunosensing of a Food Biotoxin using Gold Nanoparticles-Antibody Bioconjugate

Preface

The extremely high extinction coefficients of gold nanoparticles (AuNPs) owing to Localized Surface Plasmon Resonance (LSPR) phenomenon make AuNPs detectable down to very low concentrations by absorption spectroscopy or even by the naked-eye. In this paper, we took advantage of the high detectability of AuNPs to design a solid-phase, sandwich-type, colorimetric immunosensor for the detection of the food biotoxin staphylococcal enterotoxin A (SEA). (Figure III-A) The sensor was operated on a glass slide with a test zone comprising a capture polyclonal anti-SEA antibody (Ab). The same Ab was conjugated to 13-nm diameter AuNPs to afford the nanoimmunoprobe.

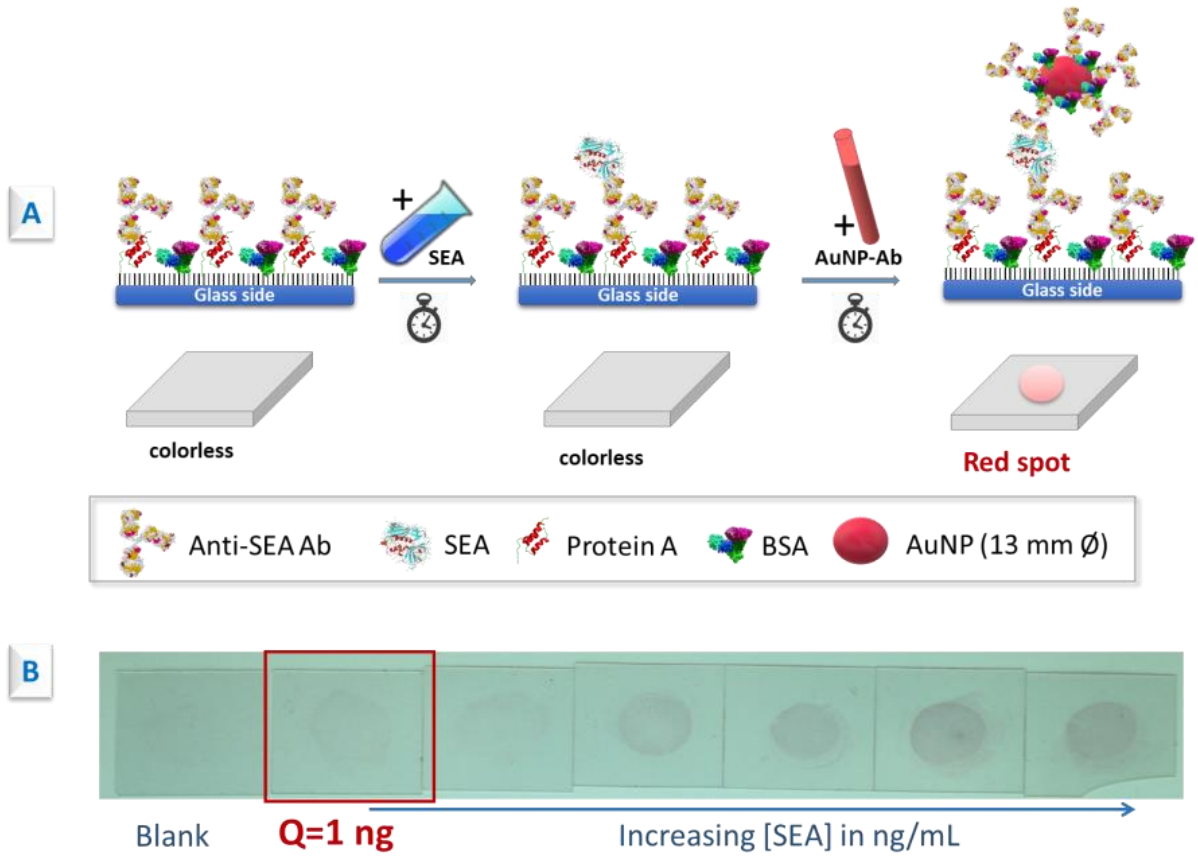

Figure III: A. Schematic representation of naked-eye biosensing of SEA. B Photo of the glass slides showing no response for the blank and red spots of increasing intensity for increasing concentrations of SEA.

During the assay, the test zone was successively exposed to SEA and AuNP-Ab bioconjugates. Eventually, a distinct red spot appeared on the glass slide with SEA quantity down to 1 ng. Along with the increasing SEA concentration, the intensity of red color increased. (Figure III-

B) For the control test without SEA in the sample, the detection zone always stayed colorless, demonstrating that the functionalized glass surface prevented non-specific protein adsorption. This shows a good semi-quantitative detection of SEA by naked-eye. Quantification of SEA was further established using a benchtop UV-visible spectrometer by integration of the LSPR band. Eventually, a limit of detection of 1.5 ng/mL SEA in spiked milk was achieved, which is lower than that obtained by quartz crystal microbalance (QCM) measurement using the same Ab.

Naked Eye Immunosensing of a Food Biotoxin using Gold Nanoparticles-Antibody Bioconjugate

Lu Zhang[1,2,3,4], Michèle Salmain[2], Bo Liedberg[3], and Souhir Boujday[1]*

[1] Sorbonne Université, CNRS, Laboratoire de Réactivité de Surface (LRS), 4 place Jussieu, F-75005 Paris, France.

[2] Sorbonne Université, CNRS, Institut Parisien de Chimie Moléculaire (IPCM), 4 place Jussieu F-75005 Paris, France.

[3] Centre for Biomimetic Sensor Science, School of Material Science and Engineering, Nanyang Technological University, 637553 Singapore.

[4] Sorbonne University and Nanyang Technological University Dual Degree PhD Programme

Figures (7), Tables (2)

Laboratoire de Réactivité de Surface, UMR CNRS 7197, *Sorbonne Université,* case 178, 4 Place Jussieu, 75252 Paris cedex 05, France.

Tel: +33144276001, Fax: +33144276033, souhir.boujday@sorbonne-universite.fr

ABSTRACT

Colorimetric immunoassays using gold nanoparticles (AuNPs) form a special type of assays where AuNPs act as transducer to monitor binding events between an antigen and an antibody. Indeed, AuNPs display unique optical properties that can be exploited in various ways to develop biosensors. One of the most striking properties of colloidal AuNPs (and more generally of noble metal nanomaterials) is their extremely high extinction coefficients in the visible range of the spectrum owing to the Localized Surface Plasmon Resonance (LSPR) phenomenon. This feature makes AuNPs detectable down to very low concentrations by absorption spectroscopy or even by the naked-eye. Herein we took advantage of the high detectability of AuNPs to design a solid-phase, sandwich-type, colorimetric immunosensor aiming at the detection of staphylococcal enterotoxin A (SEA). A test zone comprising a polyclonal anti-SEA antibody was created at the surface of amino-functionalized glass slides via high affinity binding to covalently immobilized Protein A. The same antibody was conjugated to 13-nm diameter AuNP to afford the nanoimmunoprobe. After the glass slides were successively exposed to SEA and AuNP-antibody bioconjugate, a distinct red spot appeared on the glass slides at the detection zone from as low as 1 ng SEA in buffer. Quantification of SEA in the 10 – 500 ng/mL range was established using a benchtop UV-Visible spectrometer by integration of the LSPR band centered at 530 nm. Eventually, this biosensor was applied to the detection of SEA in milk with a limit of detection of 1.5 ng/mL.

KEYWORDS. Gold Nanoparticles, Staphylococcal enterotoxin A, Localized Surface Plasmon Resonance, Immunosensor

INTRODUCTION

Colorimetric methods provide convenient and effective bioanalytical tools as they produce a response readable by standard colorimeters such as microplate readers or even sometimes by the naked-eye. A special type of colorimetric immunoassays is those employing gold nanoparticles (AuNPs) as colorimetric transducers.[1,2] Indeed, one of most remarkable features of AuNPs is to exhibit exceptionally high extinction coefficients in the visible spectral range which are several orders of magnitude larger than those of conventional dyes.[3] This optical property arises from the Localized Surface Plasmon Resonance (LSPR) phenomenon common to all noble metal nanomaterials.[4] This feature has been extensively exploited in the development of lateral flow (also called immunochromatographic) assays. In their principle, the analyte migrates together with AuNP-labeled antibody by capillarity until they reach a test zone comprising the capture antibody, giving rise to a red line.[5,6] While these self-contained devices are easy to manipulate and faster than traditional ELISA, they do not usually provide quantitative information and display limited sensitivity.[7]

Biotoxins are species produced by microorganisms (bacteria, microalgae) that, when unintentionally ingested by consumption of contaminated food, cause various diseases potentially fatal to humans. For instance, some *Staphylococcus aureus* strains produce staphylococcal enterotoxins (SEs) which are the agents responsible for food intoxication by *S. aureus*.[8] Twenty-one different heat-stable SEs have been identified to date with the serotype A (SEA) being the most frequent toxin involved in food poisoning outbreaks by *S. aureus*.[9] It is generally admitted that as low as 100 ng SEA causes intoxication symptoms in the form of severe gastroenteritis.[10] Rapid and sensitive detection of this biotoxin in foodstuff such as dairy products is therefore critical for public health and economic reasons.

Biosensing techniques appear as attractive alternatives to traditional microbiological methods regarding the detection of SEs in food matrices.[11-17] We have contributed to this field of research by setting up gravimetric immunosensors to quantity SEA.[18-20] Recently, we have also devised a homogeneous colorimetric immunosensor of SEA taking advantage of the sensitivity of the LSPR band of AuNP to local changes of refractive index.[21] Although this assay was sensitive with a calculated limit of detection (LOD) of 5 ng/mL in model buffer medium, it still required reading with a spectrometer with high spectral resolution.

Here we established a sandwich-format colorimetric immunosensor on glass slides using

antibody-conjugated AuNP as transducer to detect and quantify SEA in model buffer medium and in spiked milk. In the absence of SEA, the glass slide remained colorless while the presence of SEA in the sample resulted in the appearance of a red spot at the detection zone that could be readily observed by the naked-eye down to 1 ng SEA (Figure 1). Quantification of SEA in the 10 – 500 ng/mL range was made possible using a benchtop UV-Visible spectrometer with a limit of detection of 1.5 ng/mL in milk.

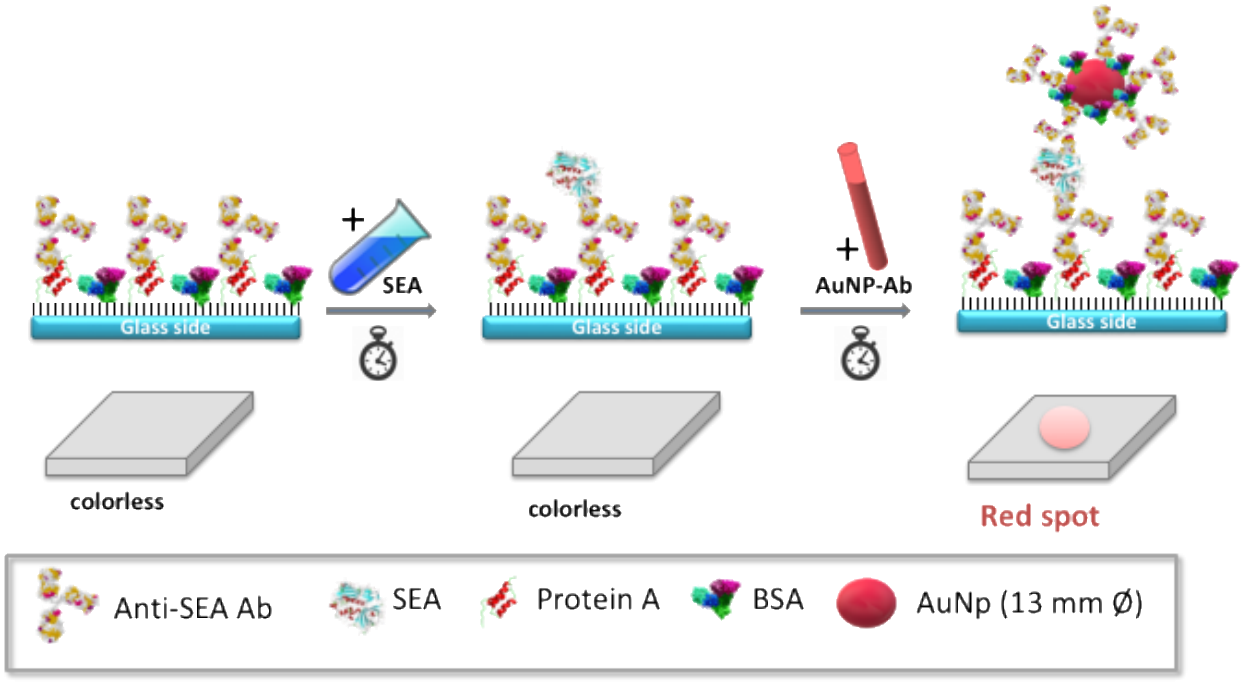

Figure 1. Schematic representation of the glass surface modification and AuNP conjugation strategies used for naked-eye detection of SEA.

EXPERIMENTAL SECTION

Materials: Gold (III) chloride trihydrate ($HAuCl_4 \cdot 3H_2O$, 99.9%), sodium citrate dihydrate ($HOC(COONa)(CH_2COONa)_2 \cdot 2H_2O$, 99%)), tannic acid ($C_{76}H_{52}O_{46}$, 99%), (3-Glycidyloxypropyl) trimethoxysilane (GOPTS, 98%), (3-Aminopropyl) triethoxysilane (APTES, 99%), glutaraldehyde solution (GA, 25% in water), 1,4-phenylenediisothiocyanate (PDITC), phosphate buffered saline (PBS), silicon wafers <111>, staphylococcal enterotoxin A (SEA), goat anti-rabbit IgG-HRP, o-phenylenediamine dihydrochloride (OPD) and bovine serum albumin (BSA) were purchased Sigma-Aldrich. Affinity-purified rabbit anti-SEA antibody (anti-SEA, ref. LAI101) was purchased from Toxin Technology (Sarasota, FL, America). Staphylococcal Protein A was purchased from Thermo scientific. Powder skimmed

milk was purchased from a local supermarket. Glass slides (18×18×0.3 mm) were obtained from Paul Marienfeld (Lauda Königshofen, Germany). Hellmanex III was purchased from Hellma Analytics (Müllheim, Germany). Milli-Q water (18 MΩ·cm, Millipore) was used for the preparation of aqueous solutions and for all rinses. All chemicals were reagent grade or higher and were used without further purification. Experiments were carried out at room temperature if not specified otherwise.

Buffers: Buffers were supplemented with BSA or Tween 20 (detergent) as required. The most commonly employed was PBS. AuNP-Ab bioconjugate was stored in 10 mM phosphate buffer pH 7.4 (2.3 mM NaH_2PO_4 and 7.7mM Na_2HPO_4 in Milli-Q water) containing 0.25% (w/v) BSA. Citrate-phosphate buffer pH 5 was prepared by mixing 1.02 g citric acid·H_2O and 1.46 g Na_2HPO_4 in 100 mL Milli-Q H_2O. The substrate for ELISA was prepared by dissolving OPD (7mg) in citrate-phosphate buffer pH 5.0 (10mL) and adding 30% H_2O_2 (4µL) prior to use.

Gold nanoparticles preparation and antibody-AuNP bioconjugate engineering: Colloidal AuNPs were prepared according to the tannic acid method of Slot and Geuze [22] slightly adapted [23,24]. Briefly, to produce 100 mL of a 13-nm diameter colloid solution, two stock solutions were prepared: solution A: 1 mL 1% (w/v) $HAuCl_4$ and 79 mL water; solution B: 4 mL 1% sodium citrate, 0.025 mL 1% tannic acid and 16 mL water. Solutions A and B were heated to 60°C under stirring then mixed. When the solution turned red, the mixture was heated up to 95°C for a few minutes and cooled on ice. This solution could be kept in an amber glass flask at 4°C for at least 2 months.

Conjugation of rabbit anti-SEA antibody was performed according to ref. [25] with minor modification. The obtained colloidal AuNP solution (5 mL) was adjusted to pH 8-9 by adding 0.1 M K_2CO_3 solution (50 µL). Rabbit anti-SEA antibody (1 mg/mL in water, 55 µL; 55 µg) was added, followed by shaking during 1 h at room temperature. BSA (28.5 mg, 0.57 % (w/v)) was added to block free binding sites on the AuNP. After an incubation of 1 h, Tween-20 (6 µL) was added to the mixture. The particles were subsequently washed with phosphate buffer supplemented with 0.25% BSA (w/v) by repeated centrifugation and finally redispersed in 4 mL storage buffer. The detailed washing process is schematically illustrated in Figure S.1 adapted from ref. [26].

Surface chemistry: Glass slides and/or silicon wafers cut into 1 x 1 cm pieces were cleaned following a procedure including a washing step in 2% Hellmanex, an etching step with HCl

solution, and finally an activation step, aiming at increasing silanol groups, with concentrated H_2SO_4. A detailed description of this procedure is given in the references[27,28]. Amine-terminated layer was generated by immersing the activated glass slides or silicon wafers in a 2% (v/v) solution of APTES in anhydrous toluene at 90°C for 1 h then rinsing with toluene.[29] The substrate finally underwent a 'curing' process at 100°C for 1 h.[30] Amine-terminated substrates were finally exposed to glutaraldehyde (5.0% GA in PBS, 1 mL) during 30 min, rinsed in Milli-Q water and dried under a flow of dry nitrogen [31].

Functionalization of substrates: The GA-activated substrates were exposed to Protein A by adding a drop of solution (20 µg/mL Protein A in PBS, 100 µL) on surfaces followed by 2 h incubation.[19] Then, the slides were rinsed twice in PBS-0.05% Tween-20 and once in Milli-Q water and dried under a flow of dry nitrogen. Covalent immobilization of capture antibody anti-SEA (20 µg/mL in PBS, pH 7.4) on glass slides or silicon wafers was carried out by depositing a drop of anti-SEA Ab solution (20 µg/mL in PBS, 50 µL) at the center of the modified substrates followed by 2 h incubation. Non-specific binding sites were blocked by treatment with 1% (w/v) BSA in PBS. After the immobilization step, the modified glass slides or silicon wafers were rinsed twice in PBS - 0.05% Tween 20 and once in Milli-Q water, dried under a flow of dry nitrogen and stored in the refrigerator at 4 °C until use.

SEA detection in buffer: A 50 µg/mL stock solution of SEA in water was first prepared. Then, standard solutions of SEA ranging from 0.005 to 2 µg/mL were prepared in PBS-0.1% BSA by successive dilutions from the stock solution. PBS-0.1% BSA was used as blank. The previously prepared glass substrates were exposed to SEA solutions by depositing a drop (200 µL) on the surfaces and incubating for 2 h. Subsequently, the surfaces were rinsed twice in PBS-0.05% Tween 20, and once in Milli-Q water then dried under a flow of nitrogen. For revelation, the as-prepared AuNP-Ab bioconjugate solution (200 µL) was spotted on the glass slides and left to react during 2 h. The slides were finally rinsed twice in PBS-0.05% Tween 20, once in Milli-Q water and dried under a flow of nitrogen prior to their analysis.

SEA detection in milk: Milk was freshly prepared as 5% (w/v) skimmed milk powder in water. SEA was spiked in milk at 0.005, 0.01, 0.05, 0.1, 0.5 and 1 µg/mL. Skimmed milk was used as blank. The glass slides were exposed to spiked milk samples (200 µL) and incubated during 2 h. Afterwards, the slides were washed and exposed to AuNP-Ab bioconjugate solution as above.

Characterization techniques: UV-Visible (***UV-Vis***) spectra were recorded using a double

beam Lambda 35 UV-Vis spectrometer (Perkin Elmer) or a Cary 50 UV-Visible spectrometer (Varian). Milli-Q water was used as reference for solution analysis and no reference was employed for glass slide analysis. Scanning Electron Microscopy (***SEM***) was performed using a FEG SU-70 scanning electron microscope with a low voltage of 1 kV at a distance of 1.9 - 2.3 mm; the secondary electron detector "in Lens" was used. Images taken at different scales and in different regions of the samples were recorded. For ***Contact Angle measurements,*** static water contact angles were measured at room temperature using the sessile drop method and image analysis of the drop profile. The instrument, equipped with a CCD camera and an image analysis processor, was purchased from Krüss Optronic GmbH (Hamburg, Germany). ***IR*** spectra were recorded on a Tensor 27 FT-IR spectrometer (Bruker). The IR spectra of Si wafers were recorded with a horizontal reflection Grazing Angle ATR accessory including a Ge crystal (VariGATR, Harrick). The angle of incidence was set to 60°. ***Dynamic light scattering (DLS)*** and ***zeta potential measurements*** were carried out using a ZetaPALS potential analyzer (Brookhaven).

ELISA: ELISA was applied to quantify the unbound Ab left in solution after conjugation of Ab to AuNP. SEA (100 µL of 1 µg/mL in carbonate buffer pH 9.5) was pipetted into each well of a 96-well plate(Greiner) and incubated at 4°C overnight. Then the content was discarded. Blocking buffer PBS-0.1%BSA (100 µL) was then pipetted in each well and incubated for 1 h at room temperature. The plate was washed with PBS 0.05%Tween 20 (3*150 µL). A series of anti-SEA Ab solutions of various concentrations (from 0.02 µg/mL to 2 µg/mL in PBS-0.1%BSA; 100µL) was added to each well for calibration in duplicate. At the same time, several dilutions of the supernatant containing unbound Ab were prepared and added to wells. The plate was incubated for 2 h at room temperature. The plate was washed with PBS-0.05%Tween 20 (3 *150 µL/well). HRP goat anti-rabbit IgG conjugate (1/4000 in PBS-0.1% BSA; 100 µL) was added to each well and incubated for 1 h. The plate was washed with PBS-0.05%Tween 20 (3*150 µL/well). The o-phenylenediamine dihydrochloride (OPD) and H_2O_2 substrate solution (7 mg OPD + 4 µL H_2O_2 in 10 mL of citrate-phosphate buffer, pH 5, 100 µL) was added to each well. The orange color was left to develop and 2.5 M H_2SO_4 was added to each well (50 µL) to stop the enzymatic reaction. After 10 min in the dark, the absorbance was read at 485 and 405 nm (as reference) with a microplate reader (BMG Labtech).

RESULTS AND DISCUSSION

Gold nanoparticles preparation and AuNP-antibody-bioconjugate engineering: Colloidal gold nanoparticles (AuNP) and the antibody bioconjugate (AuNP-Ab) were characterized using UV-Visible spectroscopy and Transition Electron Microscopy as shown in Figure 2. For the AuNP solution, Figure 2-A, a narrow resonance plasmon band was present at 520 nm, typical of a particle size around 13 nm.[32,33] This was confirmed by TEM micrograph as shown in Figure 2-B which gave a mean particle size of 13.5 ± 1 nm, Figure 2-C. The AuNP concentration of the colloidal solution was estimated to equal 3.1±0.2 nmol L^{-1}.based on a molecular extinction coefficient (Ɛ) of 2.8 10^8 $M^{-1}cm^{-1}$ [34].

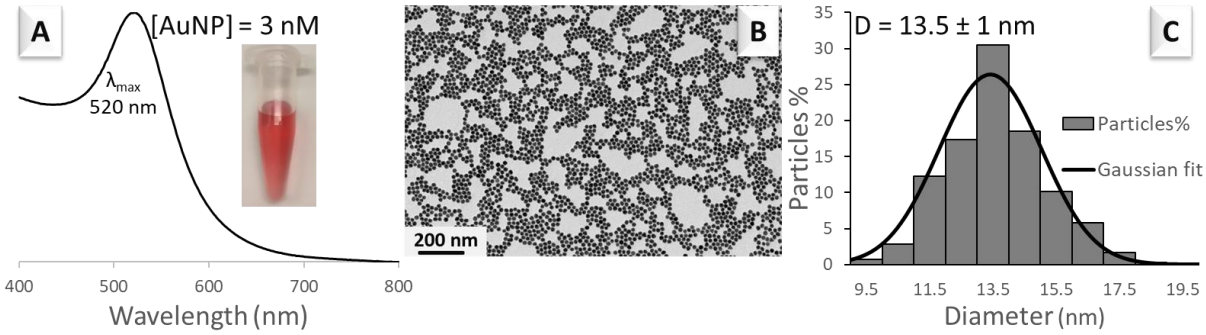

Figure 2. Nanoparticle characterization A. UV-Visible absorption spectrum; B. TEM image of the AuNPs colloidal solution; and C. Size distribution determined from the TEM micrograph.

Dynamic Light Scattering (DLS) and Zeta potential measurements gave an average size distribution centered at 22.7±0.3 nm with a mean zeta potential of -45.3±1.4 mV, Table 1. The zeta potential is consistent with previously observed data for citrate-covered nanoparticles.[21,23] The slightly higher diameter, compared to TEM measurement, is due to the solvation sphere included in the measured diameter.

Table 1. DLS (Dynamic Light Scattering) and Zeta potential of AuNP prior and after Ab bioconjugation.

	D_H (nm)	Zeta potential (mV)
AuNP	22.7 ± 0.3	- 45.3 ± 1.4
AuNP-Ab	45.3 ± 0.3	- 19.8 ± 0.6

Upon binding of anti-SEA Ab to AuNP, the LSPR band red-shifted from 520 to 528 nm (Figure 3), as a result of Ab attachment. Moreover, the hydrodynamic diameter (D_H) increased to 45.3±0.3 nm, in agreement with protein attachment and the mean zeta potential, was lowered to -19.8±0.6 mV, consistently with protein surface charge as shown previously.[21] In addition,

the UV-Visible spectrum of the AuNP-Ab conjugate (Figure 3-A) displayed a new absorption band at 285 nm, assigned to proteins present in the colloidal solution. This band is due to the physisorbed antibody and BSA, as well as to BSA in the storage buffer. Therefore, it cannot be used to quantify physisorbed Ab. To quantify Ab bound to AuNP, an indirect assay was set up where the Ab remaining in the supernatant was quantified by ELISA The amount of bound Ab and the Ab-to-AuNP ratio were then deduced as illustrated in Supplementary information. The experimental details are given in the supplementary information section and calculations led to an Ab-to-AuNP ratio of 8.3. This ratio is close, though slightly higher, to that obtained upon chemisorption of anti-SEA Ab to AuNP using Traut's reagent as a linker, *i.e.* 7 Ab per AuNP [21]

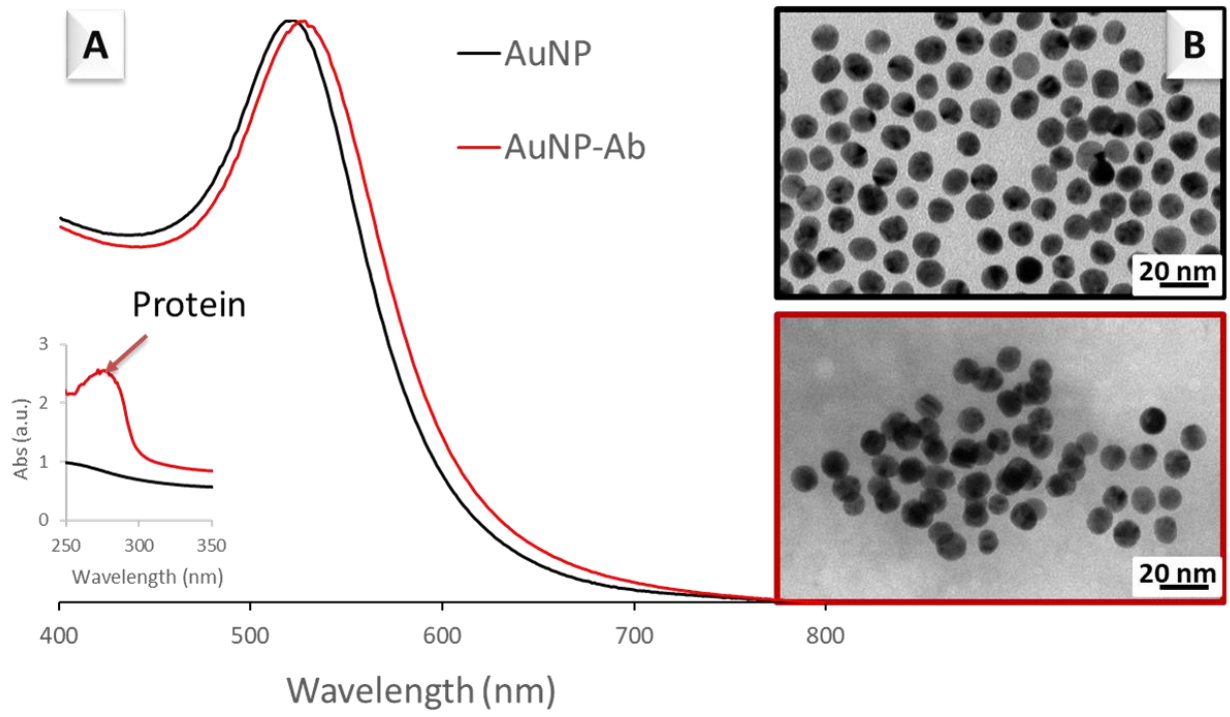

Figure 3. A. UV-Visible spectra; and B. TEM images before (AuNP) and after antibody (Ab) conjugation (AuNP-Ab).

Engineering the glass slides surface: Glass slides were chosen to immobilize the capture antibody as they are cheap and transparent, therefore allowing naked-eye readout. They were functionalized with the objective of building a sensitive and specific biosensing platform for SEA capture. Three strategies, including either epoxy- or amine-terminated silanes, were initially investigated to introduce reactive groups at the surface of the glass slides and their efficiencies compared in terms of amount of antibody bound to the glass slides. Based on the different results (discussed in the supplementary information section), the pathway depicted in

Figure S.4 was finally selected. This strategy includes the self-assembly of APTES (aminopropyltriethoxysilane) onto the clean glass slide, then addition of GA (Glutaraldehyde) as a cross-linker between surface amines and amines of the protein. The resulting surfaces were used to covalently attach Protein A and subsequently immobilize anti-SEA Ab. BSA was finally added to block the potentially uncovered areas of the sensing layer and avoid non specific adsorption.

The successive surface modification steps were monitored by FT-IR spectroscopy in ATR mode on silicon wafers. The results are shown in Figure 4.

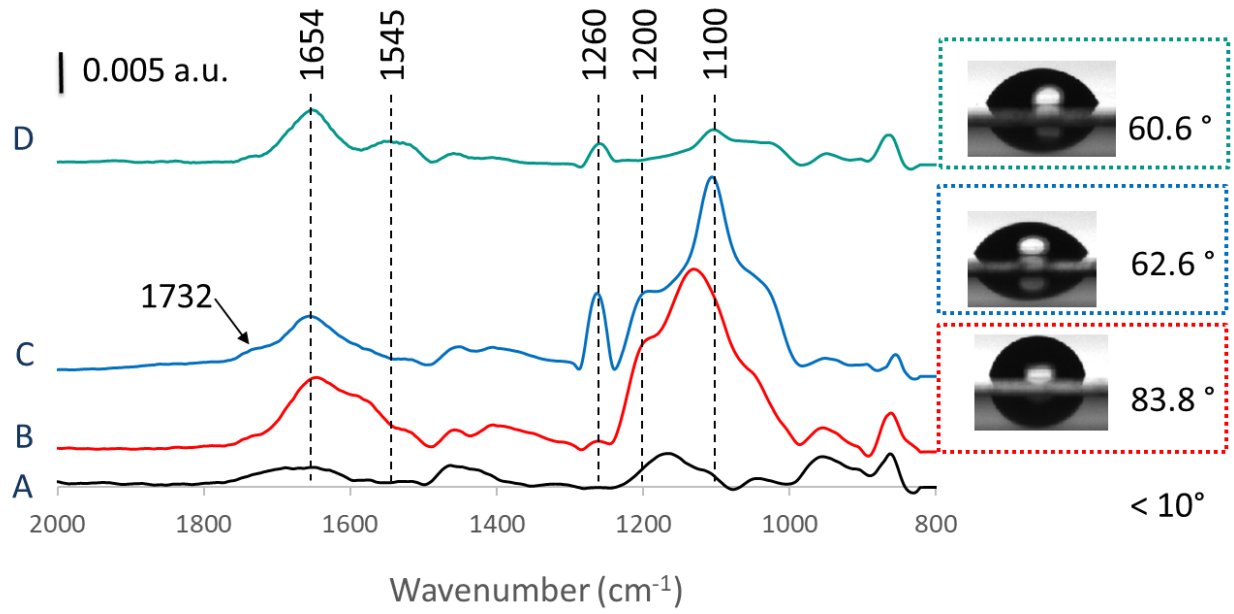

Figure 4. Surface ATR-IR spectra (measured on silicon wafers) recorded upon the successive modifications of silica surfaces and contact angle measurements (on glass slides). A: bare surfaces, B, APTES-modified, C: Glutaraldehyde-modified, D: Upon protein attachment.

On the bare clean silicon wafers, the IR spectrum is dominated by Si-O-Si stretching vibrations between 1100 cm^{-1} and 1200 cm^{-1}, in agreement with the presence of a thin layer of SiO_2 at the wafer surface, Figure 4-A Treatment by APTES resulted in the presence of several broad bands in the region 1400-1700 cm^{-1} of the IR spectrum, Figure 4-B, assigned to amine and ammonium groups and also bands around 2930 cm^{-1} (not shown) due to the stretching vibrations of CH groups. GA cross-linking is less obvious on the IR spectrum, since only a weak band at 1732 cm^{-1} characteristic of the aldehyde C=O group can be seen. Adsorption of proteins (protein A, anti-SEA antibody and BSA) was evidenced by the appearance of strong amide I and amide II bands at 1654 cm^{-1} and 1545 cm^{-1}, respectively. In parallel, surface functionalization was

monitored by contact angle measurements on glass slides. Initially the surface of clean glass slides was highly hydrophilic with a mean contact angle value below 10°. Self-assembly of APTES led to a very strong increase of the contact angle to 83.8±1.3° owing to the presence of aliphatic chains that strongly affected the hydrophilic character of the surface. This value fits with previous measurements carried on APTES-modified silicon surfaces and are ascribed to the tilting of the chains (and exposure of methylene groups) resulting from in-plane H-bonds between amine and silanols.[35] Upon GA grafting, the contact angle decreased to 60.6±1.3°. The contact angle of the glass slide after grafting and backfilling with BSA was 62.6±1.6°.

SEA biosensing in buffer: Anti-SEA antibody was spotted at the center of the glass slides to be attached by bioaffinity to Protein A layer and thus, define a capture zone. Non-specific binding sites were blocked by BSA (Figure S.3). Then the antibody-coated glass slides were incubated with solutions of SEA in PBS-0.1% BSA during 2 h. The loosely bound toxin was removed by washing and then an AuNP-Ab bioconjugate suspension was spotted on the surfaces and left to react for 2 h. The loosely bound AuNP bioconjugate was removed by washing. After careful drying, the glass slides were analyzed by UV-Visible spectroscopy. When SEA was present, the UV-Visible spectrum of the glass slides clearly showed the LSPR band of the AuNP-Ab bioconjugate, even at very low concentrations (see Figure 5-A). The presence of gold nanoparticles at the surface of a glass slide (successively exposed to a 500 ng/mL solution of SEA and to AuNP-Ab), was also evidenced by SEM (Figure 5-D). Increasing SEA concentration, led to an increase of the LSPR band intensity. The integrated area of the LSPR band was plotted as function of SEA concentration to establish a dose-response curve (Figure 5-B). Curve fitting of data was performed using the Langmuir isotherm equation:

$Area = Area_{max} \times [SEA]/([SEA] + K_D)$ where K_D refers to the dissociation constant between AuNP-Ab bioconjugate and SEA. The resulting equation (see supplementary section for the fit parameters) led to a K_D equal to 106 ng/mL, and $Area_{max}$= 0.75.

The K_D value doubled as compared to previously measured K_D (around 60 ng/mL)[18], but not really significant as it is based on a sandwich assay. The dynamic range of the biosensor extended from 10 to 500 ng/mL and, interestingly, the calculated limit of detection (LOD) was 9.1 ng/mL, *i.e.* twice lower than that by our previously developed Quartz Crystal Microbalance immunosensor using the same anti-SEA antibody in the same buffer.[19,20]

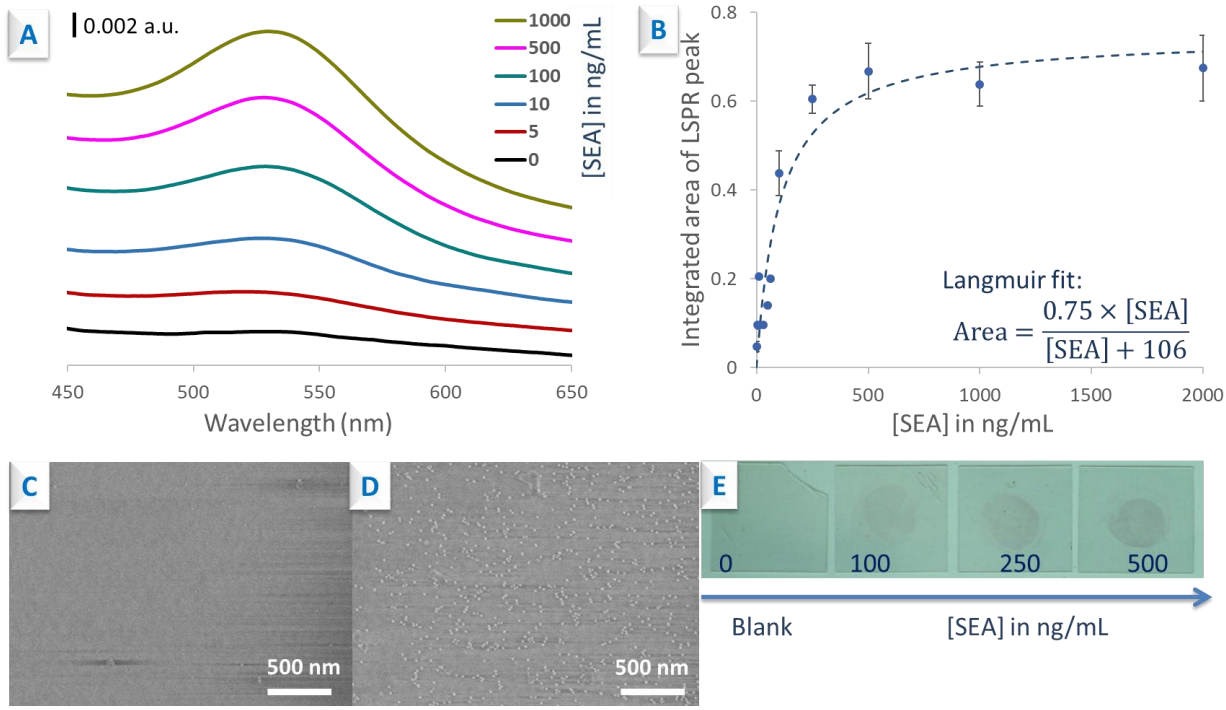

Figure 5: Detection of SEA in PBS: A. UV-Visible spectra of glass slides exposed to increasing concentrations of SEA followed by AuNP-Ab bioconjugate. B. Dose-response curve obtained by plotting the integrated area of the LSPR peak from A as function of [SEA]. C. SEM image of the glass slide exposed to 0 ng/mL SEA and AuNP-Ab. D. SEM image of the glass slide exposed to 500 ng/mL SEA and AuNP-Ab. E. Photos of the glass slides showing no response for the blank and red dots of increasing intensity for three concentrations of SEA.

Moreover, it was possible to clearly visualize, by the naked-eye, the presence of a red spot when SEA was present in the buffer (see photos in Figure 5-E). The intensity of this red spot qualitatively increased with SEA concentration in the dynamic range as expected from the UV-Visible spectra. Note that the blank slide remained colorless. No LSPR band was observed on its UV-Visible spectrum and the absence of gold nanoparticles at the surface was also evidenced by SEM (Figure 5-C), confirming the specificity of the biosensor towards SEA. By comparison, gold nanoparticle-based lateral flow immunoassays of SEs gave visual LOD values between 10 ng/ml [36,37] and 1 µg/mL[38].

SEA detection in milk: Once the biosensor optimized and tested in PBS-BSA, it was employed to assay SEA in milk. We used commercially available skimmed milk (diluted twice) with no further treatment. The same protocol was applied to milk samples spiked with SEA at increasing concentration. The glass sides were examined by the naked-eye and by UV-Visible spectrometry. The results are gathered in Figure 6.

The primary lesson to draw from these results is the absence of response to the blank sample.

Indeed, although milk is complex and rich in proteins, the blank sample remained colorless and no LSPR signal was measured by UV-Vis spectrometry. This highlights the efficiency of glass slide surface functionalization that fully prevented non-specific protein adsorption. The interaction with spiked milk led to obvious red stains, starting from 5 ng/mL SEA (see Figure 6-C). Since the sample volume was 200 µL, the overall minimum amount of SEA detected by this sensor is as low as 1 ng, by naked-eye readout. Increasing SEA concentration subsequently led to qualitatively brighter red spots on the glass slides, up to 1000 ng/mL.

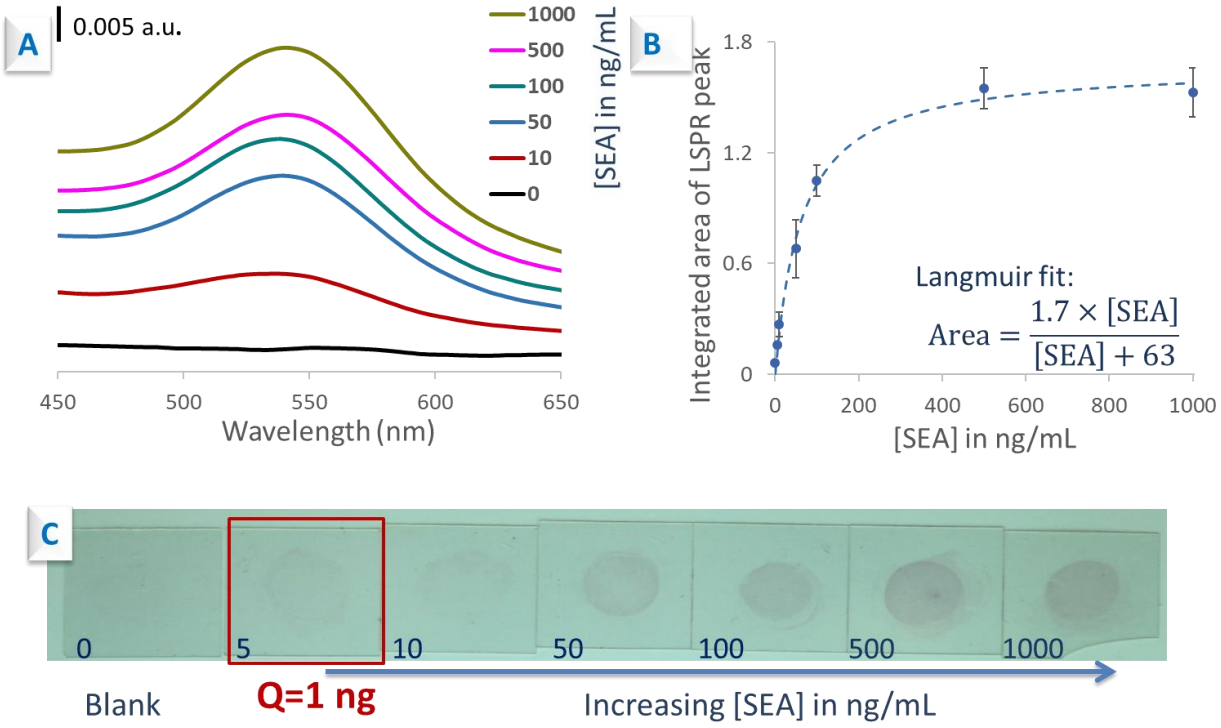

Figure 6. Detection of SEA in milk: A. UV-Visible spectra recorded on glass slides exposed to increasing concentrations of SEA followed by AuNP-Ab bioconjugate, B. Dose-response curve obtained by plotting the integrated area of the LSPR peak from A as a function of [SEA]. C. Photos of the glass slides showing no response for the blank and red spots of increasing intensity for increasing concentrations of SEA.

This concentration-dependent response was confirmed by UV-Visible analysis in Figure 6-A. A dose-response curve (Figure 6-B) was established by plotting the integrated area of the LSPR peak as a function of [SEA]. As for samples in buffer, the dynamic range extended from 10 to 500 ng/mL, but the sensor sensitivity was improved to reach a limit of detection as low as 1.5 ng/mL (0.3 ng in 200 µL). Data fitting using the Langmuir model led to an $Area_{max}$ = 1.7 and K_D = 63 ng/mL (see supplementary section for the fit parameters). These values clearly point out that the sensitivity of the biosensor is improved when working in milk. This result is quite

unexpected as milk is a complex medium rich in proteins that may interfere and hinder the molecular recognition phenomena. To try and understand this discrepancy, we performed the experiment in a different buffer. Indeed, antigen binding to antibody can be pH-dependent, and milk pH is 6.9, while PBS buffer pH is slightly higher, *i.e.* 7.4. To see whether this enhancement is pH-induced, the assay was repeated with SEA in phosphate buffer pH 6.8, *i.e.* close to milk pH. The results (Table 2) show an identical response of the sensor to SEA at 500 ng/mL in both buffers ruling out any pH-effect.

Table 2. Medium/pH effect on SEA (500 ng/mL) biosensing

Medium	pH	Integrated area of LSPR peak
PBS	7.4	0.67 ± 0.06
Milk	6.9	1.55 ± 0.1
Phosphate buffer	6.8	0.66 ± 0.05

At this point, we cannot provide a suitable explanation to this better sensitivity. Many factors are modified when working in milk, for example, calcium concentration is high and recent studies show that antibody binding to antigen can be calcium-dependent even for an antigen that does not directly bind to calcium.[39] It might also be the case for SEA binding to anti-SEA antibody.

Optimizing the biosensing format. On the whole, the assay takes 4 h (2*2 h). We investigated whether the incubation times of SEA and AuNP-Ab might be decreased. In a first series of experiments, the incubation time of SEA was varied from 15 to 120 min while keeping the AuNP-Ab incubation time to 2 h. The selected concentration of SEA for this experiment was 250 ng/mL, just below the plateau, and, therefore, not in the “comfort zone” in terms of measurement repeatability as the error bars in this region are larger. Four different regions of the glass slide (within the capture zone) were analyzed to estimate the reliability of the response. The results are shown in Figure 7-A. Starting from 30 min, the response was very large and reached 98 % of its final value. Therefore, the SEA incubation step can safely be reduced by a factor of 4 without compromising the sensor response.

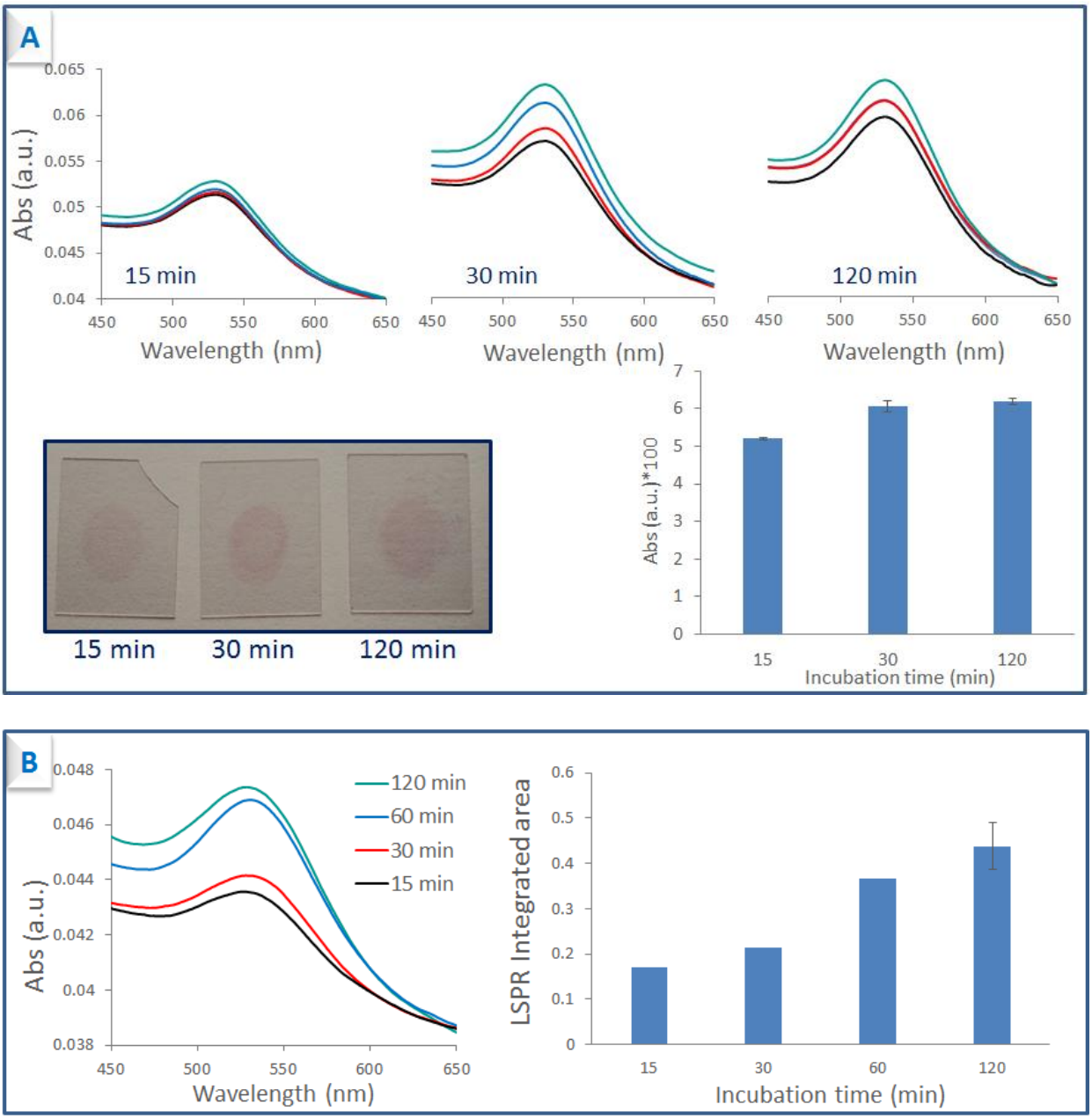

Figure 7. A: Effect of SEA incubation time on biosensor response. Top figures: LSPR spectra measured for 15, 30 and 120 min on four different regions of the glass slides. Bottom figures: photos of the slides and average absorbance values of LSPR peaks. B: Effect of AuNP-Ab incubation time on biosensor response. LSPR spectra measured for 15, 30, 60 and 120 min and integrated areas of LSPR band.

We also explored the influence of AuNP-Ab incubation time on the sensor response. The results shown in Figure 7-B, showed that 83% of the maximum response is reached after one hour incubation allowing further reduction of the assay time to a total of 1.5 h instead of 4 h.

Finally, we also tried another format where the AuNP-Ab bioconjugate is first pre-incubated

with SEA, then added to the glass slides. This format was less reliable than the one used herein as the specificity of the response was not preserved.

CONCLUSION

In summary, a colorimetric immunosensor, including gold nanoparticles as transducer was designed to visually detect the bacterial toxin SEA in food samples. This analytical device takes advantage of the extremely high extinction coefficients of colloidal gold nanoparticles, giving rise to bright colors down to nanomolar concentrations. Amino-coated glass slides were functionalized with anti-SEA antibody via affinity to Protein A. The same antibody was conjugated by physisorption to spherical gold nanoparticles to afford the colorimetric nanoimmunoprobe. A sensitive sandwich format assay was set up where SEA was selectively captured on the glass slide and its presence revealed by binding of AuNP-Ab conjugate, resulting in the appearance of a red spot for down to 1 ng toxin in buffer and in milk. Quantitative response between 10 and 500 ng/mL was extracted by integrating the LSPR band of the absorption spectrum of glass slides measured on with a benchtop UV-Visible spectrometer. Under optimized conditions, the total assay time could be reduced to 1.5 h. Transposition of this analytical system to a point-of-care assay using final readout with a smartphone[40] will be next investigated.

ACKNOWLEDGMENTS

This work was supported by the French-Singaporean PHC Merlion program (grant 5.03.15). This work was also co-financially supported by ANR (Agence Nationale de la Recherche) and FWF (Deutsche Forschungsgemeinschaft), ANR-FWF program, project NanoBioSensor, Grant no: ANR-15-CE29-0026-02, and by the iFood initiative at NTU, Singapore.

REFERENCES

(1) Zheng, W.; Jiang, X. *Analyst* **2016**, *141*, 1196-1208.

(2) Jans, H.; Huo, Q. *Chemical Society Reviews* **2012**, *41*, 2849-2866.

(3) Wang, Z.; Ma, L. *Coordination Chemistry Reviews* **2009**, *253*, 1607-1618.

(4) Mayer, K. M.; Hafner, J. H. *Chemical Reviews* **2011**, *111*, 3828-3857.

(5) Bahadır, E. B.; Sezgintürk, M. K. *TrAC Trends in Analytical Chemistry* **2016**, *82*, 286-306.

(6) Wilson, R. *Chemical Society Reviews* **2008**, *37*, 2028-2045.

(7) Cordeiro, M.; Ferreira Carlos, F.; Pedrosa, P.; Lopez, A.; Baptista, P. V. *Diagnostics* **2016**, *6*, 43.

(8) Le Loir, Y.; Baron, F.; Gautier, M. *Genet. Mol. Res.* **2003**, *2*, 63-76.

(9) Hennekinne, J.-A.; De Buyser, M.-L.; Dragacci, S. *FEMS Microbiol. Rev.* **2012**, *36*, 815–836.

(10) Evenson, M. L.; Ward Hinds, M.; Bernstein, R. S.; Bergdoll, M. S. *International Journal of Food Microbiology* **1988**, *7*, 311-316.

(11) Homola, J.; Dostálek, J.; Chen, S.; Rasooly, A.; Jiang, S.; Yee, S. S. *International Journal of Food Microbiology* **2002**, *75*, 61-69.

(12) Karaseva, N.; Ermolaeva, T. *Mikrochimica Acta* **2015**, *182*, 1329-1335.

(13) Kasama, T.; Ikami, M.; Jin, W.; Yamada, K.; Kaji, N.; Atsumi, Y.; Mizutani, M.; Murai, A.; Okamoto, A.; Namikawa, T.; Ohta, M.; Tokeshi, M.; Baba, Y. *Analytical Methods* **2015**, *7*, 5092-5095.

(14) Medina, M. B. *Journal of Rapid Methods and Automation in Microbiology* **2005**, *13*, 37-55.

(15) Naimushin, A. N.; Soelberg, S. D.; Nguyen, D. K.; Dunlap, L.; Bartholomew, D.; Elkind, J.; Melendez, J.; Furlong, C. E. *Biosensors and Bioelectronics* **2002**, *17*, 573-584.

(16) Pimenta-Martins, M. G. R.; Furtado, R. F.; Heneine, L. G. D.; Dias, R. S.; Borges, M. d. F.; Alves, C. R. *Journal of Microbiological Methods* **2012**, *91*, 138-143.

(17) Tsai, W.-C.; Li, I.-C. *Sensors and Actuators B: Chemical* **2009**, *136*, 8-12.

(18) Ben Haddada, M.; Salmain, M.; Boujday, S. *Sensors and Actuators B-Chemical* **2018**, *255*, 1604-1613.

(19) Salmain, M.; Ghasemi, M.; Boujday, S.; Pradier, C.-M. *Sensors and Actuators B: Chemical* **2012**, *173*, 148-156.

(20) Salmain, M.; Ghasemi, M.; Boujday, S.; Spadavecchia, J.; Técher, C.; Val, F.; Le Moigne, V.; Gautier, M.; Briandet, R.; Pradier, C.-M. *Biosensors and Bioelectronics* **2011**, *29*, 140-144.

(21) Ben Haddada, M.; Hu, D.; Salmain, M.; Zhang, L.; Peng, C.; Wang, Y.; Liedberg, B.; Boujday, S. *Analytical and Bioanalytical Chemistry* **2017**.

(22) Slot, J. W.; Geuze, H. J. *Ultramicroscopy* **1984**, *15*, 383.

(23) Ben Haddada, M.; Huebner, M.; Casale, S.; Knopp, D.; Niessner, R.; Salmain, M.; Boujday, S. *The Journal of Physical Chemistry C* **2016**, *120*, 29302-29311.

(24) Dalstein, L.; Ben Haddada, M.; Barbillon, G.; Humbert, C.; Tadjeddine, A.; Boujday, S.; Busson, B. *Journal of Physical Chemistry C* **2015**, *119*, 17146-17155.

(25) Neumann, A. C.; Wang, X.; Niessner, R.; Knopp, D. *Analytical Methods* **2016**, *8*, 57-63.

(26) Balasubramanian, S. K.; Yang, L.; Yung, L.-Y. L.; Ong, C.-N.; Ong, W.-Y.; Yu, L. E. *Biomaterials* **2010**, *31*, 9023-9030.

(27) Cras, J. J.; Rowe-Taitt, C. A.; Nivens, D. A.; Ligler, F. S. *Biosensors and Bioelectronics* **1999**, *14*, 683-688.

(28) Huebner, M.; Ben Haddada, M.; Methivier, C.; Niessner, R.; Knopp, D.; Boujday, S. *Biosensors and Bioelectronics* **2015**, *67*, 334-341.

(29) Aissaoui, N.; Bergaoui, L.; Landoulsi, J.; Lambert, J.-F.; Boujday, S. *Langmuir* **2012**, *28*, 656-665.

(30) Gunda, N. S. K.; Singh, M.; Norman, L.; Kaur, K.; Mitra, S. K. *Applied Surface Science* **2014**, *305*, 522-530.

(31) Boujday, S.; Bantegnie, A.; Briand, E.; Marnet, P.-G.; Salmain, M.; Pradier, C.-M. *Journal of Physical Chemistry B* **2008**, *112*, 6708-6715.

(32) Seitz, O.; Chehimi, M. M.; Cabet-Deliry, E.; Truong, S.; Felidj, N.; Perruchot, C.; Greaves, S. J.; Watts, J. F. *Colloids and Surfaces A* **2003**, *218*, 225-239.

(33) Link, S.; El-Sayed, M. A. *Journal of Physical Chemistry B* **1999**, *103*, 4212-4217.

(34) Liu, X.; Atwater, M.; Wang, J.; Huo, Q. *Colloids and Surfaces B: Biointerfaces* **2007**, *58*, 3-7.

(35) Ben Haddada, M.; Blanchard, J.; Casale, S.; Krafft, J.-M.; Vallée, A.; Méthivier, C.; Boujday, S. *Gold bulletin* **2013**, *46*, 335-341.

(36) Wang, W.; Liu, L.; Xu, L.; Kuang, H.; Zhu, J.; Xu, C. *Particle & Particle Systems Characterization* **2016**, *33*, 388-395.

(37) Hwang, J.; Lee, S.; Choo, J. *Nanoscale* **2016**, *8*, 11418-11425.

(38) Upadhyay, N.; Nara, S. *Microchemical Journal* **2018**, *137*, 435-442.

(39) Hironiwa, N.; Ishii, S.; Kadono, S.; Iwayanagi, Y.; Mimoto, F.; Habu, K.; Igawa, T.; Hattori, K. *mAbs* **2016**, *8*, 65-73.

(40) Wang, Y.; Liu, X.; Chen, P.; Tran, N. T.; Zhang, J.; Chia, W. S.; Boujday, S.; Liedberg, B.

Analyst **2016**, *141*, 3233-3238.

Supporting information for

Naked Eye Immunosensing of a Food Biotoxin using Gold Nanoparticles-Antibody Bioconjugate

Lu Zhang[1,2,3,4], Michèle Salmain[2], Bo Liedberg[3], and Souhir Boujday[1]*

[1] Sorbonne Université, CNRS, Laboratoire de Réactivité de Surface (LRS), 4 place Jussieu F-75005 Paris, France.

[2] Sorbonne Université, CNRS, Institut Parisien de Chimie Moléculaire (IPCM), 4 place Jussieu F-75005 Paris, France.

[3] Centre for Biomimetic Sensor Science, School of Material Science and Engineering, Nanyang Technological University, 637553 Singapore.

[4] Sorbonne University and Nanyang Technological University Dual Degree PhD Programme.

Figures (6), Tables (2)

Antibody-AuNP bioconjugate engineering

Conjugation of rabbit anti-SEA antibody was performed according to ref. [25], the purification process is shown in Figure S.1.

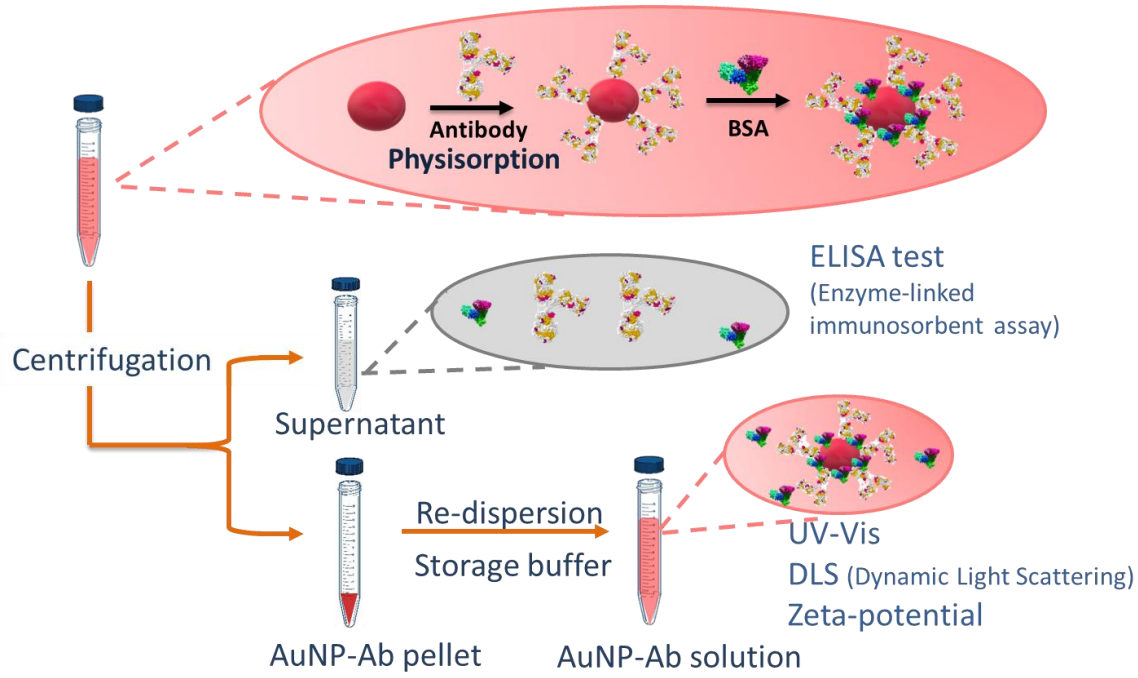

Figure S.1. Schematic purification process employed in AuNP-Ab conjugation.

Estimating antibody coverage on AuNP by ELISA

ELISA was used to quantify the concentration of unbound antibody in the supernatant. [Ab]unbound was around 6.6 µg/mL and the volume of supernatant is 5 mL; *i.e.* q (unbound Ab) = 33 µg; since the initial quantity of Ab was 55 µg, q(bound Ab) = 22 µg = 0.15 nmol. As the final AuNP-Ab conjugate volume = 4 ml, [Ab] = 37 nM; the concentration of AuNP in the conjugate which is around 4.45 nM was calculated according to Lambert-Beer's law (ε(520nm) = 2.8×10^8 $M^{-1}.cm^{-1}$). The Ab-to-AuNP ratio is 8.3.

Optimizing the surface chemistry for the sensing layer design

We investigated firstly three strategies to functionalize glass slides prior to protein chemisorption as schematized in Figure S.2. The silica substrates were exposed to epoxide- or amine- terminated alkoxysilane to create epoxide or amine functions at their surface. The anti-SEA capture antibody was attached by reaction of its amino groups with surface epoxides or with surface amines using glutaraldehyde (GA) or 1,4-phenylenediisothiocyanate (PDITC) as

cross-linkers or by affinity to covalently linked protein A to the surface amines using GA as cross-linker. The elementary surface modification steps were monitored by FT-IR spectroscopy (on silicon wafers).

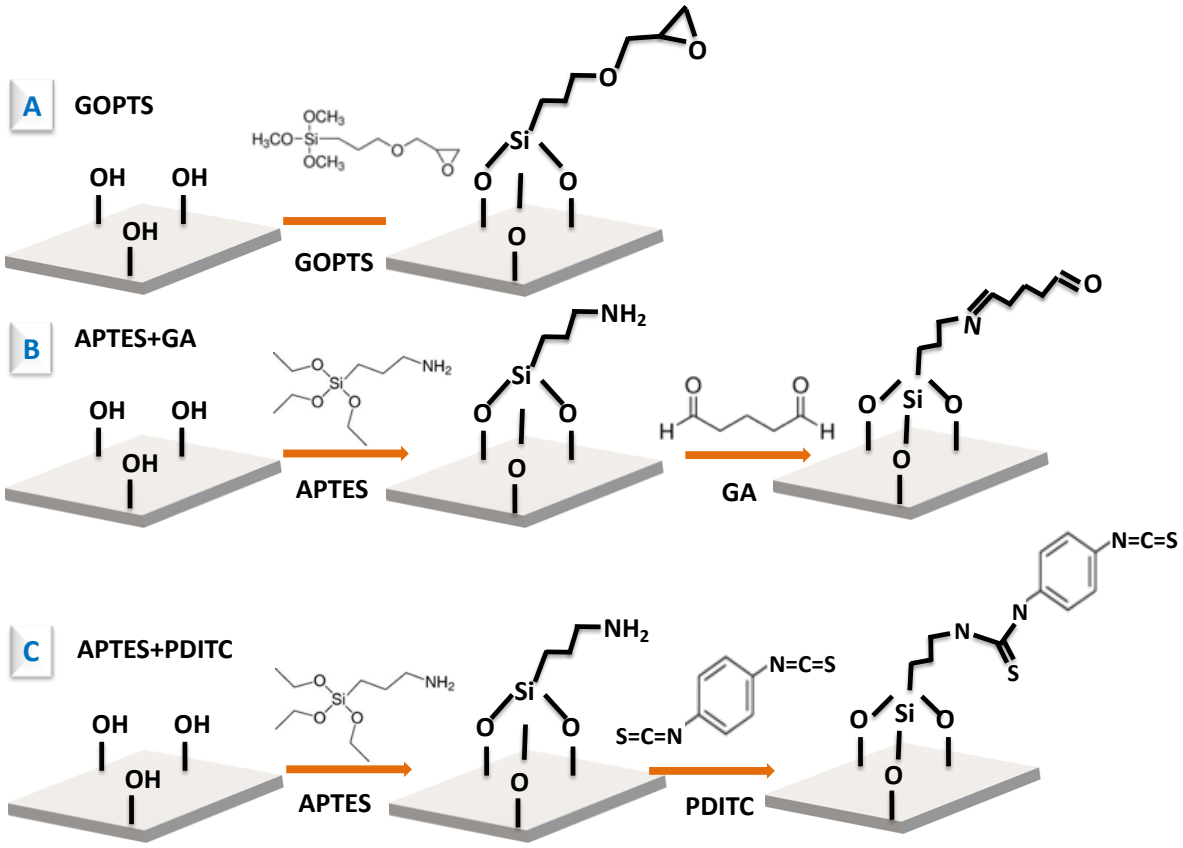

Figure S.2. The three surface functionalization strategies employed in this work. A. GOPTS (3-glycidyloxypropyl)trimethoxysilane); B. APTES + GA (aminopropyltriethoxysilane + glutaraldehyde); and C. APTES + PDITC (aminopropyltriethoxysilane + 1,4-phenylenediisothiocyanate).

IR. The GA-ATR IR spectra of silicon wafers after each surface chemical modification step are shown in Figure S.3. *GOPTS format* (Figure S.3-A): On the bare clean silicon wafers (A-a), the IR spectrum is noisy and dominated by Si-O-Si stretching vibrations around 1100 cm^{-1}, in agreement with the presence of a thin layer of SiO_2 at the wafer surface. After exposure to GOPTS (A-b), the characteristic band of the epoxy group appeared at 1260 cm^{-1}. After the protein immobilization (Ab + BSA) (A-c), the characteristic band at 1654 cm^{-1} assigned to the amide I band was observed but the band at 1545 cm^{-1} assigned to amide II was very weak. The band at 1260 cm^{-1} increased, which may be assigned to the amide III band. *APTES+GA format* (Figure S.3-B): Treatment of the bare clean silicon wafer by APTES (B-b) resulted in the presence of several bands in the region 1400-1700 cm^{-1} of the IR spectrum, assigned to amine

and ammonium groups and also bands around 2930 cm^{-1} (not shown) due to the stretching vibrations of CH groups. GA grafting (B-c) is less obvious on the IR spectrum, where only a weak band at 1732 cm^{-1}, characteristic of the aldehyde C=O group, appeared. Direct immobilization of anti-SEA antibody on GA followed by BSA blocking (B-d) resulted in an intense signal at 1654 cm^{-1} assigned to amide I band, while the band at 1545 cm^{-1} (amide II) is very weak. Affinity adsorption of anti-SEA antibody through protein A followed by BSA blocking (B-e) was evidenced by the appearance of strong amide I and amide II bands at 1654 cm^{-1} and 1545 cm^{-1}, respectively. *APTES+PDITC format* (Figure S.3-C): PDITC grafting on APTES (C-c) did not result in the appearance of a characteristic band (isothiocyanate) at around 2100 cm^{-1} (not shown here). Intense amide I and II band appeared (C-d) at 1654 cm^{-1} and at 1545 cm^{-1} respectively after protein immobilization.

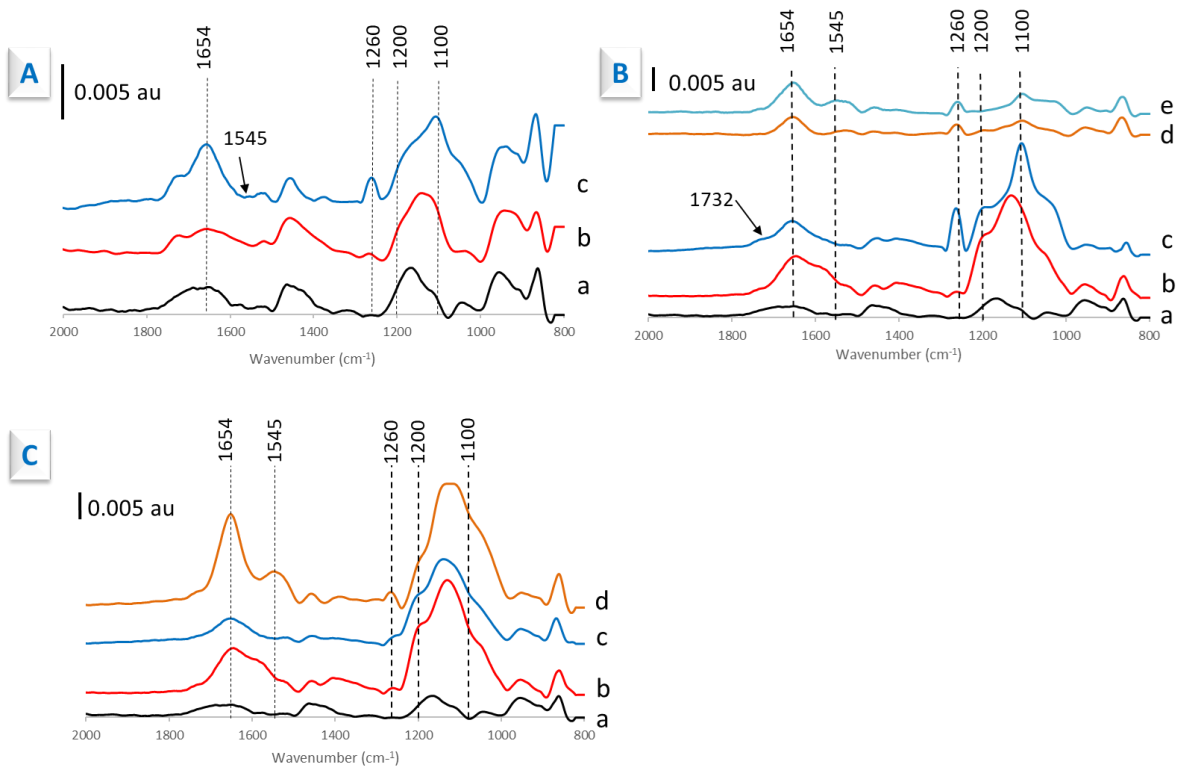

Figure S.3. Surface IR spectra (measured on silicon wafers). A. GOPTS format: (a) bare surface, (b) GOPTS-modified, (c) upon protein attachment. B. APTES+GA format: (a) bare surface, (b) APTES-modified, (c) GA-modified, and upon protein attachment without PrA (d) and with Protein A (e). C. APTES+PDITC format: (a) bare surface, (b) APTES-modified, (c) PDTIC-modified and (d) upon protein attachment.

ELISA and UV-Visible tests

The relative amount of immobilized Ab was determined by ELISA and UV-visible spectrometry

by comparing the response (integrated area of the LSPR band) of the immunosensors to 1 µg/mL SEA in PBS-0.1% BSA after exposure of the sensor to AuNP-Ab. The detailed procedure of the surface ELISA is as follows: HRP goat anti-rabbit IgG conjugate (1/4000 in PBS-0.1%BSA; 300 µL) was deposited on the glass slide surface and incubated for 1 h. The slide was washed 3 times with PBS-0.05%Tween 20. The OPD + H_2O_2 substrate solution (300 µL) was deposited on the slide surface. The orange color was left to develop. The solution was transferred into a microtiter plate (100 µL/well, 3 wells), and 2.5 M H_2SO_4 (50 µL/well) was added to stop the enzymatic reaction. After 10 min in the dark, the absorbance was read at 485 and 405 nm (as reference) with a microplate reader. The results are summarized in Table S.1.

Table S.1. Immobilization of anti-SEA Ab using various surface chemistries: the immobilized Ab was "quantified" by ELISA and response of the immunosensor to a standard 1 µg/mL solution of SEA in PBS-0.1%BSA.

surface chemistry	ELISA[a]	UV-Vis[c]
GOPTS	0.18	0
APTES-PDITC	0.26	0.08
APTES-GA	0.26	0.09
APTES-GA-Protein A	0.84[b]	0.64±0.05

[a] Absorbance of the enzymatic product at 485nm (The experiments were not done at the same time, so the results are not directly comparable).

[b] Control experiment with Protein A (without Ab): 0.079.

[c] Integrated area of LSPR band of AuNP-Ab.

The absorbance of the enzymatic product reflects the quantity of immobilized Ab on the glass slides, *i.e.* the higher the absorbance of the enzymatic product is, the more Ab is present at the surface. Among the three different surface modification methods, the APTES-GA-PrA modified surface displays the largest amount of Ab. Through UV-vis absorption of AuNP-Ab, the APTES-GA-PrA method modified surface immobilized the largest amount of AuNP-Ab. Consequently, the most efficient immunosensor configuration consisted in the immobilization of anti-SEA by affinity to protein A covalently bound to the GA-activated APTES-terminated surface. This configuration, depicted in was further used to establish the calibration curves for SEA.

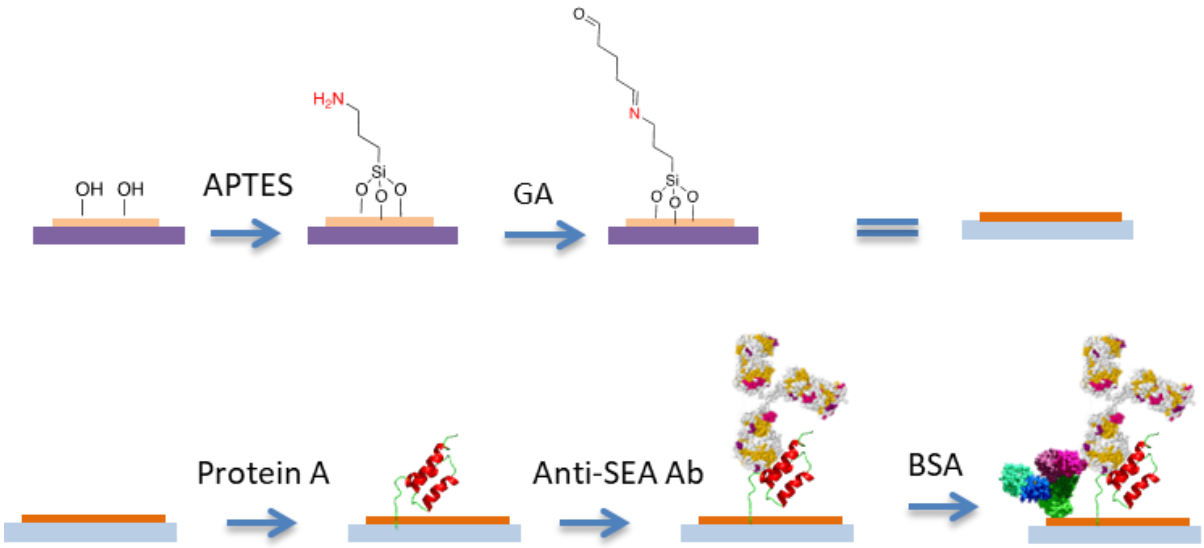

Figure S.4. The adopted surface functionalization strategy for the design of the sensing layer.

Langmuir fit parameters for SEA biosensing

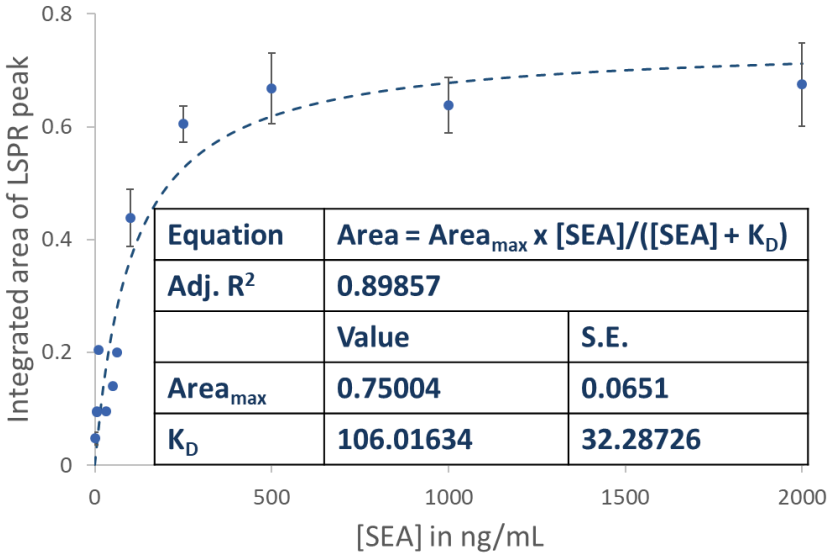

Figure S.5. Langmuir fit of the dose-response curve in buffer.

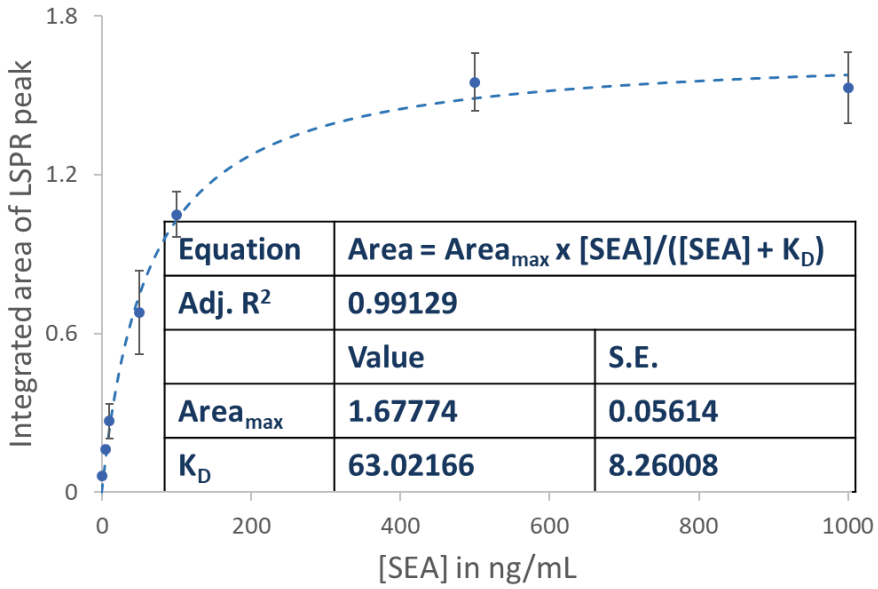

Figure S.6. Langmuir fit of the dose-response curve in milk.

By converting the Langmuir equation $\text{Area} = \frac{\text{Area}_{max} \times [\text{SEA}]}{[\text{SEA}] + K_D}$, we get $[\text{SEA}] = \frac{K_D \times \text{Area}}{\text{Area}_{max} - \text{Area}}$.

The limit of detection of SEA is related to Area_{LOD}=Area(0) + 3×S.D.(0). Therefore, the limit of detection of SEA was calculated as

$[\text{SEA}]_{LOD} = \frac{K_D \times \text{Area}_{LOD}}{\text{Area}_{max} - \text{Area}_{LOD}} = \frac{K_D \times (\text{Area}(0) + 3 \times \text{S.D.}(0))}{\text{Area}_{max} - (\text{Area}(0) + 3 \times \text{S.D.}(0))} = \frac{K_D \times 3 \times \text{S.D.}(0)}{\text{Area}_{max} - 3 \times \text{S.D.}(0)}$. All the values are shown in Table S.2. The calculated LOD in buffer is 9.1 ng/mL and in milk is 1.5 ng/mL.

Table S.2. values for calculating the LOD in buffer and milk.

	Buffer	Milk
K_D	106	63
Area_{max}	0.75	1.68
S.D. for the blank solution	0.02	0.01

Paper IV

Spatially Controlled Reduction and Growth of Silver in Hollow Gold Nanoshell Particles

Preface

Following the same strategy of SEA detection described in paper III, replacement of spherical gold nanoparticles (AuNPs) by hollow gold nanoshell (AuNS) with a higher extinction coefficient is a protential approach to improve the SEA biosensing sensitivity. AuNS was synthesized according to the galvanic replacement method using silver nanoparticles (AgNPs) as template. (Figure IV-A) The initial pH of as-synthesized AuNS is acidic with pH~4. For the preparation of antibody (Ab) bioconjugates by physisorption, the pH of colloidal solution needed to be adjusted to 8-9 which is close to the isoelectric point (pI) of Ab. In practice, we unexpectedly found that the solution color changed immediately and dramatically upon increasing the pH. (Figure IV-B from i to ii) In accordance, there was a dramatic blue shift of the LSPR band in the UV-Vis spectra. We first simply adjusted the pH back to initial pH, but the solution color did not change back, nor the position of LSPR band. We hypothesized that there was an irreversible chemical reaction that occurred by changing pH and we investigated this phenomenon in-depth. We confirmed that by increasing the pH, the reducing ability of citrate increased. More importantly, nanoconfinement of AuNS favored the reduction of Ag^+ preferentially inside the AuNS. After the inside volume of AuNS was filled, the extra additional Ag^+ was reduced on external wall of AuNS. (Figure IV-B from iii to iv) Our finding in this paper is believed to contribute a fundamental understanding of spatially controlled reactions at nanoscale.

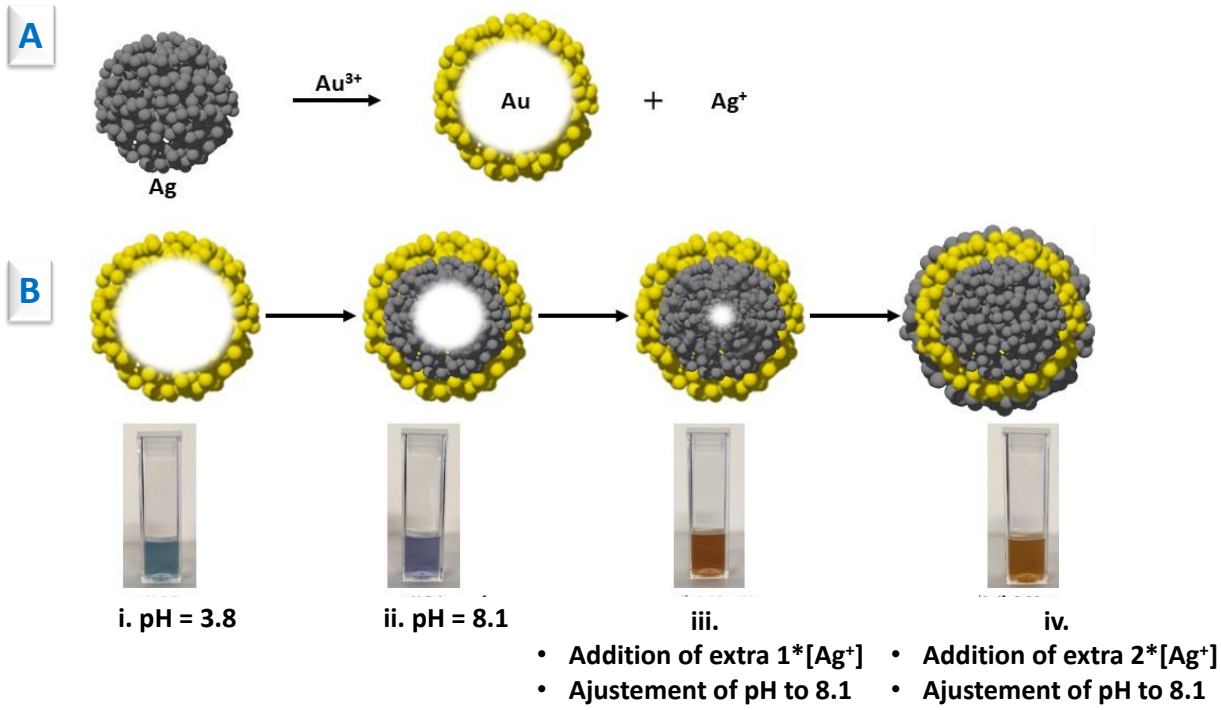

Figure IV: A. Schematic illustration of the synthesis of AuNS; B. Schematic illustration of the reduction/growth process of silver on the inner and outer surfaces of porous AuNS nanoparticles and relevant colloidal solution. (i) initial AuNS solution; (ii) simple increment of pH to 8.1; prior to the increment of the pH to 8.1, extra 1 time and 2 times [Ag^+] were added in (iii) and (iv) respectively.

Spatially Controlled Reduction and Growth of Silver in Hollow Gold Nanoshell Particles

Lu Zhang[1,2,3‡], Peng Chen[1‡], Alexis Loiseau[2], Dalil Brouri[2], Sandra Casale[2], Michèle Salmain[4], Souhir Boujday[2,], Bo Liedberg[1,*]*

[1]Centre for Biomimetic Sensor Science, School of Materials Science and Engineering, Nanyang Technological University, Singapore 637553.

[2]Sorbonne Université, CNRS, Laboratoire de Réactivité de Surface (LRS), 4 place Jussieu, F-75005 Paris, France.

[3]Sorbonne University-Nanyang Technological University Dual Degree PhD Programme.

[4]Sorbonne Université, CNRS, Institut Parisien de Chimie Moléculaire (IPCM), 4 place Jussieu F-75005 Paris, France.

ABSTRACT Spatially controlled reactions at the nanoscale have attracted increasing interest for fundamental chemistry and for the engineering of novel functional materials. Herein, we demonstrate that the pH-triggered reduction of silver ions preferentially occurs at the inner walls of porous gold nanoshell (AuNS) particles. The reaction initially relies on the presence of residual silver ions inside the AuNS particles as well as in the surrounding solution, and it proceeds upon external addition of silver ions until a solid silver core is formed inside the AuNS particles. Subsequent reduction of silver occurs on the external surface of the solidified AuNS resulting in a layered and compositionally complex silver-like nanoparticle. Growth experiments performed in the dark, under white light illumination as well as near resonance suggest that the reduction reaction is not guided by a plasmonic field enhancement effect. This is in contrast to the recently proposed hot spot mechanism of silver reduction at the rim of nanoholes in a periodic gold array. Our observations point towards a confinement process that proceeds *via* a continuous supply of silver ions that diffuse from the external solution through the porous shell into the inner volume of the AuNS particles.

KEYWORDS: Hollow Gold Nanoshell; Nanochemistry; Nanoconfinement; Silver Reduction; Localized Surface Plasmon Resonance.

Spatially controlled chemical reactions have attracted much attention both in fundamental research and applications.[1-3] More importantly, if the reaction can be precisely controlled at the nanoscale, it may even lead to a revolution in both traditional chemistry and nanotechnology.[4-6] For example, Localized Surface Plasmon Resonance (LSPR) is a phenomenon where surface electrons are brought in resonance with an external electromagnetic field and it offers opportunities to confine the light to a regime below diffraction limit. Plasmonic materials thus can be used as nanoscale light sources to selectively boost chemical reactions at the nanoscale, which is known as "plasmonic nanochemistry". Pioneering works have been done on spatially controlled chemical reactions by controlling the local plasmonic fields/hot spots of metal nanoparticles/structures.[6-9] Among those, Ai *et al.* studied the plasmonic guided chemical reduction of Ag^+ in gold nanohole array using TEM imaging.[6] They found that the sites of Ag growth perfectly matched the hotspots on the gold nanohole array predicted by finite-difference time-domain (FDTD) simulations.

In contrast to the aforementioned plasmonic strategy, nanoconfinement also has been explored to physically control chemical reactions inside the nanosized reactors.[10,11] Interestingly, in a nanosized space the chemistry, reaction paths, equilibrium, activities and dynamics *etc*. can be very different from that of bulk.[11-17] Different materials have been explored as reactors for nanoconfined chemical reactions, including porous polymers[12], charged microdroplets,[17,18] microdiameter emulsions,[19] inverted micelles,[20] aerosol particles[21] and porous silica nanoreactor[22,23] *etc*.

In this contribution, we utilized a porous plasmonic hollow nanoshell as a nanoreactor to run confined chemical reactions. Importantly, this plasmonic nanoreactor offers opportunities to spatially control chemical reactions by plasmonic and nanoconfinement effects. With the reduction of Ag^+ as a model system, we studied the reaction process systematically with UV-Vis spectroscopy, DLS, Zeta-potential, TEM and STEM coupled to X-EDS for elemental mapping. We found that the reduction of Ag^+ preferentially occurred inside the nanoreactor rather than on its external surface. Experiments performed under illumination with white light, at near plasmonic resonance and in the dark suggest that nanoconfinement plays a pivotal role in determining the preferred location of the reduction reaction.

Results and Discussion

Hollow noble metal nanoparticles are of significant interest in fundamental research as well as for chemical/biological applications due to their unique optical properties[24,25] as well as the capability to encapsulate molecular moieties.[26,27] Generally the hollow nanoparticles are synthesized by a galvanic replacement reaction, where the salt of metal with higher reduction potential is added to a metal nanoparticle with lower reduction potential. The formation of the AuNS utilizes silver nanoparticles (AgNPs) as sacrificial template according to the following reaction.

$$3Ag(s) + AuCl_4^-(aq) \rightarrow Au(s) + 3Ag^+(aq) + 4Cl^-(aq) \quad (1)$$

Specifically, the standard reduction potential of $AuCl_4^-$/Au redox pair is 0.99 V vs the standard hydrogen electrode (SHE), while that of Ag^+/Ag is 0.80V vs SHE. The difference in reduction potential causes the Au to be deposited on the AgNP template upon release of Ag^+ into the solution, see Figure 1A.

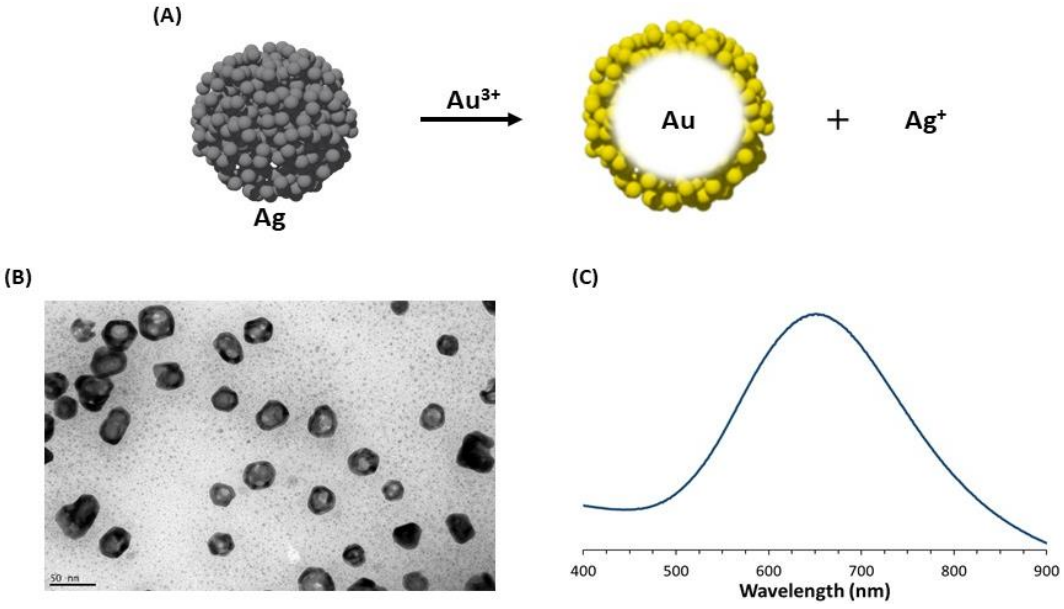

Figure 1. (A) Schematic cartoon illustrating the synthesis of AuNS particles. (B) TEM micrograph of as prepared AuNS particles. (C) UV-Vis absorption spectrum of as prepared AuNS particles.

In a typical synthesis, AuNS particles were synthesized using the galvanic replacement method developed by Xia *et. al.*[28] The Au^{3+} ions are reduced and a hollow AuNS forms, Figure 1A. A typical TEM micrograph and UV-Vis absorption spectrum of the as synthesized AuNS particles are shown in Figure 1B and 1C, respectively. The hollow interior is clearly visualized in the TEM micrograph as greyish areas surrounded by dark rings. The size of the AuNS particles is

40±10 nm and the absorption peak maximum appears at ~656 nm. The hydrodynamic size of the AuNS particles, as revealed by DLS is ~60 nm, Figure S1. The particles bear a negative surface charge owing to the presence of the citrate ions on the surface. This yields a zeta potential of -30.6 mV at the native pH of the AuNS suspension that is 3.8, Figure S1. It is worthwhile pointing out that the hollow particles prepared according to the galvanic replacement protocol, under the reaction conditions described herein, are not pure Au but rather alloy nanoparticles. For example, the X-EDS analysis in Figure S2 clearly shows that the AuNS particles consist of ~52% Au and ~48% Ag. Although we cannot distinguish between the oxidation states with X-EDS, we suggest that silver exists in the form of an Ag/Au alloy and/or as Ag^+ ions attached to the shell, most likely at shell imperfections. This observation is in line with previous studies that propose that the shell consists of an Au/Ag bimetallic alloy.[29-31] In this contribution, we merely use the term AuNS just to keep it consistent with the convention in the literature and for the sake of simplicity.

One interesting observation is that the optical spectrum of the AuNS particles is sensitive to the pH of the supporting solution. Figure 2A shows the absorption spectra and photos of AuNS solutions at pH 3.8, 5.3 and 8.1, respectively. The absorption spectrum shifts towards the blue with increasing pH values and the intensity (absorbance) increases. These optical changes are sufficiently large to be visualized by human eye as a blue to purple color transition, see the inset in Figure 2A. The trend of the changes in peak maximum and absorbance values of the AuNS suspension with increasing pH is plotted in Figure 2B. It is evident that the blue shift and the concomitant increase in absorbance start at about pH 5 and saturate at pH values above 7.

Moreover, Figure 2C shows the evolution of the absorbance at 580 nm of a typical AuNS sample with time, when the pH was adjusted to 7 upon addition of NaOH. The kinetics is fast and the reaction saturates within 10 minutes. The kinetics is substantially slower if the reaction starts at a lower pH ~5, but it eventually ends up at the same state as that of pH 8, see Figure S3. It is also worthwhile mentioning that this pH-induced transition is not reversible. Thus, when the pH changes back to 3.8, the optical spectrum of AuNS particles does not recover; see Figure 2D and Figure S3. The irreversibility of the optical response suggests that the change is not a simple response to the physical stimulus of pH, but rather due to a permanent chemical change in the sample. A plausible explanation is that Ag^+ ions are rapidly reduced into Ag and deposited onto the AuNS particles when the pH increases rather than forming individual AgNPs as no peak is seen at ~400 nm. The deposition of Ag on AuNS particles explains the blue shift

of the spectrum, as well as the increase in the intensity, because Ag has a higher extinction coefficient and higher resonance frequency (shorter wavelength) than Au.

It is worthwhile to emphasize that the AuNS particles most likely are porous, although they appear as continuous and solid in the TEM micrographs. These tiny pores allow diffusion of reactants (Ag^+, H^+ *etc*.) to and from the interior of the AuNS particles, as evidenced by the fast kinetics shown in Figure 2C. The porous nature of AuNS particles recently was proposed by a few other research groups.[29-31] For example, Halas *et. al.* reported that the AuNS particles consist of small pinholes on the alloy shell surface which allow diffusion of Ag^+ through pores into the surrounding bath.[31] This group also showed that the dealloying of the nanoshell occurred upon extending the reaction time, eventually resulting in the formation of a pure Au shell particle followed by fragmentation and decomposition. Bedzyk, *et. al.* reported that AuNS particles of similar size and chemical composition consist of an Au/Ag alloy shell with pores on the atomic scale.[30]

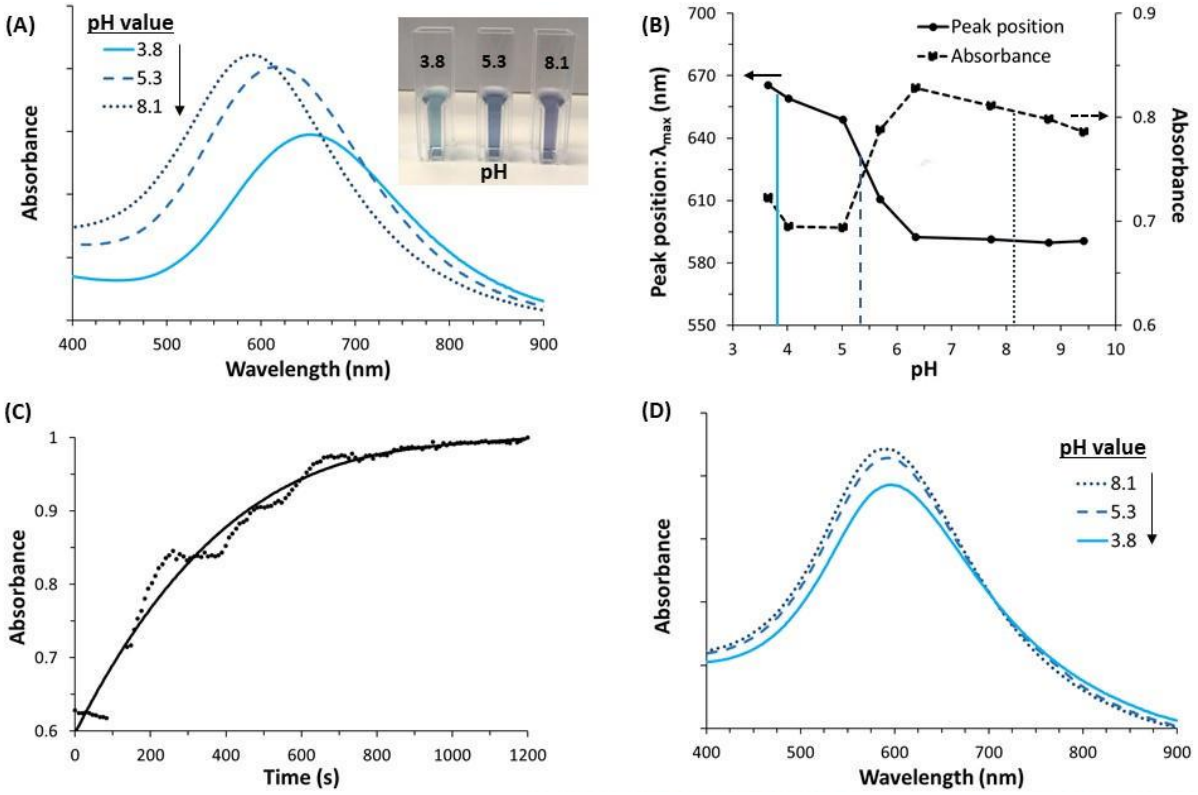

Figure 2. (A) Absorbance spectra of AuNS particles at pH 3.8, pH 5.3 and pH 8.1. The pH of the suspension was adjusted with NaOH (0.1 M) from pH 3.8 to pH 8.1. (B) Peak position and absorbance values as a function of pH. (C) Evolution of absorbance at λmax =580 nm with time (black solid line serves as a guide for the eye). (D) Absorbance spectra of AuNS particles at pH 8.1, pH 5.3 and pH 3.8. The pH of the suspension was adjusted from pH 8.1 to 3.8 upon addition of HNO3 (0.1 M).

The proposed reduction of Ag^+ and subsequent deposition of Ag onto the AuNS particles for pH > 5 is supported by previous findings suggesting that the reducing power of sodium citrate increases with pH.[32] Additional characterizations of the AuNS particles at low and high pH values were conducted to investigate the changes, Figure S1. For example, when pH increases from 3.8 to 8, the dynamic radius of the AuNS particles decreases from 60.4 nm to 54.4 nm, while the zeta potential changes from -30.6 mV to -39.2 mV. With these observations in mind there is no doubt that Ag^+ ions are reduced and deposited on the AuNS particles thereby leading to distinct changes in their physical/optical properties.

Transmission and scanning transmission electron microscope (TEM/STEM) observations/analysis were performed to further characterize the particles and to address the growth mechanism of Ag on AuNS particles. Figure 3A shows a STEM micrograph, and the individual Au, Ag and overlay STEM/X-EDS elemental mapping images for the as prepared AuNS particles at pH 3.8. From the individual and overlay elemental images it is clear that the chemical species are distributed uniformly across the nanoparticle. However, for an AuNS sample exposed to pH 8.1, an inhomogeneous distribution of Au and Ag elements is obvious (Figure 3B). In the overlay image, Figure 3B, a green circle (Ag) appears inside the red circle (Au). In addition, the average size of the Ag diameter (green sphere) and Au diameter (red sphere) are measured to equal ~48.1 nm and ~49.5 nm, respectively. These observations suggest that silver reduction preferentially occurs inside the AuNS particles rather than on its external surface. Thus, the inner volume of AuNS particles appears to work as a nanoreactor, providing spatial control of the reduction reaction and deposition of silver. To further illustrate that the reaction preferentially occurs inside the AuNS particles, we introduced more Ag^+ into the surrounding bath before triggering the reduction by increasing the pH to 8.1.

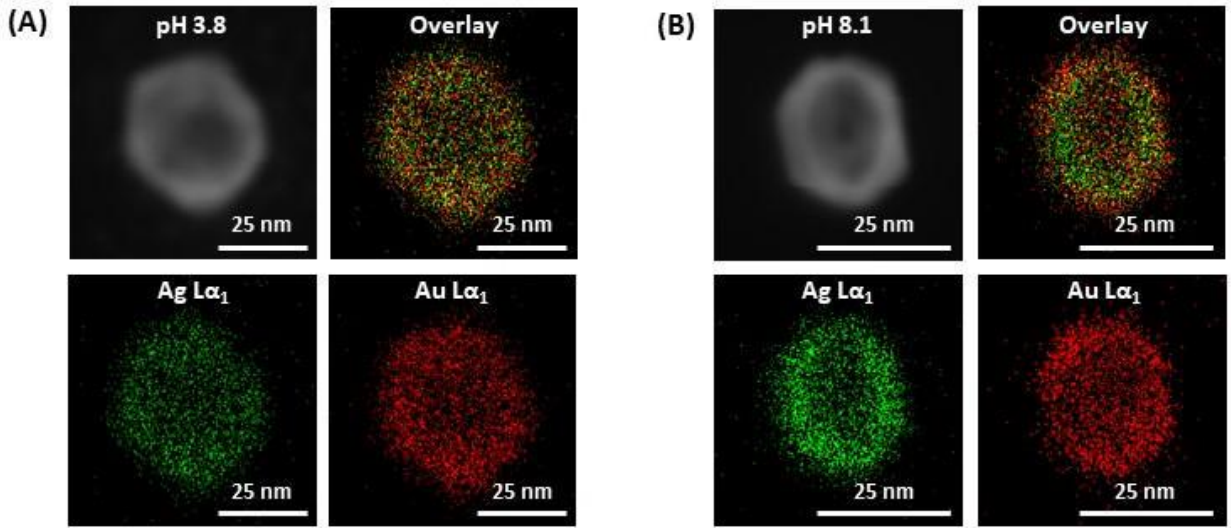

Figure 3. STEM/X-EDS elemental mapping (Ag, Au and overlay) of AuNS particles at pH 3.8 (A) and pH 8.1 (B).

The extra Ag^+ ions were introduced into the as prepared AuNS suspension and reduced by increasing the pH. Two sets of experiments were conducted by introducing $AgNO_3$ at 0.16 mM and 0.32 mM, respectively. Figure 4A shows the absorption spectra for the two AuNS samples with extra $AgNO_3$ added, as well as for AuNS suspensions without extra $AgNO_3$ for reference purposes. The absorption spectrum is further blue shifted upon addition of Ag^+, and the blue shift increases with the increasing concentration of Ag^+. In particular, for the sample with 0.32 mM $AgNO_3$ added, the resulting spectrum displays a maximum at 432 nm, which is close to the position observed for spherical silver nanoparticles. Figure 4B shows photos of the four sample solutions. It is evident that the addition of Ag induces a color change of the suspension from blue to brown. Large area TEM imaging also was conducted, Figure 4C; see TEM micrographs of the four samples in Figure 4A and B. The vast majority of the AuNS particles appear hollow (low contrast) at low pH and without addition of Ag^+ ions, see image (i), Figure 4C. The AuNS particles become slightly darker upon increasing the pH (ii). Extra added Ag^+ ions turn the particles even darker and the AuNS particles appear like solid particles; see the inserts in (iii) and (iv), Figure 4C. Thus, the TEM micrographs clearly demonstrate that the added Ag^+ ions penetrate the shell, become reduced, and fill the empty volume of the AuNS particles until a solid core of Ag is formed.

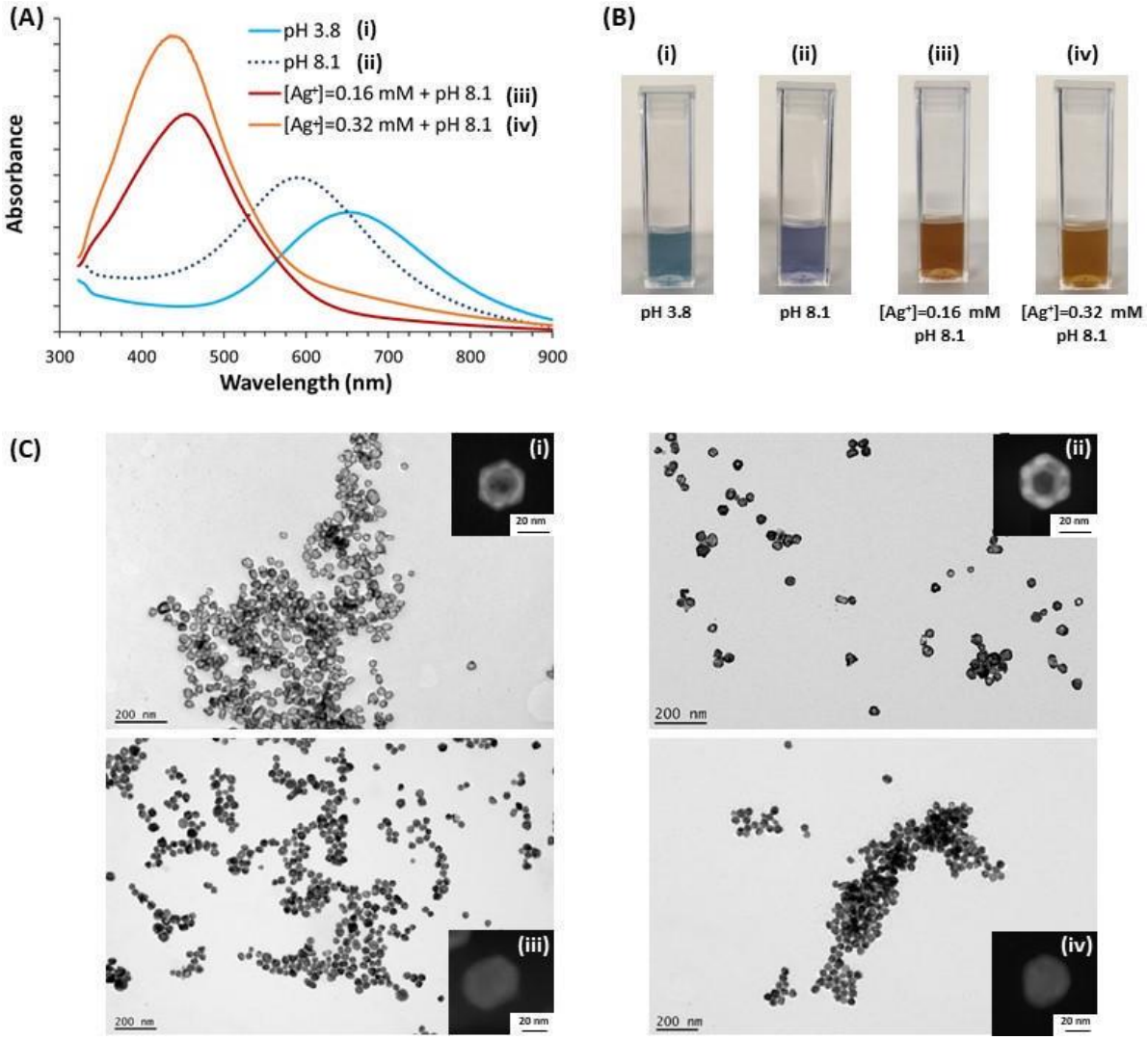

Figure 4. (A) Absorbance spectra of AuNS particles at pH 3.8 (blue curve), pH 8.1 (dotted deep blue curve) and addition of silver nitrate before adjusting the pH suspension with NaOH (0.1 M) until pH 8.1: $[Ag^+]$ = 0.16 mM (red curve) and $[Ag^+]$ = 0.32 mM (orange curve). (B) Photos of solutions; and (C) TEM/STEM micrographs of different solutions deposited on TEM grids: (i) pH 3.8; (ii) pH 8.1; (iii) $[Ag^+]$ = 0.16 mM, pH 8.1 and (iv) $[Ag^+]$ = 0.32 mM, pH 8.1, respectively.

Further characterization, including zeta potential, DLS size and X-EDS of the four samples was done; see Figure S1 and Figure S2, and the data are summarized in Table 1. With increasing amount of Ag^+ ions added, the negative zeta potential increases and the size of the resulting nanoparticle increases. Moreover, the absorption peak maximum shifts further towards the blue and the fraction of Ag increases.

TABLE 1. Summary of physical properties of the four samples prepared at pH 3.8 and pH 8.1, and upon external addition of 0.16 mM and 0.32 mM $AgNO_3$ followed by increasing the pH to 8.1.

Samples	ζ-potential (mV)	DLS (nm)	λ_{max} (nm)	X-EDS (at. %)
i	-30.6	60.4	656	$Ag_{0.48}Au_{0.52}$
ii	-39.2	54.4	592	$Ag_{0.41}Au_{0.59}$
iii	-49.7	68.9	458	$Ag_{0.75}Au_{0.25}$
iv	-55.1	80.5	437	$Ag_{0.81}Au_{0.19}$

We noticed from the TEM micrographs in Figure 4 that with 0.16 mM $AgNO_3$ (sample iii, Table 1), the empty space inside the AuNS particles appears to be completely filled. From Table 1, however, it is evident that both the size of nanoparticle and the fraction of Ag increase upon increasing the concentration of $AgNO_3$ to 0.32 mM (sample iv, Table 1), Thus, it seems that the reduction of Ag^+ continues after having completely filled the inner volume of the AuNS particles. This phenomenon was carefully investigated using elemental mapping. Figure 5A shows the TEM micrograph, elemental mapping of Au, Ag and the overlay. The profile of Au and Ag along the white hatched line (Figure 5A) is also shown for 0.16 mM $AgNO_3$, Figure 5C. The TEM micrograph reveals a solid nanoparticle and the overlay mapping shows a green core with a shallow red shell structure. The profiles of Au and Ag along the white line (Figure 5A) confirm that there is more Ag in the core of the nanoparticle. Figure 5B and D show the TEM micrograph, elemental mapping of Au, Ag and overlay as well as the profile of Au and Ag along the hatched white line after addition of 0.32 mM $AgNO_3$. The TEM micrograph reveals a solid nanoparticle, and the elemental image is dominated by green color. The size of the green sphere (Ag mapping) is larger than that of the red sphere (Au mapping). Moreover, the line profiles of Au and Ag element in Figure 5D clearly demonstrate the size of Ag is larger than that of Au, as indicated by the black oval circle, see profile plot in Figure 5D. Thus, it appears that the reduction of Ag^+ continues on the external surface when the empty volume inside the AuNS particles is completely filled.

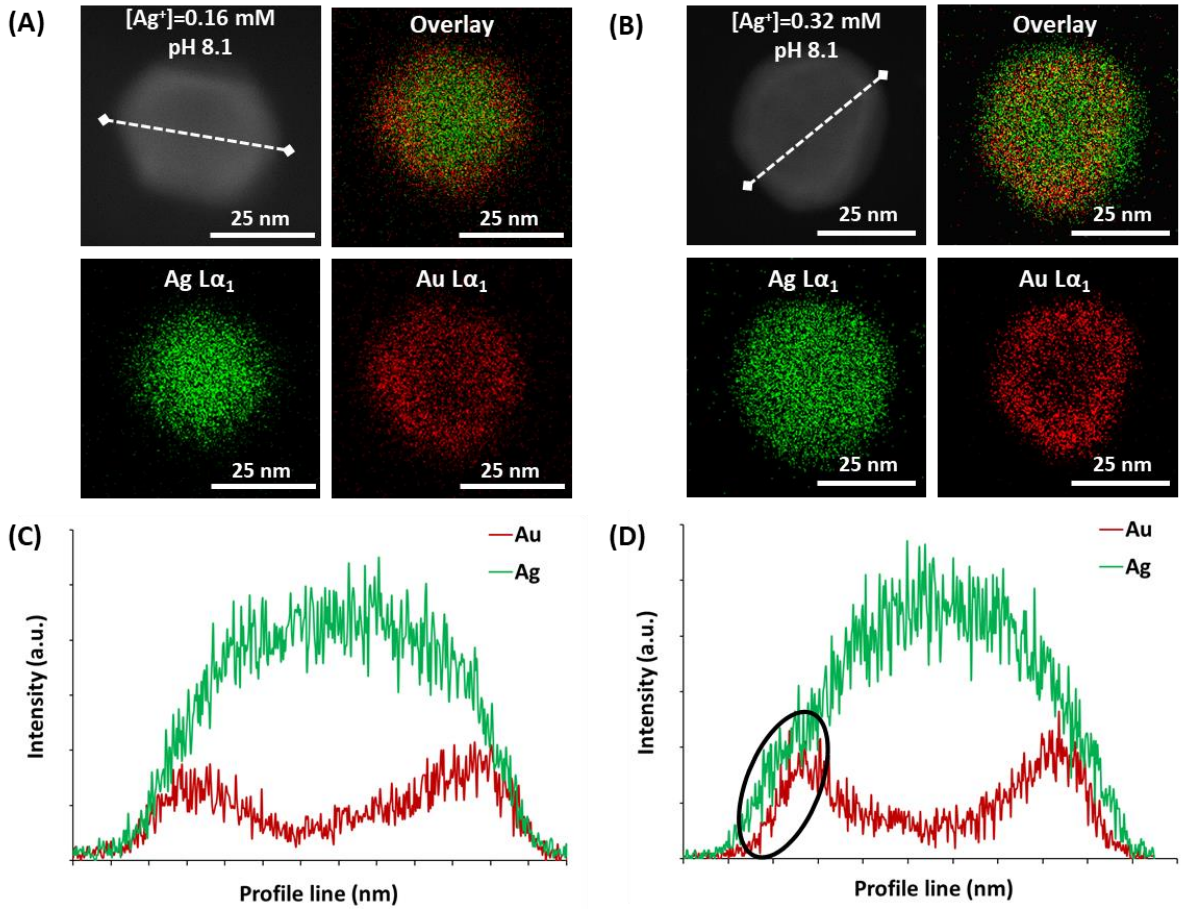

Figure 5. TEM micrograph and STEM/X-EDS elemental mapping (Ag, Au and overlay) of AuNS particles obtained after adding $AgNO_3$ at pH 3.8 and then increasing the pH to 8.1. (A) $[Ag^+]$ = 0.16 mM, pH 8.1 and (B) $[Ag^+]$ = 0.32 mM, pH 8.1. The corresponding elemental profiles along the white hatched lines in A and B are shown in (C) and (D), respectively. The black ellipse in (D) highlights the reduction and growth of silver at the external surface once the inner volume is completely filled.

The process of Ag^+ reduction and growth on AuNS particles is schematically summarized in Figure 6. The reaction preferentially takes place on the inner walls and proceeds via diffusion through the porous gold nanoshell until the inner volume of the AuNS particles is completely filled with silver. The diffusion of ions to the AuNS interior is believed to be driven by concentration gradient or osmotic pressure as observed in lipid/polymer vesicle systems.[33] Once the inner volume is completely filled with solid silver the reaction proceeds on the outer surface provided that there is an excess of silver ions in the surrounding bath. Thus, the completely filled AuNS particles simply behave in a similar way as other nanoparticle seeds that initiate deposition of elements at the outside surface.[34,35]

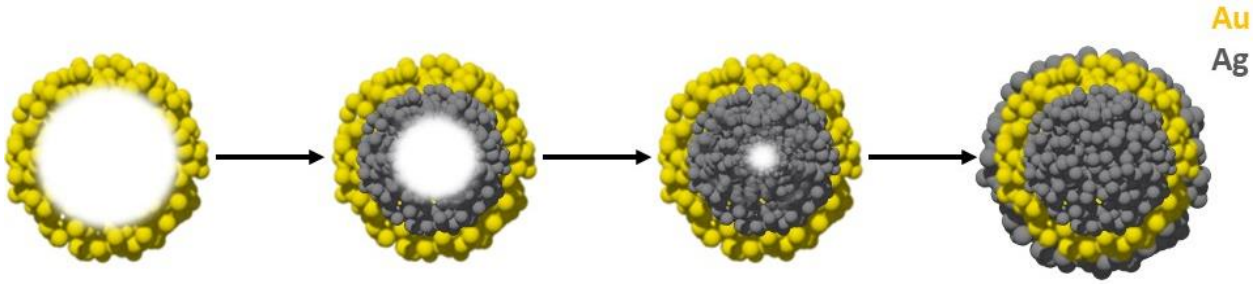

Figure 6. Schematic cartoon illustrating the reduction and growth process of silver on the inner and outer surfaces of porous AuNS particles.

The preference of silver reduction inside AuNS particles is an interesting phenomenon and of significant interest for spatially controlled chemical reactions. In a recent study, Ai *et al.* reported on spatially controlled reduction of Ag^+ at the rim of nanoholes on a periodic Au array.[6] The authors attributed this selective reduction and growth of silver to an electromagnetic field enhancement effect governed by localization of the plasmonic field inside the nanoholes of the array. This phenomenon of localized enhancement of the electric field is well known and has been discussed before for similar plasmonic field-triggered reactions.[36,37] In another study on plasmon-mediated reduction of aqueous platinum ions by Kim *et al.*, they found an additional effect that contributes to the reduction, namely hot charge carriers.[38]

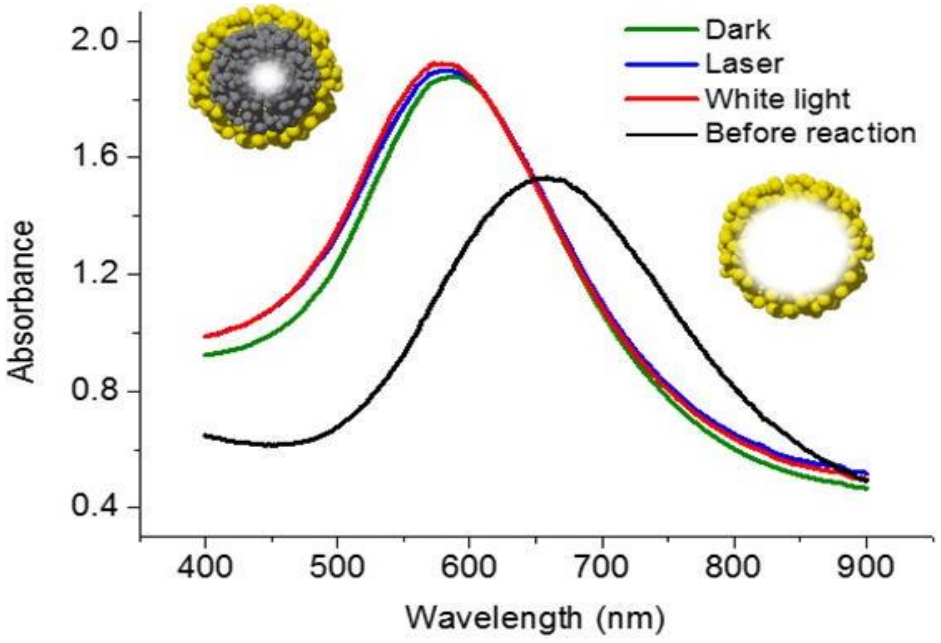

Figure 7. Absorption spectra of AuNS particles before initiation of the reaction by increasing the pH (black), and after reaction at pH 8 in dark environment (green), under white light illumination (red) and laser illumination (blue), respectively.

To further understand the mechanism and the preference of the inner surface of AuNS particles, we investigated the influence of light on the reduction of silver using AuNS particles. Three reactions were performed in parallel: at pH 8.1; under white light illumination, at near resonance using a HeNe laser λ=633 nm, and in the dark. Absorption spectra of the resulting nanoparticles are shown in Figure 7. Surprisingly, no significant differences are observed between the three samples. The reaction undoubtedly occurs in the dark, which clearly suggests that the enhanced plasmonic field inside the particle is not the key driving force for the spatially controlled reduction/deposition process. Thus, the well-established explanation of plasmonic field-guided growth and previous observations on other nanostructures[6,9,36] cannot explain the selective growth of silver on the inner walls of AuNS particles. We tentatively propose that it is due to a nanoconfinement effect initiated by reduction of residual silver ions inside the AuNS particles or in the surrounding solution. Patra *et. al.* also demonstrated that nanoconfinement facilitates the chemical reduction of Ag^+ ion in porous polystyrene beads matrix.[12] It is believed that the nanoconfinement lowers the energy barrier for the electron transfer from reducing agent to Ag^+. Other studies also suggest that the solvents molecules confined in nano space facilitate proton/electron transfer.[15,39]

As is shown before, the interior of AuNS particles makes a perfect nano space for confined chemical reactions. Moreover, the wall of the AuNS particles is porous which allows reactants to freely diffuse in and out from the inner volume. Therefore, in addition to the Ag^+ reduction demonstrated, we believe this AuNS particles should serve as a general nanosized reactor for nanoconfined chemical reactions. Moreover, the understanding of the process of Ag reduction and growth also offers new insights of the complex science and properties of AuNS particles. Interestingly, despite the straightforward synthesis of AuNS particles and decades of widespread applications,[24-26,40] the mechanism behind the AuNS formation is not fully understood.[41] However, Halas *et. al.*[31] and later by Bedzyk *et. al.*[30] have contributed substantially to the understanding of the pore formation and dealloying/fragmentation processes. The study presented herein contributes to the understanding of pH-triggered reduction of silver on the inner walls of AuNS particles that is governed by a continuous supply of Ag^+ ions that diffuse from the external bath into the confined space. Our study also shed light on the subsequent reduction and deposition occurring on the external surface of the AuNS particles once the inner volume is filled with a solid core of silver.

Conclusions

We have demonstrated using a suite of experimental techniques that the reduction of silver ions preferentially occurs on the inner surface of spherical ~40 nm AuNS particles. The reaction is facilitated by a continuous supply of silver ions that diffuse through the porous AuNS particles into the inner volume where they are rapidly reduced and subsequently deposited on the inner wall. We attribute the preferential growth inside the AuNS particles to a nanoconfinement effect rather that of a plasmonic field enhancement effect as the reaction is not influenced by illumination with white light and with a laser beam at near resonance. The finding obtained herein is expected to contribute to a fundamental understanding of spatially controlled reactions at the nanoscale, and potentially also to the development of novel smart nanoscale materials for photonic, catalytic and sensor applications.

Experimental Section

Materials

Sodium citrate tribasic dehydrate (99%), gold (III) chloride trihydrate (99.9%), silver nitrate (99%), Hydrochloric acid (37%), Sodium borohydride (98%), Hydroxylamine hydrochloride (98.0%), sodium hydroxide and nitric acid were purchased from Sigma Aldrich, Singapore. All glassware used was cleaned in a bath of freshly prepared aqua regia solution, and then rinsed thoroughly with Milli-Q water before use.

Synthesis of gold nanoshell

The AuNS particles were synthesized via a template method, where the AgNPs served as template modified from previous procedures.[42] In a typical synthesis, AgNPs were first synthesized by reducing $AgNO_3$. 50 µL sodium citrate solution (1 M, 50 µL) was added to $AgNO_3$ (0.2 mM, 50 mL) at 60 °C. After 5 minutes, $NaBH_4$ (100 mM, 1 mL) was injected into the solution. The solution was stirred for 2 hours at 60°C and allowed to cool down to room temperature. Galvanic replacement of Ag by Au occurs at room temperature. A 200 mM $NH_2OH{\cdot}HCl$ solution (1 mL) was added to as prepared AgNPs (47 mL) followed by $AgNO_3$ (0.1 M, 141 µL) 5 min later to minimize the formation of AuNPs.[40] The solution was kept for 2 hours to allow for the reaction to complete. At 60 °C, $HAuCl_4$ (25 mM, 713 µL) was added dropwise to the solution under magnetic stirring at 500 rpm. The reactions were stopped after 2 hours by lowering the temperature to 25 °C.

Reduction of silver in gold nanoshell: 4 samples

The reduction of Ag^+ was initiated by increasing the pH of AuNS suspension. In a first time, the pH of suspension was adjusted with NaOH (0.1 M) from pH 3.8 (initial pH) to pH 8.1. In a second set of experiments a silver nitrate solution was added dropwise to final concentration of 0.16 mM and 0.32 mM, respectively. After reaching the final concentration we adjusted the pH of the AuNS suspension to 8.1 by adding NaOH (0.1 M) under magnetic stirring at 500 rpm. AuNS suspensions were kept in amber glassware and stored in the refrigerator at 4°C.

Reaction in the dark and with laser and white light

The reactions in the dark were performed using Eppendorf tubes wrapped in aluminum foil. The dark control was left to stand in a dark room, while the experiments done under white light and laser control were conducted by illuminating the tubes with white LED light and with a 633 nm HeNe laser with an output power of 20 mW, respectively.

Characterization: UV-Vis, DLS, Zeta potential, TEM, and STEM coupled with X-EDS for elemental mapping

The UV-Vis absorption spectra of all the samples are measured using Lambda 35 (Perkin Elmer) or Cary 50 (Varian) spectrophotometer. Dynamic light scattering (DLS), and zeta potential (ELS) measurements were performed using Litesizer™ 500 apparatus (Anton Paar) equipped with a 658 nm laser operating at 40 mW. The backscattered light collection angle was set at 90°. The zeta potential cuvette has a Ω-shaped capillary tube cuvette with an applied potential of 150 V. The same suspensions were used for DLS and ELS measurements. Each sample was analyzed in triplicate and each measurement was an average of three 30 s runs. Transmission Electron Microscopy (TEM) micrographs were obtained using a JEOL JEM-2100 plus LaB6 (JEOL, Japan) microscope with an acceleration voltage of 200 kV equipped with an Orius 4 K CDD camera (Gatan; USA). STEM mode coupled with X-ray Energy-Dispersive Spectroscopy (X-EDS) was used to perform elemental mapping of the two metals (lines: Au-L and Ag-L). X-EDS analysis was realized with an Oxford Instrument SDD detector of 80 mm^2 area. X-ray spectra were recorded and processed with Aztec software. The samples were prepared by dropping a dilute suspension onto the carbon-coated copper grids and dried at room temperature before imagining. Size distribution was established by counting a minimum of 400 particles for TEM and was determined using ImageJ Software.

ASSOCIATED CONTENT

Supporting Information. Reversible study of pH effect on the silver deposition, DLS, zeta potential characterization of AuNS, X-EDS measurement of the composition of AuNS. This material is available free of charge via the Internet at http://pubs.acs.org.

AUTHOR INFORMATION

Corresponding Authors

Souhir Boujday, Email: souhir.boujday@sorbonne-universite.fr, Bo Liedberg, Email: bliedberg@ntu.edu.sg

Author Contributions

The manuscript was written through contributions of all authors. All authors have given approval to the final version of the manuscript. ‡These authors contributed equally.

ACKNOWLEDGMENT

We would like to thank the French-Singaporean PHC Merlion program (grant 5.03.15) for financial support and the ANR-FWF program (grant ANR-15-CE29-0026). C.P. and B.L. also acknowledge support from the Institute for Nanomedicine jointly established between Northwestern University and Nanyang Technological University.

REFERENCES

(1) Assion, A.; Baumert, T.; Bergt, M.; Brixner, T.; Kiefer, B.; Seyfried, V.; Strehle, M.; Gerber, G. *Science* **1998**, *282*, 919.

(2) Wang, L.; Nemoto, Y.; Yamauchi, Y. *J. Am. Chem. Soc.* **2011**, *133*, 9674.

(3) Lv, W.; Lee, K. J.; Li, J.; Park, T.-H.; Hwang, S.; Hart, A. J.; Zhang, F.; Lahann, J. *Small* **2012**, *8*, 3116.

(4) Gu, P.; Zhang, W.; Zhang, G. *Adv. Mater. Interfaces* **2018**, doi:10.1002/admi.201800648.

(5) Wang, Z.; Ai, B.; Möhwald, H.; Zhang, G. *Adv. Opt. Mater.* **2018**, doi:10.1002/adom.201800402.

(6) Ai, B.; Wang, Z.; Möhwald, H.; Zhang, G. *ACS nano* **2017**, *11*, 12094.

(7) Maillard, M.; Huang, P.; Brus, L. *Nano Lett.* **2003**, *3*, 1611.

(8) Kim, N. H.; Meinhart, C. D.; Moskovits, M. *J. Phys. Chem. C* **2016**, *120*, 6750.

(9) Ueno, K.; Juodkazis, S.; Shibuya, T.; Yokota, Y.; Mizeikis, V.; Sasaki, K.; Misawa, H. *J. Am. Chem. Soc.* **2008**, *130*, 6928.

(10) Polak, M.; Rubinovich, L. *Nano Lett.* **2008**, *8*, 3543.

(11) Vaida, V. *Proc. Nat. Acad. Sci.* **2017**, *114*, 12359.

(12) Patra, S.; Pandey, A. K.; Sen, D.; Ramagiri, S. V.; Bellare, J. R.; Mazumder, S.; Goswami, A. *Langmuir* **2014**, *30*, 2460.

(13) Patra, S.; Pandey, A. K.; Sarkar, S. K.; Goswami, A. *RSC Adv.* **2014**, *4*, 33366.

(14) Rubinovich, L.; Polak, M. *Nano Lett.* **2013**, *13*, 2247.

(15) Muñoz-Santiburcio, D.; Marx, D. *Chem. Sci.* **2017**, *8*, 3444.

(16) Ramaswamy, R.; González-Segredo, N.; Sbalzarini, I. F.; Grima, R. *Nature commun.* **2012**, *3*, 779.

(17) Banerjee, S.; Gnanamani, E.; Yan, X.; Zare, R. N. *Analyst* **2017**, *142*, 1399.

(18) Yan, X.; Bain, R. M.; Cooks, R. G. *Angew. Chem. Inter. Ed.* **2016**, *55*, 12960.

(19) Fallah-Araghi, A.; Meguellati, K.; Baret, J.-C.; El Harrak, A.; Mangeat, T.; Karplus, M.; Ladame, S.; Marques, C. M.; Griffiths, A. D. *Phys. Rev. Lett.* **2014**, *112*, 028301.

(20) Wiebenga-Sanford, B. P.; DiVerdi, J.; Rithner, C. D.; Levinger, N. E. *J. Phys. Chem. Lett.* **2016**, *7*, 4597.

(21) Griffith, E. C.; Vaida, V. *Proc. Nat. Acad. Sci.* **2012**.

(22) Koo, J. H.; Kumar, A.; Lee, S.; Jin, X.; Jeong, H.; Kim, J.; Lee, I. S. *Chem. Mater.* **2018**, *30*, 3010.

(23) Kim, D.; Choi, J. K.; Kim, S. M.; Hwang, I.; Koo, J.; Choi, S.; Cho, S. H.; Kim, K.; Lee, I. S. *ACS Appl. Mater. Interfaces* **2017**, *9*, 29992.

(24) Sun, Y.; Xia, Y. *Anal. Chem.* **2002**, *74*, 5297.

(25) Lu, W.; Melancon, M. P.; Xiong, C.; Huang, Q.; Elliott, A.; Song, S.; Zhang, R.; Flores, L. G.; Gelovani, J. G.; Wang, L. V.; Ku, G.; Stafford, R. J.; Li, C. *Cancer Res.* **2011**, *71*, 6116.

(26) You, J.; Zhang, G.; Li, C. *ACS Nano* **2010**, *4*, 1033.

(27) Moon, G. D.; Choi, S.-W.; Cai, X.; Li, W.; Cho, E. C.; Jeong, U.; Wang, L. V.; Xia, Y. *J. Am. Chem. Soc.* **2011**, *133*, 4762.

(28) Sun, Y.; Mayers, B. T.; Xia, Y. *Nano Lett.* **2002**, *2*, 481.

(29) Sun, Y.; Xia, Y. *Nano Lett.* **2003**, *3*, 1569.

(30) Moreau, L. M.; Schurman, C. A.; Kewalramani, S.; Shahjamali, M. M.; Mirkin, C. A.; Bedzyk, M. J. *J. Am. Chem. Soc.* **2017**, *139*, 12291.

(31) Goodman, A. M.; Cao, Y.; Urban, C.; Neumann, O.; Ayala-Orozco, C.; Knight, M. W.; Joshi, A.; Nordlander, P.; Halas, N. J. *ACS Nano* **2014**, *8*, 3222.

(32) Dong, X.; Ji, X.; Wu, H.; Zhao, L.; Li, J.; Yang, W. *J. Phys. Chem. C* **2009**, *113*, 6573.

(33) Oglęcka, K.; Rangamani, P.; Liedberg, B.; Kraut, R. S.; Parikh, A. N. *Elife* **2014**, *3*, e03695.

(34) Shahjamali, M. M.; Bosman, M.; Cao, S.; Huang, X.; Saadat, S.; Martinsson, E.; Aili, D.; Tay, Y. Y.; Liedberg, B.; Loo, S. C. J.; Zhang, H.; Boey, F.; Xue, C. *Adv. Func. Mater.* **2012**, *22*, 849.

(35) Rodríguez-Lorenzo, L.; De La Rica, R.; Álvarez-Puebla, R. A.; Liz-Marzán, L. M.; Stevens, M. M. *Nature mater.* **2012**, *11*, 604.

(36) Nguyen, V.-Q.; Ai, Y.; Martin, P.; Lacroix, J.-C. *ACS Omega* **2017**, *2*, 1947.

(37) Violi, I. L.; Gargiulo, J.; von Bilderling, C.; Cortés, E.; Stefani, F. D. *Nano Lett.* **2016**, *16*, 6529.

(38) Kim, N. H.; Meinhart, C. D.; Moskovits, M. *J.Phys. Chem. C* **2016**, *120*, 6750.

(39) Li, S.; Thompson, W. H. *J. Phys. Chem. B* **2005**, *109*, 4941.

(40) Ma, Y.; Liang, X.; Tong, S.; Bao, G.; Ren, Q.; Dai, Z. *Adv. Func. Mater.* **2013**, *23*, 815.

(41) Chee, S. W.; Tan, S. F.; Baraissov, Z.; Bosman, M.; Mirsaidov, U. *Nature Commun.* **2017**, *8*, 1224.

(42) Chen, P.; Liu, X.; Goyal, G.; Tran, N. T.; Shing Ho, J. C.; Wang, Y.; Aili, D.; Liedberg, B. *Anal. Chem.* **2018**, *90*, 4916.

TOC Figures Only

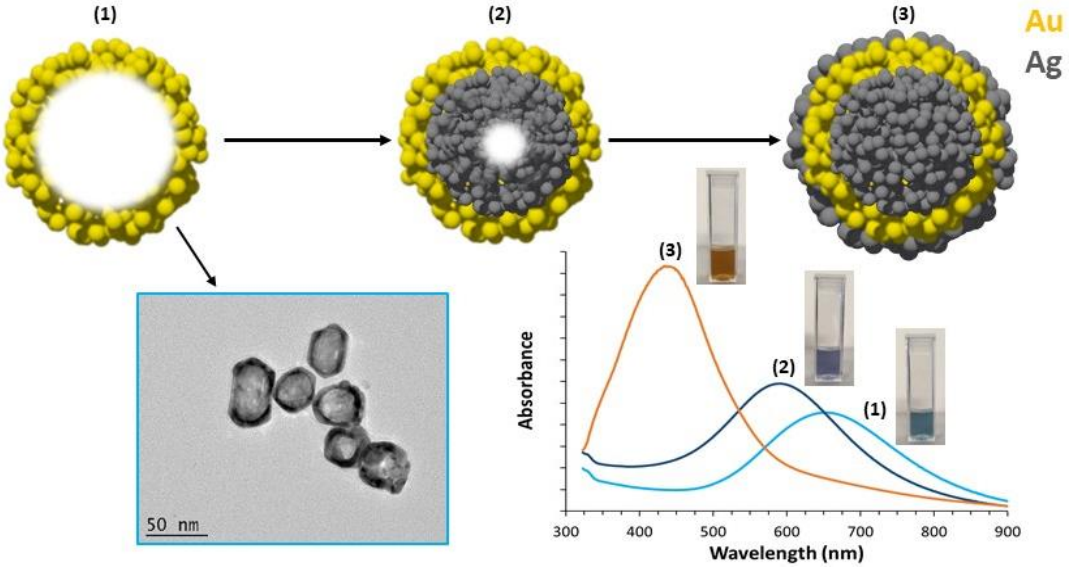

Supporting information for

Spatially Controlled Reduction and Growth of Silver in Hollow Gold Nanoshell Particles

Lu Zhang[1,2,3‡], Peng Chen[1‡], Alexis Loiseau[2], Dalil Brouri[2], Sandra Casale[2], Michèle Salmain[4], Souhir Boujday[2,], Bo Liedberg[1,*]*

[1]Centre for Biomimetic Sensor Science, School of Material Science and Engineering, Nanyang Technological University, Singapore 637553.

[2]Sorbonne Université, CNRS, Laboratoire de Réactivité de Surface (LRS), 4 place Jussieu, F-75005 Paris, France.

[3]Sorbonne University-Nanyang Technological University Dual Degree PhD Programme.

[4]Sorbonne Université, CNRS, Institut Parisien de Chimie Moléculaire (IPCM), 4 place Jussieu F-75005 Paris, France.

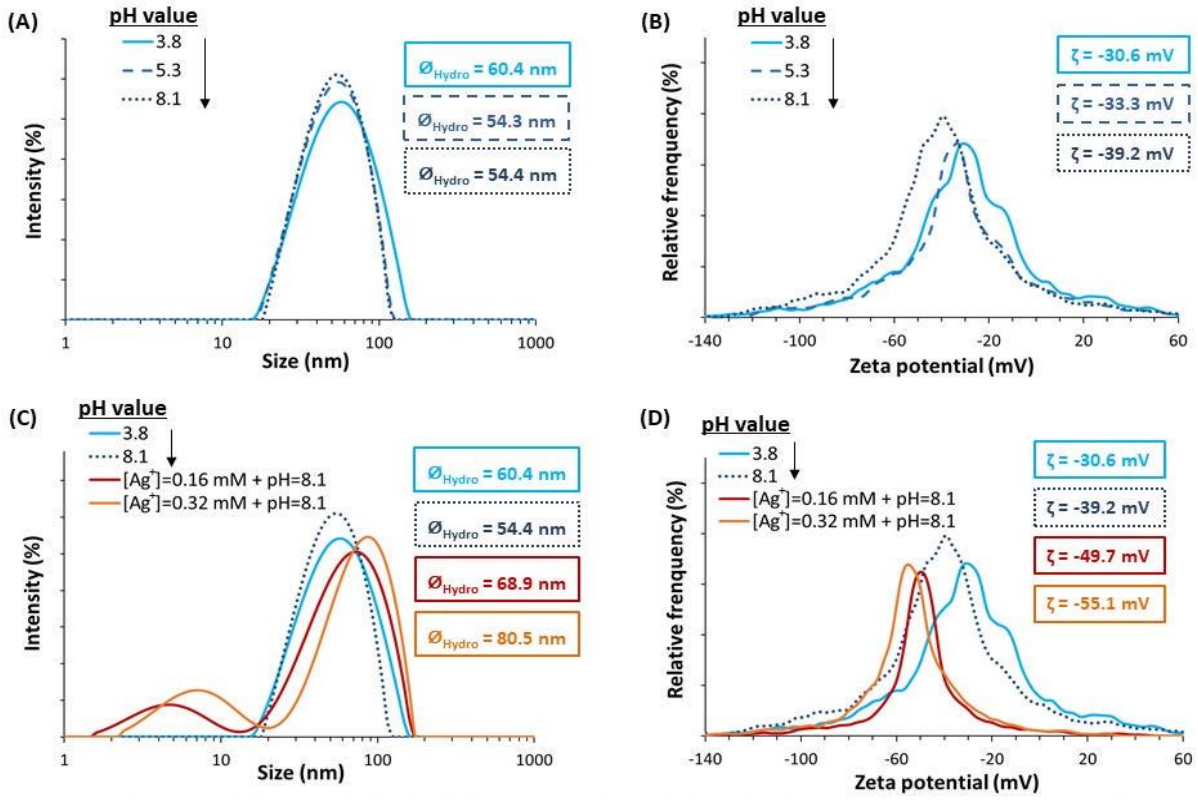

Figure S1. (A) Dynamic light scattering (DLS), and (B) zeta potential (ELS) measurements at different pH: pH 3.8, pH 5.3 and pH 8.1. (C) Dynamic light scattering (DLS), and (D) zeta potential (ELS) measurements at pH 8.1 after adding the silver nitrate ($[Ag^+]$ = 0.16 mM and $[Ag^+]$ = 0.32 mM) in suspension at pH 3.8.

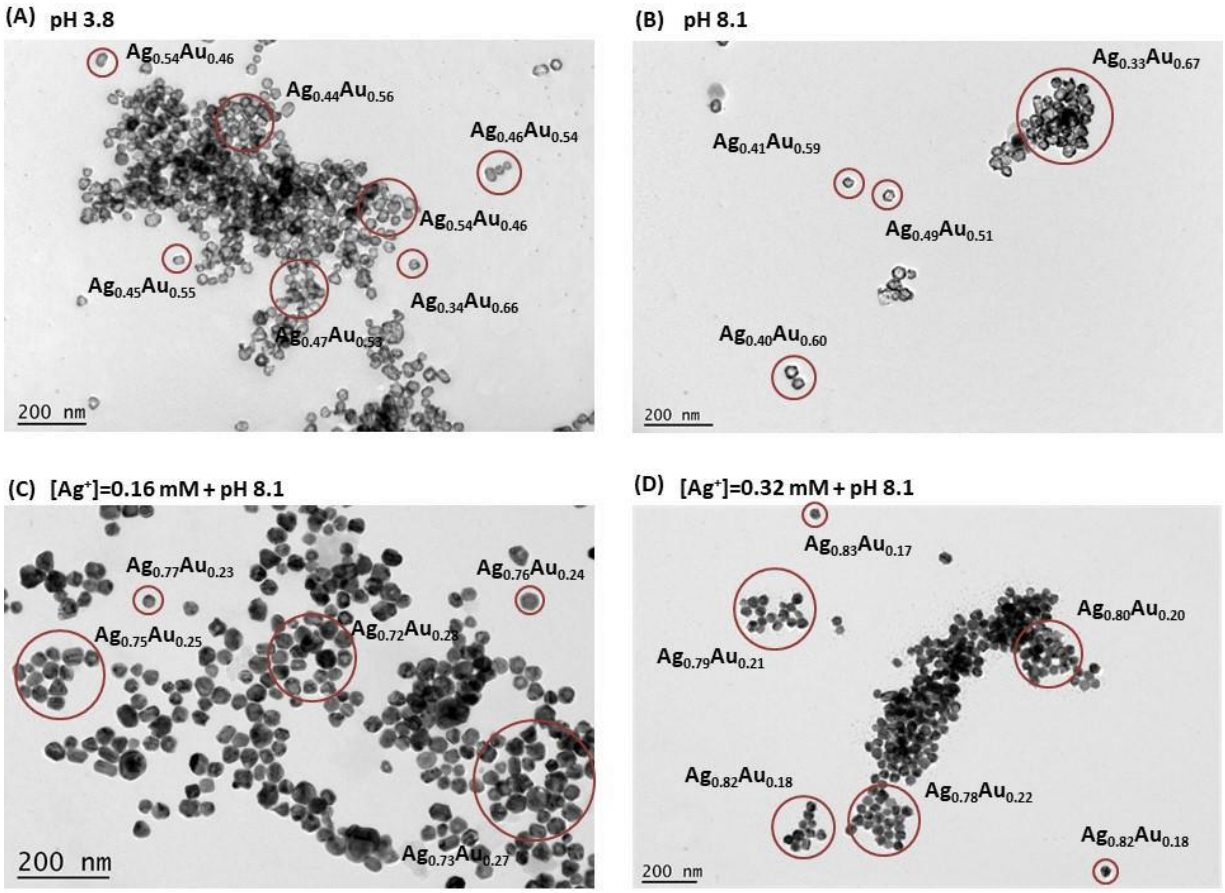

Figure S2. TEM micrographs with X-ray Energy-Dispersive Spectroscopy (X-EDS) analysis at (A) pH 3.8, (B) pH 8.1 and (C-D) after adding the silver nitrate ($[Ag^+]$ = 0.16 mM and $[Ag^+]$ = 0.32 mM, respectively) in suspension at pH 3.8 and then, raising the pH until pH 8.1.

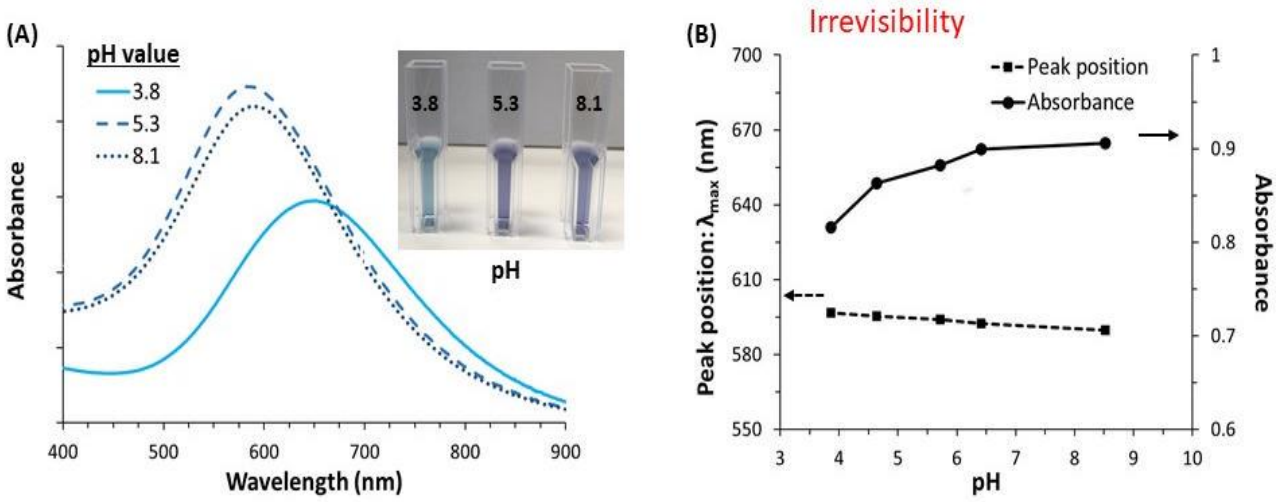

Figure S3. (A) Absorbance spectra of AuNS at pH 3.8, pH 5.3 and pH 8.1 realized 24 h after adjusting the pH of the suspension with NaOH (0.1 M) from pH 3.8 to pH 8.1. (B) Peak position and intensity by decreasing the pH from 8.5 to 3.8. The pH suspension was adjusted with HNO_3 (0.1 M). The kinetics of reaction at ~pH 5 was slower than that of at pH 8, but eventually ended up at the same state, see the dotted and dashed spectra in Figure S3A.

Irreversibility test:

The pH of suspension was firstly adjusted with NaOH (0.1 M) from pH 3.8 (initial pH) to pH 8.5. In the following, the pH of suspension was decreased stepwise by adding HNO_3 (0.1 M) until the pH reaches the initial value, 3.8. UV-Vis spectra of suspension were acquired at certain pH points while decreasing the pH. The peak position remains essentially the same upon lowering the pH indicating the irreversibility. The absorbance changes slightly with decreasing pH, but it never reaches the initial level of absorbance.

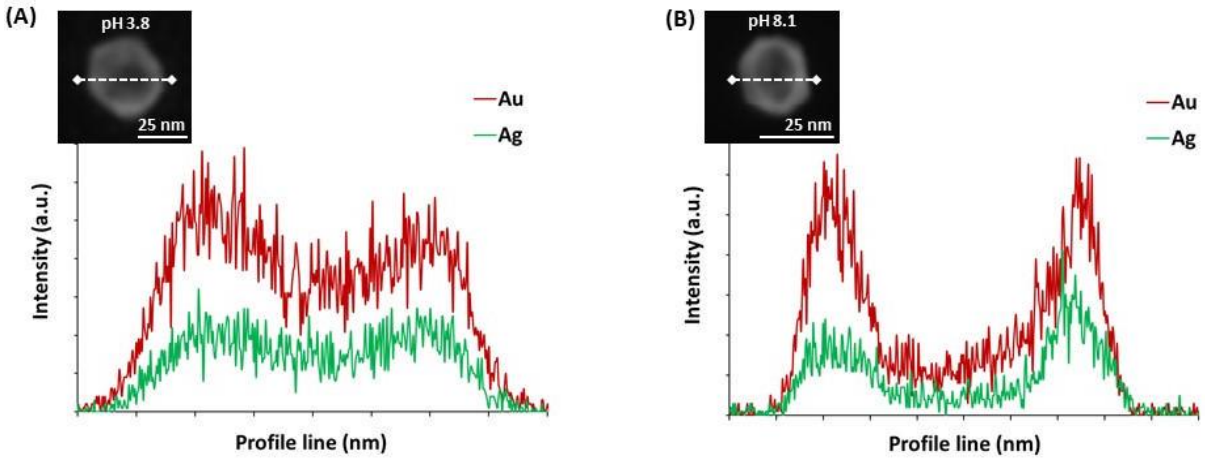

Figure S4. STEM micrographs and profiles (Ag, Au) of AuNS particles corresponding to Figure 3 at two different pH (dashed white line corresponds to the profile line): (A) pH 3.8 and (B) pH 8.1.

Paper V

Core-shell Gold Silver Nanoparticles for Plasmonic Biosensing of Toxins: Towards Naked-eye Detection

Preface

The position of LSPR band on plasmonic nanoparticles is also extremely sensitive to small changes of the refractive index at the proximity of the nanoparticles. The unique feature was exploited to try and build up a homogeneous, one-step biosensor to detect SEA in solution down to very low levels by the naked-eye.

The LSPR band of 13-nm diameter gold nanoparticles (AuNPs) that we have used in papers II and III is located in the green region of the visible spectrum. (Figure V-A) While the distribution of colors in the visible spectrum is not uniform, a sharp color transition is located at 500 nm between cyan and green. If the starting position of the LSPR band is located in the cyan region, even a small red-shift could make the color transit from cyan to green and be visualized by the naked-eye. In this paper, we aimed at synthesizing nanoparticles with starting LSPR band located at around 500 nm to further apply them as a transducer. Starting from the highly monodispersed AuNPs, a silver shell was grown on AuNP to provide core-shell gold silver nanoparticles (Au@AgNPs). (Figure V-B) By controlling the thickness of the silver shell, the LSPR band blue-shifted to ~500 nm, and the colloidal solution color changed from red to orange. (Figure V-C) Subsequent functionalization of the Au@AgNPs with anti-SEA antibody (Ab) led to a red-shift of 14 nm, together with a color change from orange to dark red. (Figure V-D and E) Yet, the red-shift of LSPR band was important upon addition of SEA and no color change detectable by naked-eye was observed. For further detection of the SEA by naked-eye, the LSPR band of bioconjugates should remain in the cyan region. Thus, smaller biorecognition elements (for example, Ab fragments) could be used for preparation of bioconjugates. Alternatively, nanoparticles with LSPR band much lower than 500 nm should be synthesized taking advantage of our finding described in paper IV.

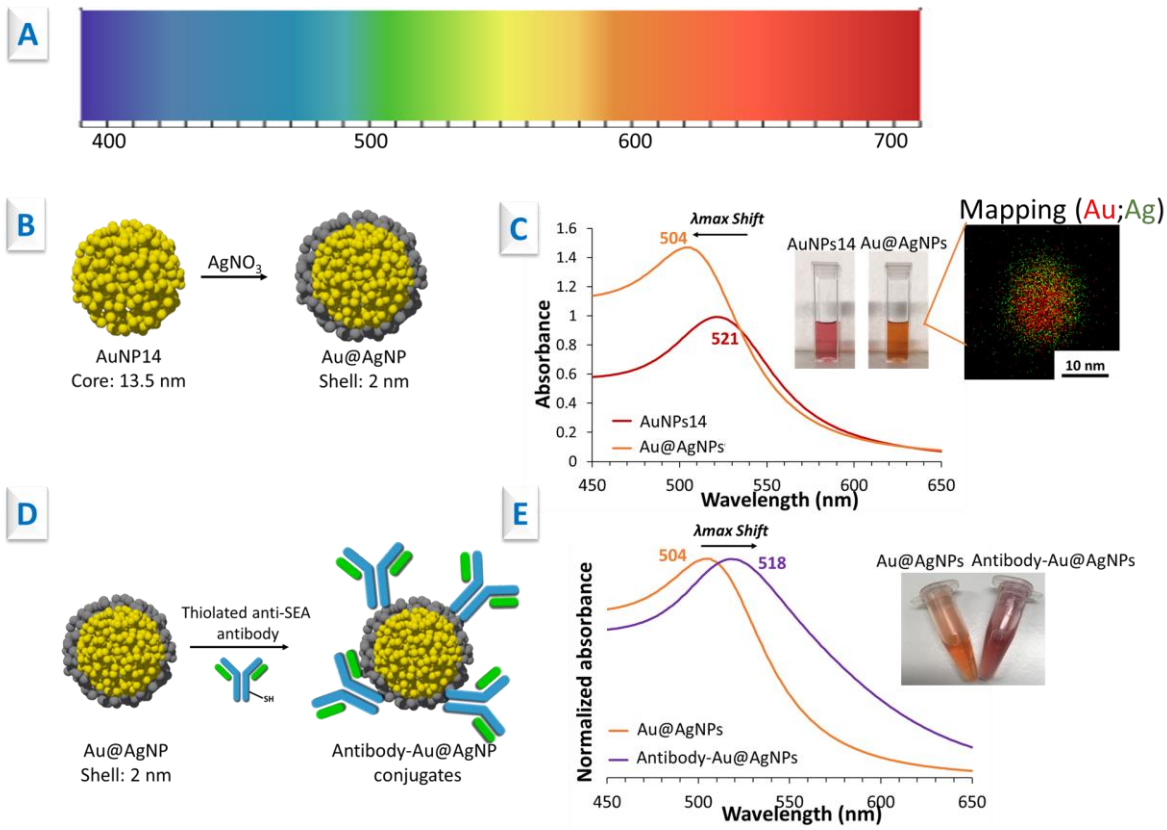

Figure V: A. Visible spectra. B: Schematic illustration of the synthesis of core-shell gold-silver nanoparticles (Au@AgNPs). C: UV-Vis spectra of pure AuNPs and Au@AgNPs, inset: colloidal solutions and elemental mapping of Au@AgNPs. D: Schematic illustration of Au@AgNP-antibody conjugation. E: UV-Vis spectra of antibody-Au@AgNP, inset: photos of the colloidal solutions before and after antibody chemisorption.

Core-shell Gold Silver Nanoparticles for Plasmonic Biosensing of Toxins: Towards Naked-eye Detection

Lu Zhang[1,2,3,4], Alexis Loiseau[2], David Hu[2], Michèle Salmain[2], Bo Liedberg[3,], Souhir Boujday[1,*]*

[1] Sorbonne Université, CNRS, Laboratoire de Réactivité de Surface (LRS), 4 place Jussieu, F-75005 Paris, France.

[2]Sorbonne Université, CNRS, Institut Parisien de Chimie Moléculaire (IPCM), 4 place Jussieu F-75005 Paris, France.

[3]Centre for Biomimetic Sensor Science, School of Materials Science and Engineering, Nanyang Technological University, Singapore 637553.

[4] Sorbonne University and Nanyang Technological University Dual Degree PhD Programme.

KEYWORDS: Plasmonic nanoparticles, Gold-silver core-shell; Toxin detection, Biosensors.

Introduction

Plasmonic metal nanoparticles (NPs) have shown a great potential for chemical and biological sensor applications over the past decades [1-5]. This is mainly due to their unique optical properties originating from localized surface plasmon resonance (LSPR) phenomenon, which is responsible for the colors of the NPs suspensions [6-8]. These nano-objects lead to dramatic improvements in the performance and sensitivity of biosensing devices due to their strong scattering or absorption and their sensitive spectral response to the local environment of the nanoparticle surface. Indeed, the position of the LSPR band can be correlated to the changes in chemical and/or physical environment of the NPs' surface [9, 10]. Thus, the refractive index (RI) changes of the surroundings play an important role on the spectral response of the LSPR absorption band to achieve a better sensitivity [4, 7, 11, 12]. The LSPR absorption band also depends on other key parameters such as size, uniformity, shape, dispersion, and material composition [4, 10, 12-16].

Among all NPs, plasmonic gold and silver NPs (AuNPs and AgNPs, respectively) have attracted great attention for biosensing platform development due to their extremely strong extinction coefficient in the visible spectral range [4, 9, 17-20]. Spherical AuNPs and AgNPs have LSPR absorption band in red and blue regions, respectively [21, 22], which can be tuned depending on the size and shape [23, 24]. For small spherical AuNPs (of an average diameter of 10 nm), the absorption band of the red-colored NPs suspensions is around 520 nm, while for spherical AgNPs with the same average diameter, the absorption band is around 395 nm, making the suspension yellow-colored [20, 25, 26]. Even if AuNPs remain the most studied system for biosensors because of their excellent chemical stability and biocompatibility [27, 28], AgNPs offer better improved extinction and sensitivity than AuNPs for a given size and shape [10, 26]. Besides, a study showed that the optical response (LPSR shift), due to aggregation in presence of avidin for the same biocytin-coated metallic spherical NPs, was more pronounced for AgNPs than for AuNPs with an equivalent concentration of avidin [26]. However, AgNPs might have a toxic effect in biological systems. They are also less stable under identical chemical conditions and barely reusable, which makes their use in repeated cycles more difficult than AuNPs [30-32]. Hence, Ag-coated NPs constitute an attractive avenue to overcome these disadvantages.

Since their pioneered preparation by Morriss and Collins [33], Au-Ag core-shell nanoparticles (Au@AgNPs) received a great interest for plasmonic applications [17, 18, 34]. Combining these two noble metals in core-shell entities offers the possibility to tune the LSPR band by changing both the size of the core and the thickness of the shell. Au@AgNPs are easy to prepare and offer better size distribution [35] as well as an enhanced refractive index (RI) sensitivity and stability in biological media compared to AgNP-based sensors [32]. To date, very few studies have investigated the Au@AgNPs for plasmonic biosensing. Examples on the couple streptavidin/biotin as a model of optical biosensor were described [36, 37]. Other examples sulfide detection [38], and antibiotics SERS aptasensing [39] and, more recently, colorimetric detection of illicit drugs was described [40]. However, to the best of our knowledge, Au-Ag core-shell plasmonic NPs have never been used for immunosensing nor for toxin detection.

Since several years, our group is especially interested in staphylococcal enterotoxin A (SEA). SEA is the most commonly encountered biotoxin involved in staphylococcal food poisoning outbreaks [41] by inducing severe gastroenteritis when ingested, and being fatal to humans even when consumed cooked food [20, 42-45]. Therefore, control of food safety is necessary to prevent food poisoning outbreaks with quick, specific, and sensitive analytical methods to detect and quantify these biotoxins. SEA is a small monomeric protein (Mw = 28 kDa) with high thermal and proteolytic stability [46]. In previous works, we mastered the engineering of stable antibody-AuNPs bioconjugates by covalent attachment of anti-SEA antibody to the metallic nanoparticles [20, 45, 47, 48]. In the one-step, this strategy was based on a direct assay strategy, in which bioconjugated AuNPs resulted in a significant red shift of LSPR band induced by the immunological response between anti-SEA antibody immobilized on NPs and SEA [20].

In this study, the high extinction coefficient of these Au@AgNPs in the visible spectral range prompted the development of immunoassays to visually detect SEA. Moreover, a robust immobilization/conjugation of bioreceptors to Au@AgNPs is required.

The aim of this work was to engineer antibody-conjugated Au@AgNPs and evaluate their potential as well as their efficacy for SEA immunosensing that could be easily visualized by naked-eye. Au@AgNPs were prepared with a gold core with 14 nm in diameter and a uniform silver shell with a thickness of 2 nm. After modifying anti-SEA antibody (anti-SEA) by Traut's reagent to generate thiol groups from some of their primary amine groups and provide stable NPs-protein bioconjugates [49], thiolated anti-SEA antibody was chemisorbed by covalent

attachment through sulfur-Au@AgNPs bonds to recognize the target SEA. The same work was realized using anti-SEA antibody-conjugated NPs based on spherical AuNPs with a similar size to Au@AgNPs (16 nm) for benchmarking purposes and as a proof of concept. In this report, each step was analyzed by exhaustive characterization techniques such as transmission electron microscopy (TEM and STEM), UV-Vis spectroscopy, dynamic light scattering (DLS), and zeta potential (ELS) measurements.

Experimental section

Material

Hydrogen tetrachloroaurate(III) trihydrate ($HAuCl_4.3H_2O$; ≥ 99.99%) was purchased from Alfa Aesar. Sodium citrate dihydrate ($Na_3C_6H_5O_7.2H_2O$; ≥ 99%), tannic acid ($C_{76}H_{52}O_{46}$), bovine serum albumin (BSA), 2-iminothiolane hydrochloride (Traut's reagent: $C_4H_7NS.HCl$; ≥ 98%) and staphylococcal enterotoxin A (SEA) were purchased from Sigma-Aldrich. Silver nitrate ($AgNO_3$; ≥ 99%) was purchased from Honeywell, Fluka. Affinity-purified rabbit polyclonal anti-SEA antibody (anti-SEA, reference in toxin technology catalog: LAI101) was purchased from Toxin Technology (Sarasota, FL, www.toxintechnology.com).

Nanoparticle preparation

Spherical gold nanoparticles (AuNPs) synthesis

Colloidal AuNPs with 2 different sizes were synthesized according to the citrate/tannic acid reduction method adapted from [50] and optimized in [45].

For particles with an average size of 13.5 nm (AuNPs14), 100 mL of citrate-coated AuNPs were prepared from two stock solutions: A solution A ($HAuCl_4.3H_2O$, 1.16 mL; 1% [w/v]) and Milli-Q water (78.84 mL)); and a solution B (sodium citrate (4 mL; 1.14%), tannic acid (TA) (0.025 mL; 1%) and Milli-Q water (16 mL)). The TA concentration was the only parameter in this synthesis, making it possible to modulate the nanoparticle size (Figure S1) [50, 51] Solutions A and B were heated to 60 °C under reflux and stirring then mixed. The molar ratio between gold ions and citrate was [1:6.1], respectively. The mixture was then heated up to 90 °C for a few minutes to form spherical AuNPs. When the color turned ruby-red, a portion of the sample suspension was heated up to boiling for 30 min under reflux and stirring to increase the colloidal stability after which the suspension was cooled on ice bath. The other portion was

used to form gold-silver core-shell NPs and is described later. Finally, gold suspension was kept in amber glassware, stored in the refrigerator at 4 °C and used within a month.

15.5 nm diameter colloid suspension (AuNPs16) was prepared similarly by changing the solution B accordingly: sodium citrate (4 mL; 1.14%), TA (13.75 µL; 1%) and Milli-Q water (16 mL). Solutions A and B were heated to 60 °C under reflux and stirring then mixed. The mixture was then heated up to 90 °C for few minutes. When the color turned ruby-red, suspension was heated up to boiling for 30 min under reflux and stirring and then cooled on ice bath. Colloidal suspension was kept in amber glassware, stored in the refrigerator at 4 °C and used within a month.

Deposition of silver shell on gold NPs (Au@AgNPs): gold-silver core-shell NPs

The silver nitrate stock solution (10 mM) was freshly prepared by dissolving $AgNO_3$ crystals in Milli-Q water. A volume of $AgNO_3$ stock solution (0.258 mL) were added to the other part of AuNPs14 suspension at 90 C after the color change, under reflux and stirring, followed by the rapid addition of the reducing solution (sodium citrate 1%; 0.454 mL). The molar ratio between Ag^+ and citrate was also [1:6.1], respectively. These volumes of silver nitrate and sodium citrate stock solutions were determined by estimating a silver shell with uniform thickness of 2 nm and assuming that the average size of gold core was 13.5 nm. The details of the equations are given in supporting information (equation S2 and S3). After addition, suspension was heated up to boiling for 1 h under reflux and stirring and then cooled on ice bath. The color became orange during reaction. Finally, Au@AgNPs suspension was kept in amber glassware, stored in the refrigerator at 4 °C and used within a month.

Engineering of antibody-conjugated nanoparticles

Thiolation of anti-SEA antibody

A covalent approach was used to engineer antibody-conjugated nanoparticles by antibody (Ab) thiolation [49, 52]. Traut's reagent (7.3 mM) was reacted with anti-SEA antibody (1 mg/mL; 3.5 µM) in 50 mM phosphate buffer pH 8.0 at room temperature (RT) to generate sulfhydryl groups [53]. After 1 h of incubation, the thiolated antibodies were separated from excess Traut's reagent by purification on Dextran desalting 10 mL gel filtration column (Hitrap desalt 10 mL, GE Healthcare) using phosphate buffer (pH 7.4) as eluent.

Biofunctionalization of nanoparticles by thiolated antibodies

Thiolated Ab solution (218 nM; 1 mL) was mixed with AuNPs16 (3.3 nM; 3 mL) or Au@AgNPs suspensions (6.3 nM, 3 mL) during 30 min at RT. Then, BSA (0.25% [w/v]) was added to the bioconjugate suspension to block non-specific binding sites [20, 54]. Finally, the biofunctionalized NPs were concentrated by centrifugation at 10,300 g for 40 min and washed twice to remove excess weakly bound and free ab. Finally, NPs were resuspended in phosphate buffer (pH 7.4) with BSA (0.25% [w/v]).

Antibody assay by ELISA

After the first centrifugation, the supernatants were collected and antibody concentration was assessed by ELISA to estimate the Ab/AuNP ratio. The calculations are detailed in the supporting information section (equation S4).

SEA (1 µg/mL in 0.1 M carbonate buffer, pH 9, 100 µL) was pipetted into each well of a flat-bottomed polystyrene 96-well plate (Greiner bio-one) and incubated overnight at 4°C. The content was discarded and non-specific sites were blocked by PBS-0.1% BSA (100 µL) for 1 h at room temperature. Wells were washed 3 times with PBS-0.05% Tween 20. Standard solutions of anti-SEA antibody or diluted supernatants (100 µL) to be quantified were dispensed into the wells. The plate was incubated 2 h at room temperature. After washing with PBS-0.05% Tween 20 (3x100 µL), HRP-labelled goat anti-rabbit IgG conjugate (1/4000, 100 µL) was added to each well and incubated 1 h at room temperature. After washing with PBS-0.05% Tween 20, a mixture of o-phenylenediamine dihydrochloride (OPD) and H_2O_2 (7 mg OPD + 4 µL H_2O_2 in 10 mL of citrate-phosphate buffer, pH 5, 100 µL) substrate solution was added to each well. After the color developed, H_2SO_4 (2.5 M, 50 µL) was added to each well to stop the enzymatic reaction. After 10 min in the dark, the absorbance of each well was read at 485 nm and 415 nm as reference with a microplate reader (Fluostar Optima, BMG Labtech). The concentration of antibody in diluted supernatants was deduced from the calibration curve established by plotting ΔAbs (A_{485}-Abs_{415}) vs. antibody concentration (Figure S2).

The resulting value was multiplied by the dilution factor (x100) to determine the actual concentration of Ab in the supernatants *i.e.* 19.7 µg/mL for AuNPs16 and 17.7 µg/mL for Au@AgNPs.

SEA immunosensing

Aliquots of SEA solution were serially added to the antibody-conjugated nanoparticles suspensions (400 μL) in a plastic cuvette to have successively SEA concentrations: 50, 100, 200, and 500 ng/mL. Absorption spectra of the mixtures were measured every 5 min with a Cary 50 spectrophotometer (Varian, Inc.) until equilibrium was reached (~ 60 min).

Techniques

UV-Vis spectroscopy

UV-Vis spectra of different suspensions were recorded in a plastic cuvette with a Cary 50 spectrophotometer (Varian, Inc.). Spectral analysis of colloidal suspensions was performed in the range 300-800 nm. Milli-Q H_2O was used as the blank. Mathematical determination of λ_{max} was done according to reference [55].

DLS and zeta potential

Dynamic light scattering (DLS), and zeta potential (ELS) measurements were performed using Litesizer™ 500 apparatus (Anton Paar) equipped with a 658 nm laser operating at 40 mW. The backscattered light collection angle was set at 90°. The zeta potential cuvette has a Ω-shaped capillary tube cuvette with an applied potential of 150 V. The same suspensions were used for DLS and ELS measurements. Each sample was analyzed in triplicate and each measurement was an average of three 30 s runs.

Electron microscopy

Transmission Electron Microscopy (TEM) micrographs of AuNPs and Au@AgNPs were obtained using a JEOL JEM-2100 plus LaB6 (JEOL, Japan) microscope with an acceleration voltage of 200 kV and equipped with an Orius 4 K CDD camera (Gatan, USA). STEM mode coupled with X-ray Energy-Dispersive Spectroscopy (X-EDS) was used to perform elemental mapping of the two metals (lines: Au-L and Ag-L). X-EDS analysis was realized with an Oxford Instrument SDD detector of 80 mm^2. X-ray spectra were recorded and processed with Aztec software. The samples were prepared by dropping a dilute suspension onto the carbon-coated copper grids and dried at room temperature before imagining. Size distribution

was established by counting a minimum of 4 00 particles for TEM and was determined using ImageJ Software.

Results and discussion

Nanoparticle synthesis

Prior to gold silver core-shell nanoparticles synthesis (Au@AgNPs), pure gold nanoparticles with a core of approx 14 nm (AuNPs14) were prepared following the strategy described in Figure 1, then a shell of approx. 2 nm was grown on the particles to form Au@AgNPs. A third series of colloids, pure gold but with a larger size (AuNPs16) were prepared to have particle with similar sizes when comparing the efficiencies of AuNPs and Au@AgNPs. All these colloids were first characterized by UV-Vis spectroscopy, DLS, and zeta potential measurements. The results are displayed in Figure 2. Then, particles size and distribution were estimation by Transmission Electron Microscopy observations, gathered in Figure 3.

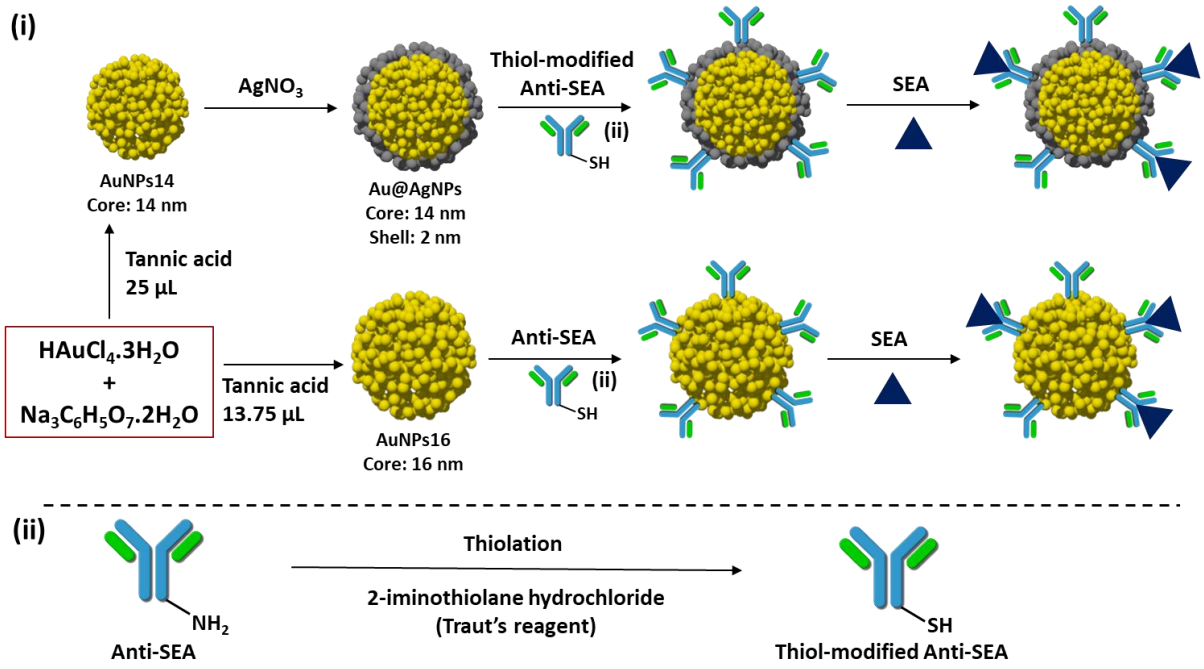

Figure 1: Strategy adopted for the synthesis of pure AuNPs and core-shell Au@AgNPs and their further bioconjugation to adsorb covalently anti-SEA antibodies.

As shown in Figure 2, both AuNP solutions are red; their LSPR bands are indeed located at 520 and 521 for AuNPs14 and AuNPs16, respectively. These values are consistent with those previously measured for gold colloids of similar size. Particle size and distribution were

confirmed by TEM observations in Figure 3, with an average size of 14.0 ± 1.5 nm, for AuNPs14, and 16.9 ± 1.8 nm, for AuNPs16.

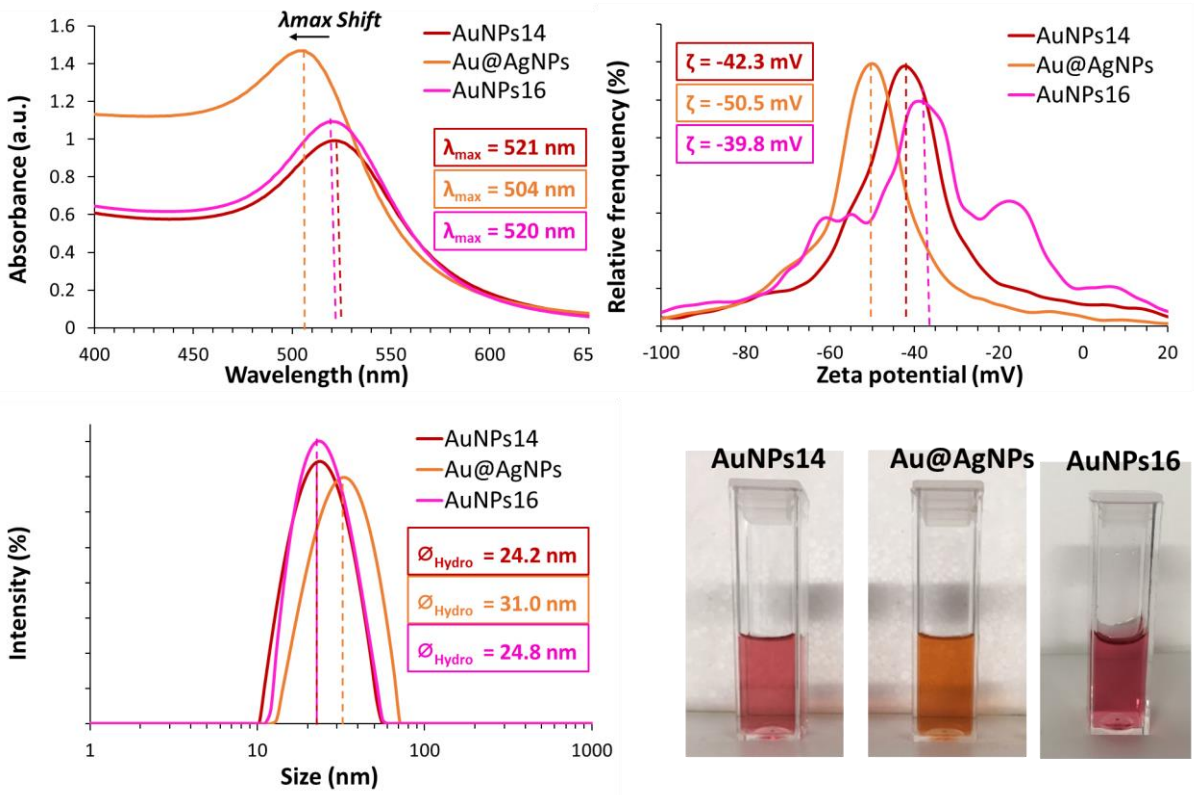

Figure 2: Characterization of pure Au and core-shell Au@Ag Nanoparticles by UV-Vis spectroscopy (A), zeta potential (B), DLS (C), and corresponding images of the solutions (D).

Upon silver growth on AuNPs14, the LSPR band is blue-shifted to 504 nm and the color of the core-shell Au@AgNPs colloidal solution turns to orange/yellow (Figure 2). This color and the position of the LSPR band are consistent with silver growth on the gold core. The average size of Au@AgNPs, deduced from TEM observations in Figure 3, were in good agreement with the growth of a silver shell of 2 nm, though slightly higher, 17.2 ± 2.0 nm.

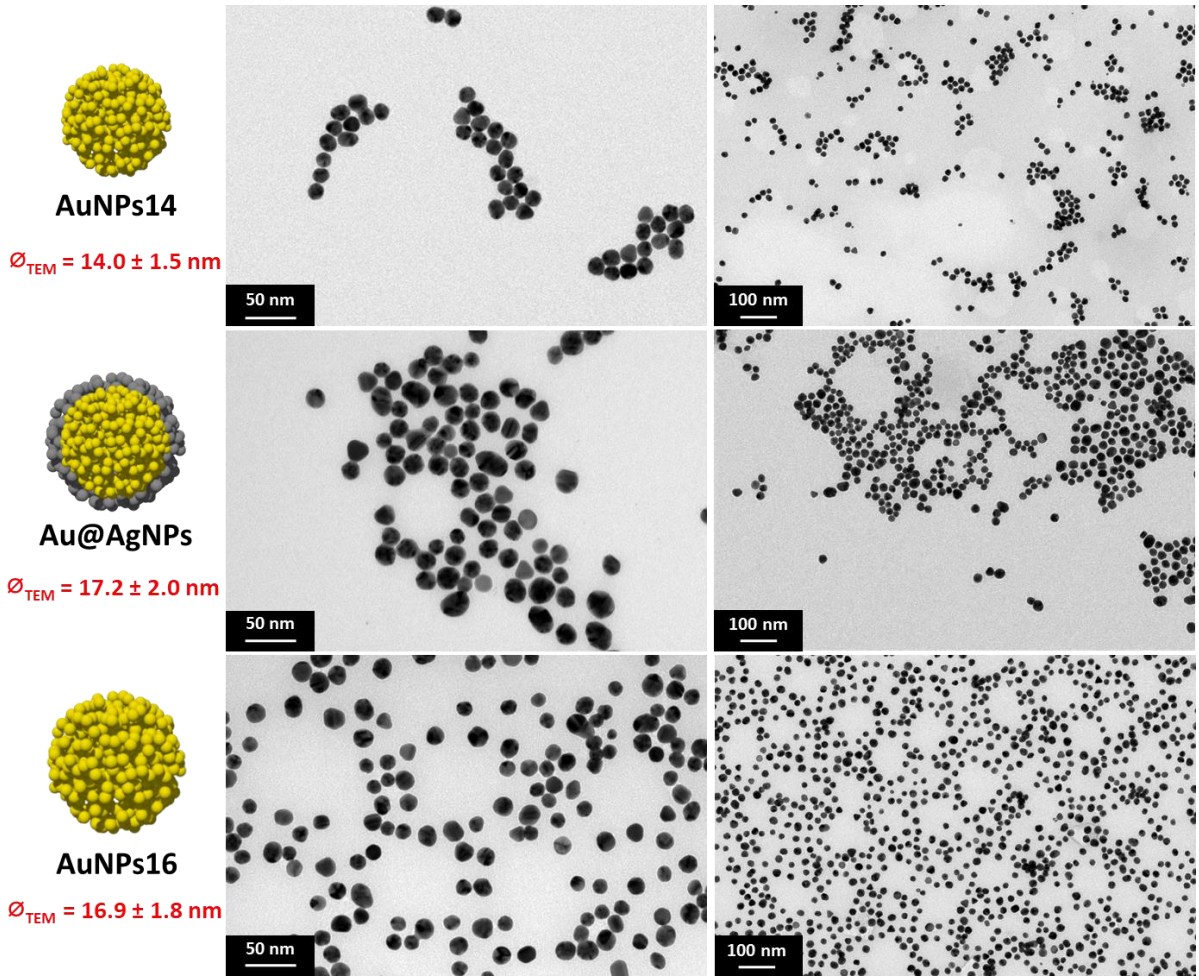

Figure 3: TEM observations of pure AuNPs and core-shell Au@Ag NPs and their average size deduced from TEM.

Zeta potential measurements shown in Figure 2, gave similar values for the two sizes of AuNPs, approx. -40 mV, a value usually observed for this material. The hydrodynamic diameters were higher than the TEM diameters (24.2 and 24.8 *vs* 14 and 16.9 nm, respectively) as the measured values include the surrounding molecules. For the core-shell Au@AgNPs, the zeta potential was more negative, approx. -50 mV, showing that silver-terminated nanoparticles require more citrates for their stabilization than gold-terminated particles of similar size. This naturally led to a higher hydrodynamic diameter for these core-shell particles, 31 nm.

To ensure their successful synthesis, Au@AgNPs, were further characterized using HR-TEM and X-EDS. The resulting TEM micrograph and STEM/X-EDS elemental mapping (Ag, Au and overlay) are shown in Figure 4.

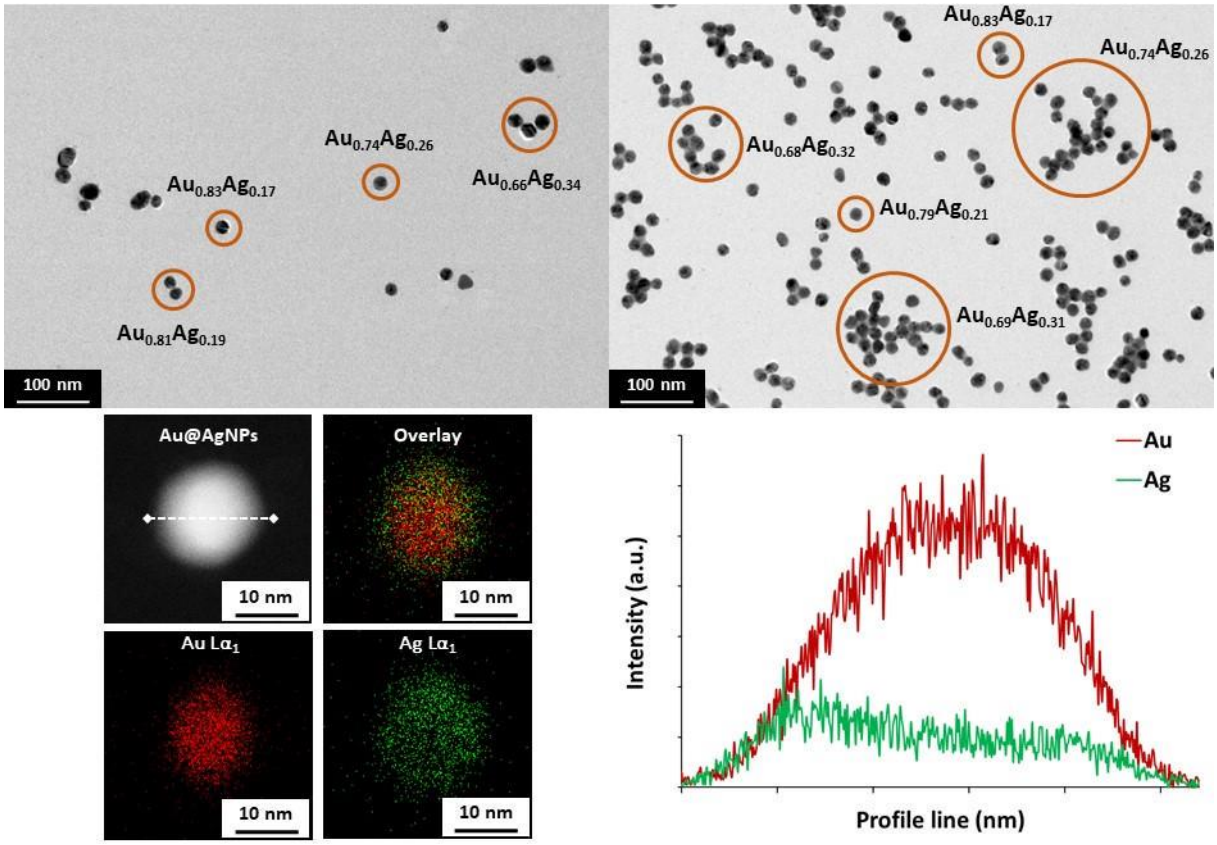

Figure 4: TEM micrograph and STEM/X-EDS elemental mapping (Ag, Au and overlay) of core-shell Au@AgNPs.

X-EDS data showed that the theoretical atomic percentages of gold and silver in Au@AgNPs, *i.e.* ≈ $Au_{0.66}Ag_{0.34}$, were perfectly verified for the grouped Au@AgNPs (≈ $Au_{0.69}Ag_{0.31}$). However, when looking at individual Au@AgNP, the amount of silver is slightly lower with an average composition ≈ $Au_{0.79}Ag_{0.21}$. This small difference may have two origins, either some small silver nanoparticles, barely detectable on the images and in the LSPR bands are formed. This first assumption is consolidated by additional experiments we ran to increase the shell size (not shown) that led to separate AgNPs in the colloidal suspension. The second assumption would be that not all the silver introduced to the solution was reduced (X-EDS analysis show the element regardless to its oxidation state). In addition, the elemental mapping (Ag, Au and overlay in Figure 4) clearly shows a relatively homogeneous layer of Silver on gold core. Therefore, we conclude that the Au@AgNPs synthesis showed to be successful.

Bioconjugate engineering

Bioconjugates Ab-NPs were engineered by attaching anti-SEA antibodies, an IgG, to either Au@AgNPs or AuNPs16 following the procedure described in Figure 1. Prior to anti-SEA

grafting on the surfaces, Traut's reagent was applied on these proteins to generate thiol groups allowing the covalent anchoring of IgG on the metallic nanoparticle surfaces by displacing the capping citrate agents. These successive steps were monitored by UV-Visible spectroscopy as shown in Figure 5. The position of the LSPR band (λmax shift) was followed by calculating the first derivative of each spectrum.

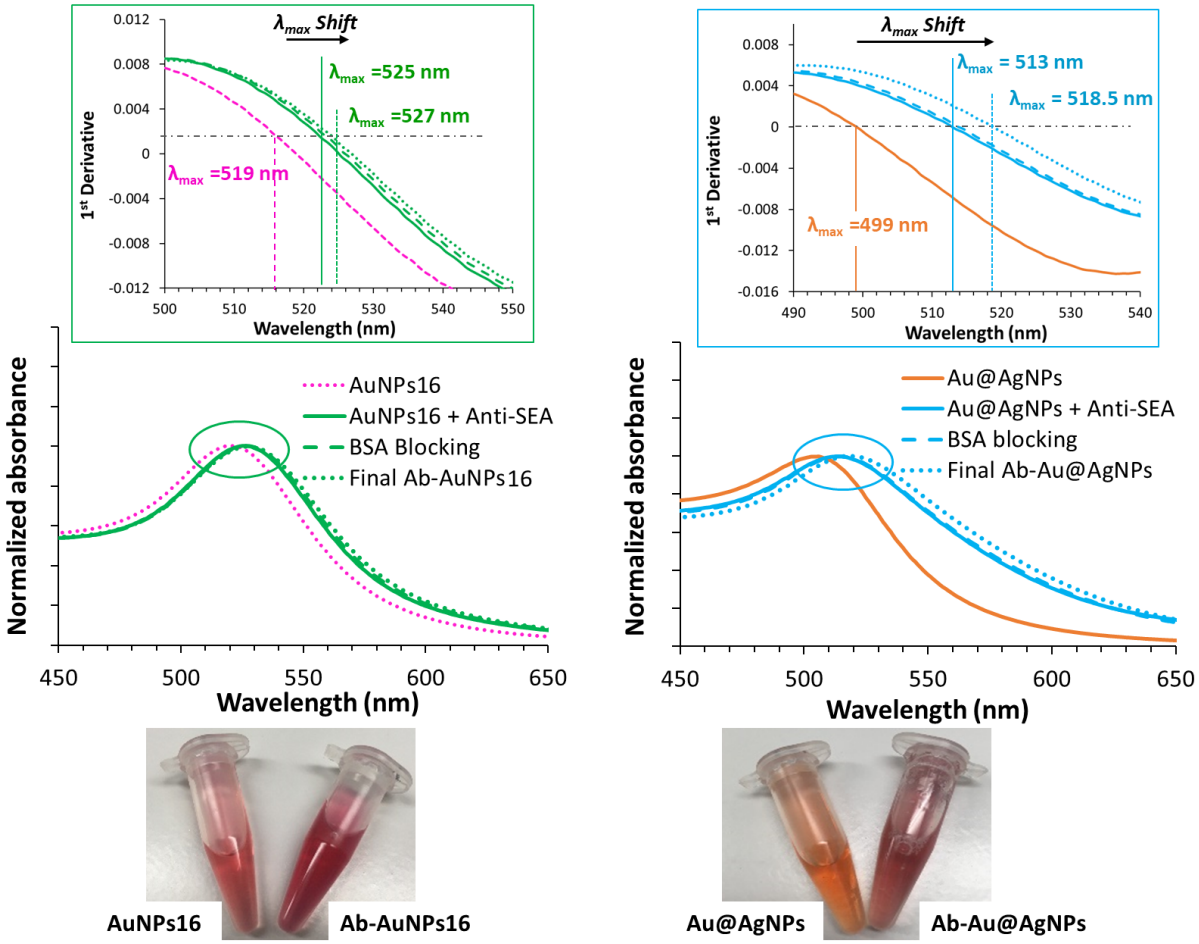

Figure 5: UV-Visible spectra recorded upon anti-SEA bioconjugation to AuNP16 (left) and to core-shell Au@AgNPs (right). The inserts (at the top) show the first derivative of the LSPR curves.

The first observation is that in identical conditions, the LSPR band red-shift was more pronounced for the core-shell Au@AgNPs compared to pure AuNPs, 6-8 nm *vs* 14-18 nm, respectively. This corroborated the assumption of better RI sensitivity for silver coated nanoparticles. In addition, and more importantly, the attachment of anti-SEA antibodies to Au@AgNPs was readily observable by naked-eye as can be seen in Figure 5. The color change for pure gold nanoparticles was less obvious as both solutions are redish. Unfortunately, the LSPR signature of the resulting Ab-Au@AgNPs bioconjugates is no longer located in the

desired wavelengths window, which compromises the visualization of SEA immunosensing. Nevertheless, we pursued the immunosensing to see whether the better sensitivity of the core-shell colloids may enhance their response to SEA recognition.

Prior to SEA immunosensing, the coverage of antibodies on each bioconjugate was estimated through the analysing of the unbound antibodies remaining in the supernatant using fluorescence assay and enzyme-linked immunosorbent assay (ELISA). This information is very important when comparing the efficiency of the bioconjugates in biosensing asit can be directly related to the amount and accessibility of the recognition sites on top of the Ab-NPs bioconjugates. ELISA test showed considerable differences in the ratio Ab/NP for AuNPs16 and Au@AgNPs. Surprisingly, this ratio appeared to be higher for AuNPs despite a lower shift in the LSPR band. Indeed, for pure gold nanoparticles, the ratio Anti-SEA/AuNP was equal to 28 ± 1, while for the core-shell nanoparticles, Anti-SEA/Au@AgNPs was 20 ± 1, 30 % lower.

The reactivity of silver and gold towards thiol groups is supposed to be similar, yet, we can expect slight differences, which may influence the coverage on the nanoparticles. As stated above, the amount of citrates needed to stabilize Au@AgNPs was higher than that required for AuNPs of the same size. This may be at the origin of this difference in coverages. It is also important to note that the ELISA analysis was performed for the supernatant, and this method has been shown to overestimate the amount of adsorbed antibodies.

SEA immunosensing

In this experiment, the positions of the LSPR bands of the colloidal solutions of Ab-Au@AgNPs and Ab-AuNPs were monitored over time upon addition of increasing amounts of SEA in the range 10 to 500 ng/mL (Figure 6). A progressive shift of the LSPR band was observed and a dose-response curve was established by plotting the band shift $\Delta\lambda$ measured after stabilization versus the concentration of analyte. (Figure 6)

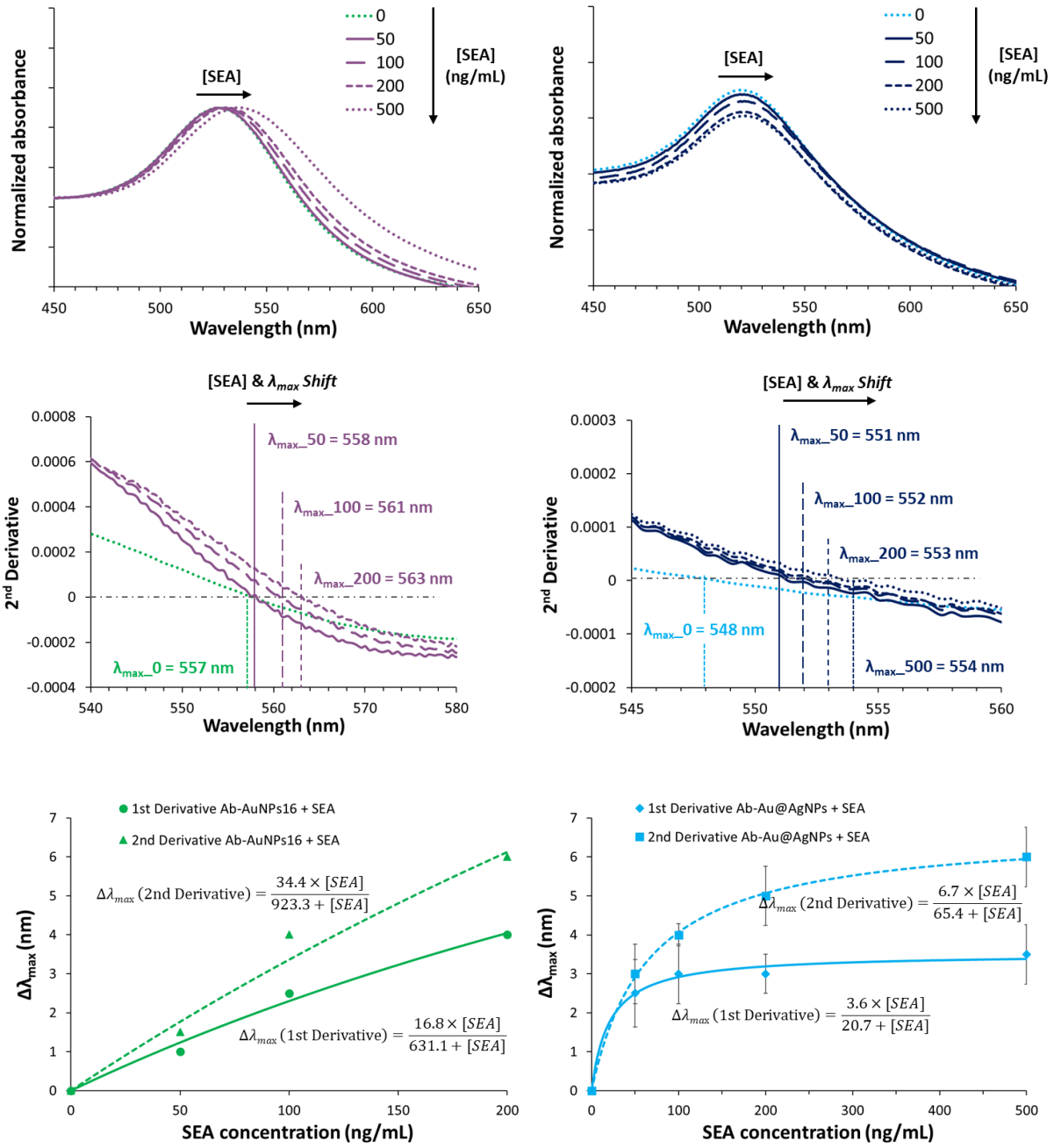

Figure 6. UV-Visible spectra and dose-response curves obtained upon LSPR immunosensing of SEA, by Ab-AuNP16 bioconjugates (left), and by Ab-Au@AgNPs bioconjugates (right). For the first and second derivative, Langmuir fit was applied and the equation was added to the figure.

Following the first and second derivative to assess SEA recognition led to an important enhancement of the sensitivity compared to our previously published data SEA [20]. Yet, at this step, no remarkable differences were observed on the responses of AuNPs and Au@AgNPs bioconjugates. Though the saturation coverage does not seem to be reached on pure gold, the overall values seem close. In addition, we were not able to visualize any color change because

of the relatively small red-shifts (<6 nm) seen in Figure 6, which confirms the predictions made above stating that the LSPR band of the Ab-Au@AgNPs was shifted outside the desired window for naked-eye sensing.

Conclusions

Core-shell gold silver nanoparticle-antibody bioconjugate (Ab-Au@AgNPs) were engineered by covalently linking anti-SEA antibody to Au@AgNPs using Traut's reagent. The core-shell nanoparticles were engineered by growing a thin layer of silver on citrate-capped gold nanoparticles. These bioconjugates were applied to the immunosensing of Staphylococcal enterotoxin A (SEA) by localized surface plasmon resonance (LSPR). Similar bioconjugates on pure AuNPs of the same size were also prepared to evidence the input of the silver shell. This input was twofold as the RI index sensitivity showed to be higher, and the wavelength window allowed visualizing biomolecules attachments on the Au@AgNPs. Indeed, starting from the antibody conjugation step, the LSPR band of Au@AgNPs nanoparticles was largely red-shifted. This led to the color change of the colloidal solution, initially orange, that visually turned to red. We therefore were able to visualize by naked-eye, antibodies attachment on the Au@AgNPs. Yet, this red shift was very important and moved the LSPR band outside the window targeted in this work. Therefore, no color change detectable by naked-eye was observed upon subsequent immunosensing of SEA. Our ongoing work is focusing on the relocation of the bioconjugates within the desired window through a different bimetallic structure or by reducing the antibodies size.

References

1. Elghanian, R., et al., *Selective Colorimetric Detection of Polynucleotides Based on the Distance-Dependent Optical Properties of Gold Nanoparticles.* Science, 1997. **277**(5329): p. 1078.
2. Daniel, M.-C. and D. Astruc, *Gold nanoparticles: assembly, supramolecular chemistry, quantum-size-related properties, and applications toward biology, catalysis, and nanotechnology*. Chemical reviews, 2004. **104**(1): p. 293-346.
3. Stuart, D.A., et al. *Biological applications of localised surface plasmonic phenomenae*. IEE Proceedings - Nanobiotechnology, 2005. **152**, 13-32.

4. Anker, J.N., et al., *Biosensing with plasmonic nanosensors.* Nature Materials, 2008. **7**: p. 442.
5. Hui, S., *Plasmonic nanoparticles: Towards the fabrication of biosensors.* IOP Conference Series: Materials Science and Engineering, 2015. **87**(1): p. 012009.
6. Gopinath, S.C.B., *Biosensing applications of surface plasmon resonance-based Biacore technology.* Sensors and Actuators B: Chemical, 2010. **150**(2): p. 722-733.
7. Mayer, K.M. and J.H. Hafner, *Localized Surface Plasmon Resonance Sensors.* Chemical Reviews, 2011. **111**(6): p. 3828-3857.
8. Chen, P., et al., *Inflection Point of the Localized Surface Plasmon Resonance Peak: A General Method to Improve the Sensitivity.* ACS Sensors, 2017. **2**(2): p. 235-242.
9. Lee, K.-S. and M.A. El-Sayed, *Gold and Silver Nanoparticles in Sensing and Imaging: Sensitivity of Plasmon Response to Size, Shape, and Metal Composition.* The Journal of Physical Chemistry B, 2006. **110**(39): p. 19220-19225.
10. Rycenga, M., et al., *Controlling the Synthesis and Assembly of Silver Nanostructures for Plasmonic Applications.* Chemical Reviews, 2011. **111**(6): p. 3669-3712.
11. Huang, X. and M.A. El-Sayed, *Gold nanoparticles: optical properties and implementations in cancer diagnosis and photothermal therapy.* Journal of advanced research, 2010. **1**(1): p. 13-28.
12. Mortazavi, D., et al. *Nano-plasmonic biosensors: A review*. in *The 2011 IEEE/ICME International Conference on Complex Medical Engineering*. 2011.
13. Zhao, J., et al., *Localized surface plasmon resonance biosensors.* Nanomedicine, 2006. **1**(2): p. 219-228.
14. Sepúlveda, B., et al., *LSPR-based nanobiosensors.* Nano Today, 2009. **4**(3): p. 244-251.
15. Petryayeva, E. and U.J. Krull, *Localized surface plasmon resonance: Nanostructures, bioassays and biosensing—A review.* Analytica Chimica Acta, 2011. **706**(1): p. 8-24.
16. Guo, X., *Surface plasmon resonance based biosensor technique: A review.* Journal of Biophotonics, 2012. **5**(7): p. 483-501.
17. Steinbrück, A., et al., *Sensoric potential of gold–silver core–shell nanoparticles.* Analytical and Bioanalytical Chemistry, 2011. **401**(4): p. 1241.
18. Lu, L., et al., *Core–shell gold/silver nanoparticles: Synthesis and optical properties.* Journal of Colloid and Interface Science, 2013. **392**: p. 90-95.
19. Sotiriou, G.A., et al., *Plasmonic biocompatible silver–gold alloyed nanoparticles.* Chemical Communications, 2014. **50**(88): p. 13559-13562.

20. Ben Haddada, M., et al., *Gold nanoparticle-based localized surface plasmon immunosensor for staphylococcal enterotoxin A (SEA) detection.* Analytical and Bioanalytical Chemistry, 2017. **409**(26): p. 6227-6234.
21. Liu, S., et al., *Synthesis of monodisperse Au, Ag, and Au–Ag alloy nanoparticles with tunable size and surface plasmon resonance frequency.* Chemistry of Materials, 2011. **23**(18): p. 4098-4101.
22. Shi, W., et al., *Synthesis and characterization of gold nanoparticles with plasmon absorbance wavelength tunable from visible to near infrared region.* ISRN Nanomaterials, 2012. **2012**.
23. Noguez, C., *Surface plasmons on metal nanoparticles: the influence of shape and physical environment.* The Journal of Physical Chemistry C, 2007. **111**(10): p. 3806-3819.
24. Lee, K.-C., et al., *Size effect of Ag nanoparticles on surface plasmon resonance.* Surface and Coatings Technology, 2008. **202**(22-23): p. 5339-5342.
25. Eustis, S. and M.A. El-Sayed, *Why gold nanoparticles are more precious than pretty gold: Noble metal surface plasmon resonance and its enhancement of the radiative and nonradiative properties of nanocrystals of different shapes.* Chemical Society Reviews, 2006. **35**(3): p. 209-217.
26. Lismont, M. and L. Dreesen, *Comparative study of Ag and Au nanoparticles biosensors based on surface plasmon resonance phenomenon.* Materials Science and Engineering: C, 2012. **32**(6): p. 1437-1442.
27. Boisselier, E. and D. Astruc, *Gold nanoparticles in nanomedicine: preparations, imaging, diagnostics, therapies and toxicity.* Chemical society reviews, 2009. **38**(6): p. 1759-1782.
28. Dreaden, E.C., et al., *The golden age: gold nanoparticles for biomedicine.* Chemical Society Reviews, 2012. **41**(7): p. 2740-2779.
29. Sastry, M., et al., *Optical Absorption Study of the Biotin−Avidin Interaction on Colloidal Silver and Gold Particles.* Langmuir, 1998. **14**(15): p. 4138-4142.
30. Jakab, A., et al., *Highly Sensitive Plasmonic Silver Nanorods.* ACS Nano, 2011. **5**(9): p. 6880-6885.
31. Navas, M.P. and R.K. Soni, *Laser generated Ag and Ag–Au composite nanoparticles for refractive index sensor.* Applied Physics A, 2014. **116**(3): p. 879-886.
32. Navas, M.P. and R.K. Soni, *Laser-Generated Bimetallic Ag-Au and Ag-Cu Core-Shell Nanoparticles for Refractive Index Sensing.* Plasmonics, 2015. **10**(3): p. 681-690.

33. Morriss, R.H. and L.F. Collins, *Optical Properties of Multilayer Colloids.* The Journal of Chemical Physics, 1964. **41**(11): p. 3357-3363.
34. Yang, X., et al., *A sensitive hydrogen peroxide and glucose biosensor based on gold/silver core–shell nanorods.* Electrochimica Acta, 2013. **108**: p. 39-44.
35. Lu, L., et al., *Seed-mediated growth of large, monodisperse core-shell gold-silver nanoparticles with Ag-like optical properties.* Chemical Communications, 2002(2): p. 144-145.
36. Dong, P., et al., *Plasmonic Biosensor Based on Triangular Au/Ag and Au/Ag/Au Core/Shell Nanoprisms onto Indium Tin Oxide Glass.* Plasmonics, 2013. **8**(4): p. 1577-1583.
37. Sun, L., et al., *The use of gold-silver core-shell nanorods self-assembled on a glass substrate can substantially improve the performance of plasmonic affinity biosensors.* Microchimica Acta, 2014. **181**(15): p. 1991-1997.
38. Hao, J., et al., *High-Throughput Sulfide Sensing with Colorimetric Analysis of Single Au–Ag Core–Shell Nanoparticles.* Analytical Chemistry, 2014. **86**(10): p. 4663-4667.
39. Yan, W., et al., *Engineered "hot" core–shell nanostructures for patterned detection of chloramphenicol.* Biosensors and Bioelectronics, 2016. **78**: p. 67-72.
40. Mao, K., et al., *A novel colorimetric biosensor based on non-aggregated Au@Ag core–shell nanoparticles for methamphetamine and cocaine detection.* Talanta, 2017. **175**: p. 338-346.
41. Le Loir, Y., F. Baron, and M. Gautier, *Staphylococcus aureus and food poisoning.* Genet Mol Res, 2003. **2**(1): p. 63-76.
42. Boujday, S., et al., *Detection of pathogenic Staphylococcus aureus bacteria by gold based immunosensors.* Microchimica Acta, 2008. **163**(3-4): p. 203.
43. Salmain, M., et al., *Piezoelectric immunosensor for direct and rapid detection of staphylococcal enterotoxin A (SEA) at the ng level.* Biosensors and Bioelectronics, 2011. **29**(1): p. 140-144.
44. Salmain, M., et al., *Elaboration of a reusable immunosensor for the detection of staphylococcal enterotoxin A (SEA) in milk with a quartz crystal microbalance.* Sensors and Actuators B: Chemical, 2012. **173**: p. 148-156.
45. Ben Haddada, M., M. Salmain, and S. Boujday, *Gold colloid-nanostructured surfaces for enhanced piezoelectric immunosensing of staphylococcal enterotoxin A.* Sensors and Actuators B: Chemical, 2018. **255**: p. 1604-1613.

46. Schantz, E.J., et al., *Purification and some chemical and physical properties of staphylococcal enterotoxin A.* Biochemistry, 1972. **11**(3): p. 360-366.
47. Rong-Hwa, S., et al., *Gold nanoparticle-based lateral flow assay for detection of staphylococcal enterotoxin B.* Food Chemistry, 2010. **118**(2): p. 462-466.
48. Wang, W., et al., *Gold-Nanoparticle-Based Multiplexed Immunochromatographic Strip for Simultaneous Detection of Staphylococcal Enterotoxin A, B, C, D, and E.* Particle & Particle Systems Characterization, 2016. **33**(7): p. 388-395.
49. Wang, X., et al., *Gold nanorod biochip functionalization by antibody thiolation.* Talanta, 2015. **136**: p. 1-8.
50. Slot, J.W. and H.J. Geuze, *A method to prepare isodisperse colloidal gold sols in the size range 3–17 NM.* Ultramicroscopy, 1984. **15**(4): p. 383.
51. Bastús, N.G., et al., *Synthesis of Highly Monodisperse Citrate-Stabilized Silver Nanoparticles of up to 200 nm: Kinetic Control and Catalytic Properties.* Chemistry of Materials, 2014. **26**(9): p. 2836-2846.
52. Wang, X., et al., *Comparison of four methods for the biofunctionalization of gold nanorods by the introduction of sulfhydryl groups to antibodies.* Beilstein Journal of Nanotechnology, 2017. **8**: p. 372-380.
53. Hermanson, G.T., *Chapter 1 - Functional Targets*, in *Bioconjugate Techniques (Second Edition)*, G.T. Hermanson, Editor. 2008, Academic Press: New York. p. 1-168.
54. Hermanson, G.T., *Chapter 24 - Preparation of Colloidal Gold-Labeled Proteins*, in *Bioconjugate Techniques (Second Edition)*, G.T. Hermanson, Editor. 2007, Academic Press: New York. p. 924-935.
55. Chen, P. and B. Liedberg, *Curvature of the Localized Surface Plasmon Resonance Peak.* Analytical Chemistry, 2014. **86**(15): p. 7399-7405.
56. Haiss, W., et al., *Determination of Size and Concentration of Gold Nanoparticles from UV−Vis Spectra.* Analytical Chemistry, 2007. **79**(11): p. 4215-4221.

Supporting information for

Core-shell Gold Silver Nanoparticles for Plasmonic Biosensing of Toxins: Towards Naked-eye Detection

Lu Zhang[1,2,3,4], Alexis Loiseau[2], David Hu[2], Michèle Salmain[2], Bo Liedberg[3,], Souhir Boujday[1,*]*

[1] Sorbonne Université, CNRS, Laboratoire de Réactivité de Surface (LRS), 4 place Jussieu, F-75005 Paris, France.

[2]Sorbonne Université, CNRS, Institut Parisien de Chimie Moléculaire (IPCM), 4 place Jussieu F-75005 Paris, France.

[3]Centre for Biomimetic Sensor Science, School of Materials Science and Engineering, Nanyang Technological University, Singapore 637553.

[4] Sorbonne University and Nanyang Technological University Dual Degree PhD Programme.

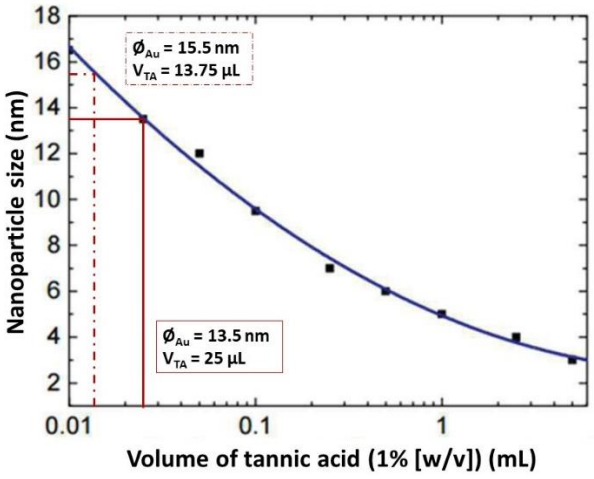

Figure S1: Effect of the TA concentration (1% [w/v]) in the reducing solution on AuNPs size [50].

Equation S2: Calculation of AuNPs concentration.

Theoretical method:

Starting from a known concentration and assuming that the reduction of the gold (III) is complete, the concentration can be deduced from the ratio number of Au atom/number of Au atoms per particle as follow:

$$\boldsymbol{C(AuNPs)_{theo}} = \frac{N_{Total}}{N_{Au/p} \times V_{Total} \times \mathcal{N}_A} = \frac{n(Au)_{Final}}{N_{Au/p} \times V_{Total}} = \frac{[Au]_{Final}}{N_{Au/p}} = \mathbf{3.34 \times 10^{-9}\ mol.L^{-1}}$$

Experimental method:

- N_{Total} = Total number of Au atoms = $n(Au)_{Final}$ x $\mathcal{N}_A$ = 2.539 x 10^{-5} x $\mathcal{N}_A$ atoms
- V_{Total} = 100 mL
- $[Au]_{Final} = \frac{n(Au)_{Final}}{V_{Total}}$ = 2.539 x 10^{-4} M
- $N_{Au/p}$ = Number of Au atoms per particle = $N_{Au/p} = \frac{V_{AuNP}}{V_{Au\_atom}}$ = 76017.5 atoms
  - $V_{AuNP} = \frac{\pi \times D^3}{6}$ with D = average diameter = 13.5 nm (volume of Au core NP)
  - $V_{Au\_atom} = \frac{M_{Au}}{\mathcal{N}_A \times \rho_{Au}}$ with M_{Au} = 197 g.mol^{-1} ; ρ_{Au} = 19.31 g.cm^{-3} ; $\mathcal{N}_A$ = 6.02 x 10^{23} atoms.mol^{-1} (volume of Au atom)

Using the absorbance and the diameter of AuNPs [56]:

$$N = \frac{A(450) \times 10^{14}}{D^2[-0.295 + 1.36 \times exp^{\left(-\left(\frac{D-96.8}{78.2}\right)^2\right)}]} = 2.330 \times 10^{12}\ \text{NP.mL}^{-1} = 3.874 \times 10^{-12}\ \text{mol.mL}^{-1}$$

- A(450) =absorbance = 0.60477
- D = 13.5 nm

$$\boldsymbol{N = C(AuNPs)_{exp} = 3.874 \times 10^{-9}\ mol.L^{-1}}$$

Equation S3: Calculation to determine the Ag shell thickness on AuNPs.

The silver amount involved to obtain a silver shell uniform thickness of 2 nm assuming that the average size of gold core was 13.5 nm and form Au-Ag core-shell NPs with 15.5 nm in diameter was described as follow:

$$V_{Ag\_shell} = \frac{\pi \times D^3}{6} = \frac{\pi \times D_{(Au+Ag)}{}^3}{6} - \frac{\pi \times D_{(Au)}{}^3}{6} = \frac{\pi}{6}(15.5^3 - 13.5^3) = 661.57 \text{ nm}^3$$

$$V_{Ag\_atom} = \frac{M_{Ag}}{\mathcal{N}_A \text{ x } \rho_{Ag}} = 1.71 \times 10^{-2} \text{ nm}^3/\text{atom}$$

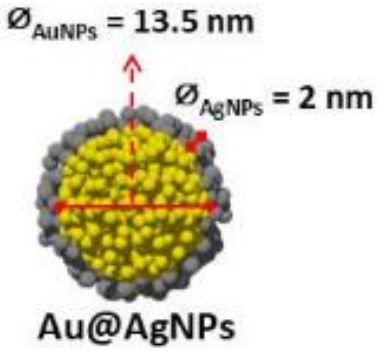

$$N_{Ag/p} = \frac{V_{Ag\_shell}}{V_{Ag\_atom}} = 38665.52 \text{ atoms}$$

$$N_{Au/p} = \frac{V_{AuNP}}{V_{Au\_atom}} = 76017.5 \text{ atoms}$$

$$\frac{n_{Ag^+}}{n_{Au^{3+}}} = \frac{C_{Ag^+} \times V_{Ag^+}}{C_{Au^{3+}} \times V_{Au^{3+}}} = \frac{N_{Ag/p}}{N_{Au/p}}$$

$$\boldsymbol{V_{Ag^+}} = \frac{N_{Ag/p}}{N_{Au/p}} \times \frac{C_{Au^{3+}} \times V_{Au^{3+}}}{C_{Ag^+}} = \frac{38665.52}{76017.5} \times \frac{0.2539 \times 20}{10} = \mathbf{0.258 \text{ mL}}$$

Theoretical chemical composition: **$Au_{0.66}Ag_{0.34}$**

- V_{Ag_shell}: Volume of Ag shell thickness
- $D_{(Au+Ag)}$: Diameter of Au@AgNP core-shell NP
- $D_{(Au)}$: Diameter of AuNP core NP
- V_{Ag_atom}: Volume of Ag atom with M_{Au} = 107.87 g.mol^{-1}, ρ_{Au} = 10.47 g.cm^{-3} ; $\mathcal{N}_A$ = 6.02 x 10^{23} atoms.mol^{-1}
- $N_{Ag/p}$: Number of Ag atoms per particle
- $N_{Ag/p}$: Number of Au atoms per particle
- $C_{Au}{}^{3+}$ = 0.2539 mM ; $C_{Ag}{}^{+}$ = 10 mM ; $V_{Au}{}^{3+}$ = 20 mL

Equation S4: Calculation of the Ab/NPs ratio.

Before bioconjugation (3 mL):

[AuNPs16] = 3.3 nM

[Au@AgNPs] = 6.3 nM

$[anti\text{-}SEA]_{initial}$ = 32.7 μg/mL = 218 nM

After bioconjugation of AuNPs16 (2 mL):

$[anti\text{-}SEA]_{supernatant}$ = 19.7 μg/mL = 131.3 nM

$[anti\text{-}SEA]_{grafted}$ = 218 – 131.3 = 86.7 nM

[AuNPs16] = 3 nM

anti-SEA/AuNPs16 = 86.7 / 3.3 = 28

After bioconjugation of Au@AgNPs (2 mL):

$[anti\text{-}SEA]_{supernatant}$ = 17.7μg/mL = 117.9 nM

$[anti\text{-}SEA]_{grafted}$ = 218 – 117.9 = 100.1 nM

[Au@AgNPs] = 5.1 nM

anti-SEA/Au@AgNPs = 100.1 / 6.3 = 20

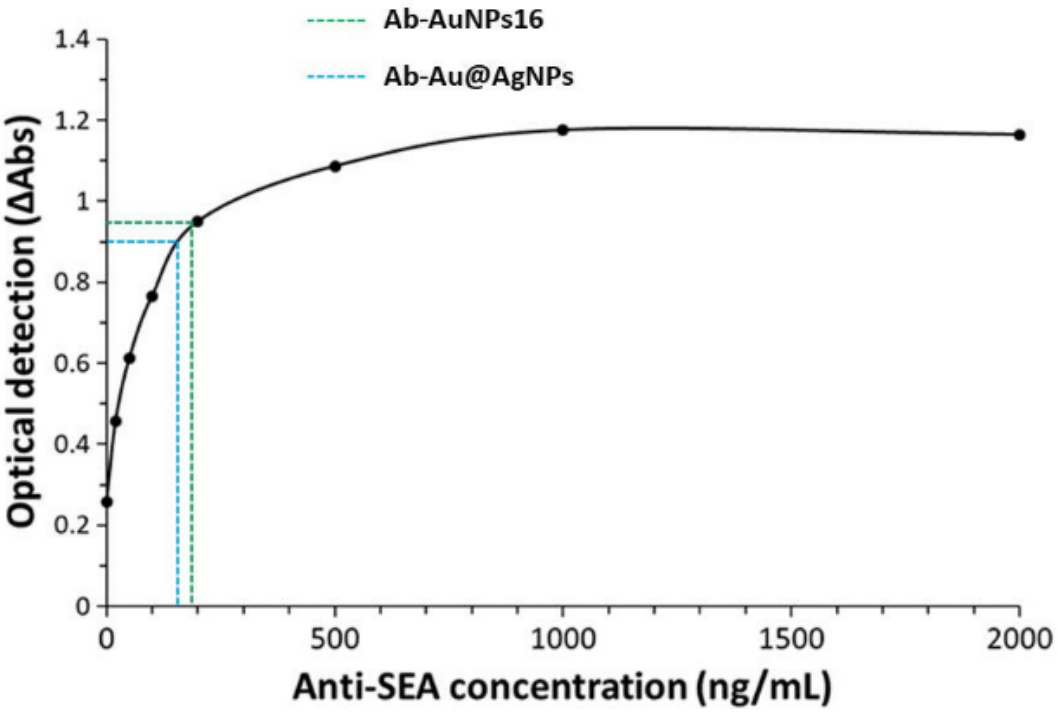

Figure S2: Standard curve for quantifying anti-SEA in the supernatant by ELISA.

General Conclusions and Perspectives

The objective of this work was to develop biosensing devices based on plasmonic nanoparticles from which detection of bacterial toxin SEA could be achieved by naked-eye readout.

First of all, a survey of the recent literature, presented in Paper I, was carried out and highlighted the different strategies employed for conjugation of antibody (Ab) to gold nanoparticles (AuNPs). Besides, several approaches to quantify the surface coverage of antibodies on AuNP and selected applications of AuNP-Ab bioconjugates in optical biosensing were presented. Subsequently, we developed a fluorescence-based method for direct quantification of Ab surface coverage on AuNPs, described in Paper II. By comparison with the indirect quantification methods, the developed method gave an accurate Ab surface coverage. Typically, IgG adsorption on AuNPs with a diameter of 15 nm led to a coverage of 4 IgGs/AuNP *via* either chemi- or physisorption, a value much lower than previously published data, based on indirect methods that led to an over-estimation of Ab coverage.

Then we proceeded to develop biosensing platforms where two strategies have been implemented. The first was based on the extremely high extinction coefficient of plasmonic nanoparticles. And the second relied on sensitivity of the Localized Surface Plasmon Resonance (LSPR) band to local refractive index change on plasmonic nanoparticles.

In the first strategy, detailed in Paper III, Ab-conjugated AuNPs were used as reporters in a solid-phase, sandwich-type, colorimetric immunosensor. The sensor was successfully applied to the detection of SEA in buffer then in spiked milk. As low as 1 ng SEA could be visualized by naked-eye detection. Using a benchtop UV-Vis spectrometer, a limit of detection of 1.5 ng/mL was achieved which is lower than that obtained by quartz crystal microbalance (QCM).

Following the same strategy, nanoparticles with higher extinction coefficient were applied to improve the biosensing sensitivity, here hollow gold nanoshell (AuNS) as described in the paper IV. These nano-objects are prepared by galvanic replacement starting from silver colloids in relatively acidic medium. Surprisingly, upon raising the pH close to isoelectric point (pI) of Ab for antibodies physisorption (pH 8-9), the colloidal solution color changed immediately and dramatically. This irreversible pH triggered phenomenon has been studied in-depth. Through UV-Visible analysis and HR-TEM this was attributed to the nanoconfinement effect of AuNS

that favored the pH-triggered reduction and deposition of silver preferentially inside AuNS. While addition of extra silver ions, after the inside volume of AuNS was filled, the silver ions was reduced and deposited on external wall of AuNS. The finding obtained herein is expected to contribute to a fundamental understanding of spatially controlled reactions at the nanoscale.

In the second strategy, the approach relied on both the sensitivity of plasmonic nanoparticles to small local refractive index change and the ability of humans to visualize color changes in the 500 nm region was attempted. For this purpose, core-shell gold silver nanoparticles (Au@AgNPs) with LSPR band at 500 nm were successfully synthesized. After conjugation of Ab, the LSPR band of nanoparticles red-shifted and the color of the colloidal solution, initially orange, visually changed to red. We therefore were able to visualize by naked-eye, antibodies attachment on the Au@AgNPs. Yet, the red shift was very important and no color change detectable by naked-eye was observed upon subsequent addition of SEA.

The optimization of bioconjugates, including the biorecognition elements and the nanoparticles, is still required to meet the demands of sensitive detection of target by naked-eye. For instance, further miniaturization of Ab should allow increment of binding sites on nanoparticle surface. On the side of nanoparticles, gold nanorods (AuNR) with a higher extinction coefficient could also be applied instead of spherical AuNP in the first strategy. An intense dot visualized by naked-eye and lower LOD are expected. The nanoconfinement of AuNS could be applied to tune the LSPR band precisely thereby allowing bioconjugates with starting LSPR band at around 500 nm to be applied for SEA detection to give a detectable color change by naked-eye.

The strategies mentioned above are not limited to SEA detection, by applying other antibodies, a wide diversity of antigens could be detected. Assays can be also further integrated into mobile phones or computers for real-time monitoring and obtaining quantitative information of target. The nanoparticles can also be immobilized on surface for potential “on chip” biosensing applications and thereby induce more advantages. For example, the immobilized nanoparticles could undergo more intense chemical and physical modification, like plasma treatment or exposure to highly alkali or acidic conditions. It also introduces more useful multiplexing capacities.